Functional Nanocomposite Surfaces for Antibacterial, Oil–Water Separation, and Optical Applications

RITCHIE, ANGUS,WILLIAM

Functional Nanocomposite Surfaces for Antibacterial, Oil–Water Separation, and Optical Applications

Angus William Ritchie

PhD Thesis

Department of Chemistry

Durham University

2020

Declaration

The work contained within this thesis was carried out at the Department of Chemistry, Durham University between October 2015 and March 2019. It is the original work of the author (except where otherwise stated) and has not been submitted for a degree at this or any other university.

H. J. Cox (Department of Chemistry, Durham University), S. N. Barrientos-Palomo (Department of Chemistry, Durham University), and Dr G. J. Sharples (Department of Biosciences, Durham University) performed antibacterial testing in Chapter 3. P. Garg (Department of Chemistry and Centre of Advanced Studies in Chemistry, Panjab University, India) synthesised metallosurfactants used in Chapter 4. S. N. Barrientos-Palomo, P. Garg, and Dr G. J. Sharples performed antibacterial testing in Chapter 4. I. Castañeda-Montes (Department of Chemistry, Durham University) acquired infrared spectra in Chapters 4 and 5. A. Carletto (Department of Chemistry, Durham University) deposited poly(maleic anhydride) and poly(2-(trifluoromethyl)maleic anhydride) films used in Appendix 1. All contributions from the above to data within figures are credited in the respective figure captions throughout the thesis.

Statement of Copyright

Acknowledgements

I would like to thank my supervisor Professor Jas Pal Badyal FRS for giving me the opportunity to carry out this PhD project and for his advice and guidance throughout.

I would also like to thank all of the members of Lab 98, past and present, for their help, advice, and friendship throughout my time in Durham: James Wigzell, Matt Wilson, Bekah Fraser, Andrea Carletto, Hannah Blacknell, Matthew Harris, Rajesh Chellappan, Samantha Barrientos-Palomo, Isaias Castañeda-Montes, Vera Bieber, Harry Cox, Indranee Das, Kamal Malhotra, Preeti Garg, Julius Downing, Natalie Mitchell, Katherine McGinn, Pippa Edge, and Jing Li.

I'm also very grateful to the following excellent technical staff in the workshops for making and repairing the glassware and equipment used, without which the work in this thesis would not have been possible: the glassblowers Malcolm Richardson and Aaron Brown; Kelvin Appleby, Bryan Denton, and Omer Ekinoglu in the electronic workshop; and Neil Holmes and Paul White in the mechanical workshop.

Thanks also go to Dr Gary J. Sharples of the Department of Biosciences at Durham University for his help with the antibacterial testing; Tracey Davey at the University of Newcastle for training me on the SEM; and Professor Jun Jie Wu of the Department of Engineering at Durham University for providing access to the microindentation equipment.

Outside of chemistry I am lucky to have made great friends through Ustinov College. I would like to acknowledge all of the friends that I have made during my PhD but would particularly like to thank Caren Hanßmann, Kumi Nakadate, Magdalena Garzón Fonseca, Rushil Seegolam, and Stephen Burrell, my flatmates in Elm, and to Stephen Rouse, my flatmate thereafter, for the many great moments shared.

Playing for Ustinov College Association Football Club provided a welcome distraction from the lab and allowed me to meet some amazing people, share many enjoyable moments, and to form great friendships. I would like to thank everyone I met through football with particular thanks to Alex Hudson, Bruce Rawlings, Craig Withers, Dani Hölck, Daniel O'Riordan, Dzulfian Syafrian, Eddy Walter, Jeroen Tummers, Matty Bainbridge, Menno de Jong, Pete Quinn, Rob Wardle, and Rodrigo Matus.

Finally, I would like to thank friends and family back home, especially my mum, for their constant support throughout my PhD. Special thanks to my partner Magdalena for her great support and encouragement throughout the writing of this thesis.

List of Publications

Arising from Thesis

Work in this thesis has been published as follows:

1. “Bioinspired Multifunctional Polymer–Nanoparticle–Surfactant Complex Nanocomposite Surfaces for Antibacterial Oil–Water Separation” Ritchie, A. W.; Cox, H. J.; Barrientos-Palomo, S. N.; Sharples, G. J.; Badyal, J. P. S. *Colloids Surf., A* **2019**, *560*, 352–359.

Collaborative Publications

1. “Palladium–Poly(Ionic Liquid) Membranes for Permselective Sonochemical Flow Catalysis” Wilson, M.; Kore, R.; Ritchie, A. W.; Fraser, R. C.; Beaumont, S. K.; Srivastava, R.; Badyal, J. P. S. *Colloids Surf., A* **2018**, *545*, 78–85.
2. “Atomised Spray Plasma Deposition of Hierarchical Superhydrophobic Nanocomposite Surfaces” Castaneda-Montes, I.; Ritchie, A. W.; Badyal, J. P. S. *Colloids Surf., A* **2018**, *558*, 192–199.

Patents

1. Ritchie, A. W.; Badyal, J. P. S. International Publication Number WO 2018/096327 A1

Abstract

Surface functionalisation can be used to modify the interaction between liquids and solid surfaces which is of importance in many applications such as self-cleaning, anti-fouling, and anti-fogging. The use of nanocomposite materials also provides a way of improving particular properties of the film even when small amounts of nano-material is used. The use of nanocomposite coatings to tailor the wettability, as well as to incorporate additional properties into surface coatings has been studied in this thesis for antibacterial, oil–water separation, and optical applications.

Chapter 1 provides an introduction to nanocomposite coatings including a brief review of how they are prepared and for what applications they are used. Chapter 2 provides information on how surface wettability is measured as well as summarising the other experimental techniques used throughout this thesis.

Chapter 3 describes the application of polymer–nanoparticle–fluorosurfactant complex nanocomposite coatings for antibacterial oil–water separation applications. Porous substrates coated with these polymer–nanoparticle–fluorosurfactant complex nanocomposite coatings are found to readily separate oil–water mixtures under both static and continuous flow as well as displaying antibacterial surface properties against *Escherichia coli* (Gram-negative bacteria) and *Staphylococcus aureus* (Gram-positive bacteria). A key advantage of this approach for coating substrates is its single-step simplicity. Potential applications include provision of safe drinking water, environmental pollution clean-up, and anti-fogging.

Chapter 4 utilises a single-step, low temperature, solventless atomised spray plasma deposition technique for the preparation of antibacterial polymer–metallosurfactant nanocomposite coatings which are highly active against both *Escherichia coli* (Gram-negative bacteria) and *Staphylococcus aureus* (Gram-positive bacteria).

Chapter 5 extends the use of the atomised spray plasma deposition technique into optical applications with the preparation of high refractive index hybrid polymer and polymer–inorganic nanocomposite coatings. Refractive indices as high as 1.936 at 635 nm wavelength have been obtained for 4-bromostyrene / toluene + TiO_2 layers using very low titania loadings (8% w/v). Thin films with any desired refractive index up to 1.936 can be easily deposited by varying the precursor mixture composition.

TABLE OF CONTENTS

List of Schemes

List of Figures

List of Tables

Chapter 1

Introduction

1.1 Nanocomposite Coatings

Composites are materials formed by combining two separate components into a single hybrid system and often have superior properties which are not achieved by either of the two individual components, resulting in their widespread use in many applications.[1,2] The two components are called the matrix and the filler with the filler phase being dispersed throughout the matrix phase. The properties of the composite not only depend on the properties of the two individual phases but also on the interfacial interactions between the two, in addition to the spatial organisation of the filler within the matrix.[3] Both phases can either consist of organic or inorganic material with the most commonly prepared composites involving an organic polymer matrix and an inorganic filler. This combines the processability and flexibility of polymer materials with the hardness and thermal stability of inorganic materials.[3] Resulting organic–inorganic composites therefore usually have enhanced mechanical and physical properties. By careful choice of filler material, further chemical functionality can also be incorporated resulting in composites with interesting properties. If the filler material is on the nanoscale (it has at least one dimension which is less than 100 nm), then such composite materials are called nanocomposites. Similarly, the use of micron-sized filler particles results in microcomposites. Nanocomposites have shown enhanced properties compared to equivalent microcomposite materials and have therefore attracted a great deal of interest in the field of materials chemistry in the past few decades.[4,5]

Polymer nanocomposites were first developed in the early 1990s by Toyota research group in Japan.[6,7] They reported a pronounced improvement in the thermal and mechanical properties of Nylon-6 upon dispersion of a small amount of nanoclay throughout the polymer. Such a material can be used as a flame-resistant material due to the enhanced thermal properties. This composite was referred to as a hybrid material. The term nanocomposite was introduced just the following year by Lan and Pinnavaia.[8] Since then there have been a vast amount of literature reporting the preparation of nanocomposite materials utilising nanoscale fillers of various shapes

and sizes. There are three types of filler which are classified by their geometries, namely nanoparticles, nanorods/nanotubes, and nanosheets.[9] These are shown schematically in Figure 1.1. It has been shown that the size, shape, and aspect ratio of the filler greatly affects the properties of the resulting nanocomposite.[10,11]

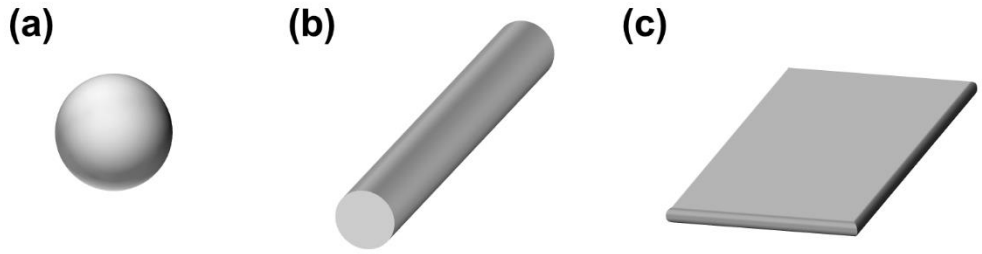

Figure 1.1: Schematic diagram of the three types of nanoscale filler: (a) nanoparticle; (b) nanotube; (c) nanosheet.

Due to the vast range of possible combinations of matrix and filler, both in terms of choice of materials and size and shape of the filler, the properties of nanocomposites can be tailored to a wide range of diverse applications. Bulk nanocomposites have been prepared for use in energy storage,[12] in biomedical applications,[13] as proton exchange membranes in fuel cells,[14] and as flame retardant materials.[15] Another reason for the increased levels of research into the preparation of nanocomposites is for their use as surface coatings either to add a required functionality to a substrate, or to provide protection from damage. The uses of these coatings can range from small scale applications such as in electronic products or biomedical devices, to much larger scale systems involving coatings on structures, buildings, and vehicles. Nanocomposite coatings have been shown to provide protection properties such as anti-corrosion,[16] anti-wear,[17] and anti-scratch,[18] as well as being able to add functionality for use in antibacterial,[19] optical,[20] gas sensing,[21] and self-cleaning[22] applications. The endless amount of possible matrix and filler combinations coupled with the continued need to develop new surface coatings for a wide range of applications has led to continued research efforts into the development of functional nanocomposite thin films.

1.2 Theory

As previously mentioned, the properties of composite materials can be very different than those of the two individual components. This is due to the interactions between the two components at the phase interface which results in the formation of an interfacial material in the vicinity of the surface of the filler material.[23] This interfacial layer plays a significant role in determining the properties of the composite. The properties of this interfacial material are usually different to the bulk properties of each component due to intermolecular forces between the two phases.[24] The nature of these forces will determine how dramatically different the properties of the interfacial material are as well as influencing the thickness of the interfacial layer. In addition to the matrix–particle interactions, the interfacial layer thickness is also affected by the polymer chain rigidity and molecular weight.[25] Although it was initially thought that the thickness was independent of the size of the filler particles,[26] it has recently been shown to have a small effect when the particles have a radius of below 50 nm.[27,28] The particle loading concentration however does not influence the thickness.[28] The interfacial layer thickness has been measured to be around 2–10 nm.[27,29] The relative volume of this interfacial material as a fraction of the overall composite will determine the extent to which the properties of the composite are enhanced or altered with respect to the bulk matrix. The surface area of the filler therefore plays a crucial role in affecting the properties.[30,31]

Even accounting for the very small decrease in interfacial layer thickness with decreasing particle size below 50 nm, a reduced particle size results in an increase in the volume of interfacial material due to the increased particle surface area which when changing the particle dimensions from the micro- to nanoscale increases the surface-to-volume ratio by three orders of magnitude.[32] Therefore, for nanocomposite materials the much larger surface-to-volume ratio of the nanoscale filler results in a dramatic increase in the volume fraction of interfacial material present. This results in the interfacial material, which has different properties to the bulk matrix, becoming a more dominant factor within the nanocomposite as compared with composites containing larger filler material, such as microcomposites.[33]

As an example, consider an inorganic filler material of spherical particles of diameter 300 nm dispersed in a polymer matrix. If the thickness of the interfacial layer is taken to be 10 nm,[27] then for a filler loading concentration of 30% by volume the

interfacial material content is only 3% of the overall composite. If the filler particle size is decreased to 50 nm, then for the same loading concentration the interfacial material now represents 22%.[24] If the particle size is reduced to 10 nm, then even now that the interfacial thickness will have decreased to around 4 nm,[27] the volume of interfacial material increases further to 52%. This example demonstrates just how much of an impact the size of the filler material has on the volume of interfacial material and therefore the properties of the resulting composite. Nanocomposite materials therefore contain a much greater proportion of interfacial material for a given filler loading concentration as compared to microcomposites. Hence, the presence of filler material has a much more significant impact on the properties of the composite for nanocomposites than for microcomposites. As a result, nanocomposites can exhibit the same level of enhancement in properties at much lower filler loading concentrations compared to microcomposites, or can show much improved properties at the same loading concentration.[34] By taking advantage of the large volume fraction of interfacial material in nanocomposites, interesting and unique properties can be achieved. A similar example to the one above is shown schematically in Figure 1.2 (not to scale) to further demonstrate the effect of filler particle size on volume fraction of interfacial material.

The use of filler particles on the nanoscale also brings further advantages due to the unique properties of these materials as a result of their size. Due to their very large surface-to-volume ratio, nano-sized materials often exhibit different properties compared to the bulk properties of the same material. This is due to the fact that the surface atoms represent a much larger percentage of the material at these sizes compared to much larger particles. Quantum effects can also play a role in determining their properties. Examples of properties affected include magnetic,[35] optical,[36] electrochemical,[37] and thermodynamic.[38] These properties will therefore influence the properties of nanocomposites which incorporate these particles as the filler material and this provides the opportunity to create nanocomposites with interesting properties.

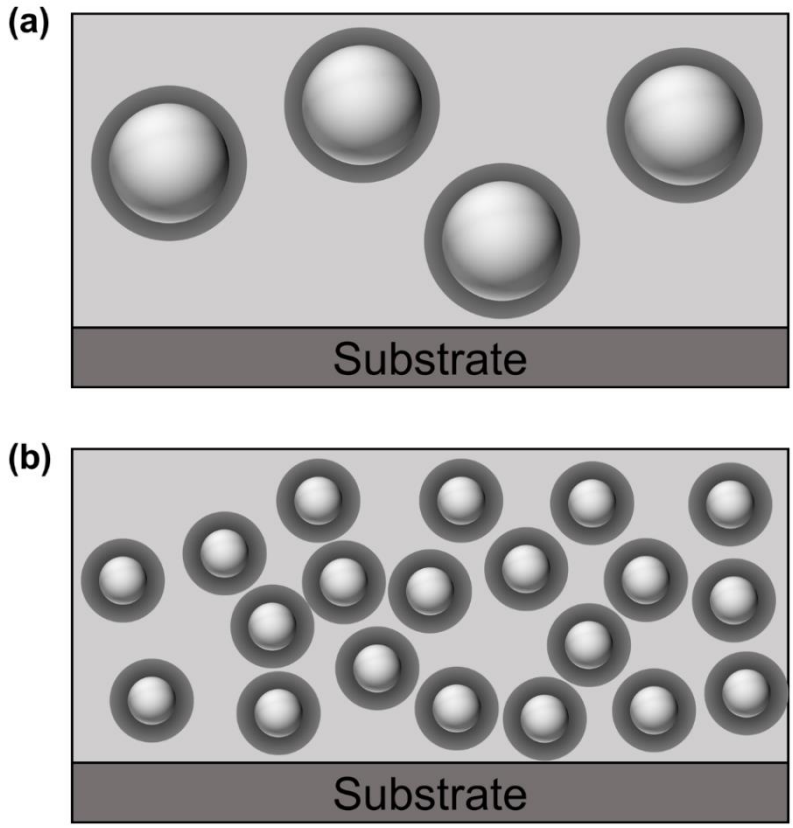

Figure 1.2: Schematic illustration showing the difference in the volume of interfacial material (shown as shaded area around filler particles) for composites with (a) micron-sized particles and (b) nanoparticles. The area of filler material is approximately the same in both figures. Adapted from schematic in Reference 23.

1.3 Fabrication Methods

Nanocomposites can be prepared using a variety of different materials which allows for a vast range of possible functional coatings. Either organic or inorganic material can be used for both the matrix and the filler resulting in four possible types of nanocomposite coating (matrix–nanofiller): organic–organic, organic–inorganic, inorganic–organic, inorganic–inorganic.[39] The shape of the filler can also be changed to tailor the nanocomposite for a certain application. There are three main types of filler which can be described as zero dimensional (0D), one dimensional (1D), or two dimensional (2D). 0D nanofillers are nanoparticles and have all three dimensions on the nanoscale. Examples of nanoparticles which can be used are metal oxides (such as silica[40] and titania[41]), metal particles (such as copper[42] and silver[43]), and semiconductors (such as PbS[44] and CdS[45]). Nanotubes or nanorods which have two dimensions on the nanoscale are classed as 1D nanofillers. Carbon nanotubes (CNT)[46] and cellulose nanocrystals (CNC)[47] represent examples of nanotubes which

can be incorporated into a matrix to form a composite. Layered nanofillers, for example nanolayered silicates (such as montmorillonite[48]) and graphene[49], have only one dimension on the nanoscale and fall into the third category, 2D nanofillers. A wide range of organic polymers can be used as the matrix whilst inorganic matrices include metals and metal alloys.

Nanocomposite coating fabrication methods can be split into wet chemical and vapour phase processes.[50] Wet chemical deposition processes generally involve the preparation of a coating solution which is then applied to the substrate whereas vapour phase process involve thin film deposition from precursor vapour using either physical processes (physical vapour deposition) or chemical reactions (chemical vapour deposition), Figure 1.3. Another deposition method not reviewed here is a method in which polymer chains are grafted from the surface. Nanocomposite coatings can be prepared through this method by grafting polymer brushes from an initiator-modified surface either prior to[51] or after[52] nanoparticle deposition. Alternatively, a polymer–nanoparticle mixture can be grafted from the surface in a single step.[53]

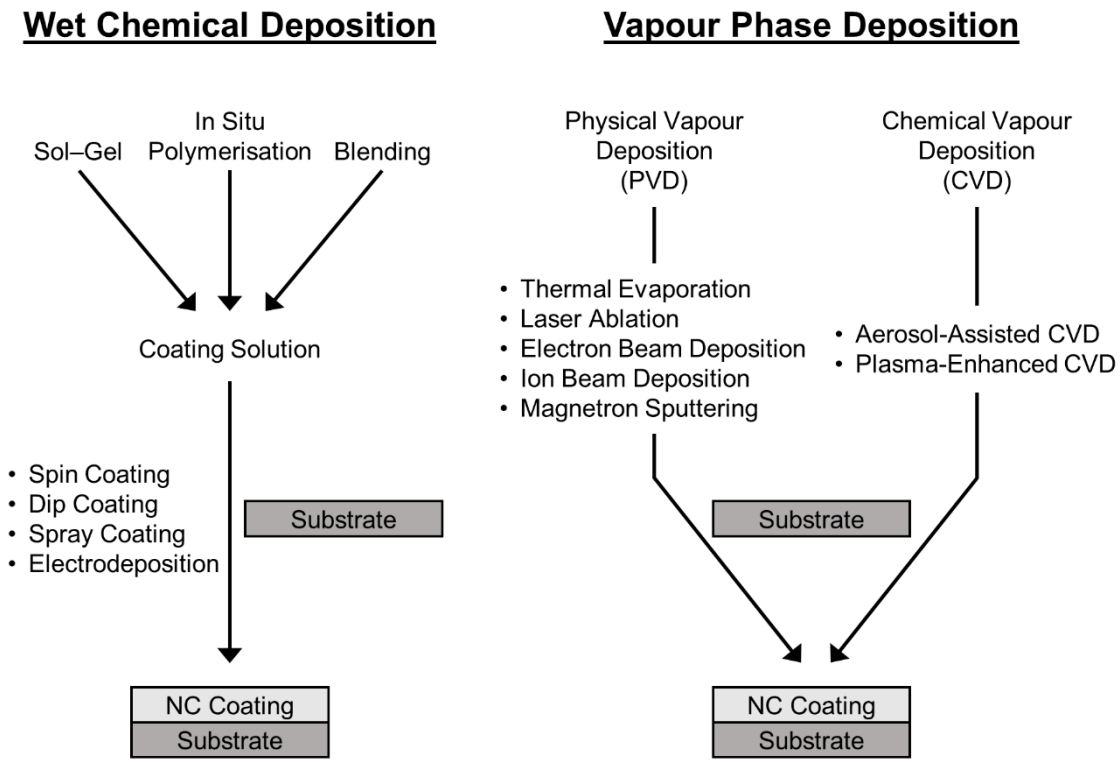

Figure 1.3: Overview of the main fabrication methods for the preparation of nanocomposite (NC) coatings.

In wet chemical deposition processes the matrix component can be introduced as either a precursor or as a preformed polymer. Similarly, the nanofiller can be introduced either as a precursor or as preformed nanoparticles. This results in there being three general methods for preparing the coating solution depending on the form of the starting materials: sol–gel, blending, and in situ polymerisation. The sol–gel process involves the hydrolysis and condensation of an inorganic precursor (typically a metal alkoxide) to generate the nanofiller species and this can be performed either in the presence of a preformed polymer[54] or with an inorganic matrix precursor.[55] Blending is the most straightforward process and simply involves the mixing of preformed nanoparticles into a polymer resulting in the coating solution.[56] In situ polymerisation involves first mixing preformed nanoparticles with a monomer before polymerisation is performed by for example emulsion polymerisation.[57] Once the coating solution has been prepared using one of these three processes, it can then be coated onto various substrates using techniques such as spin coating,[58] dip coating,[59] spray coating,[60] or electrodeposition.[61] In situ polymerisation can also be performed by performing the polymerisation after having coated the monomer–nanoparticle mixture onto a substrate using photopolymerisation.[62] Similarly, a polymer–inorganic precursor mixture can be spin coated onto a surface and the inorganic nanoparticles generated using a high temperature baking step.[63] While these wet chemical techniques are relatively cheap and simple processes, they generally suffer from the high agglomeration tendency of nanoparticles which can have a negative impact on the properties of the resulting nanocomposites.[64] In addition, the above techniques often require high temperature[65] or lengthy[66] post deposition curing steps, multiple coating steps to ensure homogenous film formation,[67] as well as the need to use crosslinking agents and catalysts in the synthesis of the coating solution.[68]

Various physical vapour deposition (PVD) processes have been used in the preparation of nanocomposite coatings. These techniques typically involve the evaporation of a solid or liquid under vacuum. The vapour produced then condenses onto a substrate forming a thin film. The evaporation of the source material can be performed using various methods including thermal evaporation,[69] pulsed laser ablation,[70] electron beam deposition,[71] and ion beam deposition.[72] Thermal evaporation simply uses high temperatures to evaporate the coating material whilst pulsed laser ablation, electron beam deposition, and ion beam deposition focus high energy laser, electron, and ion beams respectively onto the material in order to achieve

evaporation. Due to the high energy required for vaporisation, the substrates used in these techniques reach high temperatures and these processes are therefore not suitable for all substrate materials. Magnetron sputtering represents another PVD technique which can be used to deposit thin films. This involves the use of a plasma discharge between the target and the substrate which induces sputtering of the target material resulting in deposition. This technique can be used to prepare nanocomposite coatings either by sputtering of a single composite target material[73] or by co-sputtering of two independent targets.[74] However, this process still suffers from high substrate temperatures in addition to relatively slow deposition rates.

In contrast to PVD which uses physical processes to prepare coatings, chemical vapour deposition (CVD) utilises chemical reactions in the preparation of thin films. In CVD, heated substrates are exposed to volatile precursors which, due to the high temperatures, decompose, react and deposit onto the surface. There are various different types of the CVD technique however the most useful for the preparation of nanocomposite coatings is aerosol-assisted CVD (AACVD). This technique utilises a liquid or gas aerosol to deliver some or all of the precursor materials into the reaction chamber. Nanocomposite coatings can be prepared using AACVD either by using an aerosol to inject nanoparticles into the chamber whilst performing CVD of a volatile precursor,[75] or by using an aerosol to deliver a liquid CVD precursor containing pre-dispersed nanoparticles.[76] The latter variation of AACVD offers the ability to deposit non-volatile precursors however both variations of this technique require the use of solvents. As with the previously mentioned PVD techniques, AACVD again suffers from the need for substrates to withstand very high temperatures.

Plasma-enhanced chemical vapour deposition (PECVD) utilises a gas discharge to provide the energy required for deposition, thereby removing the need for high substrate temperatures. PECVD can be combined with the previously mentioned magnetron sputtering to deposit nanocomposite coatings. The matrix is deposited using PECVD whilst the nanoparticles are incorporated into the coating by simultaneous sputtering of a metal target.[77] Alternatively, PECVD can be performed using a metal–organic precursor to prepare nanocomposite polymer–metal coatings.[78] The range of possible nanocomposite coatings is however restricted when using these techniques due to the requirement for the precursor to have a suitably high vapour pressure. Additionally, the size and shape of the incorporated nanoparticles is limited due to the fact that they are formed in situ. Another form of PECVD in which an

atomiser is utilised to deliver the nanoparticles into the reaction chamber whilst simultaneously depositing the matrix using PECVD permits the use of preformed nanoparticles.[79] This technique allows many more types of nanoparticles to be used however still requires the use of a high vapour pressure precursor and requires the use of solvents to deliver the nanoparticles into the reaction chamber.

Another form of plasmachemical deposition which uses a dielectric barrier discharge (DBD) has been reported for the preparation of nanocomposite thin films.[80] This technique utilises an atomiser to deliver a mixture containing preformed nanoparticles dispersed in a liquid precursor into the DBD reactor. Similarly, atomised spray plasma deposition (ASPD) utilises an atomiser to deliver a precursor–nanoparticle dispersion into a gas discharge resulting in the formation of excited species which react at the substrate surface forming a polymer–nanoparticle nanocomposite coating.[81] Whilst both of these techniques offer the ability to deposit nanocomposite coatings using non-volatile precursors, the aerosol-assisted DBD technique requires the use of solvents in addition to an expensive carrier gas in order to deliver the dispersion into the reaction chamber. The solventless ASPD technique therefore offers a more environmentally friendly way to prepare nanocomposite thin films. The ASPD technique is described in more detail in Section 2.2.2.(b) (page 45).

Regardless of the fabrication method used, one of the crucial requirements in the preparation of nanocomposite coatings is the need to avoid nanoparticle agglomeration.[82] As previously discussed, the enhanced properties of nanocomposites are due to the increased matrix–filler interfacial region as a result of the increased surface-to-volume ratio of nanoparticles compared to larger particles. This greater surface-to-volume ratio does however strongly increase the tendency of the nanoparticles to agglomerate due to attractive van der Waals forces between the particles which act to reduce the surface energy. Agglomeration therefore results in a negative enthalpy change and if this outweighs the decrease in entropy upon nanoparticle agglomeration then the overall negative Gibbs free energy change will provide a driving force for agglomeration. This will increase the particle size reducing the surface-to-volume ratio and as a result, the desired properties of the nanocomposite will not be achieved. Agglomeration can however be prevented by ensuring good dispersion of the nanoparticles within the matrix. This can be achieved simply by using physical methods such as a ball-milling process[83] or ultrasonic treatment[84] to provide energy to overcome the attractive forces between particles and

to disperse the nanoparticles prior to film deposition. The dispersion using these physical methods is driven by the increase in entropy. Alternatively, surface modification of the nanoparticles can improve the interactions between the matrix and the filler enhancing the compatibility between the two which results in an improved dispersion. Surface modification can be performed using various techniques such as chemical absorption,[85] grafting of polymer,[86] and ligand exchange.[87]

1.4 Applications

As discussed in Section 1.3 (page 24), there is a vast range of possible matrix–filler combinations which can be prepared using a wide selection of different fabrication methods. As a result, the properties of nanocomposite coatings can be tailored towards a variety of different applications. These properties can be split into those in which the nanofiller enhances the physical properties of the nanocomposite, those which enhance the optical properties, and those in which chemical functionality is incorporated into the coating.

One of the main benefits of incorporating nanoparticles into a thin film is the resulting enhancement in the physical and mechanical properties. Properties such as hardness,[88] tensile strength,[89] and elastic modulus[90] have been shown to be greatly improved even at low nanofiller loading concentrations.[91] The enhancement in these properties is due to the incorporation of hard inorganic nanofiller particles as well as the strong interactions between the matrix and filler particles which allow an applied load to be easily transferred to the hard filler particles.[92] The improved mechanical properties also enhance the scratch and abrasion resistance[93] of the coatings leading to their use as wear-resistant films to protect surfaces such as display screens from damage.[94]

Another physical property that is enhanced through nanoparticle incorporation is the increased barrier properties of nanocomposite thin films which utilise nanolayered filler particles such as layered silicates[95] or graphene oxide.[96] As well as increasing the tensile strength and toughness of the coatings, these impermeable nanolayered particles force a tortuous path for diffusion of gas molecules through the film due to their high aspect ratio. This lengthens the mean diffusion path and as a result decreases the permeability of gases such as oxygen, nitrogen, and hydrogen.[97]

This has resulted in the use of nanocomposites as barrier films for food packaging applications to increase the shelf-life of foods.[98]

The excellent barrier properties of nanocomposite films have also led to their use in protecting metallic substrates and their alloys such as iron[99] and steel[100] from corrosion. In addition to increasing the mean diffusion path through the coating, the incorporated nanoparticles have been shown to fill pores present in polymer films increasing their anti-corrosive properties with respect to the pure polymer film.[101] These barrier properties protect the substrates from oxygen, water, and corrosive ions such as H^+ and Cl^-, all of which contribute to the corrosion of metallic substrates.[102] Such anti-corrosive nanocomposite coatings are therefore very useful in for example aerospace[103] and automotive[104] applications.

Nanoparticle incorporation into a surface coating can also be used to add surface roughness. The addition of surface roughness can be used to alter the wettability of a coating towards different liquids. As discussed in more detail in Section 2.3.1 (page 47), the wettability of a surface depends on both the surface chemistry and surface roughness. For coatings repellent towards water (hydrophobic) or oils (oleophobic), the addition of surface roughness upon nanoparticle incorporation into a polymer coating can result in an increase in the liquid repellency providing superhydrophobic[105] and superoleophobic[106] nanocomposite films. Superhydrophobic surfaces can be used in self-cleaning[107] or anti-icing[108] applications. If the surface chemistry is such that water droplets spread on the particle-free surface (hydrophilic) then nanocomposite formation can increase the droplet wetting ability giving a superhydrophilic surface which is useful for anti-fogging[109] applications.

Inorganic nanoparticles can also be incorporated into polymer matrices in order to tune the optical properties of the resulting thin film. For optical applications, the coating must remain highly transparent and therefore nanoparticle agglomeration must be avoided in order to avoid scattering of the light which would reduce film clarity. The ability to tailor the optical properties whilst maintaining the high transparency of coatings is required for use as passive films in optical devices[110] as well as for optical planar waveguides.[111] Furthermore, coatings which are both highly transparent and have UV-absorbing properties due to the nanofiller have found use in various UV-shielding applications.[112] High refractive index coatings or coatings tuned to a desired refractive index are desirable for use as antireflection coatings[113] as well as for use in light-emitting diodes[114] and photovoltaic cells.[115]

Nanoparticles can also be added into polymer matrices in order to incorporate chemical properties. Until now all discussion of the properties of nanocomposites has been due to the incorporation of nanoparticles into the coating as a permanent part of the film. Another form of nanocomposite coating exists whereby the matrix can be used as a host for the nanoparticles which can be released from the coating. When antibacterial nanofiller species such as silver[116] and copper[117] are used then these nanocomposite films can be used as antibacterial coatings with the released antibacterial nanoparticles able to inhibit the growth of bacterial species in addition to preventing biofilm formation. When an anti-fouling polymer is used as the matrix then it is also possible to prepare dual-function antibacterial and anti-fouling coatings.[118] Antibacterial nanocomposite thin films are desirable to prevent biofilm formation on biomedical devices[119] as well as to functionalise wound dressings[120] and medical implants.[121]

1.5 Thesis Scope

In this thesis, the use of simple spraying fabrication techniques in order to prepare various functional nanocomposite thin films has been reported. These nanocomposite coatings have been characterised and tested for their antibacterial, oil–water separation, and optical properties.

Oil-spill clean-up is still a very important environmental challenge. In addition, simultaneous oil–water separation and killing of bacteria during filtration is highly desirable for safe human water consumption. Nanocomposite films which display opposite wetting behaviour towards water compared to oil have been widely utilised for oil–water separation. Those which are wet by oils but are repellent towards water are most common however these coatings suffer from substrate fouling by oil and the formation of a water layer at the surface, both of which reduce the separation efficiency. Nanocomposites which are wet by water but repel oils are therefore more desirable however previously reported coatings of this type require multi-step fabrication methods or take several minutes to achieve the final wetting state. Furthermore, multifunctional coatings of this type (wet by water, repellent towards oils) for antibacterial oil–water separation have yet to be reported. Chapter 3 reports the fabrication of antibacterial oleophobic–hydrophilic polymer–nanoparticle–fluorosurfactant nanocomposite surfaces using a simple spray coating or solvent

casting technique. The incorporation of silica nanoparticles greatly enhances both the oleophobicity and hydrophilicity of the nanocomposite in comparison to the parent polymer–fluorosurfactant complex coating. Addition of nanoparticles is also shown to enhance the hardness (durability) of the thin films. Such surfaces have been tested for both oil–water separation and antibacterial applications.

Highly resistant bacterial biofilms on surfaces such as those in healthcare settings pose a huge threat to human health due to the possible spreading of infections. As a result, surfaces capable of killing bacteria are highly desirable. Antibacterial nanocomposite coatings have gained interest for such applications. These can be fabricated using various different methods however most of these suffer from the need to use high temperatures and solvents, in addition to being multi-step or lengthy processes. For other fabrication methods the deposition rate is slow. Furthermore, the most commonly utilised antibacterial nanofiller material is silver which has however been shown to be cytotoxic and there is the increasing risk of silver-resistant bacteria. Nanocomposites which are more easily prepared and which utilise biocompatible antibacterial agents are therefore more desirable. In Chapter 4, antibacterial metallosurfactants are incorporated into polymer films resulting in the preparation of highly antibacterial polymer–metallosurfactant nanocomposite coatings. These metallosurfactants have previously been shown to be biocompatible. The plasmachemical deposition technique used, atomised spray plasma deposition, has many advantages compared to previously reported fabrication techniques such as being single-step, low temperature, solventless, and can be used to coat substrates of any material.

Thin films of high refractive index are widely used in optical applications such as in optical lenses, optical waveguides, and as anti-reflective coatings. Nanoparticles of materials with a high refractive index have been incorporated into polymer matrices in order to achieve such high refractive index coatings. It is also possible to retain the transparency of these nanocomposite thin films due to the fact that the nanoparticles are much smaller than the wavelength of visible light and the light is therefore not scattered. These high refractive index coatings can be fabricated using several different fabrication techniques however they typically require high temperatures and post-deposition curing steps. Additionally, the nanoparticle loading is often very high. Therefore, an ambient temperature single-step method for preparing such coatings is desirable. In Chapter 5, the atomised spray plasma deposition technique is utilised to

prepare high refractive index polymer–titania nanocomposite thin films. Incorporation of titania nanoparticles greatly enhances the refractive index of the nanocomposites compared to the parent polymer, even at relatively low titania loading concentrations.

Thus, the use of nanocomposite thin films is shown to be very useful for various different applications. These results are then discussed with respect to future work that could be undertaken.

1.6 References

[1] Daniel, I. M.; Ishai, O. Engineering Mechanics of Composite Materials, 2nd ed.; Oxford University Press, Inc.: New York, 2006.

[2] Chung, D. D. L. Composite Materials: Science and Applications, 2nd ed.; Derby, B., Ed.; Springer-Verlag: London, 2010.

[3] Zou, H.; Wu, S.; Shen, J. Polymer/Silica Nanocomposites: Preparation, Characterization, Properties, and Applications. *Chem. Rev.* **2008**, *108*, 3893–3957.

[4] Sanchez, C.; Belleville, P.; Popall, M.; Nicole, L. Applications of Advanced Hybrid Organic–Inorganic Nanomaterials: From Laboratory to Market. *Chem. Soc. Rev.* **2011**, *40*, 696–753.

[5] Kumar, S. K.; Benicewicz, B. C.; Vaia, R. A.; Winey, K. I. 50th Anniversary Perspective: Are Polymer Nanocomposites Practical for Applications? *Macromolecules* **2017**, *50*, 714–731.

[6] Usuki, A.; Kojima, Y.; Kawasumi, M.; Okada, A.; Fukushima, Y.; Kurauchi, T.; Kamigaito, O. Synthesis of Nylon 6-Clay Hybrid. *J. Mater. Res.* **1993**, *8*, 1179–1184.

[7] Kojima, Y.; Usuki, A.; Kawasumi, M.; Okada, A.; Fukushima, Y.; Kurauchi, T.; Kamigaito, O. Mechanical Properties of Nylon 6-Clay Hybrid. *J. Mater. Res.* **1993**, *8*, 1185–1189.

[8] Lan, T.; Pinnavaia, T. J. Clay-Reinforced Epoxy Nanocomposites. *Chem. Mater.* **1994**, *6*, 2216–2219.

[9] Schaefer, D. W.; Justice, R. S. How Nano are Nanocomposites? *Macromolecules* **2007**, *40*, 8501–8517.

[10] Hussain, F.; Hojjati, M.; Okamoto, M.; Gorga, R. E. Review Article: Polymer-Matrix Nanocomposites, Processing, Manufacturing, and Application: An Overview. *J. Compos. Mater.* **2006**, *40*, 1511–1575.

[11] Dastjerdi, Z.; Cranston, E. D.; Berry, R.; Fraschini, C.; Dubé, M. A. Polymer Nanocomposites for Emulsion-Based Coatings and Adhesives. *Macromol. React. Eng.* **2019**, *13*, 1800050.

[12] Xie, L.; Huang, X.; Huang, Y.; Yang, K.; Jiang, P. Core@Double-Shell Structured $BaTiO_3$–Polymer Nanocomposites with High Dielectric Constant and Low Dielectric Loss for Energy Storage Application. *J. Phys. Chem. C* **2013**, *117*, 22525–22537.

[13] Xu, R.; Manias, E.; Snyder, A. J.; Runt, J. New Biomedical Poly(urethane urea)–Layered Silicate Nanocomposites. *Macromolecules* **2001**, *34*, 337–339.

[14] Singha, S.; Jana, T. Structure and Properties of Polybenzimidazole/Silica Nanocomposite Electrolyte Membrane: Influence of Organic/Inorganic Interface. *ACS Appl. Mater. Interfaces* **2014**, *6*, 21286–21296.

[15] Gilman, J. W.; Jackson, C. L.; Morgan, A. B.; Harris, Jr., R. Flammability Properties of Polymer–Layered-Silicate Nanocomposites. Polypropylene and Polystyrene Nanocomposites. *Chem. Mater.* **2000**, *12*, 1866–1873.

[16] Yeh, J.-M.; Huang, H.-Y.; Chen, C.-L.; Su, W.-F.; Yu, Y.-H. Siloxane-Modified Epoxy Resin–Clay Nanocomposite Coatings with Advanced Anticorrosive Properties Prepared by a Solution Dispersion Method. *Surf. Coat. Technol.* **2006**, *200*, 2753–2763.

[17] Zhang, M. Q.; Rong, M. Z.; Yu, S. L.; Wetzel, B.; Friedrich, K. Improvement of Tribological Performance of Epoxy by the Addition of Irradiation Grafted Nano-Inorganic Particles. *Macromol. Mater. Eng.* **2002**, *287*, 111–115.

[18] Sangermano, M.; Messori, M.; Martin Galleco, M.; Rizza, G.; Voit, B. Scratch Resistant Tough Nanocomposite Epoxy Coatings Based on Hyperbranched Polyesters. *Polymer* **2009**, *50*, 5647–5652.

[19] Santos, C. M.; Tria, M. C. R.; Vergara, R. A. M. V.; Ahmed, F.; Advincula, R. C.; Rodriges, D. F. Antimicrobial Graphene Polymer (PVK-GO) Nanocomposite Films. *Chem. Commun.* **2011**, *47*, 8892–8894.

[20] Kim, J.-Y.; Kim, M.; Kim, H.; Joo, J.; Choi, J.-H. Electrical and Optical Studies of Organic Light Emitting Devices Using SWCNTs-Polymer Nanocomposites. *Opt. Mater.* **2002**, *21*, 147–151.

[21] Tai, H.; Jiang, Y.; Xie, G.; Yu, J.; Chen, X. Fabrication and Gas Sensitivity of Polyaniline–Titanium Dioxide Nanocomposite Thin Film. *Sens. Actuators, B* **2007**, *125*, 644–650.

[22] Kamegawa, T.; Shimizu, Y.; Yamashita, H. Superhydrophobic Surfaces with Photocatalytic Self-Cleaning Properties by Nanocomposite Coating of TiO_2 and Polytetrafluoroethylene. *Adv. Mater.* **2012**, *24*, 3697–3700.

[23] Schadler, L. S.; Kumar, S. K.; Benicewicz, B. C.; Lewis, S. L.; Harton, S. E. Designed Interfaces in Polymer Nanocomposites: A Fundamental Viewpoint. *MRS Bull.* **2007**, *32*, 335–340.

[24] Fernando, R. H. Nanocomposite and Nanostructured Coatings: Recent Advancements. In *Nanotechnology Applications in Coatings*; ACS Symposium Series; American Chemical Society: Washington, D.C., 2009.

[25] Cheng, S.; Carroll, B.; Bocharova, V.; Carrillo, J.-M. Y.; Sumpter, B. G.; Sokolov, A. P. Focus: Structure and Dynamics of the Interfacial Layer in Polymer Nanocomposites with Attractive Interactions. *J. Chem. Phys.* **2017**, *146*, 203201.

[26] Winey, K. I.; Vaia, R. A. Polymer Nanocomposites. *MRS Bull.* **2007**, *32*, 314–322.

[27] Jouault, N.; Moll, J. F.; Meng, D.; Windsor, K.; Ramcharan, S.; Kearney, C.; Kumar, S. K. Bound Polymer Layer in Nanocomposites. *ACS Macro Lett.* **2013**, *2*, 371–374.

[28] Gong, S.; Chen, Q.; Moll, J. F.; Kumar, S. K.; Colby, R. H. Segmental Dynamics of Polymer Melts with Spherical Nanoparticles. *ACS Macro Lett.* **2014**, *3*, 773–777.

[29] Cheng, S.; Carroll, B.; Lu, W.; Fan, F.; Carrillo, J.-M. Y.; Martin, H.; Holt, A. P.; Kang, N.-G.; Bocharova, V.; Mays, J. W.; Sumpter, B. G.; Dadmun, M.; Sokolov, A. P. Interfacial Properties of Polymer Nanocomposites: Role of Chain Rigidity and Dynamic Heterogeneity Length Scale. *Macromolecules* **2017**, *50*, 2397–2406.

[30] Ciprari, D.; Jacob, K.; Tannenbaum, R. Characterization of Polymer Nanocomposite Interphase and Its Impact on Mechanical Properties. *Macromolecules* **2006**, *39*, 6565–6573.

[31] Schadler, L. S.; Brinson, L. C.; Sawyer, W. G. Polymer Nanocomposites: A Small Part of the Story. *JOM* **2007**, *59*, 53–60.

[32] Thostenson, E. T.; Li, C.; Chou, T.-W. Nanocomposites in Context. *Compos. Sci. Technol.* **2005**, *65*, 491–516.

[33] Roy, M.; Nelson, J. K.; MacCrone, R. K.; Schadler, L. S.; Reed, C. W.; Keefe, R.; Zenger, W. Polymer Nanocomposites Dielectrics – The Role of the Interface. *IEEE Trans. Dielectr. Electr. Insul.* **2005**, *12*, 629–643.

[34] Vaia, R. A.; Giannelis, E. P. Polymer Nanocomposites: Status and Opportunities. *MRS Bull.* **2001**, *26*, 394–401.

[35] Park, T.-J.; Papaefthymiou, G. C.; Viescas, A. J.; Moodenbaugh, A. R.; Wong, S. S. Size-Dependent Magnetic Properties of Single-Crystalline Multiferroic $BiFeO_3$ Nanoparticles. *Nano Lett.* **2007**, *7*, 766–772.

[36] Lopez, R.; Feldman, L. C.; Haglund, Jr., R. F. Size-Dependent Optical Properties of VO_2 Nanoparticle Arrays. *Phys. Rev. Lett.* **2004**, *93*, 177403.

[37] Jiang, C.; Wei, M.; Qi, Z.; Kudo, T.; Honma, I.; Zhou, H. Particle Size Dependence of the Lithium Storage Capability and High Rate Performance of Nanocrystalline Anatase TiO_2 Electrode. *J. Power Sources* **2007**, *166*, 239–243.

[38] Zhang, H.; Banfield, J. F. Thermodynamic Analysis of Phase Stability of Nanocrystalline Titania. *J. Mater. Chem.* **1998**, *8*, 2073–2076.

[39] Nguyen-Tri, P.; Nguyen, T. A.; Carriere, P.; Xuan, C. N. Nanocomposite Coatings: Preparation, Characterization, Properties, and Applications. *Int. J. Corros.* **2018**, *2018*, 1–19.

[40] Wang, J.; Chen, X.; Kang, Y.; Yang, G.; Yu, L.; Zhang, P. Preparation of Superhydrophobic Poly(methyl methacrylate)-Silicon Dioxide Nanocomposite Films. *Appl. Surf. Sci.* **2010**, *257*, 1473–1477.

[41] Mallakpour, S.; Barati, A. Efficient Preparation of Hybrid Nanocomposite Coatings Based on Poly(vinyl alcohol) and Silane Coupling Agent Modified TiO_2 Nanoparticles. *Prog. Org. Coat.* **2011**, *71*, 391–398.

[42] Cioffi, N.; Torsi, L.; Ditaranto, N.; Tantillo, G.; Ghibelli, L.; Sabbatini, L.; Bleve-Zacheo, T.; D'Alessio, M.; Zambonin, G.; Traversa, E. Copper Nanoparticle/Polymer Composites with Antifungal and Bacteriostatic Properties. *Chem. Mater.* **2005**, *17*, 5255–5262.

[43] Balan, L.; Schneider, R.; Lougnot, D. J. A New and Convenient Route to Polyacrylate/Silver Nanocomposites by Light-Induced Cross-Linking Polymerization. *Prog. Org. Coat.* **2008**, *62*, 351–357.

[44] Lewis, E. A.; McNaughter, P. D.; Yin, Z.; Chen, Y.; Brent, J. R.; Saah, S. A.; Raftery, J.; Awudza, J. A. M.; Malik, M. A.; O'Brien, P.; Haigh, S. J. In Situ Synthesis of PbS Nanocrystals in Polymer Thin Films from Lead(II) Xanthate and Dithiocarbamate Complexes: Evidence for Size and Morphology Control. *Chem. Mater.* **2015**, *27*, 2127–2136.

[45] Pethkar, S.; Patil, R. C.; Kher, J. A.; Vijayamohanan, K. Deposition and Characterization of CdS Nanoparticle/Polyaniline Composite Films. *Thin Solid Films* **1999**, *349*, 105–109.

[46] Dhand, C.; Arya, S. K.; Datta, M.; Malhotra, B. D. Polyaniline–Carbon Nanotube Composite Film for Cholesterol Biosensor. *Anal. Biochem.* **2008**, *383*, 194–199.

[47] Kaboorani, A.; Auclair, N.; Riedl, B.; Landry, V. Mechanical Properties of UV-Cured Cellulose Nanocrystal (CNC) Nanocomposite Coating for Wood Furniture. *Prog. Org. Coat.* **2017**, *104*, 91–96.

[48] Xu, Y.; Ren, X.; Hanna, M. A. Chitosan/Clay Nanocomposite Film Preparation and Characterization. *J. Appl. Polym. Sci.* **2006**, *99*, 1684–1691.

[49] Zhang, L.; Li, Y.; Wang, H.; Qiao, Y.; Chen, J.; Cao, S. Strong and Ductile Poly(lactic acid) Nanocomposite Films Reinforced with Alkylated Graphene Nanosheets. *Chem. Eng. J.* **2015**, *264*, 538–546.

[50] Faupel, F.; Zaporojtchenko, V.; Strunskus, T.; Elbahri, M. Metal-Polymer Nanocomposites for Functional Applications. *Adv. Eng. Mater.* **2010**, *12*, 1177–1190.

[51] Sun, C.; Li, Y.; Li, Z.; Su, Q.; Wang, Y.; Liu, X. Durable and Washable Antibacterial Copper Nanoparticles Bridged by Surface Grafting Polymer Brushes on Cotton and Polymeric Materials. *J. Nanomater.* **2018**, *2018*, 1–7.

[52] Wassel, E.; Es-Souni, M.; Berger, N.; Schopf, D.; Dietze, M.; Solterbeck, C.-H.; Es-Souni, M. Nanocomposite Films of Laponite/PEG-Grafted Polymers and Polymer Brushes with Nonfouling Properties. *Langmuir* **2017**, *33*, 6739–6750.

[53] Gao, J.; Martin, A.; Yatvin, J.; White, E.; Locklin, J. Permanently Grafted Icephobic Nanocomposites with High Abrasion Resistance. *J. Mater. Chem. A* **2016**, *4*, 11719–11728.

[54] Facio, D. S.; Mosquera, M. J. Simple Strategy for Producing Superhydrophobic Nanocomposite Coatings In Situ on a Building Substrate. *ACS Appl. Mater. Interfaces* **2013**, *5*, 7517–7526.

[55] Talebian, N.; Nilforoushan, M. R.; Zargar, E. B. Enhanced Antibacterial Performance of Hybrid Semiconductor Nanomaterials: ZnO/SnO_2 Nanocomposite Thin Films. *Appl. Surf. Sci.* **2011**, *258*, 547–555.

[56] Sow, C; Riedl, B.; Blanchet, P. UV-Waterborne Polyurethane-Acrylate Nanocomposite Coatings Containing Alumina and Silica Nanoparticles for Wood: Mechanical, Optical, and Thermal Properties Assessment. *J. Coat. Technol. Res.* **2011**, *8*, 211–221.

[57] Mizutani, T.; Arai, K.; Miyamoto, M.; Kimura, Y. Application of Silica-Containing Nano-Composite Emulsion to Wall Paint: A New Environmentally Safe Paint of High Performance. *Prog. Org. Coat.* **2006**, *55*, 276–283.

[58] Conde, A.; Durán, A.; de Damborenea, J. J. Polymeric Sol–Gel Coatings as Protective Layers of Aluminium Alloys. *Prog. Org. Coat.* **2003**, *46*, 288–296.

[59] Chen, F.; Wan, P.; Xu, H.; Sun, X. Flexible Transparent Supercapacitors Based on Hierarchical Nanocomposite Films. *ACS Appl. Mater. Interfaces* **2017**, *9*, 17865–17871.

[60] Lakshmi, R. V.; Bharathidasan, T.; Basu, B. J. Superhydrophobic Sol–Gel Nanocomposite Coatings with Enhanced Hardness. *Appl. Surf. Sci.* **2011**, *257*, 10421–10426.

[61] Toledano, R.; Shacham, R.; Avnir, D.; Mandler, D. Electrochemical Co-Deposition of Sol–Gel/Metal Thin Nanocomposite Films. *Chem. Mater.* **2008**, *20*, 4276–4283.

[62] Martin-Gallego, M.; Verdejo, R.; Lopez-Manchado, M. A.; Sangermano, M. Epoxy-Graphene UV-Cured Nanocomposites. *Polymer* **2011**, *52*, 4664–4669.

[63] Gradess, R.; Abargues, R.; Habbou, A.; Canet-Ferrer, J.; Pedrueza, E.; Russell, A.; Valdés, J. L.; Martínez-Pastor, J. P. Localized Surface Plasmon Resonance Sensor Based on Ag-PVA Nanocomposite Thin Films. *J. Mater. Chem.* **2009**, *19*, 9233–9240.

[64] Hanemann, T.; Szabó, D. V. Polymer-Nanoparticle Composites: From Synthesis to Modern Applications. *Materials* **2010**, *3*, 3468–3517.

[65] Du, Y. J.; Damron, M.; Tang, G.; Zheng, H.; Chu, C.-J.; Osborne, J. H. Inorganic/Organic Hybrid Coatings for Aircraft Aluminium Alloy Substrates. *Prog. Org. Coat.* **2001**, *41*, 226–232.

[66] Shi, X.; Nguyen, T. A.; Suo, Z.; Liu, Y.; Avci, R. Effect of Nanoparticles on the Anticorrosion and Mechanical Properties of Epoxy Coating. *Surf. Coat. Technol.* **2009**, *204*, 237–245.

[67] Nagarajan, S.; Mohana, M.; Sudhagar, P.; Raman, V.; Nishimura, T.; Kim, S.; Kang, Y. S.; Rajendran, N. Nanocomposite Coatings on Biomedical Grade Stainless Steel for Improved Corrosion Resistance and Biocompatibility. *ACS Appl. Mater. Interfaces* **2012**, *4*, 5134–5141.

[68] Dhoke, S. K.; Bhandari, R.; Khanna, A. S. Effect of Nano-ZnO Addition on the Silicone-Modified Alkyd-Based Waterborne Coatings on its Mechanical and Heat-Resistance Properties. *Prog. Org. Coat.* **2009**, *64*, 39–46.

[69] Biswas, A.; Marton, Z.; Kanzow, J.; Kruse, J.; Zaporojtchenko, V.; Faupel, F. Controlled Generation of Ni Nanoparticles in the Capping Layers of Teflon AF by Vapor-Phase Tandem Evaporation. *Nano Lett.* **2003**, *3*, 69–73.

[70] Voevodin, A. A.; Fitz, T. A.; Hu, J. J.; Zabinski, J. S. Nanocomposite Tribological Coatings with “Chameleon” Surface Adaptation. *J. Vac. Sci. Technol.* **2002**, *20*, 1434–1444.

[71] Yi, J.; He, X. D.; Sun, Y.; Li, Y.; Li, M. W. Influence of Remaining C on Hardness and Emissivity of SiC/SiO_2 Nanocomposite Coating. *Appl. Surf. Sci.* **2007**, *253*, 7100–7103.

[72] Akbari, A.; Templier, C.; Beaufort, M. F.; Eyidi, D.; Riviere, J. P. Ion Beam Assisted Deposition of TiN–Ni Nanocomposite Coatings. *Surf. Coat. Technol.* **2011**, *206*, 972–975.

[73] Sergeev, V.; Psakhie, S.; Chubik, P.; Cherniavsky, A.; Soloviev, V.; Solntsev, V.; Khristenko, Y. Magnetron Sputtering of Si-Al-N Nanocomposite Coatings on Quartz for Protection Against Impacts of High Speed Microparticles. *Vacuum* **2017**, *143*, 454–457.

[74] Ribeiro, E.; Malczyk, A.; Carvalho, S.; Rebouta, L.; Fernandes, J. V.; Alves, E.; Miranda, A. S. Effects of Ion Bombardment on Properties of D.C. Sputtered Superhard (Ti, Si, Al)N Nanocomposite Coatings. *Surf. Coat. Technol.* **2002**, *151–152*, 515–520.

[75] Saeli, M.; Binions, R.; Piccirillo, C.; Hyett, G.; Parkin, I. P. Templated Growth of Smart Nanocomposite Thin Films: Hybrid Aerosol Assisted and Atmospheric Pressure Chemical Vapour Deposition of Vanadyl Acetylacetonate, Auric Acid and Tetraoctyl Ammonium Bromide. *Polyhedron* **2009**, *28*, 2233–2239.

[76] Palgrave, R. G.; Parkin, I. P. Aerosol Assisted Chemical Vapor Deposition Using Nanoparticle Precursors: A Route to Nanocomposite Thin Films. *J. Am. Chem. Soc.* **2006**, *128*, 1587–1597.

[77] Laurent, C.; Kay, E. Properties of Metal Clusters in Polymerized Hydrocarbon Versus Fluorocarbon Matrices. *J. Appl. Phys.* **1989**, *65*, 1717–1723.

[78] Duque, L.; Förch, R. Plasma Polymerization of Zinc Acetyl Acetonate for the Development of a Polymer-Based Zinc Release System. *Plasma Process. Polym.* **2011**, *8*, 444–451.

[79] Ross, A. D.; Gleason, K. K. The CVD of Nanocomposites Fabricated via Ultrasonic Atomization. *Chem. Vap. Deposition* **2006**, *12*, 225–230.

[80] Bardon, J.; Bour, J.; Del Frari, D.; Arnoult, C.; Ruch, D. Dispersion of Cerium-Based Nanoparticles in an Organosilicon Plasma Polymerized Coating: Effect on Corrosion Protection. *Plasma Process. Polym.* **2009**, *6*, S655–S659.

[81] Wood, T. J.; Ward, L. J.; Badyal, J. P. S. Super-Adhesive Polymer–Silica Nanocomposite Layers. *ACS Appl. Mater. Interfaces* **2013**, *5*, 9678–9683.

[82] Kango, S.; Kalia, S.; Celli, A.; Njuguna, J.; Habibi, Y.; Kumar, R. Surface Modification of Inorganic Nanoparticles for Development of Organic–Inorganic Nanocomposites—A Review. *Prog. Polym. Sci.* **2013**, *38*, 1232–1261.

[83] Castrillo, P. D.; Olmos, D.; Amador, D. R.; González-Benito, J. Real Dispersion of Isolated Fumed Silica Nanoparticles in Highly Filled PMMA Prepared by High Energy Ball Milling. *J. Colloid Interf. Sci.* **2007**, *308*, 318–324.

[84] Dean, K.; Krstina, J.; Tian, W.; Varley, R. J. Effect of Ultrasonic Dispersion Methods on Thermal and Mechanical Properties of Organoclay Epoxy Nanocomposites. *Macromol. Mater. Eng.* **2007**, *292*, 415–427.

[85] Sabzi, M.; Mirabedini, S. M.; Zohuriaan-Mehr, J.; Atai, M. Surface Modification of TiO_2 Nano-Particles with Silane Coupling Agent and Investigation of its Effect on the Properties of Polyurethane Composite Coating. *Prog. Org. Coat.* **2009**, *65*, 222–228.

[86] Fan, X.; Lin, L.; Messersmith, P. B. Surface-Initiated Polymerization from TiO_2 Nanoparticle Surfaces Through a Biomimetic Initiator: A New Route Toward Polymer–Matrix Nanocomposites. *Compos. Sci. Technol.* **2006**, *66*, 1198–1204.

[87] Lokteva, I.; Radychev, N.; Witt, F.; Borchert, H.; Parisi, J.; Kolny-Olesiak, J. Surface Treatment of CdSe Nanoparticles for Application in Hybrid Solar Cells: The Effect of Multiple Ligand Exchange with Pyridine. *J. Phys. Chem. C* **2010**, *114*, 12784–12791.

[88] Fogelström, L.; Malmström, E.; Johansson, M.; Hult, A. Hard and Flexible Nanocomposite Coatings Using Nanoclay-Filled Hyperbranched Polymers. *ACS Appl. Mater. Interfaces* **2010**, *2*, 1679–1684.

[89] Siddiqui, N. A.; Sham, M.-L.; Tang, B. Z.; Munir, A.; Kim, J.-K. Tensile Strength of Glass Fibres with Carbon Nanotube–Epoxy Nanocomposite Coating. *Compos. Part A* **2009**, *40*, 1606–1614.

[90] Allahverdi, A.; Ehsani, M.; Janpour, H.; Ahmadi, S. The Effect of Nanosilica on Mechanical, Thermal and Morphological Properties of Epoxy Coating. *Prog. Org. Coat.* **2012**, *75*, 543–548.

[91] Cyras, V. P.; Manfredi, L. B.; Ton-That, M.-T.; Vázquez, A. Physical and Mechanical Properties of Thermoplastic Starch/Montmorillonite Nanocomposite Films. *Carbohydr. Polym.* **2008**, *73*, 55–63.

[92] Maitra, U.; Prasad, K. E.; Ramamurty, U.; Rao, C. N. R. Mechanical Properties of Nanodiamond-Reinforced Polymer-Matrix Composites. *Solid State Commun.* **2009**, *149*, 1693–1697.

[93] Wang, Y.; Lim, S.; Luo, J. L.; Xu, Z. H. Tribological and Corrosion Behaviors of Al_2O_3/Polymer Nanocomposite Coatings. *Wear* **2006**, *260*, 976–983.

[94] Choi, G.-M.; Jin, J.; Shin, D.; Kim, Y. H.; Ko, J.-H.; Im, H.-G.; Jang, J.; Jang, D.; Bae, B.-S. Flexible Hard Coating: Glass-Like Wear Resistant, Yet Plastic-Like Compliant, Transparent Protective Coating for Foldable Displays. *Adv. Mater.* **2017**, *29*, 1700205.

[95] Takahashi, S.; Goldberg, H. A; Feeney, C. A; Karim, D. P.; Farrell, M.; O'Leary, K.; Paul, D. R. Gas Barrier Properties of Butyl Rubber/Vermiculite Nanocomposite Coatings. *Polymer* **2006**, *47*, 3083–3093.

[96] Layek, R. K.; Das, A. K.; Park, M. U.; Kim, N. H.; Lee, J. H. Layer-Structured Graphene Oxide/Polyvinyl Alcohol Nanocomposites: Dramatic Enhancement of Hydrogen Gas Barrier Properties. *J. Mater. Chem. A* **2014**, *2*, 12158–12161.

[97] Choudalakis, G.; Gotsis, A. D. Permeability of Polymer/Clay Nanocomposites: A Review. *Eur. Polym. J.* **2009**, *45*, 967–984.

[98] Ozcalik, O.; Tihminlioglu, F. Barrier Properties of Corn Zein Nanocomposite Coated Polypropylene Films for Food Packaging Applications. *J. Food Eng.* **2013**, *114*, 505–513.

[99] Olad, A.; Rashidzadeh, A. Preparation and Anticorrosive Properties of PANI/Na-MMT and PANI/O-MMT Nanocomposites. *Prog. Org. Coat.* **2008**, *62*, 293–298.

[100] Yeh, J.-M.; Liou, S.-J.; Lai, C.-Y.; Wu, P.-C.; Tsai, T.-Y. Enhancement of Corrosion Protection Effect in Polyaniline via the Formation of Polyaniline–Clay Nanocomposite Materials. *Chem. Mater.* **2001**, *13*, 1131–1136.

[101] Yu, Z.; Di, H.; Ma, Y.; Lv, L.; Pan, Y.; Zhang, C.; He, Y. Fabrication of Graphene Oxide–Alumina Hybrids to Reinforce the Anti-Corrosion Performance of Composite Epoxy Coatings. *Appl. Surf. Sci.* **2015**, *351*, 986–996.

[102] Gu, H.; Ma, C.; Gu, J.; Guo, J.; Yan, X.; Huang, J.; Zhang, Q.; Guo, Z. An Overview of Multifunctional Epoxy Nanocomposites. *J. Mater. Chem. C* **2016**, *4*, 5890–5906.

[103] Rodič, P.; Milošev, I. Corrosion Properties of UV Cured Hybrid Sol-Gel Coatings on AA7075-T6 Determined Under Simulated Aircraft Conditions. *J. Electrochem. Soc.* **2014**, *161*, C412–C420.

[104] Jena, K. K.; Rout, T. K.; Narayan, R.; Raju, K. V. S. N. Novel Organic–Inorganic Hybrid Coatings Prepared by the Sol–Gel Process: Corrosion and Mechanical Properties. *Polym. Int.* **2012**, *61*, 1101–1106.

[105] Zhou, H.; Wang, H.; Niu, H.; Gestos, A.; Wang, X.; Lin, T. Fluoroalkyl Silane Modified Silicone Rubber/Nanoparticle Composite: A Super Durable, Robust Superhydrophobic Fabric Coating. *Adv. Mater.* **2012**, *24*, 2409–2412.

[106] Steele, A.; Bayer, I.; Loth, E. Inherently Superoleophobic Nanocomposite Coatings by Spray Atomization. *Nano Lett.* **2009**, *9*, 501–505.

[107] Kim, D.-Y.; Lee, J.-G.; Joshi, B. N.; Latthe, S. S.; Al-Deyab, S. S.; Yoon, S. S. Self-Cleaning Superhydrophobic Films by Supersonic-Spraying Polytetrafluoroethylene–Titania Nanoparticles. *J. Mater. Chem. A* **2015**, *3*, 3975–3983.

[108] Zhan, X.; Yan, Y.; Zhang, Q.; Chen, F. A Novel Superhydrophobic Hybrid Nanocomposite Material Prepared by Surface-Initiated AGET ATRP and its Anti-Icing Properties. *J. Mater. Chem. A* **2014**, *2*, 9390–9399.

[109] England, M. W.; Urata, C.; Dunderdale, G. J.; Hozumi, A. Anti-Fogging/Self-Healing Properties of Clay-Containing Transparent Nanocomposite Thin Films. *ACS Appl. Mater. Interfaces* **2016**, *8*, 4318–4322.

[110] Yu, Y.-Y.; Chen, C.-Y.; Chen, W.-C. Synthesis and Characterization of Organic–Inorganic Hybrid Thin Films from Poly(acrylic) and Monodispersed Colloidal Silica. *Polymer* **2003**, *44*, 593–601.

[111] Chang, C.-C.; Chen, W.-C. Synthesis and Optical Properties of Polyimide-Silica Hybrid Thin Films. *Chem. Mater.* **2002**, *14*, 4242–4248.

[112] Tu, Y.; Zhou, L.; Jin, Y. Z.; Gao, C.; Ye, Z. Z.; Yang, Y. F.; Wang, Q. L. Transparent and Flexible Thin Films of ZnO-Polystyrene Nanocomposite for UV-Shielding Applications. *J. Mater. Chem.* **2010**, *20*, 1594–1599.

[113] Krogman, K. C.; Druffel, T.; Sunkara, M. K. Anti-Reflective Optical Coatings Incorporating Nanoparticles. *Nanotechnology* **2005**, *16*, S338–S343.

[114] Mont, F. W.; Kim, J. K.; Schubert, M. F.; Schubert, E. F.; Siegel, R. W. High-Refractive-Index TiO_2-Nanoparticle-Loaded Encapsulants for Light-Emitting Diodes. *J. Appl. Phys.* **2008**, *103*, 083120.

[115] Ma, M.; Mont, F. W.; Poxson, D. J.; Cho, J.; Schubert, E. F.; Welser, R. E.; Sood, A. K. Enhancement of Photovoltaic Cell Response due to High-Refractive-Index Encapsulants. *J. Appl. Phys.* **2010**, *108*, 043102.

[116] Guo, L.; Yuan, W.; Lu, Z.; Li, C. M. Polymer/Nanosilver Composite Coatings for Antibacterial Applications. *Colloids Surf., A* **2013**, *439*, 69–83.

[117] Tamayo, L.; Azócar, M.; Kogan, M.; Riveros, A.; Páez, M. Copper-Polymer Nanocomposites: An Excellent and Cost-Effective Biocide for use on Antibacterial Surfaces. *Mater. Sci. Eng. C* **2016**, *69*, 1391–1409.

[118] Yu, Q.; Wu, Z.; Chen, H. Dual-Function Antibacterial Surfaces for Biomedical Applications. *Acta Biomater.* **2015**, *16*, 1–13.

[119] Agarwala, M.; Barman, T.; Gogoi, D.; Choudhury, B.; Pal, A. R.; Yadav, R. N. S. Highly Effective Antibiofilm Coating of Silver–Polymer Nanocomposite on Polymeric Medical Devices Deposited by One Step Plasma Process. *J. Biomed. Mater. Res. B* **2014**, *102B*, 1223–1235.

[120] Spange, S.; Pfuch, A.; Wiegand, C.; Beier, O.; Hipler, U. C.; Grünler, B. Atmospheric Pressure Plasma CVD as a Tool to Functionalise Wound Dressings. *J. Mater. Sci.: Mater. Med.* **2015**, *26*, 76.

[121] De Giglio, E.; Cafagna, D.; Cometa, S.; Allegretta, A.; Pedico, A.; Giannossa, L. C.; Sabbatini, L.; Mattioli-Belmonte, M.; Iatta, R. An Innovative, Easily Fabricated, Silver Nanoparticle-Based Titanium Implant Coating: Development and Analytical Characterization. *Anal. Bioanal. Chem.* **2013**, *405*, 805–816.

Chapter 2

Experimental Techniques

2.1 Introduction

Throughout this thesis, a range of characterisation techniques are utilised in order to study various properties of the prepared coatings such as wettability, morphology, hardness, and chemical structure. This chapter includes a summary of the experimental techniques used in addition to introducing atomised spray plasma deposition which is one of the main deposition techniques used.

2.2 Fabrication Techniques

2.2.1 Solvent Casting

Thin surface coatings can be fabricated using various simple, low-cost coating techniques such as spin coating, dip coating, drop casting (solvent casting), and spray coating. In each of these coating processes the precursor solution is deposited over the substrate and the film is formed upon solvent evaporation.[1]

Spin coating is a technique in which the precursor solution is dropped onto the centre of a flat substrate which is being rotated at high angular speed by a spin coater. The substrate is usually held in place by vacuum chuck. Due to centrifugal force, the solution spreads out evenly over the substrate decreasing the liquid film thickness and simultaneous solvent evaporation results in the formation of a thin film. It is also possible to drop the coating solution onto a stationary substrate before then rotating at high angular speed. Spin coating results in very uniform thin films, the thickness of which can easily be controlled by changing the angular spinning speed, the solution concentration, or the solvent used. The main disadvantage of spin coating is that it can only be used to coat small, smooth substrates. Another downside is that a lot of the coating solution is wasted due to being cast off of the substrate as a result of the high centrifugal force.

Drop casting, or solvent casting, is a similar technique to spin coating however after dropping the precursor solution onto the substrate, the solvent is allowed to naturally evaporate from the stationary substrate rather than being aided through

spinning of the substrate. Given that the substrate remains stationary, the problem of solution wastage is overcome and so much lower volumes of precursor solution are required for solvent casting. This technique also does not require any equipment, unlike spin coating which requires both a spin coater and a vacuum pump. Solvent casting does however still suffer from the inability to coat anything other than a small, flat substrate. Furthermore, the solvent drying time is significantly longer than that for spin coating. Both spin coating and solvent casting are limited to batch processing and are not suitable as large-scale coating techniques.

An alternative to the previously mentioned batch coating techniques is that of dip coating which can be performed as a continuous large-scale roll-to-roll process. In dip coating, the substrate is immersed into the precursor solution for a desired length of time and upon removal a thin liquid film is deposited on all surfaces of the substrate. A surface coating is formed following solvent evaporation, the thickness of which depends on the viscosity and surface tension of the liquid, as well as the substrate immersion time and withdrawal speed. Dip coating coats all sides of the substrate simultaneously however this could be a disadvantage if only one side is required to be coated. It also offers the ability to coat much larger substrates than spin coating or solvent casting. Furthermore, thin films can be deposited onto substrates with more complex shapes. Dip coating does however require large volumes of coating solution in order to fully immerse the substrate and this can result in a large volume of waste solution being produced.

Spray coating also offers a technique which could be used for large-scale processing. In spray coating, the precursor solution is loaded into a pressurised spray gun which is used to spray the solution onto the substrate in the form of a fine mist of small droplets. The spraying is usually performed using a carrier gas such as nitrogen and the spray gun is passed over the substrate a few times, moving from side to side slightly, to ensure even coverage. Quick solvent evaporation results in the formation of a surface coating. As with dip coating, spray coating can be used to coat substrates of varying shapes and sizes however spray coating offers the advantage of being able to selectively coat individual sides of the substrate as desired. Spray coating can also be performed with lower volumes of precursor solution compared to dip coating, reducing wastage of coating solution.

2.2.2 Plasmachemical Deposition

2.2.2.(a) Plasmas

Plasma, often referred to as the fourth state of matter, is used to describe a partially ionised gas consisting of both charged and neutral species such as ions, electrons, radicals, atoms, and molecules.[2] Despite the presence of charged species, the overall charge within the plasma remains neutral in the absence of external disturbances.[3] The plasma, or glow discharge, is formed by transfer of energy from an applied electric field to free electrons present in the gaseous monomer. These electrons are accelerated and can then inelastically collide with gas molecules causing excitation, ionisation, or dissociation of reactant species. Ionisation generates more electrons which are in turn also accelerated undergoing further collisions. This results in a cascade producing a self-sustaining plasma containing electrons, ions, free radicals, and molecules in excited states.[4] The applied electric field can be done so using either direct current or alternating current however alternating current discharges (such as radio frequency discharges) are more advantageous due to the ability to sustain the plasma using external electrodes or coils, thereby reducing contamination of the plasma with the electrodes.[5]

The excited fragments and species present in plasmas are very reactive both towards each other and towards surfaces in contact with the plasma. A glow discharge can therefore be used to modify surface properties either through etching of surface layers, surface modification, or film deposition. In all cases, the surface properties are modified without affecting the bulk properties of the substrate.[5] Surface etching and surface modification result from exposing surfaces to discharges of non-polymerising gases such as oxygen, nitrogen, or ammonia which can cause physical and chemical changes to the surface.[6] Film deposition on the other hand requires a polymerisable precursor (virtually any organic compound with a sufficiently high vapour pressure) and results in the formation of a coating at the surface through plasma dissociation and excitation of the precursor material followed by subsequent polymerisation (recombination) and deposition. This plasma polymerisation technique is a process for preparing new types of material rather than a form of polymerisation with the resulting highly branched and highly cross-linked polymer films found to be quite different compared to polymers formed by conventional polymerisation.[7] The structure of the

plasma-deposited films is influenced by factors such as reactor geometry, power input, substrate temperature, precursor pressure, and precursor flow rate.[5]

Continuous wave plasma polymerisation offers a single-step, solventless, low temperature, substrate-independent technique for depositing highly cross-linked polymer films with excellent adhesion to substrate materials. Furthermore, due to the non-equilibrium nature of most plasmas, the reactant species remain close to ambient temperature and it is therefore possible to coat substrates which lack the thermal stability required for other high temperature coating processes. The high degree of crosslinking in the resultant polymers is due to fragmentation of the monomer (and growing plasma polymer film) during plasma exposure which allows for the deposition of a wide range of precursor materials, even those which do not contain a polymerisable double bond. Functional group retention is however difficult to achieve due to this fragmentation and the polymers often have quite different structures compared to the precursor monomer used.[4] Retention of functional groups can more easily be achieved by using a pulsed plasma polymerisation technique in which the plasma pulse on-period is on a much shorter timescale than the off-period. This reduces the fragmentation of the precursor and allows polymerisation to take place during the off-periods through plasma-induced conventional carbon-carbon double bond polymerisation mechanisms.[8,9] This however greatly reduces the deposition rate of the technique as well as limiting the choice of precursor to only those containing a double bond. Atomised spray plasma deposition (ASPD) offers an alternative way of providing functional group retention but however does not reduce deposition rate and does not necessarily require the presence of a double bond in the precursor. ASPD is discussed further in Section 2.2.2.(b) below.

2.2.2.(b) Atomised Spray Plasma Deposition

Atomised spray plasma deposition is a form of continuous wave plasma deposition however the precursor monomer is introduced into the plasma chamber as an atomised liquid rather than a vapour.[10] Atomisation of the liquid is performed by feeding the monomer into an atomiser nozzle which is attached to the plasma chamber with the substrate to be coated being placed downstream from the nozzle. The ultrasonic nozzle generates a fine mist of droplets around 20 µm in size leading to an increase in the liquid–plasma interface due to the large surface-to-volume ratio of the droplets.[11] As the droplets travel through the plasma towards the substrate, excited

species present in the plasma initiate polymerisation at the carbon-carbon double bond of the precursor molecules within the droplets.[12] The excited plasma species also act to activate the surface of the substrate and upon droplet impact with the surface, polymer chain growth continues resulting in film deposition.[13] If the precursor does not contain a double bond then film growth occurs through fragmentation of the plasma-excited precursor droplets.[14] Atomised spray plasma deposition can be carried out either at low or atmospheric pressure however the low-pressure approach avoids the need to use an expensive diluent gas.[15]

One major advantage of introducing the precursor into the plasma as an atomised liquid rather than a vapour is the ability to greatly increase the flow rate of monomer which raises the precursor density within the reaction chamber.[16] This decreases the average plasma power per reactant molecule which reduces precursor fragmentation resulting in high levels of structural retention in the polymer coating.[7,17] A similar strategy could be used in vapour phase plasma processes however the flow rate is limited by the vapour pressure of the precursor and high vapour pressures can result in instabilities in the plasma.[16] ASPD therefore benefits from the ability to introduce atomised liquids at relatively fast flow rates and in addition to increasing structural retention, this also has the added benefit of increasing the deposition rate by several orders of magnitude.[13] Complex or fragile precursor molecules which would otherwise be damaged using conventional continuous wave plasma can be deposited using ASPD. It is also possible to form coatings using precursor molecules which lack the required vapour pressure to be used as a gas phase monomer. Furthermore, ASPD offers the ability to dissolve or disperse solids in the precursor liquid which allows the deposition of organic–inorganic composite coatings which would otherwise require more complex deposition techniques.

In addition to the advantages mentioned above, atomised spray plasma deposition still retains the benefits previously mentioned for plasma processes in Section 2.2.2.(a) (page 44), namely it being a quick (single-step), low temperature, substrate-independent technique which does not require the use of solvents. ASPD has been used to prepare coatings with excellent gas barrier,[10,15] super-adhesive,[12] protein-resistant,[13] and superhydrophobic[14,18] properties.

2.3 Characterisation Techniques

2.3.1 Contact Angle Analysis

2.3.1.(a) Sessile Drop

The wetting properties of a solid surface, whether it be surfaces that are wet by liquids or surfaces repellent towards them, is an important parameter for a wide range of applications including anti-fogging,[19] self-cleaning,[20] inkjet printing,[21] anti-icing,[22] drag reduction,[23] anti-fouling,[24] and oil–water separation.[25] The behaviour of a liquid droplet on a surface is determined by both the properties of the liquid and of the solid surface (both surface chemistry and topography). Consider a liquid droplet placed on a solid surface. Within the droplet, molecules in the bulk are interacting equally in all directions with neighbouring liquid molecules resulting in a net force of zero.[26] Molecules at the surface however do not have equal interactions in all directions and therefore a net force acts on these molecules pulling them inward. This net force acts to reduce the number of molecules at the surface. This increases the intermolecular distance between surface molecules which requires energy and as a result there is an energy difference between the bulk and the surface.[27] This excess energy at the surface is known as the surface energy which the droplet will try to minimise by contracting to reduce its surface area. The intermolecular force acting to minimise the surface area is known as the surface tension. Solid surfaces also have a surface energy, again due to a difference in energy between the bulk and the surface as a result of the reduced bonding and hence unbalanced intermolecular forces for surface atoms/molecules. The wettability of a surface is therefore governed by the respective surface energies of the liquid droplet and the solid surface and hence by the interfacial energy between the two.

The wetting properties of a surface by a liquid can be characterised by the contact angle, θ_Y, defined as the angle between the solid–liquid and liquid–vapour interfaces, Figure 2.1.[26] This contact angle is dictated by the balance of interfacial tensions at the three-phase contact line between the solid, liquid, and vapour. On a smooth surface, the equilibrium contact angle is related to the surface tensions at the solid–vapour (γ_{SV}), solid–liquid (γ_{SL}), and liquid–vapour (γ_{LV}) interfaces by Young's equation[28]:

$$\cos\theta_Y = \frac{\gamma_{SV} - \gamma_{SL}}{\gamma_{LV}} \quad (2.1)$$

Liquids can interact favourably with a surface resulting in spreading of the droplet to minimise the surface energy. This results in a low contact angle being measured. If a water droplet spreads on the surface with a contact angle of between 0° and 90° then the surface is said to be hydrophilic. Unfavourable interactions would lead to the droplet beading up on the surface and hence a high contact angle of greater than 90° would be measured. Surfaces which show a water contact angle of > 90° are described as being hydrophobic. In a similar way, surfaces are oleophilic if the contact angle of an oil droplet is less than 90° and are oleophobic if the angle is greater than 90°.

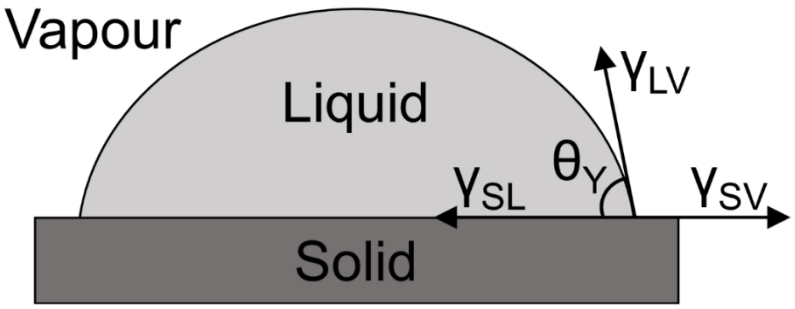

Figure 2.1: Balance of surface tensions at the solid–vapour (γ_{SV}), solid–liquid (γ_{SL}), and liquid–vapour (γ_{LV}) interfaces resulting in the contact angle (θ_Y) of a liquid droplet on a solid surface.

Until now, it has been assumed that the contact angle is the equilibrium contact angle which is measured using a static droplet with the surface horizontal and not tilted in any way. When the surface is titled, the droplet will move and as a result the contact angle of the leading edge (advancing contact angle) will be different to that of the trailing edge (receding contact angle). The advancing and receding contact angles are the maximum and minimum contact angles respectively for a given droplet on a surface and are metastable states.[29,30] The static equilibrium contact angle value lies somewhere between these two extremes. The difference between the advancing and receding angles is known as the contact angle hysteresis and characterises how easily a droplet moves over the surface. A large hysteresis results in the droplet becoming

pinned to the surface even at large tilt angles whereas a low hysteresis indicates that a droplet will easily roll along the surface, even at low tilt angles. Further to the definitions above, a surface is described as being superhydrophobic if the water contact angle is greater than 150° in addition to having a low hysteresis of less than 5°.

Another assumption until now has been that the solid surface is perfectly smooth. In reality however this is never the case and therefore the surface roughness must be considered in addition to the previously mentioned surface energies of both the liquid and the solid surface. Given that it is very difficult to obtain a perfectly smooth surface, the measured contact angle will often differ from that predicted by Young's equation (Equation 2.1). When a droplet is placed on a rough surface it can either be in the Wenzel[31] state or the Cassie–Baxter[32] state.

The Wenzel state is a fully-wetted state in which the liquid fills the cavities of the rough surface resulting in a homogeneous solid–liquid interface, Figure 2.2. For a liquid droplet in the Wenzel state, the Wenzel contact angle for the rough surface (θ_W) is given by:

$$\cos\theta_W = r\cos\theta_Y \qquad (2.2)$$

where θ_Y is the Young's contact angle for the equivalent smooth surface and r is a roughness factor defined as the ratio between the true surface area of the solid and its projection onto a horizontal surface. Given that the area of the projection of a roughened surface will always be greater than the area of the smooth surface, $r \geq 1$. As a result, the Wenzel model predicts that the apparent contact angle of a surface will decrease if $\theta_Y < 90°$ and increase if $\theta_Y > 90°$. Hence, when in the fully-wetted Wenzel state, hydrophilic surfaces become more hydrophilic and hydrophobic surfaces become more hydrophobic. This is intuitive because for a hydrophilic surface (favourable liquid–solid interactions), roughening the surface increases the real surface area in contact with the liquid, increasing the extent of favourable interaction resulting in increased spreading of the droplet. The opposite is true for hydrophobic surfaces with unfavourable liquid–solid interactions.

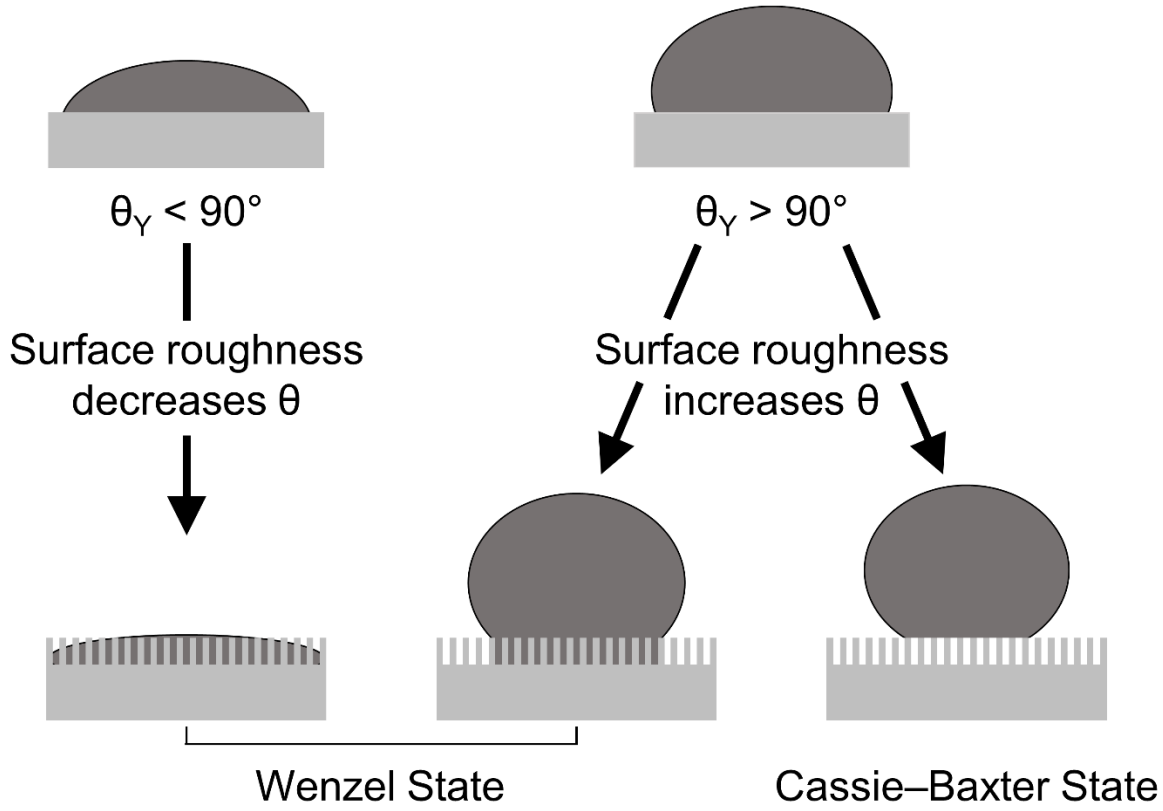

Figure 2.2: Changes in wetting behaviour, and hence contact angle (θ_Y), of a liquid droplet on a solid surface upon surface roughening. Liquid droplets on a roughened surface can either be in the Wenzel state (liquid fills cavities of rough surface resulting in a homogeneous solid–liquid interface) or in the Cassie–Baxter state (air pockets become trapped in cavities under droplet resulting in a composite solid–air–liquid interface).

The Cassie–Baxter state represents another possible wetting state for liquids on roughened surfaces which occurs when air becomes trapped in the cavities under the liquid droplet resulting in the formation of air pockets and as a consequence a composite solid–air–liquid interface, Figure 2.2. For a liquid droplet in the Cassie–Baxter state, the contact angle (θ_{CB}) is given by:

$$\cos\theta_{CB} = f_{SL}\cos\theta_{SL} + f_{LV}\cos\theta_{LV} \qquad (2.3)$$

where f_{SL} and f_{LV} are the local area fractions of the solid–liquid and liquid–vapour interfaces respectively ($f_{SL} + f_{LV} = 1$). θ_{SL} and θ_{LV} are the Young's contact angles for the equivalent smooth surfaces for the solid–liquid and liquid–vapour interfaces respectively. The air pockets in this state are considered to be perfectly hydrophobic and so the contact angle on air (θ_{LV}) is taken to be 180° and therefore $\cos\theta_{LV} = -1$.

The solid–liquid fraction is also affected by roughness as described by Wenzel and so the equation becomes:

$$\cos\theta_{CB} = f_{SL}\, r \cos\theta_{SL} - f_{LV} \qquad (2.4)$$

where r is the roughness factor previously described. From Equation 2.4 above it can be seen that the apparent contact angle θ_{CB} is always greater than the Young's contact angle θ_{SL} due to the f_{LV} term always causing a reduction in cos θ_{CB}. Therefore, θ_{CB} increases for both hydrophilic and hydrophobic surfaces and the extent to which it increases depends on the magnitude of f_{LV}—in other words it depends on how much air is trapped in the cavities. In fact, it is even possible for a hydrophilic surface to become hydrophobic upon roughening as f_{LV} approaches 1 (f_{SL} << 1). If there is no air trapped in the cavities, f_{LV} = 0 and f_{SL} = 1. Therefore, the Cassie–Baxter equation becomes the Wenzel equation as expected for a droplet which completely wets the cavities.

The contact angle is experimentally measured using the sessile drop technique. This involves dispensing a small droplet (typically 1 µL in volume) of probe liquid onto the surface under study using a motorised syringe. An image of the droplet is then taken and the static contact angle is measured using drop analysis software.

2.3.1.(b) Captive Bubble

The captive bubble contact angle is alternative measure of the wettability of a surface. For this technique the surface under study is immersed in the testing liquid and an air bubble is placed beneath the solid, Figure 2.3. The contact angle between the air bubble and the surface is then measured in the same way as for the sessile drop contact angle measurement. The sessile drop contact angle (θ) can then be calculated from the measured captive bubble contact angle (ϕ) using the following equation[33]:

$$\theta = 180 - \phi \qquad (2.5)$$

The shape of the air bubble therefore depends on the wettability of the surface with respect to the testing liquid. If testing with water, air bubbles will bead up (ϕ > 90°) on hydrophilic surfaces (θ < 90°) due to a water layer forming on the surface. For

hydrophobic surfaces (θ > 90°), the air bubble will displace the water and will spread out in a thin layer on the surface (ϕ < 90°).

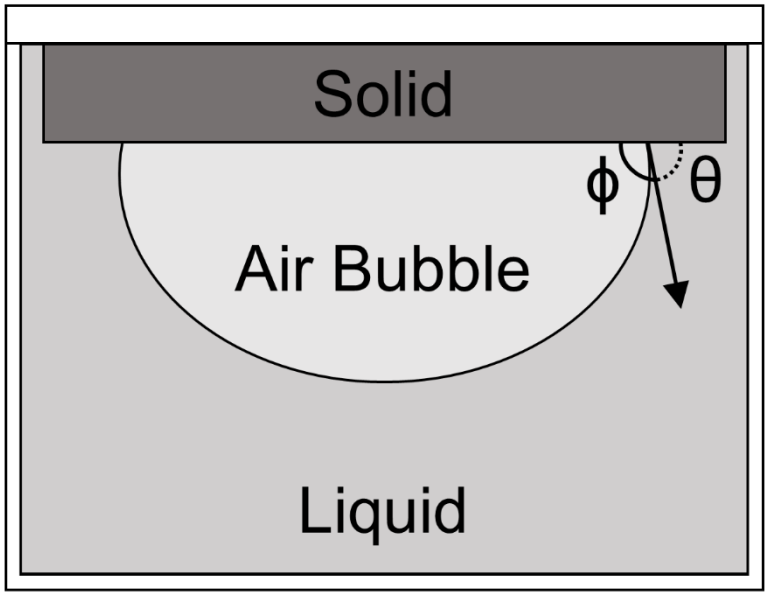

Figure 2.3: Captive bubble contact angle (ϕ) measurement of an air bubble on a solid surface immersed in testing liquid. The sessile drop contact angle (θ) of the testing liquid on the solid surface can be calculated from Equation 2.5.

The captive bubble method has a few advantages over the sessile drop method.[26] Having the sample immersed in the testing liquid minimises contamination of the solid–vapour interface. It is also easier to study the temperature dependence of contact angles because the temperature of the testing liquid that the sample is immersed in is more easily controlled than the temperature of the small droplets used in the sessile drop method. Furthermore, for superhydrophilic surfaces with a contact angle close to 0°, it is often difficult to obtain an accurate sessile drop measurement due to the water droplet being almost completely spread out. With the captive bubble method however, air bubbles on superhydrophilic surfaces will bead up allowing an accurate contact angle to be measured. The captive bubble method does however have the drawback of required much larger volumes of the testing liquid compared to the sessile drop method and is a much more time-consuming method.

2.3.2 Scanning Electron Microscopy

Scanning electron microscopy can be used to obtain a high-resolution image of a surface allowing the study of the surface topography. The resolution achieved is much greater than that possible with an optical microscope due to the much shorter wavelength of electrons compared to light.[34] Another advantage of the scanning electron microscope over an optical microscope is the much larger depth of field.

In scanning electron microscopy, a tungsten filament or field emission gun are used to generate a narrow high energy electron beam (typically 10–40 keV) which is focussed onto the surface.[35] The electron beam is of high enough energy to ionise the atoms on the surface resulting in the emission of low energy secondary electrons. Importantly, because of their low energies, the secondary electrons can only travel short distances and so those which are emitted from the sample must originate close to the surface resulting in a very surface specific technique.[34] Using a positively biased grid, these secondary electrons are accelerated towards a photomultiplier for detection. Images, or scanning electron micrographs, are created by analysing the signal produced by the secondary electrons as the electron beam is scanned across the surface. For non-conducting samples such as ceramics or polymers, excess electrons can build up on the surface as a result of the high energy of the electron beam. Consequently, the surface will become negatively charged which then affects the incident electron beam leading to distorted images. To avoid this, non-conducting samples are usually coated prior to analysis with a thin (10 nm) conductive layer (e.g. gold) which helps to prevent surface charging.

2.3.3 Microindentation

The durability of a surface can be characterised by many techniques such as by measuring abrasion resistance, wear resistance, or scratch resistance. Another way is to measure the hardness of the surface, which is defined as the resistance to indentation. Hardness measurements involve forcing an indenter under a known applied force into a flat surface of the material under study and then measuring the resultant depth of indentation, Figure 2.4. The harder the material, the smaller the indentation. There are many different forms of indentation testing such as Rockwell hardness, Brinell hardness, Knoop hardness, and Vickers hardness all of which operate in a similar way but use differently shaped indentation tips. Indentation measurements are characterised as being microindentation if the indent can be

measured using light microscopy. If the indent is too small to be resolved by an optical microscope, this is given the term nanoindentation. In this thesis, a Vickers tip is used to perform microindentation measurements.

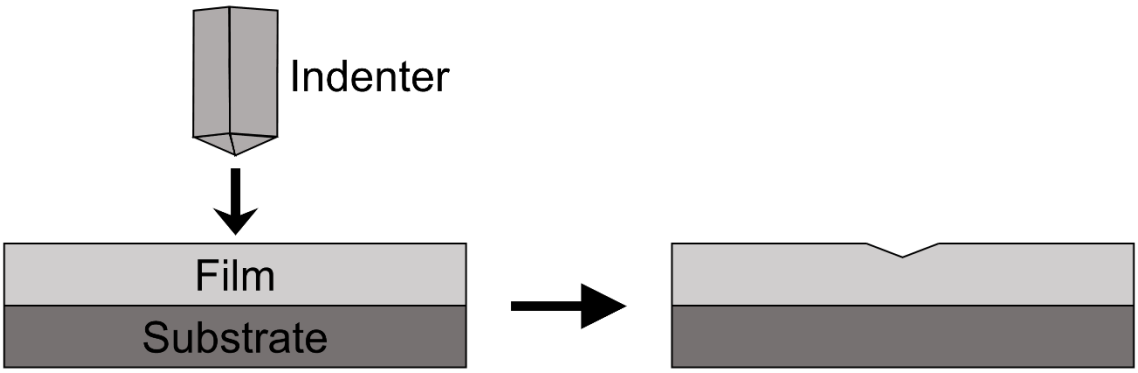

Figure 2.4: Microindentation measurements are performed by forcing an indenter tip under a known applied force into the material under study. The durability, or hardness, is then measured by determining the size of the indent made.

For Vickers microindentation testing the applied load is relatively low and therefore this technique is useful for testing thin materials (e.g. thin films). The Vickers test uses a square base pyramid shaped diamond indenter with an apex angle of 136° between opposite faces of the pyramid, Figure 2.5.[36] The Vickers hardness (*HV*) is determined from the applied load (*P*, units of gram-force (gf)) and the mean diagonal length of the indentation formed (*d*, in µm) as given by Equation 2.6.[37]

$$HV = \frac{2\text{x}10^3\ P \sin\left(\frac{\theta}{2}\right)}{d^2} \qquad (2.6)$$

where θ is the apex angle of the pyramid indenter tip (136°). Therefore Equation 2.6 can be simplified to give Equation 2.7. Vickers hardness numbers can be converted into megapascals (MPa) by multiplying by 9.807.

$$HV = 1854.4\ \text{x}\frac{P}{d^2} \qquad (2.7)$$

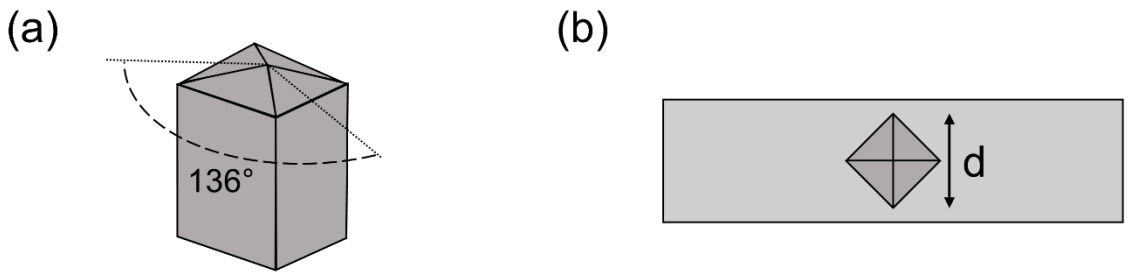

Figure 2.5: (a) A Vickers indenter tip; and (b) the indentation formed from a Vickers tip viewed from directly above the surface.

A typical microindentation test instrument contains the following main features: a loading unit for applying the load, an indenter tip, an X-Y stage where the sample is placed and which can be used to manipulate the sample, objective lenses of an optical microscope, and a measuring mechanism for measuring the diameter of indentation made. The indenter tip and the objective lenses are usually fitted onto a revolver so that the tip can easily be switched out for the lens after indentation. This also ensures that the lens is placed directly over the indentation making it easier to spot the indent. After an indent has been made, the measuring mechanism requires the user to measure both diagonals of the indentation. The instrument can then calculate the hardness using the applied force and an average of these two diagonal distances as described above.

2.3.4 Infrared Spectroscopy

Infrared spectroscopy is a very useful technique for determining the chemical groups present in samples in a range of states such as gases, liquids, powders, and films. The technique utilises the fact that molecules can absorb infrared radiation undergoing vibrational excitation. Different chemical bonds will absorb at different wavelengths and therefore chemical groups can be identified by determining which wavelengths are absorbed after the infrared radiation has either passed through or has been reflected off of the sample. A given vibrational excitation will only occur if the energy of the absorbed photon of infrared radiation is exactly equal to the energy gap between the initial and excited energy levels. In order for a given stretching or bending vibration to be observed in infrared spectroscopy, the stretch or bend must result in a net change in the overall electric dipole moment of the molecule. The energy absorbed

due to the vibrational excitation depends on the spring constant and reduced mass of the chemical bond in question.

Older infrared spectrometers used a dispersive element to sequentially pass different wavelengths of light through the sample and therefore spectrum acquisition time was long. Fourier transform infrared spectroscopy (FTIR) overcomes this problem by simultaneously analysing the entire wavelength range under study.[38] This is done by first passing the infrared radiation through an interferometer which splits the incident radiation using a beamsplitter. One beam is reflected onto a fixed mirror and the other transmitted onto a movable mirror and after reflection from the mirrors the beams recombine to produce an interference spectrum. By adjusting the movable mirror, the pathlength of one of the beams is changed which alters the interference spectrum. For each wavelength a different spectrum is generated. The resulting signal, known as the interferogram, therefore contains information about all wavelengths and this is then passed through the sample before it finally reaches the detector. The detected data contains information about the radiation absorbed in the distance domain (light absorbed as a function of path difference) and so it is then Fourier transformed to give an absorption spectrum as a function of wavelength (usually plotted in wavenumbers with units cm^{-1}) after being compared to a background or reference sample. Due to quick data acquisition, FTIR allows for many spectra to be acquired and averaged resulting in better signal-to-noise ratios.

Infrared spectroscopy is usually performed using transmission methods with absorption of infrared radiation being determined after passing through the sample. For samples difficult to analyse in this way, for example thin films, reflectance methods such as reflection-absorption infrared spectroscopy (RAIRS) or attenuated total reflectance (ATR) spectroscopy are used. RAIRS requires the thin film under study to be deposited onto a reflective substrate such as silicon. The incident beam is then directed towards the surface at grazing angle and is reflected from the substrate towards a detector after having passed through the film. Some of the infrared radiation will be absorbed due to vibrational excitation of the coating and by subtracting the spectrum of the uncoated substrate, the infrared spectrum of the film is obtained. For films deposited onto non-reflective substrates (or for liquids and powders), ATR spectroscopy can be used. ATR uses an accessory containing an infrared transparent crystal of high refractive index (e.g. diamond) which is brought into contact with the sample. The incident radiation is directed into the crystal where it undergoes total

internal reflection at the crystal–sample interface producing evanescent waves which extend into the sample.[39] By directing these waves towards a detector after they have interacted with the sample, and having again subtracted a reference spectrum (in this case the spectrum of the crystal used), an infrared spectrum of the sample is obtained.

2.3.5 Spectrophotometry

Various properties of thin films including the refractive index (*n*), absorption coefficient (k), and film thickness (d) can be determined by spectrophotometry which involves measuring the reflection and/or transmission properties of the surface as a function of wavelength of light in the UV-visible region. The refractive index describes how fast light travels through a medium relative to the speed of light in a vacuum. The absorption coefficient is a measure of how much light is absorbed by the film and therefore affects the intensity of light that is reflected. Both of these properties vary with wavelength of light.

A beam of incident light at an interface of two materials with different refractive indices can either be reflected, transmitted, or absorbed. For a thin film, the initial incident beam of light will encounter the air–film interface and the beam transmitted into the film will encounter the film–substrate interface, Figure 2.6. The beams reflected from both of these interfaces (I_1 and I_2) will recombine resulting in ether constructive or destructive interference depending upon the path difference between the two reflected beams. The optical path difference is given by Equation 2.8 which shows that the interference pattern depends upon incident angle (which affects the angle of transmittance, θ_t), refractive index of the film, and film thickness.

$$Optical\ Path\ Difference = 2n_2 d \cos\theta_t \qquad (2.8)$$

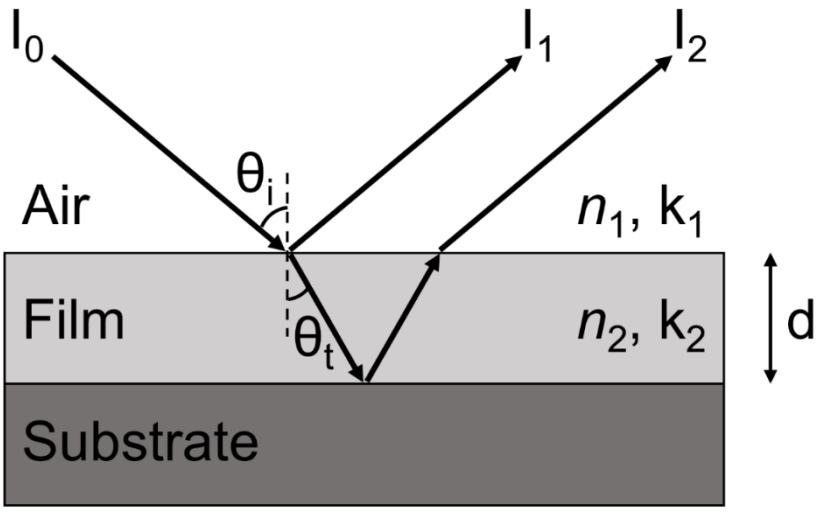

Figure 2.6: A beam of light (I_0) incident at a thin film on a substrate will be partially reflected at the air–film interface (I_1) and partially transmitted. The transmitted light will reflect at the film–substrate interface (I_2). The reflected beams (I_1 and I_2) will interfere, the nature of which will depend on the optical path difference of the reflected beams which is dictated by the refractive index (n_2) and thickness (d) of the film.

Measuring the reflectance as a function of wavelength results in an oscillating spectrum of which the period and amplitude of the oscillations are strongly connected to the film thickness and refractive index, respectively, Figure 2.7. Hence, by fitting the resultant reflectance spectrum of a thin film, the refractive index and film thickness can be determined. Reflectance spectra are fitted by carrying out regression analysis which involves comparing a calculated theoretical curve with the measured data. How well these curves match is described by a parameter called chi-squared (χ^2) and the calculated curve is iteratively refined until χ^2 is at its minimum (the smaller χ^2 is the better the fit). In this thesis, reflectance curves are fitted with a Cauchy model (which assumes that the absorption coefficient is approximately zero) using a modified Levenberg-Marquardt (LM) method.[40] The LM algorithm performs non-linear curve fitting by calculating the derivatives of the reflectance curves.

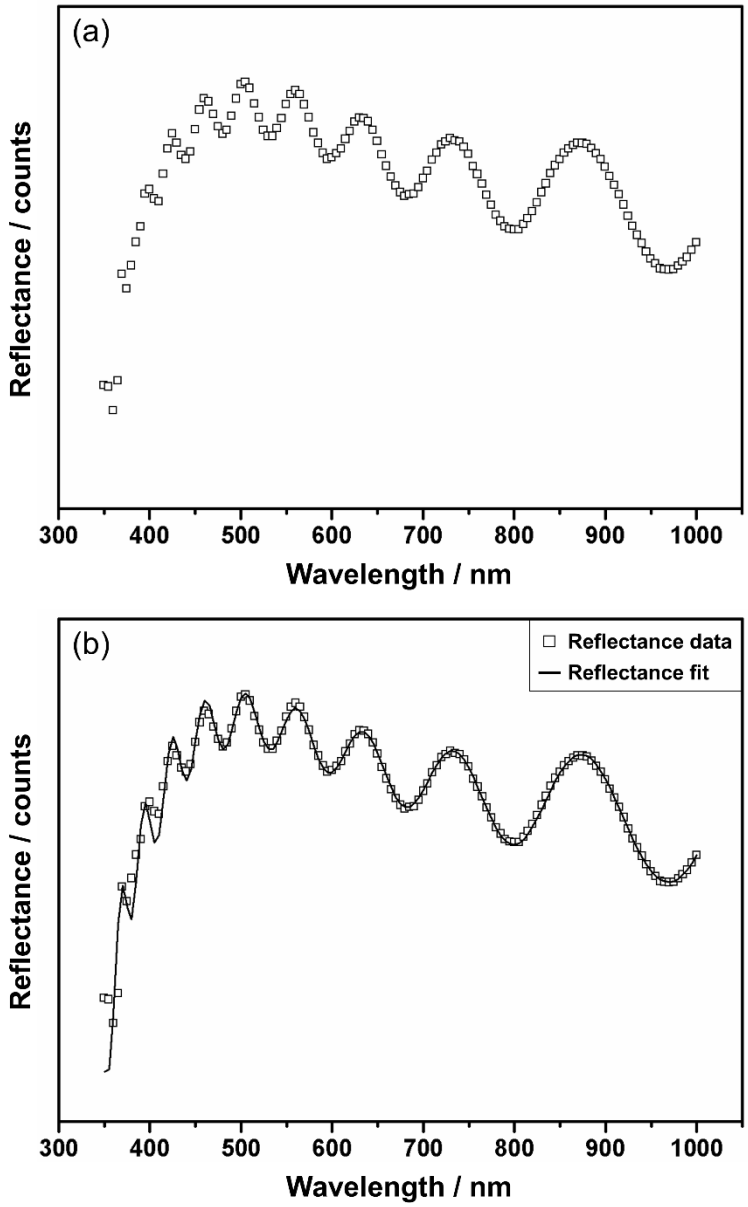

Figure 2.7: (a) Reflectance as a function of wavelength for a thin film on an opaque substrate; and (b) regression analysis fitting of the reflectance spectrum yields the refractive index and thickness of the thin film.

2.3.6 UV-Vis Spectroscopy

UV-vis spectroscopy can be used to study how a material interacts with light usually by measuring how much light it absorbs. Molecules will absorb light, resulting in the excitation of electrons to higher energy levels, provided the photons have enough energy. For some molecules, particularly those containing unsaturated bonds, the energy required will correspond to UV or visible light. Assuming that there are no other interactions between the light and the material under study, such as reflection or

scattering, the amount of light absorbed (*A*) is defined as the negative log of the transmitted intensity (*I*) as a fraction of the incident intensity (I_0), Equation 2.9.

$$A = -\log_{10}\left(\frac{I}{I_0}\right) \quad (2.9)$$

This can also be expressed in terms of light transmittance with percentage transmittance (*% T*) being defined as:

$$\%\, T = \left(\frac{I}{I_0}\right) \text{ x } 100 \quad (2.10)$$

Therefore, absorbance and transmittance are related by Equation 2.11.

$$A = -\log_{10} T \quad (2.11)$$

Absorbance can also be expressed in terms of concentration (*c*) and path length (*L*) by Equation 2.12 where ε is the molar absorption coefficient, a measure of how strongly a species absorbs light at a certain wavelength under a defined set of conditions. This is known as the Beer-Lambert law.

$$A = \varepsilon c L \quad (2.12)$$

Most UV-vis spectrophotometers use two lights sources in order to achieve a broad band of radiation. Typically, a deuterium arc lamp is used to provide UV radiation and a tungsten-halogen lamp to provide visible light. The light from these sources is then directed through a dispersion device, such as a prism or grating, to disperse the light. By using the appropriate slit, particular wavelengths can then be directed to pass through the sample towards the detector. The intensity of the light reaching the detector is then measured and the absorbance can be calculated as described above. Incident intensity is determined by measuring light intensity with a blank substrate or sample holder (cuvette) in place of the sample under study. More modern spectrophotometers allow both the blank and the sample to be run at the same time,

reducing errors associated with lamp drift (changes in lamp intensity) between measurements. This is done by placing a chopper after the slit which is able to quickly switch the beam path between the blank sample and the sample under study allowing them to be studied simultaneously.[41]

As mentioned above, when measuring absorbance, assumptions have to be made with regards to scattering and reflection. When equating the difference between initial and final intensities to the proportion of light absorbed it is assumed than nothing is scattered or reflected. Similarly, if the level of transmittance is measured, the proportion of light not transmitted is not necessarily absorbed, some may have been scattered or reflected. For a more accurate measurement of absorbance, or for opaque samples, an integrating sphere could be used.[42] This collects all reflected or scattered light and therefore absorbance can be measured much more accurately.

2.3.7 Antibacterial Activity

2.3.7.(a) Bacterial Strains

Escherichia coli BW25113 (CGSC 7636; rrnB3 ΔlacZ4787 hsdR514 Δ(araBAD)567 Δ(rhaBAD)568 rph-1) and *Staphylococcus aureus* (FDA209P, an MSSA strain; ATCC 6538P) were used in this work as representative Gram-negative and Gram-positive strains, respectively.

BW25113, a wild-type K-12 strain, was chosen as the *Escherichia coli* strain because it is the parent strain used in the Keio collection.[43] Therefore, if required, the mechanism of action of the tested surfaces could easily be explored further by testing against any of the single-gene knockouts of this strain.

FDA209P was chosen as the *Staphylococcus aureus* strain as it is a methicillin-sensitive *Staphylococcus aureus* (MSSA) strain and is therefore less problematic to treat in the event that someone doing the antibacterial testing picks up an infection.[44] This strain is also widely used for antibiotic sensitivity testing.

2.3.7.(b) Colony Counting

There are several methods which can be used to assess cell viability such as colony counting, measuring solution turbidity, fluorescent tagging, and bright-field microscopy. Colony counting is the simplest method and this was the method chosen in this work. For this technique, the bacteria are first allowed to interact with the surface

being tested for a period of time (usually 16 h) under incubation. Appropriate media is then added to the sample in order to recover the bacteria and further serial dilutions are made. Drops from these serial dilutions are then placed onto solid nutrient agar plates followed by incubation at optimal growth temperature (usually for 16 h). After incubation, visible cell colonies appear on the surface of the agar plates. The number of colonies visible at each dilution are then counted and from this it is possible to determine the quantity of bacteria present in the solution after interaction with the surface, expressed as colony forming units per millilitre (CFU mL^{-1}).

2.4 References

[1] Schwartz, R. W.; Schneller, T.; Waser, R. Chemical Solution Deposition of Electronic Oxide Films. *C. R. Chim.* **2004**, *7*, 433–461.

[2] Langmuir, I. The Interaction of Electron and Positive Ion Space Charges in Cathode Sheaths. *Phys. Rev.* **1929**, *33*, 954.

[3] Bittencourt, J. A. Fundamentals of Plasma Physics, 3rd ed.; Springer-Verlag: New York, 2004.

[4] d'Agostino, R., Ed. Plasma Deposition, Treatment, and Etching of Polymers; Academic Press, Inc.: London, U.K., 1990.

[5] Chan, C.-M.; Ko, T.-M.; Hiraoka, H. Polymer Surface Modification by Plasmas and Photons. *Surf. Sci. Rep.* **1996**, *24*, 1–54.

[6] Grill, A. Cold Plasma in Materials Fabrication; IEEE Press: New York, 1994.

[7] Yasuda, H. Plasma Polymerization; Academic Press, Inc.: London, U.K., 1985.

[8] Tarducci, C.; Kinmond, E. J.; Brewer, S. A.; Willis, C.; Badyal, J. P. S. Epoxide-Functionalized Solid Surfaces. *Chem. Mater.* **2000**, *12*, 1884–1889.

[9] Kinmond, E. J.; Coulson, S. R.; Brewer, S. A.; Willis, C.; Badyal, J. P. S. High Structural Retention During Pulsed Plasma Polymerization of 1H,1H,2H-perfluorododecene: An NMR and TOF-SIMS Study. *Polymer* **2005**, *46*, 6829–6835.

[10] Ward, L. J.; Schofield, W. C. E.; Badyal, J. P. S.; Goodwin, A. J.; Merlin, P. J. Atmospheric Pressure Plasma Deposition of Structurally Well-Defined Polyacrylic Acid Films. *Chem. Mater.* **2003**, *15*, 1466–1469.

[11] Chen, Q.; Li, J.; Li, Y. A Review of Plasma–Liquid Interactions for Nanomaterial Synthesis. *J. Phys. D: Appl. Phys.* **2015**, *48*, 424005.

[12] Wood, T. J.; Ward, L. J.; Badyal, J. P. S. Super-Adhesive Polymer–Silica Nanocomposite Layers. *ACS Appl. Mater. Interfaces* **2013**, *5*, 9678–9683.

[13] Wood, T. J.; Brown, P. S.; Badyal, J. P. S. Atomized Spray Plasma Deposition of Structurally Well-Defined Bioactive Coatings. *Plasma Chem. Plasma Process.* **2014**, *34*, 1019–1031.

[14] Castaneda-Montes, I.; Ritchie, A. W.; Badyal, J. P. S. Atomised Spray Plasma Deposition of Hierarchical Superhydrophobic Nanocomposite Surfaces. *Colloids Surf., A* **2018**, *558*, 192–199.

[15] Ward, L. J.; Schofield, W. C. E.; Badyal, J. P. S.; Goodwin, A. J.; Merlin, P. J. Atmospheric Pressure Glow Discharge Deposition of Polysiloxane and SiO_x Films. *Langmuir* **2003**, *19*, 2110–2114.

[16] Wood, T. J.; Badyal, J. P. S. Atomised Spray Plasma Deposition (ASPD) of Structurally Well-Defined Alkyl Functionalised Layers. *Surf. Coat. Technol.* **2013**, *227*, 28–31.

[17] Friedrich, J. Mechanisms of Plasma Polymerization – Reviewed from a Chemical Point of View. *Plasma Process. Polym.* **2011**, *8*, 783–802.

[18] Fanelli, F.; Mastrangelo, A. M.; Fracassi, F. Aerosol-Assisted Atmospheric Cold Plasma Deposition and Characterization of Superhydrophobic Organic–Inorganic Nanocomposite Thin Films. *Langmuir* **2014**, *30*, 857–865.

[19] Cebeci, F. C.; Wu, Z.; Zhai, L.; Cohen, R. E.; Rubner, M. F. Nanoporosity-Driven Superhydrophilicity: A Means to Create Multifunctional Antifogging Coatings. *Langmuir* **2006**, *22*, 2856–2862.

[20] Fürstner, R.; Barthlott, W.; Neinhuis, C.; Walzel, P. Wetting and Self-Cleaning Properties of Artificial Superhydrophobic Surfaces. *Langmuir* **2005**, *21*, 956–961.

[21] Son, Y.; Kim, C.; Yang, D. H.; Ahn, D. J. Spreading of an Inkjet Droplet on a Solid Surface with a Controlled Contact Angle at Low Weber and Reynolds Numbers. *Langmuir* **2008**, *24*, 2900–2907.

[22] Cao, L.; Jones, A. K.; Sikka, V. K.; Wu, J.; Gao, D. Anti-Icing Superhydrophobic Coatings. *Langmuir* **2009**, *25*, 12444–12448.

[23] Truesdell, R.; Mammoli, A.; Vorobieff, P.; van Swol, F.; Brinker, C. J. Drag Reduction on a Patterned Superhydrophobic Surface. *Phys. Rev. Lett.* **2006**, *97*, 044504.

[24] Zhang, H.; Lamb, R.; Lewis, J. Engineering Nanoscale Roughness on Hydrophobic Surface—Preliminary Assessment of Fouling Behaviour. *Sci. Technol. Adv. Mat.* **2005**, *6*, 236–239.

[25] Feng, L.; Zhang, Z.; Mai, Z.; Ma, Y.; Liu, B.; Jiang, L.; Zhu, D. A Super-Hydrophobic and Super-Oleophilic Coating Mesh Film for the Separation of Oil and Water. *Angew. Chem. Int. Ed.* **2004**, *43*, 2012–2014.

[26] Yaun, Y.; Lee, T. R. In *Surface Science Techniques*; Bracco, G., Holst, B., Eds.; Springer: Berlin/Heidelberg, **2013**; Vol. 51, pp 3–34.

[27] Kinloch, A. J. Adhesion and Adhesives: Science and Technology; Chapman and Hall: London, U.K., 1987.

[28] Young, T. An Essay on the Cohesion of Fluids. *Phil. Trans. R. Soc.* **1805**, *95*, 65–87.

[29] Blossey, R. Self-Cleaning Surfaces — Virtual Realities. *Nat. Mater.* **2003**, 2, 301–306.

[30] Extrand, C. W. Contact Angles and Hysteresis on Surfaces with Chemically Heterogeneous Islands. *Langmuir* **2003**, *19*, 3793-3796.

[31] Wenzel, R. N. Resistance of Solid Surfaces to Wetting by Water. *Ind. Eng. Chem.* **1936**, *28*, 988–994.

[32] Cassie, A. B. D.; Baxter, S. Wettability of Porous Surfaces. *Trans. Faraday Soc.* **1944**, *40*, 546–551.

[33] Montes Ruiz-Cabello, F. J.; Rodríguez-Valverde, M. A.; Marmur, A.; Cabrerizo-Vílchez, M. A. Comparison of Sessile Drop and Captive Bubble Methods on Rough Homogeneous Surfaces: A Numerical Study. *Langmuir* **2011**, *27*, 9638–9643.

[34] Stokes, D. J. Principles and Practice of Variable Pressure/Environmental Scanning Electron Microscopy (VP-ESEM); John Wiley & Sons Ltd.: Chichester, U.K., 2008.

[35] Goodhew, P. J.; Humphreys, J.; Beanland, R. Electron Microscopy and Analysis, 3rd ed.; Taylor and Francis: London, U.K., 2001.

[36] Baltá Calleja, F. J.; Fakirov, S. Microhardness of Polymers; Cambridge University Press: Cambridge, U.K., 2000.

[37] ASTM Standard E384–11e1, Standard Test Method for Knoop and Vickers Hardness of Materials, ASTM International, West Conshohocken, PA, 2011, DOI: 10.1520/E0384-11E01, www.astm.org.

[38] Stuart, B. Infrared Spectroscopy: Fundamentals and Applications; John Wiley & Sons Ltd.: Chichester, U.K., 2004.

[39] Vickerman, J. C. Surface Analysis – The Principle Techniques; John Wiley & Sons Ltd.: Chichester, U.K., 1997.

[40] Lovering, D. NKD-6000 Technical Manual; Aquila Instruments: Cambridge, U.K., 1998.

[41] Owen, T. Fundamentals of Modern UV-Visible Spectroscopy; Agilent Technologies Inc.: Germany, 2000.

[42] Wilson, M. Functional Catalytic Surfaces for Environmental Sustainability. PhD Thesis, Durham University, 2018.

[43] Coli Genetic Stock Centre (CGSC), Strain BW25113. https://cgsc.biology.yale.edu/Strain.php?ID=64667 (accessed Sep 10, 2020).

[44] Singh, M.; Sasaki, T.; Matsuo, M.; Morimoto, Y.; Aiba, Y.; Hiramatsu, K. Complete Genome Sequence of the Drug-Naive Classical *Staphylococcus aureus* Strain FDA209P. *Genome Announc.* **2015**, *3*, e01343-15.

Chapter 3

Bioinspired Multifunctional Polymer Nanoparticle Surfactant Complex Nanocomposite Surfaces for Antibacterial Oil–Water Separation

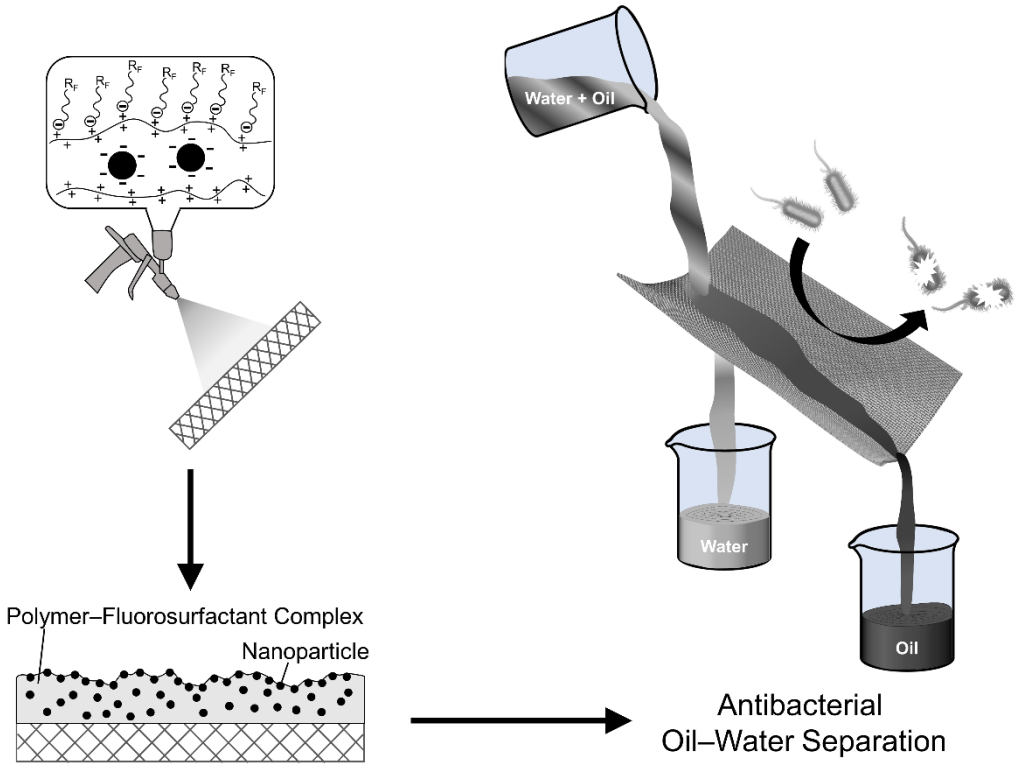

3.1 Introduction

Oil-spill clean-up is an important environmental challenge due to the significant long-term effects such accidents have on oceans and aquatic species.[1,2,3,4,5,6] Absorbent materials are reported to remove oil from oil–water mixtures—however, these materials need additional steps to remove the absorbed oil and to regenerate the material for re-use; and water absorption during oil recovery reduces their efficiency (unsuitable for continuous oil–water separation processes).[7,8,9,10,11,12,13] Separation membranes which have opposing wetting properties towards water versus oil can be utilised for continuous oil–water mixture separation.[14,15,16,17,18,19,20,21] Due to the relative surface energies of typical oils (20–30 mN m^{-1}) versus water (72 mN m^{-1}), conventional membranes repel water while allowing oil to pass through.[22,23,24]

However, these oleophilic–hydrophobic materials are easily fouled by oils causing blockage and a drop in efficiency. Furthermore, the greater density of water compared to oils can lead to the formation of a surface water layer which blocks the passage of oil.[25] Simply by reversing the wettability, these drawbacks can be overcome (oleophobic–hydrophilic surfaces repel oil but are wetted by water). Oils are repelled and so do not easily foul the surface, while the hydrophilic nature of such materials helps to remove any contaminants in contact with the surface.[26] The main disadvantage of such oleophobic–hydrophilic surfaces has been the complexity of their preparation and methods of application. One approach for oleophobic–hydrophilic surfaces has been the use of superhydrophilic surfaces—when underwater, the water layer formation on the surface helps to repel oils providing an underwater oleophobic surface.[27,28,29] The major disadvantage of these underwater oleophobic–hydrophilic systems is that the filter must constantly be kept in a wetted state (as soon as the filter dries up the oil will pass through).[30] They are also easily contaminated by oils due to their in-air oleophilic properties. Therefore, surfaces which display both in-air oleophobicity and hydrophilicity are more desirable for oil–water separation applications. In addition, these are also suitable for other uses such as anti-fogging[26,31,32,33] and self-cleaning.[26,31,32]

One way to fabricate oleophobic–hydrophilic surfaces is to utilise polymer–fluorosurfactant complexes (the fluorosurfactant complexes to the polymer backbone through electrostatic interaction).[34,35,36,37] These surfaces can be prepared either by a multi-step layer-by-layer approach[38,39,40] or by direct application of the polymer–fluorosurfactant complex onto the substrate.[41,42,43] For both cases, the oil repellency of the polymer–fluorosurfactant coating stems from the low-surface-energy fluorinated tail of the fluorosurfactant being orientated towards the air–solid interface.[44] This localises the hydrophilic fluorosurfactant head groups in the sub-surface region where they are complexed to the hydrophilic groups of the polymer. When water molecules are placed onto the surface, they wick down towards the hydrophilic subsurface resulting in surface wetting.[45] It has been suggested that this happens through defects in the fluorinated layer, whilst oil molecules are too large to penetrate them.[46,47] Another possible mechanism is water-induced surface rearrangement of the fluorinated chains allowing penetration of the water molecules; whilst in the presence of oils, this rearrangement does not take place, and so the top-most low-surface-energy fluorinated chains repel oil.[48]

Early reports of polymer–fluorosurfactant coated surfaces showed little difference between the oil and water contact angles.[34,37,44,49] Improvements in hydrophilicity were subsequently achieved through the utilisation of plasma polymer–fluorosurfactant coatings leading to larger switching parameters (the difference in the static hexadecane and water contact angles)—however, this remained a two-step process.[50,51,52] Although single-step processes have been reported, these surfaces tend to be initially hydrophobic, and it can take several minutes for them to achieve their final hydrophilic state.[41,42] One notable exception has been fast-switching copolymer–fluorosurfactant surfaces where water wets within 10 s whilst oleophobicity is retained.[43] This oil repellency was improved further through the use of solvent-induced roughening to yield switching parameters in the order of 100°. A comparable switching parameter (90–95°) has been reported by adding nanoparticles to the polymer–fluorosurfactant complex solution mixture—however, oil–water separation experiments take several minutes to allow the water to pass through due to the requirement for very small aperture meshes (~42 to 60 μm), therefore this system is not suitable for continuous oil–water separation.[48] Although good initial oil repellency and hydrophilicity have been reported for a layer-by-layer approach where the polymer, fluorosurfactant, and silica nanoparticles are deposited in sequential steps—this is a lengthy process and not well suited to industrial scale-up.[39,53] Appendix 2, Section A2.1 (page 185) provides a summary of all previously reported coatings which are simultaneously oleophobic and hydrophilic. Surface coatings which switch from being oleophobic–hydrophobic to oleophobic–hydrophilic through time are summarised in Appendix 2, Section A2.2 (page 191).

In this study, nanocomposite oleophobic–hydrophilic surfaces have been deposited in a single step by using polymer–nanoparticle–fluorosurfactant complexes which display a marked enhancement in the switching parameter. Coating of large aperture (310 μm) meshes provides for high efficiency continuous oil–water separation performance, Scheme 3.1. The incorporation of nanoparticles improves the hardness (durability) and enhances oleophobicity / hydrophilicity (switching parameter) of the coatings. The latter is akin to how the roughness of plant leaves can give rise to either hydrophobicity or hydrophilicity depending upon surface functional groups.[54,55] The constituent cationic polymer poly(diallyldimethylammonium) imparts antibacterial properties. Although polymeric quaternary ammonium–surfactant complexes have previously been utilised for their antimicrobial properties, they have not been

developed for oil–water separation to provide multi-functional surfaces.[56,57] This concept is important in relation to real-world scenarios, where the simultaneous oil–water separation and killing of bacteria during filtration is highly desirable for safe human water consumption and pollution clean-up. The only previous reports of antimicrobial surfaces capable of oil–water separation utilise oleophilic–hydrophobic[58,59] or hydrophilic–underwater oleophobic[60] coatings which have many disadvantages as mentioned above. Furthermore, the antimicrobial properties of these coatings are relatively poor (<90% killing).[58,60] Previously reported coatings capable of antibacterial oil–water separation are summarised in Appendix 2, Section A2.3 (page 199). An oleophobic(in air)–hydrophilic coating with antibacterial properties has never previously been reported.

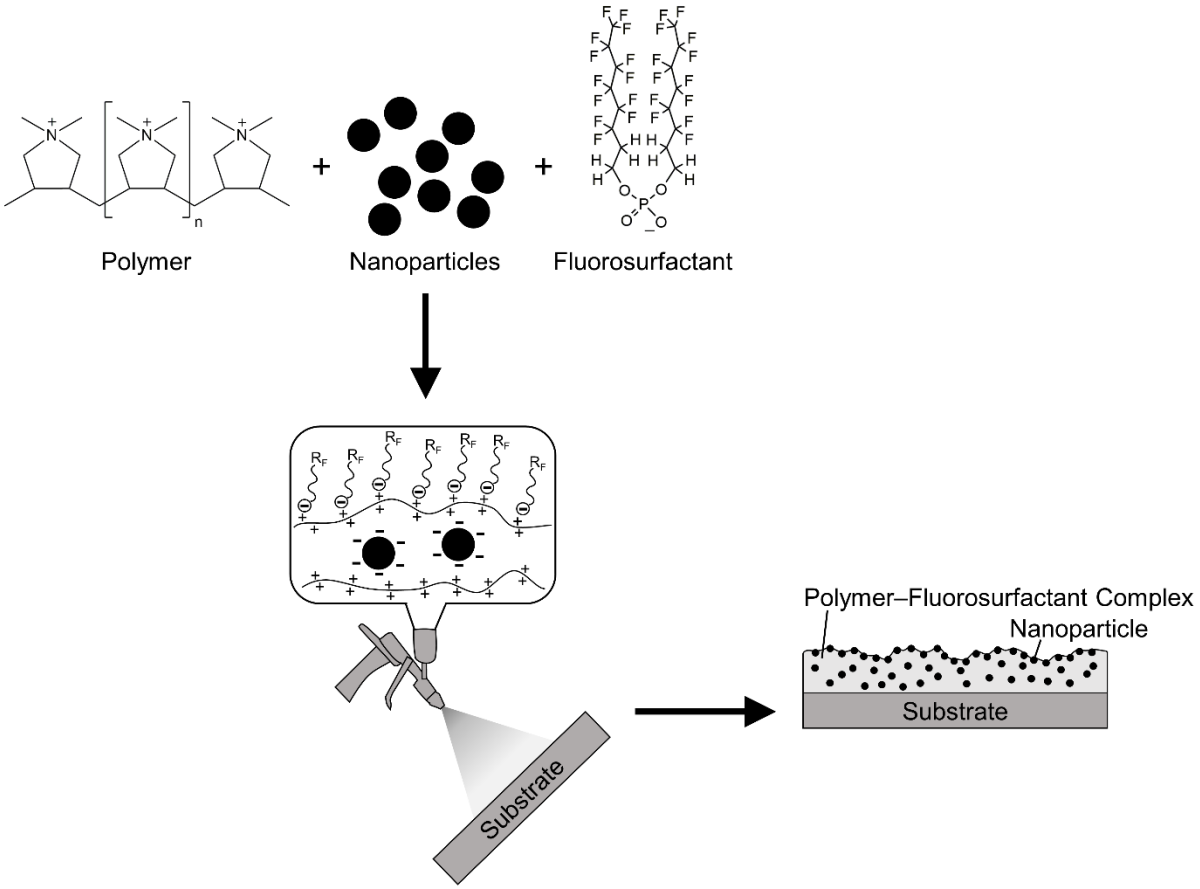

Scheme 3.1: Spray coating of cationic poly(diallyldimethylammonium)–anionic fluorosurfactant complex containing negative surface charged nanoparticles.

3.2 Experimental

3.2.1 Polymer–Particle–Fluorosurfactant Complex Coatings

Poly(styrene-co-maleic anhydride) (Polyscope Polymers BV, Grade: XIRAN® SZ26080) was dissolved in acetone (+99.8%, Sigma-Aldrich Ltd.) and aqueous poly(diallyldimethylammonium chloride) (PDDA; Sigma-Aldrich Ltd., 20 wt % in H_2O) was diluted in high-purity water (ISO 3696 grade 2), both at a concentration of 2% w/v. The polymer solutions were allowed to shake for 2 h. If particles were to be incorporated into the coating, then these were ultrasonically dispersed for 1 h in the polymer solution at various loadings (loadings are percentage weights by volume (% w/v) of the particle dispersed in the polymer solution). The range of particles investigated are detailed in Table 3.1.

Table 3.1: Details of the particles used.

Particle	Surface Charge	Average Particle Size	Supplier
SiO_2	Negative	7 nm	Degussa Aerosil® 300
SiO_2	Negative	100 µm	Crosfield Catalysts
SiO_2, methacryloyl functionalised	Negative	12 nm (100–200 nm average aggregate size)	Degussa Aerosil® R711
SiO_2, hexadecylsilane functionalised	Negative	12 nm	Degussa Aerosil® R816
Graphene	Negative	<2 µm	Strem Chemicals
Al_2O_3	Positive	13 nm	Degussa Aluminiumoxid C
ZnO	Positive	<100 nm	Sigma-Aldrich Ltd.

Anionic phosphate fluorosurfactant (Capstone FS-63, DuPont Ltd.), amphoteric betaine fluorosurfactant (Capstone FS-50, DuPont Ltd.) or isostearic acid (Tokyo Chemical Industry Co., Ltd.) were further diluted in high-purity water at a concentration of 5% v/v. The fluorosurfactant solution was added dropwise in a 1:4 volume ratio to the prepared polymer–particle solution whilst stirring leading to the formation of a polymer–particle–fluorosurfactant complex. The isostearic acid was added in a similar

manner in a 1:2 volume ratio to prepared polymer–particle solution leading to the formation of a polymer–particle–surfactant complex. The precipitated solid complex was collected from the liquid phase and rinsed with high-purity water followed by drying on a hotplate. The obtained dry solids were dissolved as follows to provide the coating solutions: poly(styrene-co-maleic anhydride)–amphoteric fluorosurfactant complex was dissolved at a concentration of 2% w/v in dimethylformamide (≥99.5%, Fisher Scientific UK Ltd.) or a 1:2 v/v dimethylformamide / methanol (>95%, Fisher Scientific UK Ltd.) mixture; poly(diallyldimethylammonium)–amphoteric fluorosurfactant and poly(diallyldimethylammonium)–amphoteric fluorosurfactant complexes were dissolved at a concentration of 1% w/v in ethanol (+99.8 wt %, Fisher Scientific UK Ltd.); and poly(diallyldimethylammonium)–isostearic acid complex was dissolved at a concentration of 2% w/v in methanol. Glass microscope slides (Academy Science Ltd.) and silicon wafers (Silicon Valley Microelectronics Inc.) were used as flat substrates. These were cleaned prior to coating by sonication in a 50%:50% propan-2-ol (>99.5 wt %, Fisher Scientific UK Ltd.) / cyclohexane (≥99.7%, Sigma-Aldrich Ltd.) mixture, followed by UV/ozone treatment (BioForce Nanosciences Inc., model UV.TC.EU.003), and finally another sonication step in the propan-2-ol / cyclohexane mixture. Coatings were applied either by dip coating, spin coating using a spincoater (model PRS14E, Cammax Precima Ltd.), solvent casting (solution was dispensed onto the substrate and the solvent allowed to evaporate), or by spray coating using a pressurised spray gun (RG-3L, Anest Iwata Inc.). For the oil–water separation experiments, the following stainless steel meshes were spray coated: #30 (0.20 mm wire diameter, 0.65 mm aperture, The Mesh Company Ltd.); #40 (0.22 mm wire diameter, 0.41 mm aperture, The Mesh Company Ltd.); #50 (0.20 mm wire diameter, 0.31 mm aperture, The Mesh Company Ltd.); #100 (0.10 mm wire diameter, 0.15 mm aperture, The Mesh Company Ltd.). The stainless steel mesh substrates were cleaned prior to coating by rinsing with propan-2-ol. For antibacterial testing, pieces of non-woven polypropylene sheet (0.11 mm thickness, 22.7 ± 1.1 μm fibre diameter, Spunbound, 70 g m^{-2}, Avoca Technical Ltd, UK) were spray coated. The non-woven polypropylene substrates were cleaned prior to coating by soaking in ethanol for 15 min before being dried under vacuum.

3.2.2 Sessile Drop Contact Angle

Sessile drop contact angle analysis was carried out on coated glass slide substrates with a video capture system in combination with a motorised syringe (VCA2500XE,

AST Products Inc.). 1 µL droplets of ultrahigh-purity water (BS 3978 grade 1) and hexadecane (99%, Sigma-Aldrich Ltd.) were dispensed for water and oil contact angle measurements respectively. Following dispensation of the probe liquid onto the coated substrate, a snapshot of the image was taken and analysed using the VCA-2500 Dynamic/Windows software. The water contact angle (WCA) was measured as soon as the droplet was placed onto the surface and again after a period of 10 s—this was done in order to observe any change in the WCA over a short time period due to the "switching" behaviour of these surfaces (a short time of 10 s was chosen because coatings required for oil–water separation applications need to switch quickly in order to attain high efficiencies). The hexadecane contact angle (HCA) was measured as soon as the droplet was placed onto the surface and it was observed not to vary with time. The reported contact angle measurements were made after rinsing samples with water and drying in air. Switching parameters were determined by calculating the difference between the equilibrium hexadecane and water static contact angles.

3.2.3 Captive Bubble Contact Angle

Captive bubble contact angle analysis was carried out on coated glass slide substrates with the video capture system in combination with a captive bubble attachment dispensing approximately 1 µL air bubbles (VCA captive bubble accessory, AST Products Inc.). Following release of the air bubble onto the coated substrate under water, the droplet was viewed using the VCA-2500 Dynamic/Windows software.

3.2.4 Scanning Electron Microscopy

Coated silicon wafer substrates were mounted onto carbon disks supported on aluminium stubs, and then coated with a thin gold layer (5–10 nm, Polaron SEM Coating Unit, Quorum Technologies Ltd.). Surface morphology images were acquired using a scanning electron microscope (model Vega 3LMU, Tescan Orsay Holdings a.s.) operating in secondary electron detection mode, in conjunction with an 8 kV accelerating voltage, and a working distance of 8–11 mm.

3.2.5 Microindentation

Hardness values were obtained for coated silicon wafer substrates using a microhardness tester (model MVK-H2, Mitutoyo Inc.) fitted with a standard Vickers tip.

The tip force was applied for 10 s. Five microindentation measurements were made across the surface for each applied force (international standard ASTM E384–11e1).[61]

3.2.6 Oil–Water Separation

Oil–water separation experiments were carried out using the coated stainless steel mesh substrates. An agitated mixture of oil and water (high-purity, ISO 3696 grade 2) was poured over the stainless steel mesh. The following oils were used: hexadecane (99%, Sigma-Aldrich Ltd.), tetradecane (+99%, Sigma-Aldrich Ltd.), octane (+99%, Sigma-Aldrich Ltd.), vegetable oil (Tesco PLC), and olive oil (Tesco PLC). The mesh was either placed horizontally above one beaker or at an incline above two beakers for batch and continuous separations respectively. In order to enhance the visual contrast, Oil Red O (≥75% dye content, Sigma-Aldrich Ltd.) and Procion Blue MX-R (35% dye content, Sigma-Aldrich Ltd.) were added to the oil (red) and water (blue) respectively. Oil–water separation efficiency was calculated from the masses of liquid collected using the horizontal coated meshes.

3.2.7 Antibacterial Activity

Gram-negative *Escherichia coli* BW25113 (CGSC 7636; *rrnB3* Δ*lacZ4787 hsdR514* Δ(*araBAD*)*567* Δ(*rhaBAD)568 rph-1*) and Gram-positive *Staphylococcus aureus* (FDA209P, an MSSA strain; ATCC 6538P) bacterial cultures were prepared using autoclaved (Autoclave Vario 1528, Dixons Ltd) Luria-Bertani broth (L3022, Sigma-Aldrich Ltd.) media (2% w/v in Milli-Q water). A 5 mL bacterial culture was grown from a single colony for 16 h at 37 °C and 50 µL used to inoculate a sterile polystyrene cuvette (67.742, Sarstedt AG) containing Luria-Bertani broth (1 mL). The cuvette was covered with Parafilm (Cole-Parmer Ltd) and then placed inside a bacterial incubator shaker (Stuart Orbital Incubator S1500, Cole-Parmer Ltd) set at 37 °C and 120 rpm. An optical density OD_{650nm} = 0.4 was verified using a spectrophotometer (BOECO S-30, Boeckel GmbH) to obtain bacteria at the mid-log phase of growth.

Pieces of non-woven polypropylene sheet (0.11 mm thickness, 22.7 ± 1.1 µm fibre diameter, Spunbound, 70 g m^{-2}, Avoca Technical Ltd, UK) were spray coated with either poly(diallyldimethylammonium)–anionic fluorosurfactant complex or poly(diallyldimethylammonium)–3% w/v silica (7 nm)–anionic fluorosurfactant complex solutions, and the carrier solvent allowed to evaporate. Uncoated control samples were washed in absolute ethanol for 15 min and then dried under vacuum in order to

make sure they were sterile and clean. At least 4 different batches of each type of coated sample, as well as the control uncoated non-woven polypropylene sheet, were tested for antimicrobial activity.

Sterile microtubes (1.5 mL, Sarstedt AG) were loaded with the uncoated, polymer–fluorosurfactant or polymer–nanoparticle–fluorosurfactant coated non-woven polypropylene sheet. Next, 100 µL of the prepared bacteria solution was placed onto each sheet (so that the microorganisms could interact with the surface), and left to incubate (Bacterial Incubator 250, LMS Ltd) at 30 °C for 16 h. Next, autoclaved Luria-Bertani broth media (900 µL) was pipetted into each microtube and vortexed (Vortex-Genie 2, Scientific Industries Inc.) in order to recover the bacteria as a 10-fold dilution (10^{-1}). Further ten-fold serial dilutions were performed to give 10^{-2}, 10^{-3}, 10^{-4}, 10^{-5} and 10^{-6} samples. Colony-forming unit (CFU) plate counting was performed by placing 10 µL drops from each sample onto autoclaved Luria-Bertani solid agar plates (EZMix^{TM} powder, dust free, fast dissolving fermentation medium, L7533, Sigma-Aldrich Ltd.) which was incubated (Bacterial Incubator 250, LMS Ltd) at 30 °C for 16 h. The number of colonies visible at each dilution were then counted.

3.3 Results

3.3.1 Sessile Drop Contact Angle

Oleophobic–hydrophilic surfaces were first prepared by spin coating of the poly(styrene-co-maleic anhydride)–amphoteric fluorosurfactant complex dissolved in DMF, Figure 3.1. The obtained results are similar to those reported previously using a cationic fluorosurfactant of similar surface tension to the one used in this work ($\gamma_{\text{amphoteric fluorosurfactant}}$ = 15.5[62] mN m^{-1}; $\gamma_{\text{cationic fluorosurfactant}}$ = 19.8[63] mN m^{-1}).[43] Further enhancement in the hexadecane contact angle, and therefore switching parameter, was achieved through solvent-induced roughening of the coating by changing the casting solution from DMF to a 1:2 v/v DMF / methanol mixture, Figure 3.1. This solvent-induced roughness arises due to the poor solubility of styrene block segments in methanol.[64] In all cases, the water contact angle reached equilibrium after a time period of 10 s, while the hexadecane contact angle did not change with time. Both uncoated silicon wafer and control poly(styrene-co-maleic anhydride) coated silicon wafer surfaces showed the opposite wetting behaviour with the WCA being greater than the HCA.

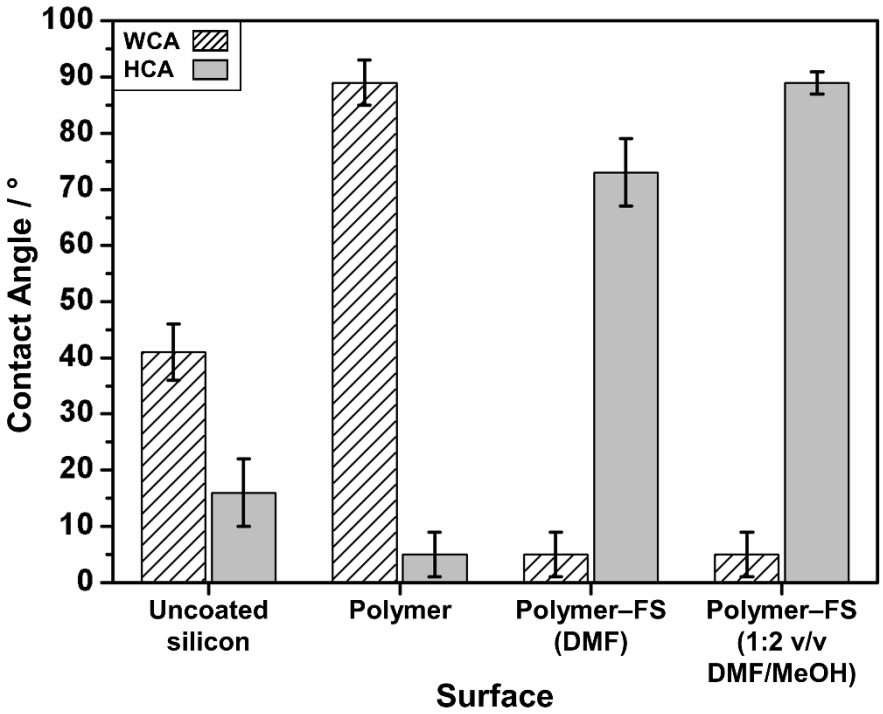

Figure 3.1: Water contact angle (WCA) after 10 s (reached equilibrium) and hexadecane contact angle (HCA) for spin-coated flat silicon wafer substrates. Fluorosurfactant is abbreviated as FS. Error bars denote the sample standard deviation.

The effect of solvent roughening was not as great as previously reported with the hexadecane contact angle only increasing from 73° ± 6° to 89° ± 2° (compared to HCA = 112° ± 5°[43]). This is thought to be due to the change in fluorosurfactant used for complexation. Another way of introducing roughness into the coating is by mixing roughening particles into the polymer–fluorosurfactant complex. At this point the choice of polymer was reconsidered to align with the aim of preparing a coating capable of antibacterial oil–water separation. The cationic polymer poly(diallyldimethylammonium chloride) was chosen as this has previously been reported to have antibacterial properties.[65] The choice of a cationic polymer also now allows for negatively charged silica nanoparticles to be used as the roughening particles, as these will complex to the oppositely charged polymer upon mixing. The same amphoteric fluorosurfactant can be used as this will also form a complex with the positively charged polymer.

Before mixing of any roughening particles, the particle-free poly(diallyldimethylammonium)–amphoteric fluorosurfactant complex was first prepared and oleophobic–hydrophilic surfaces were prepared using various coating methods (spin-coating, dip-coating, solvent casting, and spray coating) from ethanol

solvent, Figure 3.2. Both the water and hexadecane contact angles for the poly(diallyldimethylammonium)–amphoteric fluorosurfactant complex are slightly greater than those for the poly(styrene-co-maleic anhydride)–amphoteric fluorosurfactant complex however the overall switching parameter (difference in water and hexadecane contact angles) is similar. For the poly(diallyldimethylammonium)–amphoteric fluorosurfactant complex, the use of the solvent casting and spray coating techniques resulted in slightly larger hexadecane contact angles compared to the spin and dip coating techniques, Figure 3.2. The solvent casting and spray coating techniques were therefore used when incorporating roughening nanoparticles. An anionic fluorosurfactant of similar surface tension to the amphoteric fluorosurfactant was also tested ($\gamma_{\text{anionic fluorosurfactant}}$ = 19.0[66] mN m^{-1}).

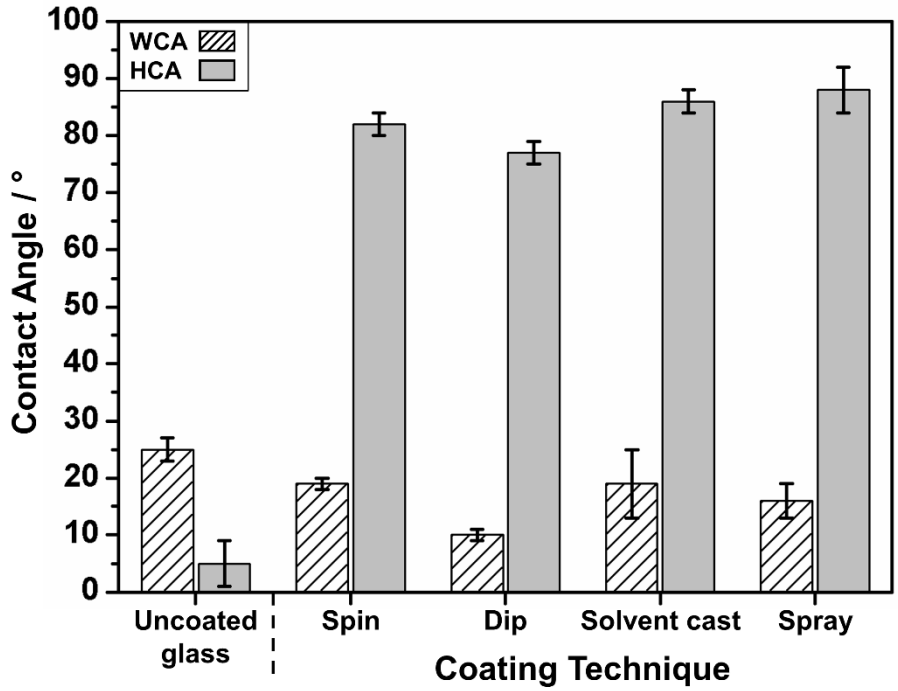

Figure 3.2: Water contact angle (WCA) after 10 s (reached equilibrium) and hexadecane contact angle (HCA; does not change with time) for poly(diallyldimethylammonium)–amphoteric fluorosurfactant coated flat glass substrates. Error bars denote the sample standard deviation.

Oleophobic–hydrophilic surfaces were prepared using either anionic or amphoteric fluorosurfactants in combination with poly(diallyldimethylammonium chloride). Nanoparticle incorporation into these coatings led to an enhancement in the switching parameter (the difference between the equilibrium oil and water static contact angles) by either decreasing the water contact angle (WCA) or by increasing

the hexadecane contact angle (HCA)—optimally a combination of both, Figure 3.3. Eventually, a critical nanoparticle loading value is reached beyond which the switching behaviour starts to deteriorate. Prior to a drop in performance, the poly(diallyldimethylammonium)–anionic fluorosurfactant complex system was found to accommodate higher loadings of 7 nm silica nanoparticles (3% w/v) compared to the poly(diallyldimethylammonium)–amphoteric fluorosurfactant complex system (1.5% w/v), and therefore the former was chosen for further investigation. At these optimum nanoparticle loadings, the surface became completely wetting towards water within 10 s, Table 3.2, Table 3.3, Table 3.4, and Table 3.5. Such hydrophilicity is suitable for anti-fogging applications[43]. Similar trends were observed for both spray coating and solvent casting methods of application.

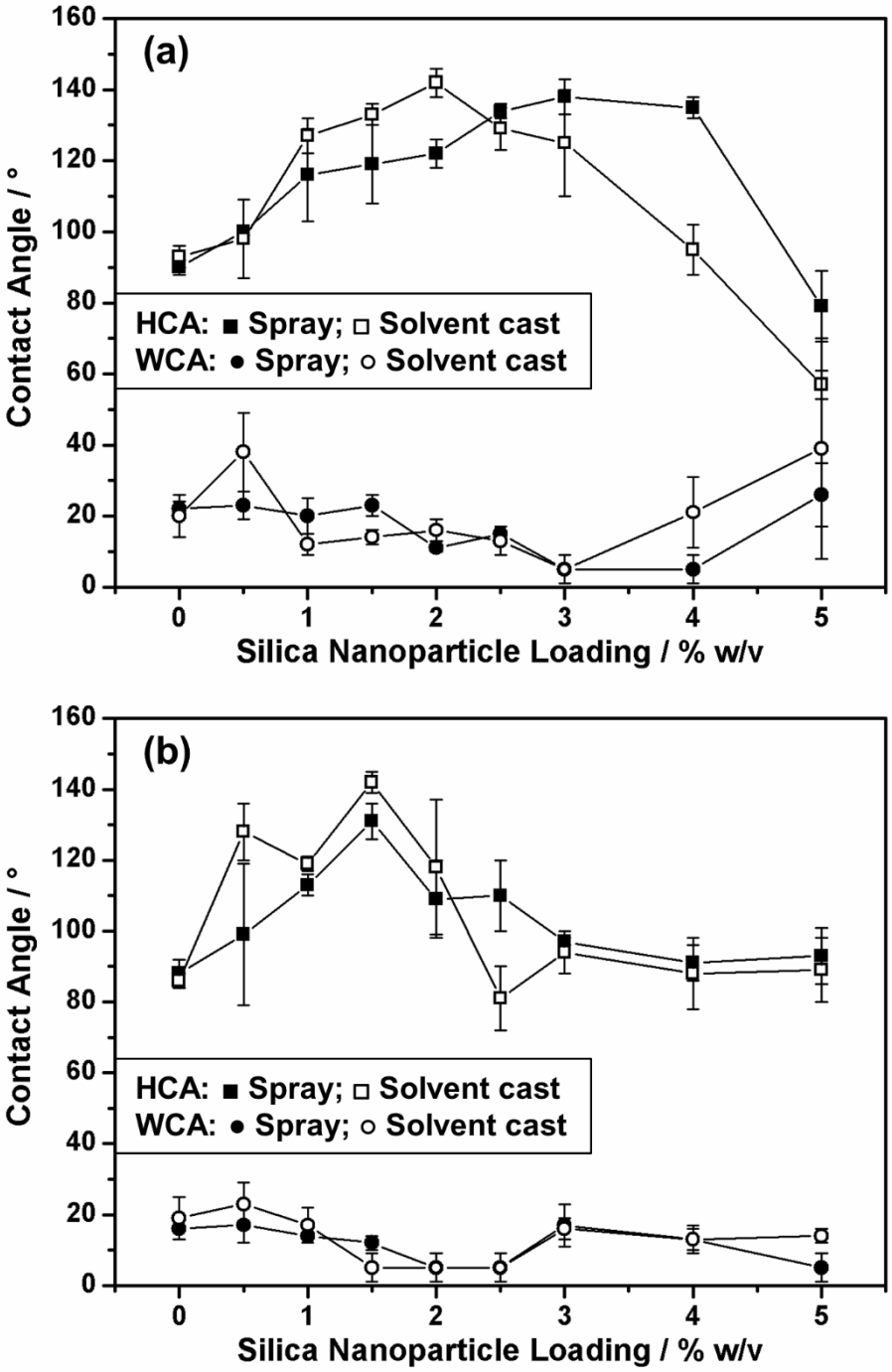

Figure 3.3: Water contact angle (WCA after 10 s) and hexadecane contact angle (HCA) for coated flat glass substrates as a function of 7 nm silica nanoparticle loading concentration in poly(diallyldimethylammonium)–silica precursor solution mixed with: (a) anionic fluorosurfactant; and (b) amphoteric fluorosurfactant. Error bars denote the sample standard deviation.

Table 3.2: Water contact angle after 0 s and 10 s (reached equilibrium) and hexadecane contact angle (does not change with time) for spray coated flat glass substrates as a function of 7 nm silica nanoparticle loading concentration in poly(diallyldimethylammonium)–silica precursor solution mixed with anionic fluorosurfactant. Error bars denote the sample standard deviation.

Method	**Coating**	**Contact Angle / °**			
		Water ***t*** **= 0 s**	**Water** ***t*** **= 10 s**	**Hexadecane**	**Switching**
Spray	poly(diallyldimethylammonium)–anionic fluorosurfactant	48 ± 4	22 ± 2	90 ± 2	68 ± 3
	poly(diallyldimethylammonium)–0.5% w/v silica–anionic fluorosurfactant	59 ± 6	23 ± 4	100 ± 1	77 ± 4
	poly(diallyldimethylammonium)–1% w/v silica–anionic fluorosurfactant	55 ± 10	20 ± 5	116 ± 13	96 ± 14
	poly(diallyldimethylammonium)–1.5% w/v silica–anionic fluorosurfactant	51 ± 2	23 ± 3	119 ± 11	96 ± 11
	poly(diallyldimethylammonium)–2% w/v silica–anionic fluorosurfactant	63 ± 11	11 ± 1	122 ± 4	111 ± 4
	poly(diallyldimethylammonium)–2.5% w/v silica–anionic fluorosurfactant	58 ± 24	15 ± 2	134 ± 2	119 ± 3
	poly(diallyldimethylammonium)–3% w/v silica–anionic fluorosurfactant	54 ± 17	<10	138 ± 5	128 ± 5
	poly(diallyldimethylammonium)–4% w/v silica–anionic fluorosurfactant	66 ± 13	<10	135 ± 3	125 ± 3
	poly(diallyldimethylammonium)–5% w/v silica–anionic fluorosurfactant	70 ± 18	26 ± 9	79 ± 10	53 ± 13

Table 3.3: Water contact angle after 0 s and 10 s (reached equilibrium) and hexadecane contact angle (does not change with time) for solvent cast coated flat glass substrates as a function of 7 nm silica nanoparticle loading concentration in poly(diallyldimethylammonium)–silica precursor solution mixed with anionic fluorosurfactant. Error bars denote the sample standard deviation.

Method	**Coating**	**Contact Angle / °**			
		Water ***t*** **= 0 s**	**Water** ***t*** **= 10 s**	**Hexadecane**	**Switching**
Solvent cast	poly(diallyldimethylammonium)–anionic fluorosurfactant	55 ± 9	20 ± 6	93 ± 3	73 ± 7
	poly(diallyldimethylammonium)–0.5% w/v silica–anionic fluorosurfactant	76 ± 16	38 ± 11	98 ± 11	60 ± 16
	poly(diallyldimethylammonium)–1% w/v silica–anionic fluorosurfactant	53 ± 4	12 ± 3	127 ± 5	115 ± 6
	poly(diallyldimethylammonium)–1.5% w/v silica–anionic fluorosurfactant	44 ± 7	14 ± 2	133 ± 3	119 ± 4
	poly(diallyldimethylammonium)–2% w/v silica–anionic fluorosurfactant	85 ± 13	16 ± 3	142 ± 4	126 ± 5
	poly(diallyldimethylammonium)–2.5% w/v silica–anionic fluorosurfactant	50 ± 16	13 ± 4	129 ± 6	116 ± 7
	poly(diallyldimethylammonium)–3% w/v silica–anionic fluorosurfactant	65 ± 7	<10	125 ± 15	115 ± 15
	poly(diallyldimethylammonium)–4% w/v silica–anionic fluorosurfactant	68 ± 20	21 ± 10	95 ± 7	74 ± 12
	poly(diallyldimethylammonium)–5% w/v silica–anionic fluorosurfactant	87 ± 14	39 ± 31	57 ± 4	18 ± 31

Table 3.4: Water contact angle after 0 s and 10 s (reached equilibrium) and hexadecane contact angle (does not change with time) for spray coated flat glass substrates as a function of 7 nm silica nanoparticle loading concentration in poly(diallyldimethylammonium)–silica precursor solution mixed with amphoteric fluorosurfactant. Error bars denote the sample standard deviation.

Method	**Coating**	**Contact Angle / °**			
		Water *t* = 0 s	**Water *t* = 10 s**	**Hexadecane**	**Switching**
Spray	poly(diallyldimethylammonium)–amphoteric fluorosurfactant	36 ± 3	16 ± 3	88 ± 4	72 ± 5
	poly(diallyldimethylammonium)–0.5% w/v silica–amphoteric fluorosurfactant	32 ± 8	17 ± 5	99 ± 20	82 ± 21
	poly(diallyldimethylammonium)–1% w/v silica–amphoteric fluorosurfactant	38 ± 9	14 ± 2	113 ± 3	99 ± 4
	poly(diallyldimethylammonium)–1.5% w/v silica–amphoteric fluorosurfactant	32 ± 5	12 ± 2	131 ± 5	119 ± 5
	poly(diallyldimethylammonium)–2% w/v silica– amphoteric fluorosurfactant	14 ± 2	<10	109 ± 11	99 ± 11
	poly(diallyldimethylammonium)–2.5% w/v silica–amphoteric fluorosurfactant	19 ± 3	<10	110 ± 10	100 ± 10
	poly(diallyldimethylammonium)–3% w/v silica–amphoteric fluorosurfactant	28 ± 5	17 ± 6	97 ± 1	80 ± 6
	poly(diallyldimethylammonium)–4% w/v silica–amphoteric fluorosurfactant	27 ± 9	13 ± 4	91 ± 5	78 ± 6
	poly(diallyldimethylammonium)–5% w/v silica–amphoteric fluorosurfactant	21 ± 5	<10	93 ± 8	83 ± 8

Table 3.5: Water contact angle after 0 s and 10 s (reached equilibrium) and hexadecane contact angle (does not change with time) for solvent cast coated flat glass substrates as a function of 7 nm silica nanoparticle loading concentration in poly(diallyldimethylammonium)–silica precursor solution mixed with amphoteric fluorosurfactant. Error bars denote the sample standard deviation.

Method	**Coating**	**Contact Angle / °**			
		Water ***t*** **= 0 s**	**Water** ***t*** **= 10 s**	**Hexadecane**	**Switching**
Solvent cast	poly(diallyldimethylammonium)–amphoteric fluorosurfactant	42 ± 4	19 ± 6	86 ± 2	67 ± 6
	poly(diallyldimethylammonium)–0.5% w/v silica–amphoteric fluorosurfactant	44 ± 1	23 ± 6	128 ± 8	105 ± 10
	poly(diallyldimethylammonium)–1% w/v silica–amphoteric fluorosurfactant	37 ± 7	17 ± 5	119 ± 2	102 ± 5
	poly(diallyldimethylammonium)–1.5% w/v silica–amphoteric fluorosurfactant	14 ± 4	<10	142 ± 3	132 ± 3
	poly(diallyldimethylammonium)–2% w/v silica– amphoteric fluorosurfactant	15 ± 3	<10	118 ± 19	108 ± 19
	poly(diallyldimethylammonium)–2.5% w/v silica–amphoteric fluorosurfactant	<10	<10	81 ± 9	71 ± 9
	poly(diallyldimethylammonium)–3% w/v silica–amphoteric fluorosurfactant	25 ± 4	16 ± 3	94 ± 6	78 ± 7
	poly(diallyldimethylammonium)–4% w/v silica–amphoteric fluorosurfactant	19 ± 6	13 ± 3	88 ± 10	75 ± 10
	poly(diallyldimethylammonium)–5% w/v silica–amphoteric fluorosurfactant	24 ± 4	14 ± 2	89 ± 9	75 ± 9

A range of other unfunctionalised and functionalised negatively charged nano- and micron-size particles were also found to enhance the switching parameter, Figure 3.4. On the other hand, positively charged alumina and zinc oxide nanoparticles performed less well. In the case of alumina nanoparticles, their inclusion at a loading of 3% w/v gave rise to a detrimental effect on the switching parameter stemming from a large rise in the water contact angle. Alkyl functionalised silica nanoparticles showed greater oleophobicity at low loadings (1% w/v) compared to unfunctionalised silica nanoparticles. At higher loadings (3% w/v), the alkyl functionalisation of nanoparticles appeared not to provide any significant advantage, Figure 3.4. Given that the poly(diallyldimethylammonium)–anionic fluorosurfactant complex system with 3% w/v loading of 7 nm silica nanoparticles displayed the largest switching parameter, this was selected for further investigation.

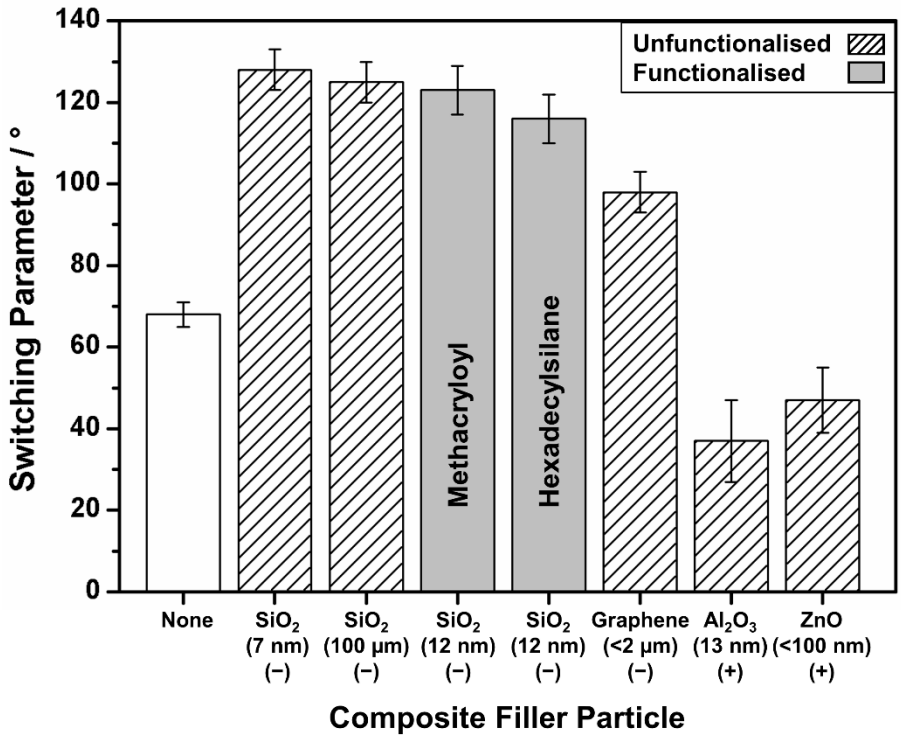

Figure 3.4: Oleophobic–hydrophilic switching parameters for flat glass substrates spray coated with various poly(diallyldimethylammonium)–particle–anionic fluorosurfactant complex coatings at 3% w/v particle loading in poly(diallyldimethylammonium)–particle precursor solution. Switching parameters are calculated from the difference between the hexadecane and water static contact angles (after 10 s). Nanoparticle surface charge is indicated within brackets as (−) or (+). Error bars denote the sample standard deviation.

Introducing hierarchical roughness (surface roughness on multiple length scales) into an oleophobic coating is an effective way of further increasing the oil repellency.[67] Poly(diallyldimethylammonium)–particle–anionic fluorosurfactant complexes containing a mixture of differently sized particles (total particle loading kept constant at optimum loading of 3% w/v) have been prepared in an attempt to increase the hexadecane contact angle further by introducing hierarchical roughness, Figure 3.5. A combination of nano- and micron-sized silica (1:1 w/w; 3% w/v total loading) resulted in both an increase in water contact angle and a decrease in hexadecane contact angle considerably reducing the switching parameter. A similar result was obtained when using a combination of nano-sized silica and micron-sized graphene (1:1 w/w; 3% w/v total loading) although the effect was not as large and therefore the switching parameter still remained greater than that of the particle-free poly(diallyldimethylammonium)–anionic fluorosurfactant complex coating.

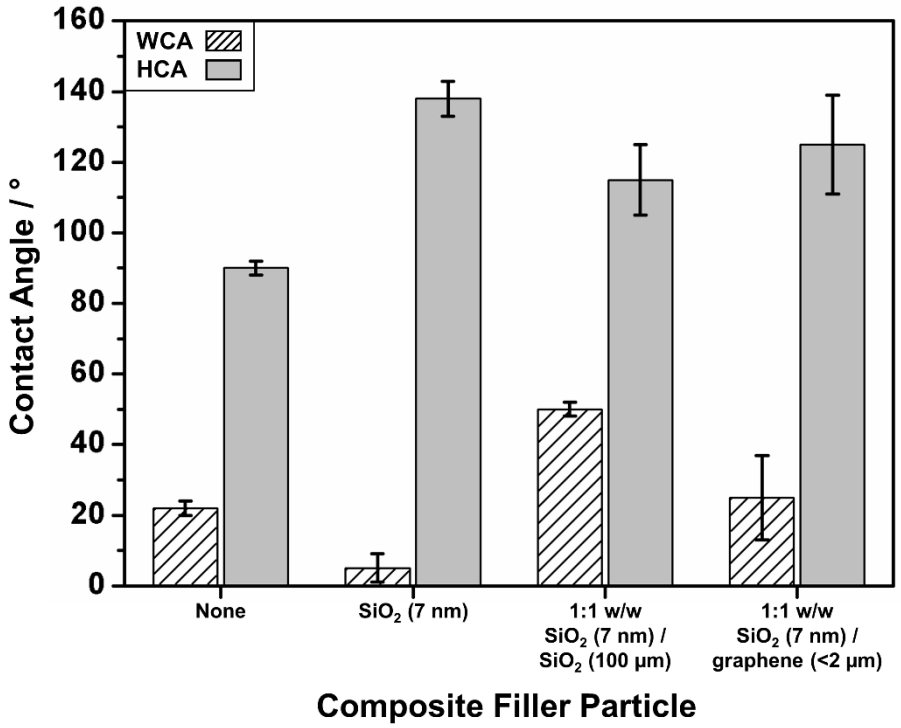

Figure 3.5: Water contact angle (WCA) after 10 s (reached equilibrium) and hexadecane contact angle (HCA; does not change with time) for flat glass substrates spray coated with poly(diallyldimethylammonium)–anionic fluorosurfactant and various poly(diallyldimethylammonium)–particle–anionic fluorosurfactant complex coatings at 3% w/v total particle loading in poly(diallyldimethylammonium)–particle precursor solution. Error bars denote the sample standard deviation.

One drawback of the oleophobic–hydrophilic polymer–particle–fluorosurfactant coatings reported in this work is the use of a fluorine-containing surfactant to provide the low surface energy tail groups required for oil repellency. This is because fluorinated materials are harmful to the environment with recent studies highlighting the persistence and bioaccumulation of fluorocarbons.[68,69,70,71,72,73,74] Therefore, preparation of oleophobic–hydrophilic surfaces using non-fluorinated materials is more desirable. However, it is difficult to prepare surfaces with sufficiently low surface energy to render the surface oleophobic without using fluorine. Two previous studies reporting fluorine-free coatings with HCA (in air) greater than WCA are in fact not actually oleophobic as evidenced by their low motor oil contact angles of 57°[75] and 64.7°[76]. Other reports of fluorine-free oleophobic–hydrophilic surfaces are actually only oleophobic when underwater and are therefore easily contaminated by oils and these oils will even pass through the filter when it dries up.[77,78,79]

Superhydrophobic, fluorine-free surfaces have been reported using highly branched hydrocarbon chains.[80] Although oil repellency has not been reported for such fluorine-free coatings, it was envisaged that a hyperbranched hydrocarbon chain (such as isostearic acid[81]) could be used as a replacement for the fluorosurfactant in the oleophobic–hydrophilic polymer–particle–fluorosurfactant coatings reported in this work. Fluorine-free polymer–surfactant complex coatings were prepared using isostearic acid in combination with poly(diallyldimethylammonium chloride) and although these coatings showed a positive switching parameter (HCA is greater than WCA), the oil repellency is poor resulting in a relatively low switching parameter, Figure 3.6. Incorporation of silica nanoparticles into these coatings led to a small enhancement in the switching parameter up to silica nanoparticle loadings of 1.5% w/v. However, the highest hexadecane contact angle measured was 40 ± 5° for dip coated poly(diallyldimethylammonium)–1.5% w/v silica–isostearic acid which is too low for these surfaces to be considered oleophobic.

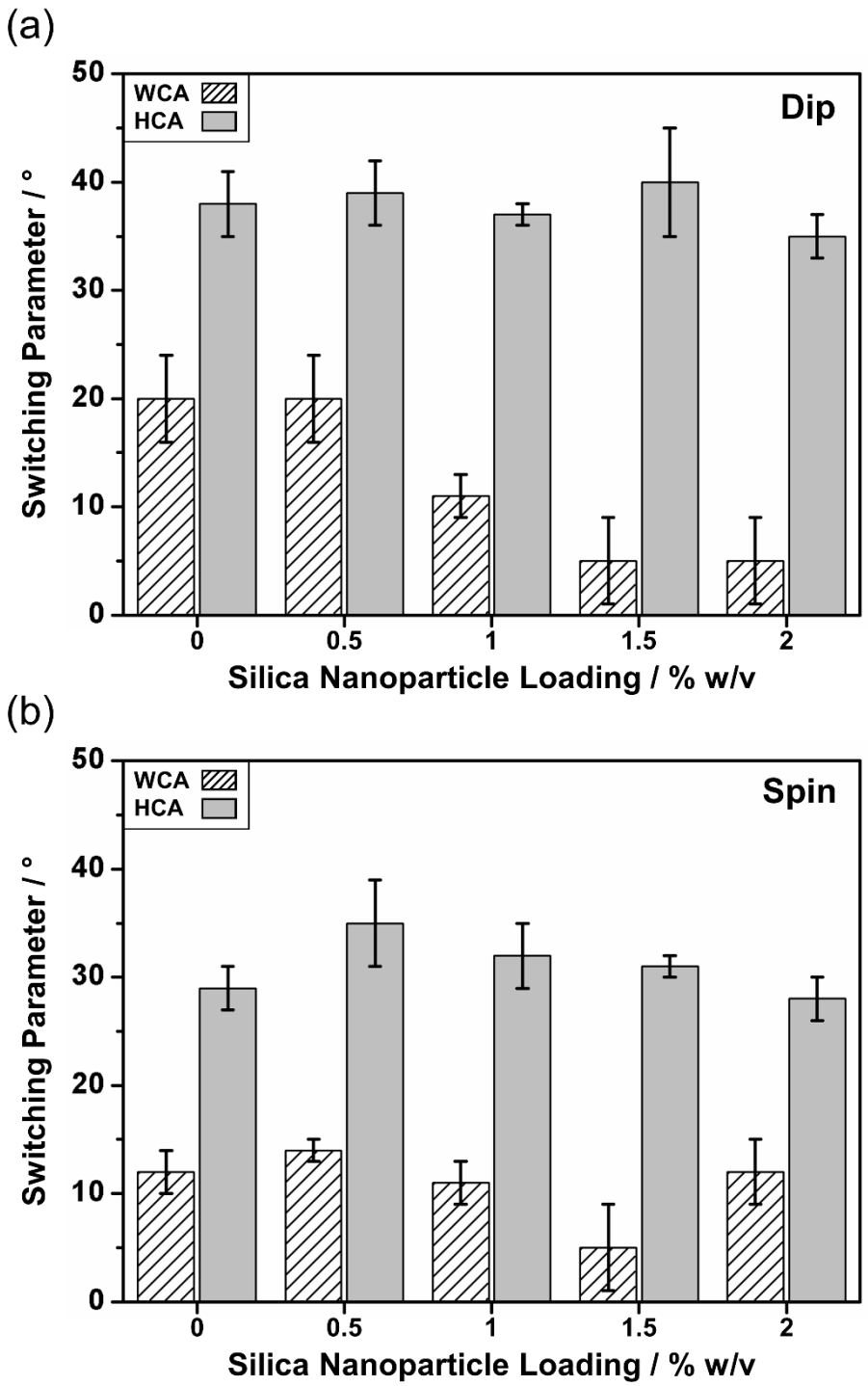

Figure 3.6: Water contact angle (WCA) after 10 s (reached equilibrium) and hexadecane contact angle (HCA; does not change with time) for flat glass substrates (a) dip coated and (b) spin coated with poly(diallyldimethylammonium)–particle–isostearic acid complex coatings as a function of 7 nm silica nanoparticle loading in poly(diallyldimethylammonium)–particle precursor solution. Error bars denote the sample standard deviation.

In order to be able to separate oil–water mixtures, this oleophobic–hydrophilic coating needs to be applied to a porous substrate to allow passage of the water

through the pores. Sessile drop contact angle analysis of poly(diallyldimethylammonium)–anionic fluorosurfactant and poly(diallyldimethylammonium)–3% w/v silica–anionic fluorosurfactant spray coated mesh substrates confirmed that the same wettability (oleophobicity and hydrophilicity) is observed when applied to mesh substrate as compared to the flat glass substrates, Table 3.6 and Figure 3.7. The poly(diallyldimethylammonium)–anionic fluorosurfactant coated mesh shows a larger water contact angle than expected however this is thought to be due to the small droplet size used. In Section 3.3.5 (page 94), it is shown that water does pass through this poly(diallyldimethylammonium)–anionic fluorosurfactant coated mesh when the volume of water is greater than the 1 µL droplet used here. The poly(diallyldimethylammonium)–anionic fluorosurfactant coated mesh also displays a larger hexadecane contact angle than for the same coating on flat glass substrate—this is due to the roughness of the mesh. A similar, although smaller, effect is observed in the HCA for poly(diallyldimethylammonium)–3% w/v silica–anionic fluorosurfactant coated mesh compared to flat glass substrate.

Table 3.6: Water contact angle (WCA after 10 s) and hexadecane contact angle (HCA; does not change with time) for poly(diallyldimethylammonium)–anionic fluorosurfactant and poly(diallyldimethylammonium)–3% w/v silica–anionic fluorosurfactant spray coated glass and stainless steel mesh substrates. Error bars denote the sample standard deviation.

Substrate	**Coating**	**Contact Angle / °**		
		Water *t* = 10 s	**Hexadecane**	**Switching**
Glass	Uncoated	25 ± 2	<10	−15 ± 2
	Poly(diallyldimethylammonium)–anionic fluorosurfactant	22 ± 2	90 ± 2	68 ± 3
	Poly(diallyldimethylammonium)–3% w/v silica–anionic fluorosurfactant	<10	138 ± 5	128 ± 5
Mesh	Uncoated	106 ± 3	35 ± 3	−71 ± 4
	Poly(diallyldimethylammonium)–anionic fluorosurfactant	70 ± 5	111 ± 2	41 ± 5
	Poly(diallyldimethylammonium)–3% w/v silica–anionic fluorosurfactant	<10	143 ± 4	133 ± 4

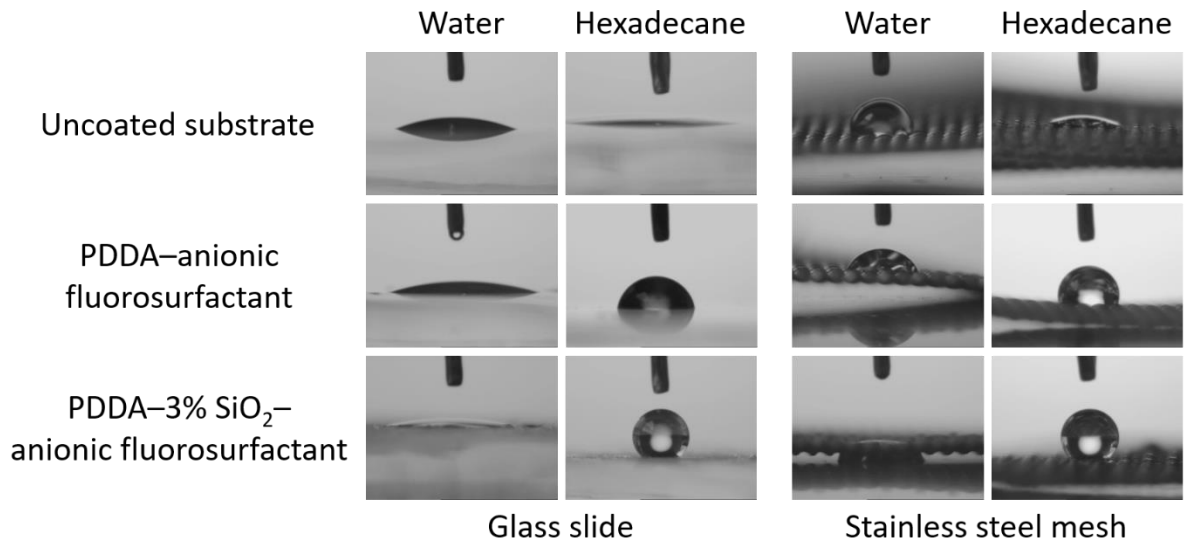

Figure 3.7: Microlitre water and hexadecane droplets dispensed onto poly(diallyldimethylammonium)–anionic fluorosurfactant and poly(diallyldimethylammonium)–3% w/v silica–anionic fluorosurfactant spray coated glass and stainless steel mesh substrates. Poly(diallyldimethylammonium) is abbreviated as PDDA.

Further to the coating of stainless steel mesh for oil–water separation applications, pieces of non-woven polypropylene cloth were required to be coated for antibacterial testing and so the wettability of the coating on this substrate was also tested. Sessile drop contact analysis was carried out on both the dimpled and non-dimpled areas of the coated non-woven polypropylene cloth used.[82] Both regions of the poly(diallyldimethylammonium)–anionic fluorosurfactant and poly(diallyldimethylammonium)–3% w/v silica–anionic fluorosurfactant coated cloths displayed the oleophobic–hydrophilic behaviour expected, Table 3.7 and Figure 3.8. The oil repellency of the particle-free coating on cloth is much greater than when coated onto glass and stainless steel mesh substrates—this is due to the roughness of the non-woven polypropylene substrate. Therefore, when coated onto cloth, the added roughness due to the incorporation of silica nanoparticles only has a small effect on the oil repellency with HCA increasing by only a small amount. The water and hexadecane contact angles of the particle-containing coating on cloth are very similar to those when coated onto glass or stainless steel mesh, Table 3.6 and Table 3.7. The dimpled regions of the non-woven polypropylene cloth display lower contact angles compared to the non-dimpled regions—this is due to the dimples interfering with the Cassie-Baxter enhancement of oleophobicity.[82]

Table 3.7: Water contact angle (WCA) after 0 s and 10 s (reached equilibrium) and hexadecane contact angle (HCA; does not change with time) for poly(diallyldimethylammonium)–anionic fluorosurfactant and poly(diallyldimethylammonium)–3% w/v silica–anionic fluorosurfactant spray coated non-woven polypropylene cloth substrate. Error bars denote the sample standard deviation.

Substrate	**Coating**	**Contact Angle / °**			
		Water *t* = 0 s	**Water *t* = 10 s**	**Hexadecane**	**Switching**
Cloth (non-dimpled region)	Uncoated	139 ± 6	139 ± 6	<10	−129 ± 6
	Poly(diallyldimethylammonium)–anionic fluorosurfactant	47 ± 4	<10	138 ± 5	128 ± 5
	Poly(diallyldimethylammonium)–3% w/v silica–anionic fluorosurfactant	34 ± 9	<10	142 ± 6	132 ± 6
Cloth (dimpled region)	Uncoated	109 ± 3	109 ± 3	<10	−99 ± 3
	Poly(diallyldimethylammonium)–anionic fluorosurfactant	40 ± 6	<10	96 ± 10	86 ± 10
	Poly(diallyldimethylammonium)–3% w/v silica–anionic fluorosurfactant	18 ± 4	<10	109 ± 3	99 ± 3

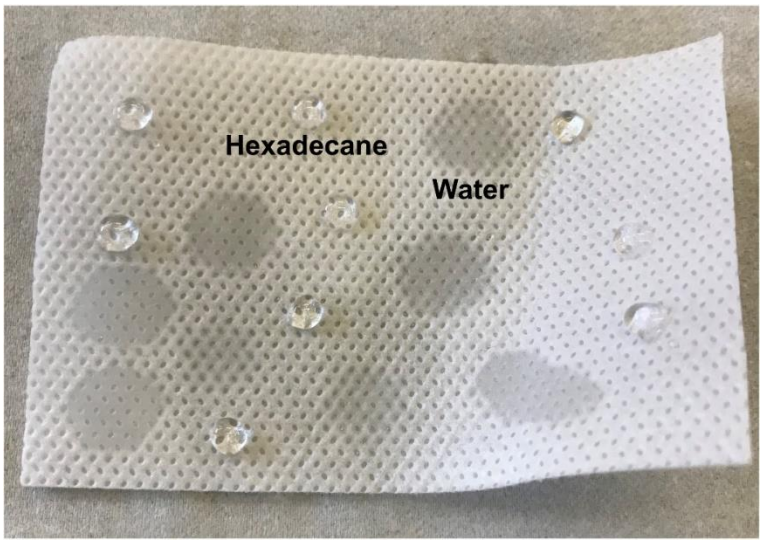

Figure 3.8: Water and hexadecane droplets on poly(diallyldimethylammonium)–3% w/v silica–anionic fluorosurfactant spray coated non-woven polypropylene cloth substrate.

Oleophobic–hydrophilic surfaces have also successfully been prepared using a two-step process consisting of plasma polymer deposition followed by fluorosurfactant complexation, Appendix 1. When complexed with an amphoteric fluorosurfactant, both pulsed plasma maleic anhydride and pulsed plasma 2-(trifluoromethyl)maleic anhydride coated glass substrates showed oleophobic–hydrophilic properties with switching parameters of around 70°. Both pulsed plasma polymer coatings displayed the opposite wetting behaviour prior to fluorosurfactant complexation.

3.3.2 Captive Bubble Contact Angle

For the superhydrophilic poly(diallyldimethylammonium)–3% w/v silica (7 nm)–anionic fluorosurfactant and poly(diallyldimethylammonium)–1.5% w/v silica (7 nm)–amphoteric fluorosurfactant complex coated substrates, it was found that the air bubble did not release from the needle upon contact with the sample surfaces (superhydrophilicity[83]). Increasing the size of the air bubble until it eventually released from the needle led to the bubble simply rising towards the sample followed by running along the coating surface and off the edge, Figure 3.9. Hence, the captive bubble contact angle value of 180° correlates to the calculated WCA of 0° (at 10 s) from the sessile drop technique.[84] This surface hydrophilicity (low water contact angle) can be attributed to a water layer being present on the surface—the water layer effectively repels the air bubble preventing it from adhering to the coating surface.[85]

The difference observed between the sessile drop and the captive bubble methods for measurements made at t = 0 s is because the timescale to "switch" is about 10 s for the former, whereas the prior immersion of sample into water for the latter has already caused the surface rearrangement ("switch")—thereby effectively making the captive bubble WCA unchanged between t = 0 s and t = 10 s.

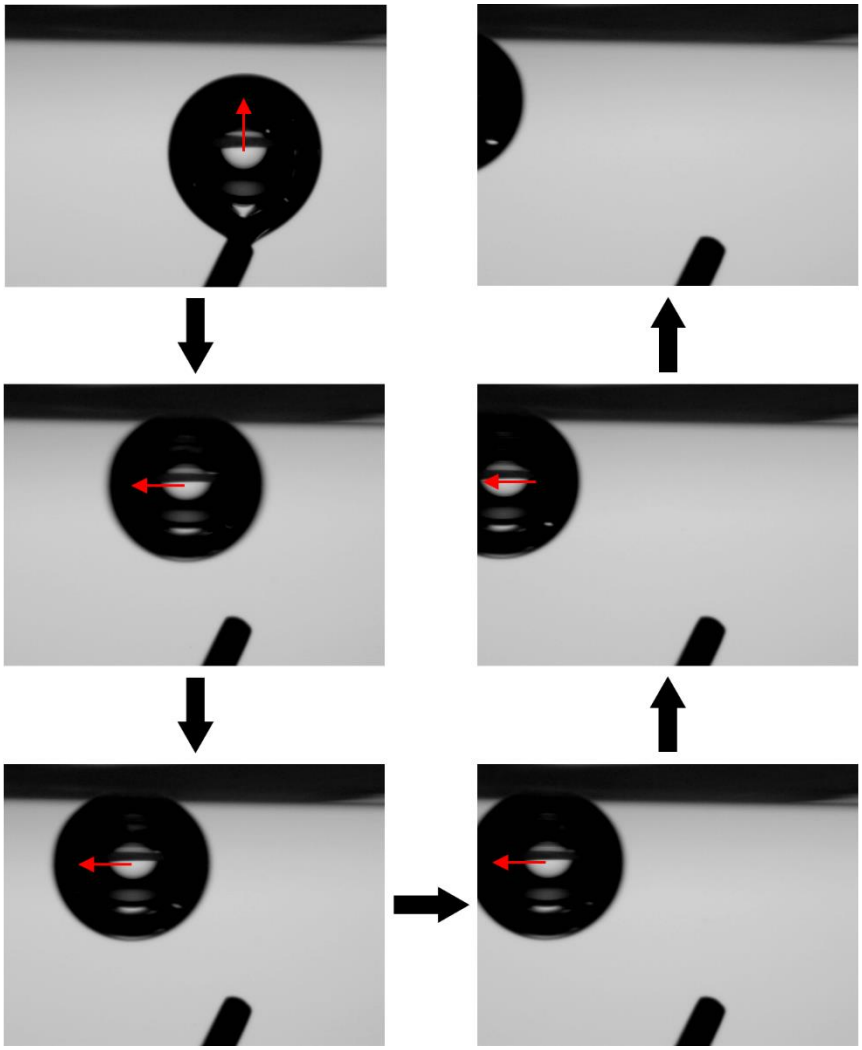

Figure 3.9: Captive bubble contact angle measurement on a poly(diallyldimethylammonium)–3% w/v silica (7 nm)–anionic fluorosurfactant spray coated flat glass substrate. Air bubble did not adhere to coating surface and was observed to run along the surface and off the edge of the sample. Red arrows show direction of movement of air bubble.

3.3.3 Scanning Electron Microscopy

Scanning electron microscopy (SEM) showed that in the absence of silica nanoparticles, the coatings are relatively smooth with any minor roughness features attributable to the spray coating process, Figure 3.10 and Figure 3.11. The incorporation of nanoparticles enhances the coating surface roughness for both the poly(diallyldimethylammonium)–anionic fluorosurfactant and poly(diallyldimethylammonium)–amphoteric fluorosurfactant systems. The scale of the surface roughness features is approximately 100–200 nm in size which is consistent with there being encapsulation of the nanoparticles within the polymer–fluorosurfactant complex host matrix (rather than due to discrete individual 7 nm silica nanoparticles).

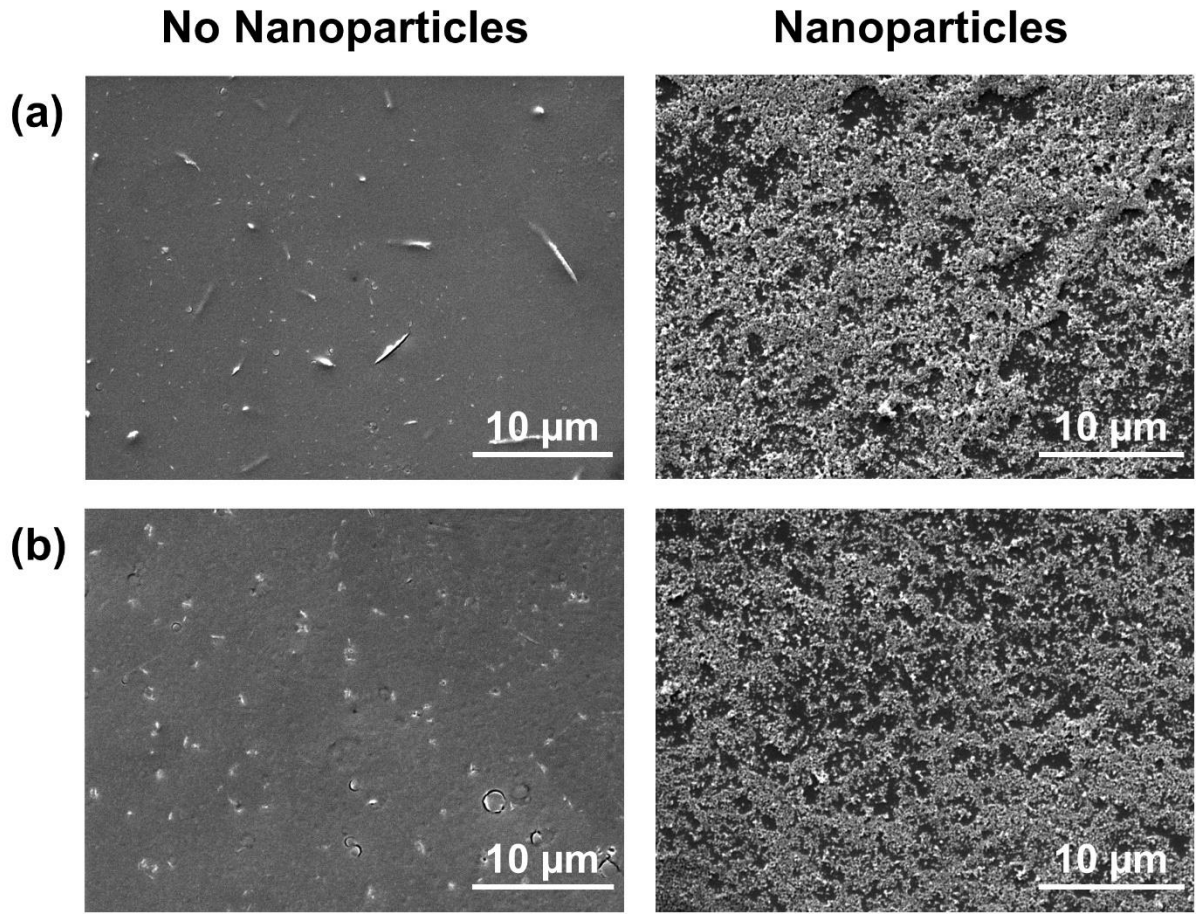

Figure 3.10: SEM micrographs of spray coatings with and without nanoparticles on flat silicon wafer substrates: (a) poly(diallyldimethylammonium)–anionic fluorosurfactant; and (b) poly(diallyldimethylammonium)–amphoteric fluorosurfactant. The silica (7 nm) nanoparticle loadings correspond to the best switching parameters (3% w/v and 1.5% w/v for (a) and (b) respectively).

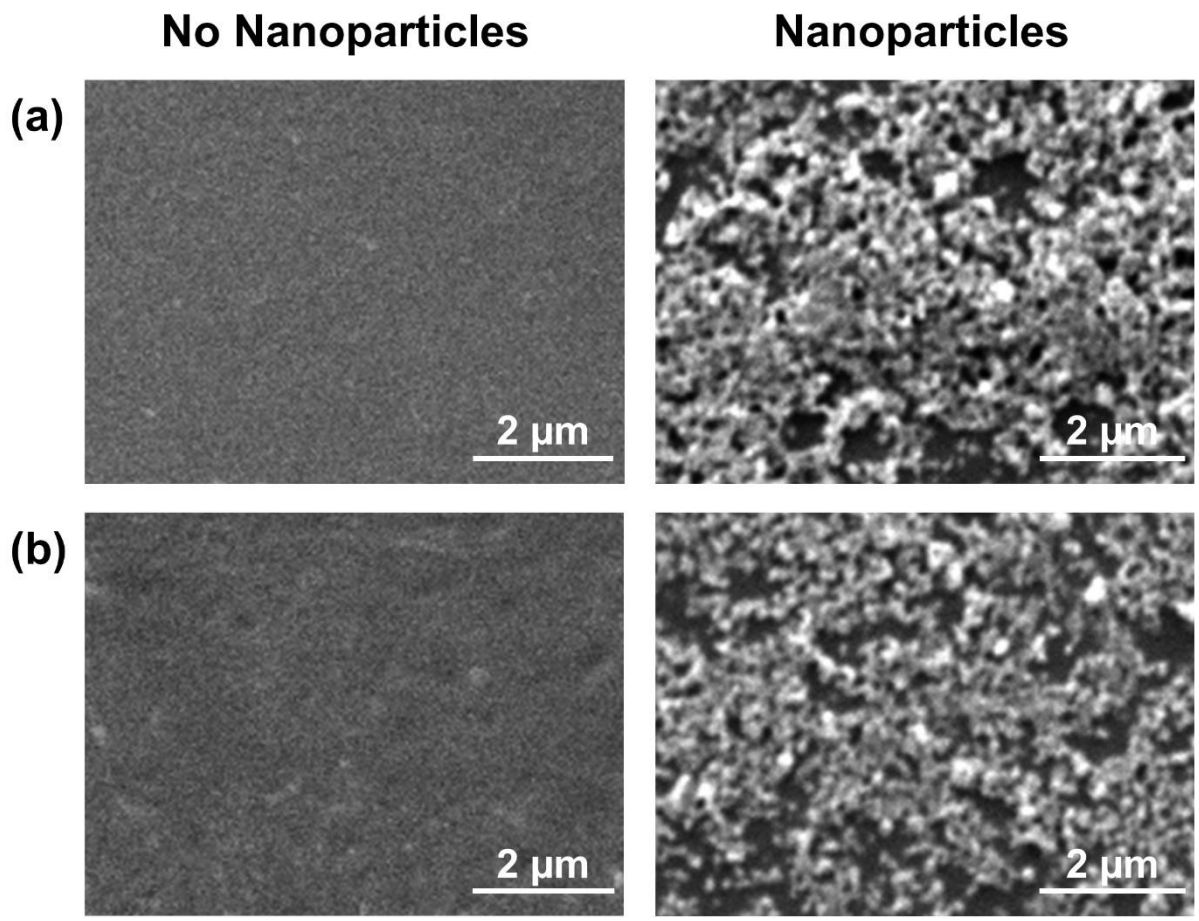

Figure 3.11: Higher resolution SEM micrographs of spray coatings with and without nanoparticles on flat silicon wafer substrates: (a) poly(diallyldimethylammonium)–anionic fluorosurfactant; and (b) poly(diallyldimethylammonium)–amphoteric fluorosurfactant. The silica (7 nm) nanoparticle loadings correspond to the best switching parameters (3% w/v and 1.5% w/v for (a) and (b) respectively).

3.3.4 Microindentation

Microindentation measurements showed that for a given indentation force, the hardness improved with rising silica nanoparticle loading, Figure 3.12. In the absence of or at low loadings of silica nanoparticles (1% w/v silica), a large indentation force of 490 mN was sufficient to pierce through the coatings causing the underlying silicon substrate to crack (i.e. a hardness value could not be measured at this high force). At low indentation forces (20 mN), the coatings with 2% w/v and 3% w/v nanoparticle loadings displayed no visible indent (i.e. scratch-resistant). Therefore, a force of 98 mN or 245 mN was employed in order to follow the effect of varying silica loading—both forces showed that the hardness increases with rising silica loading, Figure 3.12.

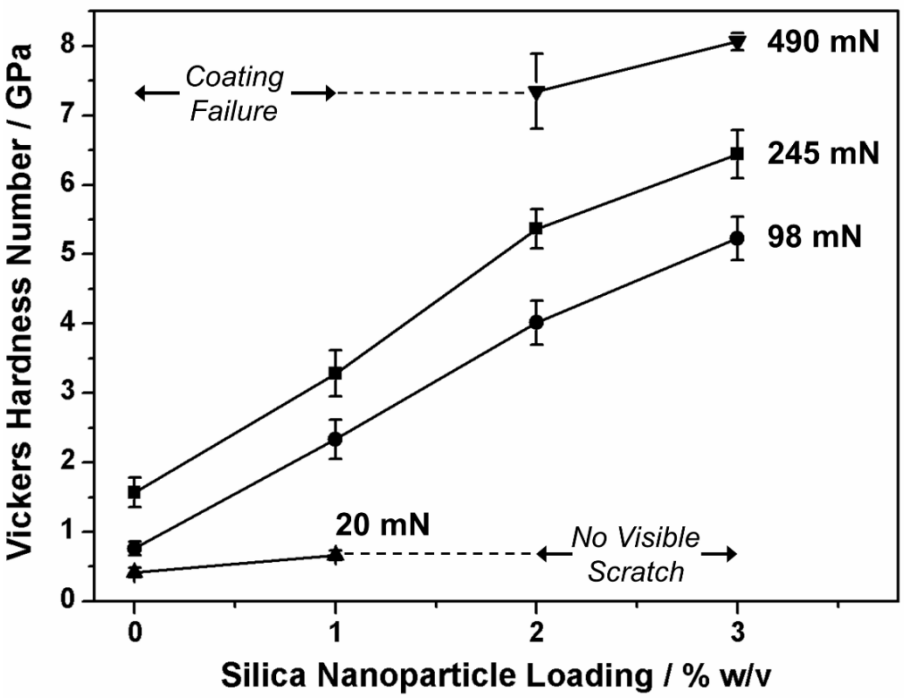

Figure 3.12: Vickers hardness number measured for various applied microindentation forces as a function of 7 nm silica nanoparticle loading concentration for poly(diallyldimethylammonium)–silica–anionic fluorosurfactant spray coated onto silicon wafer substrates. Error bars denote the sample standard deviation.

3.3.5 Oil–Water Separation

Poly(diallyldimethylammonium)–anionic fluorosurfactant complex and poly(diallyldimethylammonium)–3% w/v silica (7 nm)–anionic fluorosurfactant coated horizontal meshes displayed oil–water separation behaviour, Figure 3.13. High-purity water passed through both uncoated and coated meshes, whilst oil (hexadecane) did not pass through the coated mesh—thereby demonstrating that the coated mesh can separate oil from water. Separation of a larger volume of oil–water mixture using a poly(diallyldimethylammonium)–3% w/v silica (7 nm)–anionic fluorosurfactant spray coated mesh is shown in Figure 3.14.

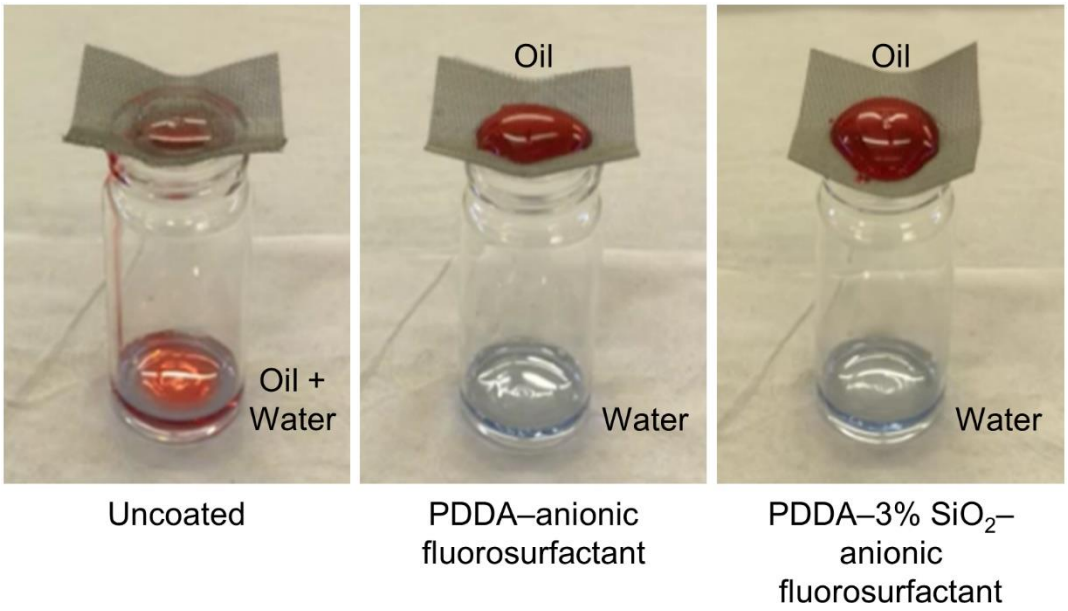

Figure 3.13: Oil (hexadecane)–water separation performance of uncoated mesh (#50 mesh), poly(diallyldimethylammonium)–anionic fluorosurfactant complex spray coated mesh (#50 mesh), and poly(diallyldimethylammonium)–3% w/v silica (7 nm)–anionic fluorosurfactant spray coated mesh (#50 mesh). Oil is dyed red and water is dyed blue. Poly(diallyldimethylammonium) is abbreviated as PDDA.

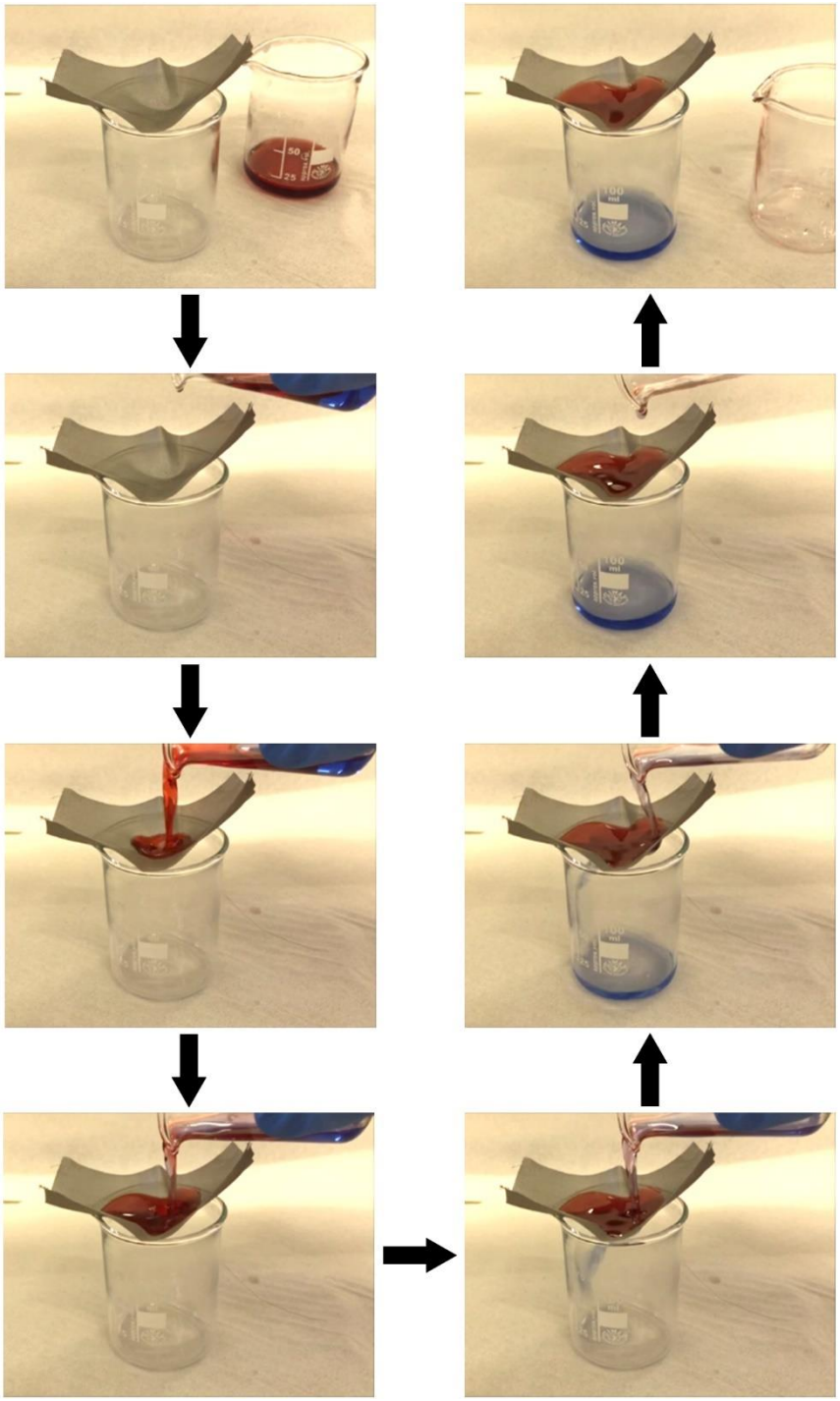

Figure 3.14: Separation of an oil (hexadecane)–water mixture using a poly(diallyldimethylammonium)–3% w/v silica (7 nm)–anionic fluorosurfactant spray coated mesh (#50 mesh). Oil is dyed red and water is dyed blue.

Poly(diallyldimethylammonium)–3% w/v silica (7 nm)–anionic fluorosurfactant spray coated horizontal meshes of different aperture sizes were then tested for oil (tetradecane)–water separation properties, Figure 3.15. A mesh aperture size of 310 µm (#50 mesh) was sufficiently small enough to separate oil from water with 98.87 ± 2.26% efficiency. Meshes with a slightly larger aperture size (410 µm, #40 mesh) showed a small drop in separation efficiency whilst even larger apertures (650 µm, #30 mesh) were not successful in separating the oil–water mixture (% separation = 29.18 ± 6.27%). Decreasing the aperture to 150 µm (#100 mesh) resulted in a similar separation efficiency within the error compared to the #50 mesh. The #50 mesh however has a higher mechanical strength compared to the #100 mesh and therefore the #50 mesh was chosen for further separations due to its ability to be held at an incline for oil–water separations without buckling under the weight of the oil–water mixture.

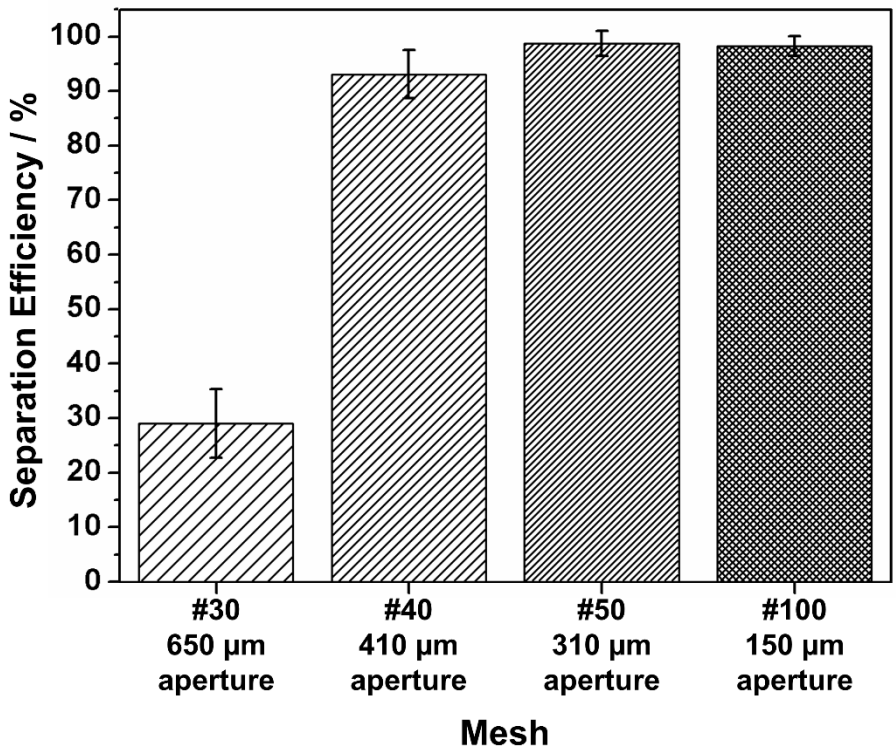

Figure 3.15: Oil (tetradecane)–water separation efficiencies of poly(diallyldimethylammonium)–3% w/v silica (7 nm)–anionic fluorosurfactant spray coated meshes of various aperture sizes. Error bars denote the sample standard deviation.

By inclining the poly(diallyldimethylammonium–3% w/v silica (7 nm)–anionic fluorosurfactant coated #50 meshes above two beakers, oil–water mixtures could be separated into the respective beakers, Figure 3.16. The small amount of water (less than 5 % vol.) which passes into the oil beaker is due to some of the water being dragged along by the oil across the mesh as it passes across it, and could be easily removed by repeating the procedure.

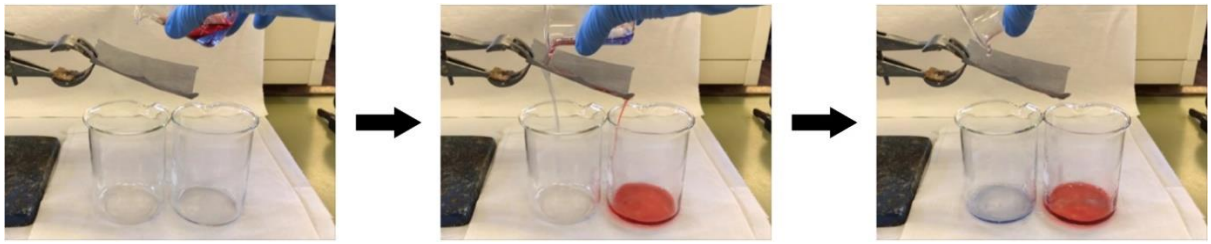

Figure 3.16: Separation of an oil (hexadecane)–water mixture using a poly(diallyldimethylammonium)–3% w/v silica (7 nm)–anionic fluorosurfactant spray coated mesh (#50 mesh). Oil is dyed red and water is dyed blue.

Poly(diallyldimethylammonium)–3% w/v silica (7 nm)–anionic fluorosurfactant spray coated horizontal meshes (#50 mesh) were then tested for oil–water separation properties using various different oils, Figure 3.17. Both long (tetradecane) and short (octane) chain alkanes can be separated from water with 99.81 ± 0.33% and 98.23 ± 3.53% separation efficiency respectively. Similar performance was measured for vegetable cooking oil, Figure 3.17, Figure 3.18. It is also possible to separate olive oil from water, Figure 3.19.

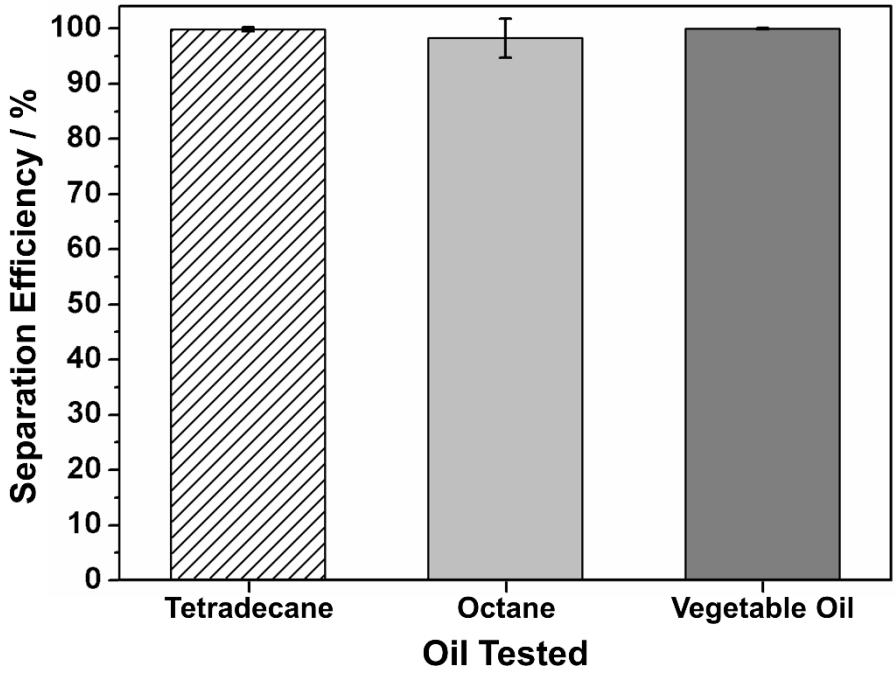

Figure 3.17: Oil–water separation efficiencies of poly(diallyldimethylammonium)–3% w/v silica (7 nm)–anionic fluorosurfactant spray coated meshes (#50 mesh) tested with tetradecane, octane, and vegetable oil. Error bars denote the sample standard deviation.

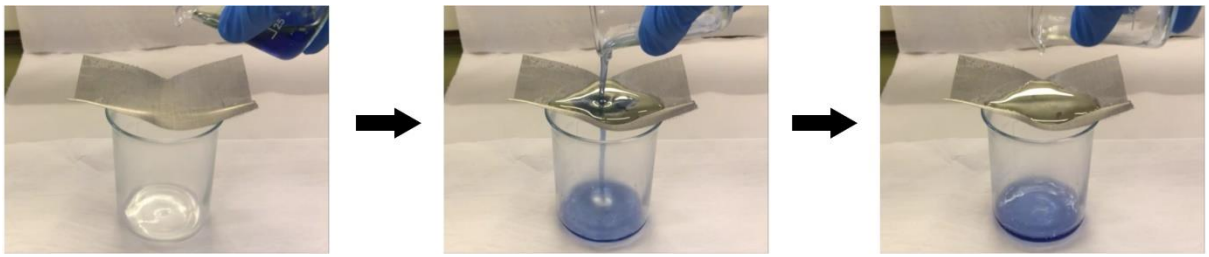

Figure 3.18: Separation of an oil (vegetable cooking oil)–water mixture using a poly(diallyldimethylammonium)–3% w/v silica (7 nm)–anionic fluorosurfactant spray coated mesh (#50 mesh). Water is dyed blue.

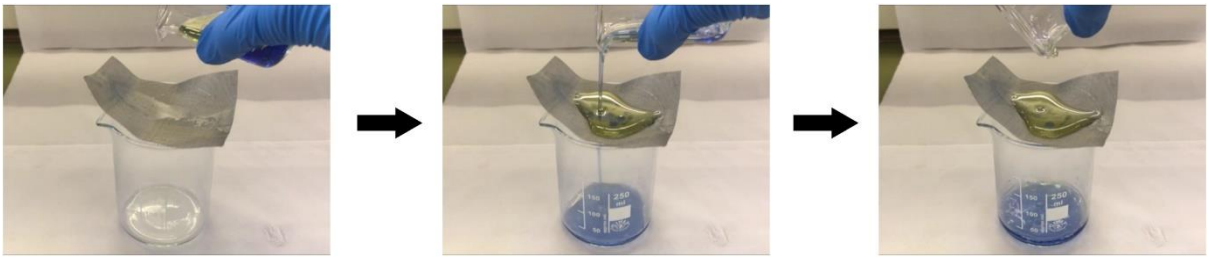

Figure 3.19: Separation of an oil (olive oil)–water mixture using a poly(diallyldimethylammonium)–3% w/v silica (7 nm)–anionic fluorosurfactant spray coated mesh (#50 mesh). Water is dyed blue.

The recyclability of the coated mesh was tested by using the same poly(diallyldimethylammonium)–3% w/v silica (7 nm)–anionic fluorosurfactant spray coated horizontal mesh (#50 mesh) for four successive oil (tetradecane)–water separations. No drop in separation efficiency was observed, Figure 3.20.

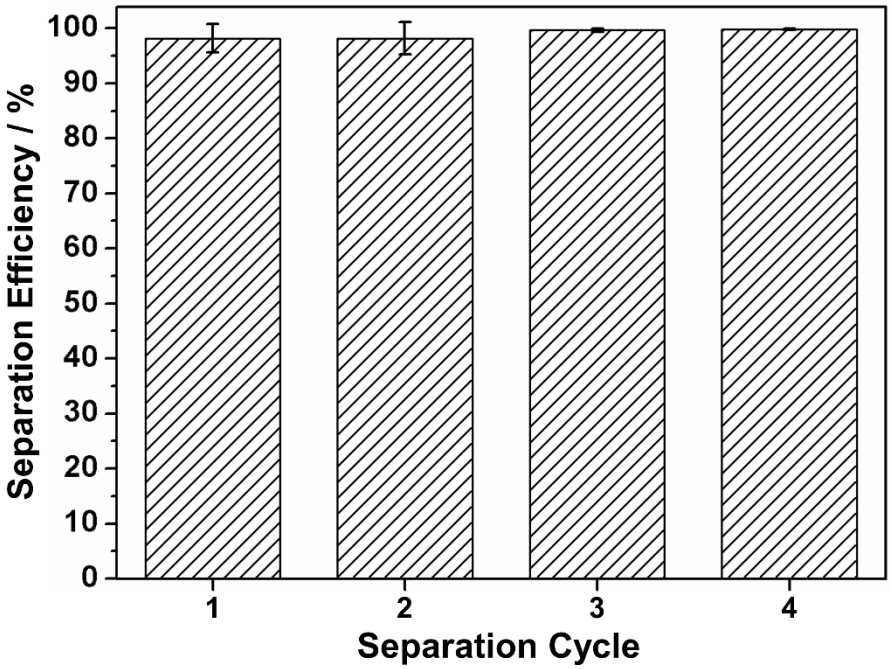

Figure 3.20: Oil (tetradecane)–water separation efficiency of the same poly(diallyldimethylammonium)–3% w/v silica (7 nm)–anionic fluorosurfactant spray coated mesh used for four successive separations. Error bars denote the sample standard deviation.

3.3.6 Antibacterial Activity

These polymer–fluorosurfactant complexes were tested for their antibacterial properties against *E. coli* bacteria (often found in drinking water supplies[86]) and *S. aureus* bacteria (present in seawater[87]) which are both harmful to human health. The control untreated non-woven polypropylene sheet displayed *E. coli* and *S. aureus* bacterial counts of 2.88 ± 0.39 x 10^9 CFU mL^{-1} at 10^{-6} dilution (n = 6, standard deviation error) and 2.70 ± 0.73 x 10^9 CFU mL^{-1} at 10^{-6} dilution (n = 4, standard deviation error) respectively, Figure 3.21. Both poly(diallyldimethylammonium)–anionic fluorosurfactant and poly(diallyldimethylammonium)–3% w/v silica (7 nm)–anionic fluorosurfactant complex coated non-woven polypropylene sheets showed high antibacterial activity against the *E. coli* and *S. aureus* bacteria tested. The former reduced the number of both *E. coli* and *S. aureus* bacteria to zero at 10^{-1} dilution,

whilst the latter exceeded +99.99% killing (2.83 ± 4.34 x 10^4 CFU mL^{-1}) of *E. coli* bacteria at 10^{-2} dilution (*n* = 6, standard deviation error) and +99.97% killing (6.50 ± 6.65 x 10^5 CFU mL^{-1}) of *S. aureus* bacteria at 10^{-3} dilution (n = 4, standard deviation error), Figure 3.21.

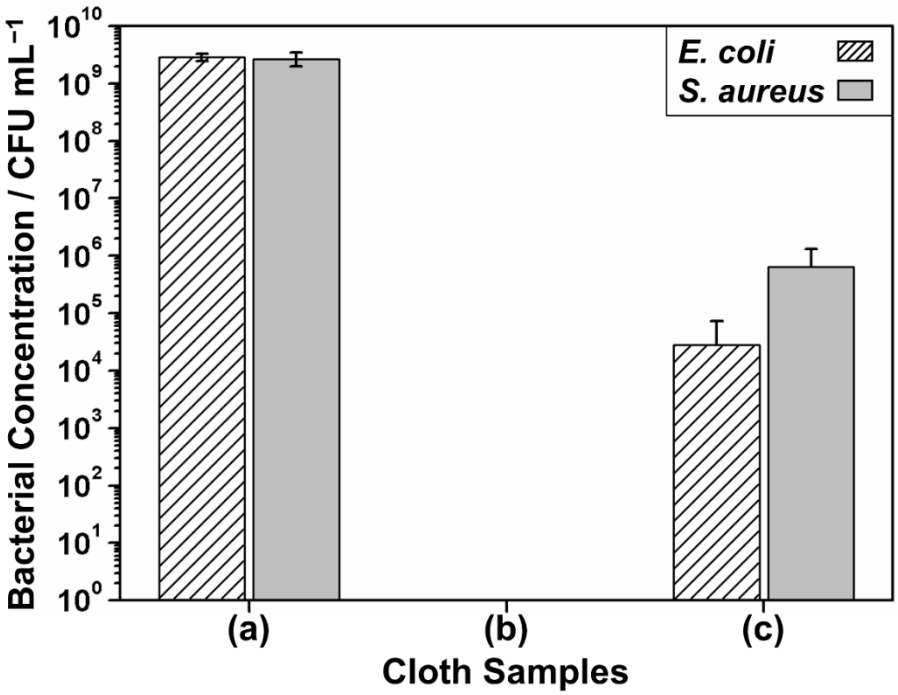

Figure 3.21: Antibacterial activity against *E. coli* (Gram-negative) and *S. aureus* (Gram-positive) bacteria: (a) untreated non-woven polypropylene sheet control; (b) poly(diallyldimethylammonium)–anionic fluorosurfactant complex spray coated non-woven polypropylene sheet; (c) poly(diallyldimethylammonium)–3% w/v silica (7 nm)–anionic fluorosurfactant spray coated non-woven polypropylene sheet. Reported values are averaged over at least 4 different values with standard deviation error. [Antibacterial testing performed by H. J. Cox, S. N. Barrientos-Palomo, and Dr G. J. Sharples].

3.4 Discussion

Various different polymer–fluorosurfactant complex coatings have been shown to exhibit fast-switching oleophobic–hydrophilic properties, Figure 3.1, Figure 3.2, and Figure 3.3. Silica nanoparticle incorporation into two of these complexes with optimised silica loading concentrations (3% w/v and 1.5% w/v for the polymer–anionic fluorosurfactant and polymer–amphoteric fluorosurfactant respectively) improves the surface hydrophilicity and oleophobicity relative to the nanoparticle-free control samples due to the impact of surface roughening upon Wenzel[88] and Wenzel/Cassie-Baxter[89] states of wetting respectively. Furthermore, a range of other nano- and

micron-sized particles are found to enhance the switching parameter relative to the particle-free surfaces, Figure 3.4. At a loading of 3% w/v, negatively charged particles enhance the hydrophilic and oleophobic properties whilst positively charged particles perform less well—this can be attributed to their ability to complex to the positively charged polymer backbone. Negatively charged alkyl functionalised silica nanoparticles improve the switching parameter further at lower loadings due to their greater oleophobicity compared to complexes containing unfunctionalised silica—this can be attributed to the presence of the oleophobic alkyl groups on the functionalised silica nanoparticles. Such incorporation of nanoparticles into coating surfaces mimic nanoscale roughness widely found on plant surfaces for the enhancement of liquid wettability[90] / repellency[91].

The oleophobicity of polymer–fluorosurfactant complex surfaces can be attributed to the fluorinated surfactant tails being orientated towards the air–solid interface exposing the low surface energy terminal CF_3 groups.[44] Consequently, the hydrophilic ionic surfactant head groups and the complexed polymer counterionic groups are buried within the subsurface region. When droplet water molecules come into contact with these polymer–fluorosurfactant surfaces, they are able to diffuse towards these underlying hydrophilic groups via one of two mechanisms: either the water molecules wick down towards the hydrophilic subsurface region due to defects at the air–solid interface,[45] or the hydrophilic subsurface is exposed to the water molecules as a consequence of water-induced molecular rearrangement of the fluorinated chains.[48] Both mechanisms can account for the time-dependent hydrophilicity of the polymer–fluorosurfactant complex surfaces (it either takes time for the water molecules to penetrate through the defects, or it takes time for the fluorinated chains to orientate during the water-induced molecular rearrangement). The oleophobic behaviour can also be accounted for on the basis of either mechanism. In the case of the defect mechanism, the much larger oil molecules are unable to penetrate any film defects, and so only come into contact with the low surface energy fluorinated tails. Alternatively, if the mechanism involves a water-induced molecular rearrangement, then the oleophobicity occurs as a result of the fluorinated chains remaining exposed at the air–solid interface when in contact with oil. Hence, the polymer–fluorosurfactant complex surfaces display the observed switching oleophobic–hydrophilic properties (the difference between the static water and oil contact angles).

An attempt was made to prepare fluorine-free polymer–surfactant oleophobic–hydrophilic surfaces using a highly branched hydrocarbon surfactant as a replacement for the fluorosurfactant. Increasing the level of branching in alkyl chains results in greater packing of the CH_3– and –CH_2– groups at the surface which in turn lowers the surface energy of such coatings down to values comparable to fluorinated surfactants.[92] However, these surfaces were not oleophobic with a maximum HCA of 40 ± 5°, Figure 3.6. Nevertheless, given that the switching parameter is positive (HCA greater than WCA), it is thought that fluorine-free oleophobic–hydrophilic polymer–surfactant complexes could be possible, potentially through the use of a more highly branched surfactant.

The nanoparticle-containing polymer–fluorosurfactant coatings display improved hardness (durability) relative to the particle-free control samples, Figure 3.12. Coating of the polymer–nanoparticle–fluorosurfactant complexes onto stainless steel mesh provides for oil(hexadecane)–water mixture separation, Figure 3.13, Figure 3.14 and Figure 3.16. It is also possible to separate both shorter chain alkanes (tetradecane and octane) and vegetable oil from water with >98% efficiency, Figure 3.17. Furthermore, coated stainless steel meshes are also able to separate olive oil from water Figure 3.19. Although olive oil is considered nonpolar and mostly consists of triglycerides, it also contains minor polar components such as mono- and diglycerides as well as phospholipids.[93] These minor polar components are large molecules and so the ability to separate olive oil from water can be attributed to the fact that these large polar molecules cannot wick down towards the hydrophilic subsurface region and are therefore repelled by the low surface energy fluorinated tails of the fluorosurfactant. Repeated use of the same polymer–nanoparticle–fluorosurfactant coated mesh for oil(tetradecane)–water separation did not result in a drop in performance demonstrating the recyclability of the coated mesh, Figure 3.20.

Such utilisation of cationic poly(diallyldimethylammonium) polymers for fluorosurfactant complex formation incorporates the added benefit of antibacterial poly(diallyldimethylammonium) quaternary ammonium centres.[65,94] These antimicrobial properties arise due to the interactions of the positively charged ammonium group with the negatively charged head groups of phospholipids in bacterial membranes which cause disruption of the membrane leading to cell leakage and eventually cell death.[95,96,97] The measured +99.99% (*E. coli*) and +99.97% (*S. aureus*) bacterial kill rate for poly(diallyldimethylammonium)–3% w/v silica (7 nm)–

anionic fluorosurfactant complex coated non-woven polypropylene sheets can be attributed to surface roughness lowering available anchoring points for bacteria attachment (reduction in available area of contact with the bacteria's outer surface[98]). The small difference in bacteria kill rates between *E. coli* and *S. aureus* for poly(diallyldimethylammonium)–3% w/v silica (7 nm)–anionic fluorosurfactant complex coated non-woven polypropylene sheets may be due to differences in the outer surface structures of the two species.[99]

Previously reported polymer–fluorosurfactant complex surfaces have tended to exhibit relatively small switching parameters[34,35,37,44,48,49] (usually as a result of poor oleophobicity) or display long switching times[41,42] (taking several minutes for the water droplets to fully wet the surface). Both of these problems are overcome using the polymer–nanoparticle–fluorosurfactant coating reported here. Furthermore, the current single-step application methodology is far more straightforward compared to earlier lengthy layer-by-layer approaches involving multiple steps.[39] In addition, the antimicrobial properties of these coatings allows for simultaneous oil–water separation and killing of bacteria—the first time this has been reported for an oleophobic(in air)–hydrophilic coating (previous reports of antibacterial oil–water separation utilise coatings that are oleophilic in air and are therefore easily fouled by oils[58,59,60]).

3.5 Conclusions

Multifunctional fast-switching oleophobic–hydrophilic coatings have been prepared using polymer–nanoparticle–fluorosurfactant complexes. These can be deposited in a single step by spraying or solvent-casting. Electrostatic attraction of negatively charged nanoparticles (silicas and graphene) within cationic poly(diallyldimethylammonium)–anionic fluorosurfactant complex films introduces surface roughening which enhances hydrophilicity and oleophobicity as a consequence of Wenzel and Wenzel/Cassie–Baxter wetting states respectively. These surfaces provide high-efficiency continuous oil–water separation. Nanoparticle incorporation also improves coating hardness (durability). The cationic polymer quaternary ammonium centres present within these polymer–nanoparticle–fluorosurfactant complex systems impart antibacterial surface properties (including against water-borne *E. coli* (Gram-negative) and *S. aureus* (Gram-positive) bacteria). Other applications include antibacterial–antifogging surfaces.

3.6 References

[1] Kingston, P. F. Long-term Environmental Impact of Oil Spills. *Spill Sci. Technol. Bull.* **2002**, *7*, 53–61.

[2] Gossen, L. P.; Velichkina, L. M. Environmental Problems of the Oil-and-Gas Industry. *Pet. Chem.* **2006**, *46*, 67–72.

[3] Ivshina, I. B.; Kuyukina, M. S.; Krivoruchko, A. V.; Elkin, A. A.; Makarov, S. O.; Cunningham, C. J.; Peshkur, T. A.; Atlas, R. M.; Philp, J. C. Oil Spill Problems and Sustainable Response Strategies Through New Technologies. *Environ. Sci.: Processes Impacts* **2015**, *17*, 1201–1219.

[4] Joye, S. B. Deepwater Horizon, 5 years on. *Science* **2015**, *349*, 592–593.

[5] Dubansky, B.; Whitehead, A.; Miller, J. T.; Rice, C. D.; Galvez, F. Multitissue Molecular, Genomic, and Developmental Effects of the Deepwater Horizon Oil Spill on Resident Gulf Killifish (*Fundulus grandis*). *Environ. Sci. Technol.* **2013**, *47*, 5074–5082.

[6] Peterson, C. H.; Rice, S. D.; Short, J. W.; Esler, D.; Bodkin, J. L.; Ballachey, B. E.; Irons, D. B. Long-Term Ecosystem Response to the Exxon Valdez Oil Spill. *Science* **2003**, *302*, 2082–2086.

[7] Choi, H.–M.; Cloud, R. M. Natural Sorbents in Oil Spill Cleanup. *Environ. Sci. Technol.* **1992**, *26*, 772–776.

[8] Teas, Ch.; Kalligeros, S.; Zanikos, F.; Stournas, S.; Lois, E.; Anastopoulos, G. Investigation of the Effectiveness of Absorbent Materials in Oil Spill Clean Up. *Desalination* **2001**, *140*, 259–264.

[9] Adebajo, M. O.; Frost, R. L.; Kloprogge, J. T.; Carmody, O.; Kokot, S. Porous Materials for Oil Spill Cleanup: A Review of Synthesis and Absorbing Properties. *J. Porous Mater.* **2003**, *10*, 159–170.

[10] Bayat, A.; Aghamiri, S. F.; Moheb, A.; Vakili-Nezhaad, G. R. Oil Spill Cleanup from Sea Water by Sorbent Materials. *Chem. Eng. Technol.* **2005**, *28*, 1525–1528.

[11] Yang, Y.; Liu, Z.; Huang, J.; Wang, C. Multifunctional, Robust Sponges by a Simple Adsorption–Combustion Method. *J. Mater. Chem. A* **2015**, *3*, 5875–5881.

[12] Ceylan, D.; Dogu, S.; Karacik, B.; Yakan, S. D.; Okay, O. S.; Okay, O. Evaluation of Butyl Rubber as Sorbent Material for the Removal of Oil and Polycyclic Aromatic Hydrocarbons from Seawater. *Environ. Sci. Technol.* **2009**, *43*, 3846–3852.

[13] Zhou, X.; Zhang, Z.; Xu, X.; Men, X.; Zhu, X. Facile Fabrication of Superhydrophobic Sponge with Selective Absorption and Collection of Oil from Water. *Ind. Eng. Chem. Res.* **2013**, *52*, 9411–9416.

[14] Howarter, J. A.; Youngblood, J. P. Amphiphile Grafted Membranes for the Separation of Oil-in-Water Dispersions. *J. Colloid Interface Sci.* **2009**, *329*, 127–132.

[15] Kota, A. K.; Kwon, G.; Choi, W.; Mabry, J. M.; Tuteja, A. Hygro-Responsive Membranes for Effective Oil–Water Separation. *Nat. Commun.* **2012**, *3*, 1025.

[16] Kwon, G.; Kota, A. K.; Li, Y.; Sohani, A.; Mabry, J. M.; Tuteja, A. On-Demand Separation of Oil–Water Mixtures. *Adv. Mater.* **2012**, *24*, 3666–3671.

[17] Pan, S.; Guo, R.; Xu, W. Durable Superoleophobic Fabric Surfaces with Counterintuitive Superwettability for Polar Solvents. *AIChE J.* **2014**, *60*, 2752–2756.

[18] Xu, Z.; Zhao, Y.; Wang, H.; Wang, X.; Lin, T. A Superamphiphobic Coating with an Ammonia-Triggered Transition to Superhydrophilic and Superoleophobic for Oil–Water Separation. *Angew. Chem. Int. Ed.* **2015**, *54*, 4527–4530.

[19] Kwon, G.; Post, E.; Tuteja, A. Membranes with Selective Wettability for the Separation of Oil–Water Mixtures. *MRS Commun.* **2015**, *5*, 475–494.

[20] Shen, T.; Li, S.; Wang, Z.; Wang, L. Rare Bi-Wetting TiO_2-F/SiO_2/F-PEG Fabric Coating for Self-Cleaning and Oil/Water Separation. *RSC Adv.* **2016**, *6*, 115196–115203.

[21] Crick, C.; Gibbins, J. A.; Parkin, I. P. Superhydrophobic Polymer-Coated Copper-Mesh; Membranes for Highly Efficient Oil–Water Separation. *J. Mater. Chem. A* **2013**, *1*, 5943–5948

[22] Feng, L.; Zhang, Z.; Mai, Z.; Ma, Y.; Liu, B.; Jiang, L.; Zhu, D. A Super-Hydrophobic and Super-Oleophilic Coating Mesh Film for the Separation of Oil and Water. *Angew. Chem. Int. Ed.* **2004**, *43*, 2012–2014.

[23] Wang, C.; Yao, T.; Wu, J.; Ma, C.; Fan, Z.; Wang, Z.; Cheng, Y.; Lin, Q.; Yang, B. Facile Approach in Fabricating Superhydrophobic and Superoleophilic Surface for Water and Oil Mixture Separation. *ACS Appl. Mater. Interfaces* **2009**, *1*, 2613–2617.

[24] Nguyen, D. D.; Tai, N. H.; Lee, S. B.; Kuo, W. S. Superhydrophobic and Superoleophilic Properties of Graphene-Based Sponges Fabricated using a Facile Dip Coating Method. *Energy Environ. Sci.* **2012**, *5*, 7908–7912.

[25] Lee, C. H.; Johnson, N.; Drelich, J.; Yap, Y. K. The Performance of Superhydrophobic and Superoleophilic Carbon Nanotube Meshes in Water–Oil Filtration. *Carbon* **2011**, *49*, 669–676.

[26] Howarter, J. A.; Youngblood, J. P. Self-Cleaning and Anti-Fog Surfaces via Stimuli-Responsive Polymer Brushes. *Adv. Mater.* **2007**, *19*, 3838–3843.

[27] Xue, Z.; Wang, S.; Lin, L.; Chen, L.; Liu, M.; Feng, L.; Jiang, L. A Novel Superhydrophilic and Underwater Superoleophobic Hydrogel-Coated Mesh for Oil/Water Separation. *Adv. Mater.* **2011**, *23*, 4270–4273.

[28] Zhu, Y.; Zhang, F.; Wang, D.; Pei, X. F.; Zhang, W.; Jin, J. A Novel Zwitterionic Polyelectrolyte Grafted PVDF Membrane for Thoroughly Separating Oil from Water with Ultrahigh Efficiency. *J. Mater. Chem. A* **2013**, *1*, 5758–5765.

[29] Gao, X.; Xu, L.–P.; Xue, Z.; Feng, L.; Peng, J.; Wen, Y.; Wang, S.; Zhang, X. Dual-Scaled Porous Nitrocellulose Membranes with Underwater Superoleophobicity for Highly Efficient Oil/Water Separation. *Adv. Mater.* **2014**, *26*, 1771–1775.

[30] Gondal, M. A.; Sadullah, M. S.; Dastageer, M. A.; McKinley, G. H.; Panchanathan, D.; Varanasi, K. K. Study of Factors Governing Oil–Water Separation Process Using TiO_2 Films Prepared by Spray Deposition of Nanoparticle Dispersions. *ACS Appl. Mater. Interfaces* **2014**, *6*, 13422–13429.

[31] Howarter, J. A.; Youngblood, J. P. Self-Cleaning and Next Generation Anti-Fog Surfaces and Coatings. *Macromol. Rapid Commun.* **2008**, *29*, 455–466.

[32] Howarter, J. A.; Genson, K. L.; Youngblood, J. P. Wetting Behavior of Oleophobic Polymer Coatings Synthesized from Fluorosurfactant-Macromers. *ACS Appl. Mater. Interfaces* **2011**, *3*, 2022–2030.

[33] Wang, Y.; Dong, Q.; Wang, Y.; Wang, H.; Li, G.; Bai, R. Investigation on RAFT Polymerization of a Y-Shaped Amphiphilic Fluorinated Monomer and Anti-Fog and Oil-Repellent Properties of the Polymers. *Macromol. Rapid Commun.* **2010**, *31*, 1816–1821.

[34] Antonietti, M.; Henke, S.; Thünemann, A. Highly Ordered Materials with Ultra-Low Surface Energies: Polyelectrolyte–Surfactant Complexes with Fluorinated Surfactants. *Adv. Mater.* **1996**, *8*, 41–45.

[35] Turri, S.; Valsecchi, R.; Viganò, M.; Levi, M. Hydrophilic–Oleophobic Behaviour in Thin Films from Fluoromodified Nanoclays and Polystyrene. *Polym. Bull.* **2009**, *63*, 235–243.

[36] Goddard, E. D. Polymer–Surfactant Interaction Part II. Polymer and Surfactant of Opposite Charge. *Colloids Surf.* **1986**, *19*, 301–329.

[37] Thünemann, A. F.; Lochhaas, K. H. Surface and Solid-State Properties of a Fluorinated Polyelectrolyte–Surfactant Complex. *Langmuir* **1999**, *15*, 4867–4874.

[38] Tang, H.; Fu, Y.; Yang, C.; Zhu, D.; Yang, J. A UV-Driven Superhydrophilic/Superoleophobic Polyelectrolyte Multilayer Film on Fabric and its Application in Oil/Water Separation. *RSC Adv.* **2016**, *6*, 91301–91307.

[39] Brown, P. S.; Bhushan, B. Mechanically Durable, Superoleophobic Coatings Prepared by Layer-by-Layer Technique for Anti-Smudge and Oil–Water Separation. *Sci. Rep.* **2015**, *5*, 8701.

[40] Liu, D.; Yu, Y.; Chen, X.; Zheng, Y. Selective Separation of Oil and Water with Special Wettability Mesh Membranes. *RSC Adv.* **2017**, *7*, 12908–12915.

[41] Yang, J.; Zhang, Z.; Xu, X.; Zhu, X.; Men, X.; Zhou, X. Superhydrophilic–Superoleophobic Coatings. *J. Mater. Chem.* **2012**, *22*, 2834–2837.

[42] Yang, J.; Yin, L.; Tang, H.; Song, H.; Gao, X.; Liang, K.; Li, C. Polyelectrolyte–Fluorosurfactant–Complex–Based Meshes with Superhydrophilicity and Superoleophobicity for Oil/Water Separation. *Chem. Eng. J.* **2015**, *268*, 245–250.

[43] Brown, P. S.; Atkinson, O. D. L. A.; Badyal, J. P. S. Ultrafast Oleophobic–Hydrophilic Switching Surfaces for Antifogging, Self-Cleaning, and Oil–Water Separation. *ACS Appl. Mater. Interfaces* **2014**, *6*, 7504–7511.

[44] Thünemann, A. F.; Lieske, A.; Paulke, B.–R. Low Surface Energy Coatings from Waterborne Nano-Dispersions of Polymer Complexes. *Adv. Mater.* **1999**, *11*, 321–324.

[45] Li, L.; Wang, Y.; Gallaschun, C.; Risch, T.; Sun, J. Why Can a Nanometer-Thick Polymer Coated Surface Be More Wettable to Water than to Oil? *J. Mater. Chem.* **2012**, *22*, 16719–16722.

[46] Wang, Y.; Knapp, J.; Legere, A.; Raney, J.; Li, L. Effect of End-Groups on Simultaneous Oleophobicity/Hydrophilicity and Anti-Fogging Performance of Nanometer-Thick Perfluoropolyethers (PFPEs). *RSC Adv.* **2015**, *5*, 30570–30576.

[47] Wang, Y.; Dugan, M.; Urbaniak, B.; Li, L. Fabricating Nanometer-Thick Simultaneously Oleophobic/Hydrophilic Polymer Coatings via a Photochemical Approach. *Langmuir* **2016**, *32*, 6723–6729.

[48] Yoon, H.; Na, S. H.; Choi, J. Y.; Latthe, S. S.; Swihart, M. T.; Al-Deyab, S. S.; Yoon, S. S. Gravity-Driven Hybrid Membrane for Oleophobic–Superhydrophilic Oil–Water Separation and Water Purification by Graphene. *Langmuir* **2014**, *30*, 11761–11769.

[49] Thünemann, A. F.; Schnöller, U.; Nuyken, O.; Voit, B. Self-Assembled Complexes of Diazosulfonate Polymers with Low Surface Energies. *Macromolecules* **1999**, *32*, 7414–7421.

[50] Lampitt, R. A.; Crowther, J. M.; Badyal, J. P. S. Switching Liquid Repellent Surfaces. *J. Phys. Chem. B* **2000**, *104*, 10329–10331.

[51] Hutton, S. J.; Crowther, J. M.; Badyal, J. P. S. Complexation of Fluorosurfactants to Functionalized Solid Surfaces: Smart Behavior. *Chem. Mater.* **2000**, *12*, 2282–2286.

[52] Molina, R.; Gómez, M.; Kan, C.–W.; Bertran, E. Hydrophilic–Oleophobic Coatings on Cellulosic Materials by Plasma Assisted Polymerization in Liquid Phase and Fluorosurfactant Complexation. *Cellulose* **2014**, *21*, 729–739.

[53] Brown, P. S.; Bhushan, B. Bioinspired, Roughness-Induced, Water and Oil Super-philic and Super-phobic Coatings Prepared by Adaptable Layer-by-Layer Technique. *Sci. Rep.* **2015**, *5*, 14030.

[54] Koch, K.; Barthlott, W. Superhydrophobic and Superhydrophilic Plant Surfaces: An Inspiration for Biomimetic Materials. *Phil. Trans. R. Soc. A* **2009**, *367*, 1487–1509.

[55] Wen, G.; Guo, Z.; Liu, W. Biomimetic Polymeric Superhydrophobic Surfaces and Nanostructures: From Fabrication to Applications. *Nanoscale* **2017**, *9*, 3338–3366.

[56] Ushimaru, K.; Hamano, Y; Katano, H. Antimicrobial Activity of ε-Poly-L-lysine after Forming a Water-Insoluble Complex with an Anionic Surfactant. *Biomacromolecules* **2017**, *18*, 1387–1392.

[57] Ashiuchi, M; Hakumai, Y.; Nakayama, S.; Higashiuchi, H; Shimada, K. Engineering Antimicrobial Coating of Archael Poly-γ-Glutamate-Based Materials using Non-Covalent Crosslinkages. *Sci. Rep.* **2018**, *8*, 4645.

[58] Upadhyay, R. K.; Dubey, A.; Waghmare, P. R.; Priyadarshini, R.; Roy, S. S. Multifunctional Reduced Graphene Oxide Coated Cloths for Oil/Water Separation and Antibacterial Application. *RSC Adv.* **2016**, *6*, 62760–62767.

[59] Liu, L.; Yuan, W. A Hierarchical Functionalized Biodegradable PLA Electrospun Nanofibrous Membrane with Superhydrophobicity and Antibacterial Properties for Oil/Water Separation. *New J. Chem.* **2018**, *42*, 17615–17624.

[60] Fu, Y.; Jin, B.; Zhang, Q.; Zhan, X.; Chen, F. pH-Induced Switchable Superwettability of Efficient Antibacterial Fabrics for Durable Selective Oil/Water Separation. *ACS Appl. Mater. Interfaces* **2017**, *9*, 30161–30170.

[61] ASTM Standard E384–11e1, Standard Test Method for Knoop and Vickers Hardness of Materials, ASTM International, West Conshohocken, PA, 2011, DOI: 10.1520/E0384-11E01, www.astm.org.

[62] ChemPoint, DuPont™ Capstone® Fluorosurfactant FS-50 Technical Information. https://www.chempoint.com/products/chemours/capstone-fluorosurfactants/capstone-surfactants-and-coating-additives/capstone-fs-50 (accessed Aug 15, 2019).

[63] O'Donoghue, D.; Young, T. M.; Pembroke, J. T.; O'Dwyer, T. F. An Investigation of Surfactant and Enzyme Formulations for the Alleviation of Insect Contamination on Hybrid Laminar Flow Control (HLFC) Surfaces. *Aerosp. Sci. Technol.* **2002**, *6*, 19–29.

[64] Spatz, J. P.; Möller, M.; Noeske, M.; Behm, R. J.; Pietralla, M. Nanomosaic Surfaces by Lateral Phase Separation of a Diblock Copolymer. *Macromolecules* **1997**, *30*, 3874–3880.

[65] van der Mei, H. C.; Rustema-Abbing, M.; Langworthy, D. E.; Collias, D. I.; Mitchell, M. D.; Bjorkquist, D. W.; Busscher, H. J. Adhesion and Viability of Waterborne Pathogens on P-DADMAC Coatings. *Biotechnol. Bioeng.* **2008**, *99*, 165–169.

[66] ChemPoint, DuPont™ Capstone® Fluorosurfactant FS-63 Technical Information. https://www.chempoint.com/products/chemours/capstone-fluorosurfactants/capstone-surfactants-and-coating-additives/capstone-fs-63 (accessed Aug 15, 2019).

[67] Steele, A.; Bayer, I.; Loth, E. Inherently Superoleophobic Nanocomposite Coatings by Spray Atomization. *Nano Lett.* **2009**, *9*, 501–505.

[68] Giesy, J. P.; Kannan, K. Global Distribution of Perfluorooctane Sulfonate in Wildlife. *Environ. Sci. Technol.* **2001**, 35, 1339–1342.

[69] Kudo, N.; Kawashima, Y. Toxicity and Toxicokinetics of Perfluorooctanoic Acid in Humans and Animals. *J. Toxicol. Sci.* **2003**, 28, 49–57.

[70] Begley, T. H.; White, K.; Honigfort, P.; Twaroski, M. L.; Neches, R.; Walker, R. A. Perfluorochemicals: Potential Sources of and Migration from Food Packaging. *Food Addit. Contam.* **2005**, 22, 1023–1031.

[71] Prevedouros, K.; Cousins, I. T.; Buck, R. C.; Korzeniowski, S. H. Sources, Fate and Transport of Perfluorocarboxylates. *Environ. Sci. Technol.* **2006**, 40, 32–44.

[72] Houde, M.; Martin, J. W.; Letcher, R. J.; Soloman, K. R.; Muir, D. C. G.; Biological Monitoring of Polyfluoroalkyl Substances: A Review. *Environ. Sci. Technol.* **2006**, 40, 3463–3473.

[73] Conder, J. M.; Hoke, R. A.; Wolf, W. d.; Russell, M. H.; Buck, R. C. Are PFCAs Bioaccumulative? A Critical Review and Comparison with Regulatory Criteria and Persistent Lipophilic Compounds. *Environ. Sci. Technol.* **2008**, 42, 995–1003.

[74] Müller, C. E.; De Silva, A. O.; Small, J.; Williamson, M.; Wang, X.; Morris, A.; Katz, S.; Gamberg, M.; Muir, D. C. G. Biomagnification of Perfluorinated Compounds in a Remote Terrestrial Food Chain: Lichen–Caribou–Wolf. *Environ. Sci. Technol.* **2011**, 45, 8665–8673.

[75] Jiang, L.; Tang, Z.; Park-Lee, K. J.; Hess, D. W.; Breedveld, V. Fabrication of Non-Fluorinated Hydrophilic-Oleophobic Stainless Steel Mesh for Oil-Water Separation. *Sep. Purif. Technol.* **2017**, *184*, 394–403.

[76] Tang, Z.; Hess, D. W.; Breedveld, V. Fabrication of Oleophobic Paper with Tunable Hydrophilicity by Treatment with Non-Fluorinated Chemicals. *J. Mater. Chem. A* **2015**, 3, 14651–14660.

[77] Rohrbach, K.; Li, Y.; Zhu, H.; Liu, Z.; Dai, J.; Andreasen, J.; Hu, L. A Cellulose Based Hydrophilic, Oleophobic Hydrated Filter for Water/Oil Separation. *Chem. Commun.* **2014**, 50, 13296–13299.

[78] Cao, Y.; Liu, N.; Zhang, W.; Feng, L.; Wei, Y. One-Step Coating Toward Multifunctional Applications: Oil/Water Mixtures and Emulsions Separation and Contaminants Adsorption. *ACS Appl. Mater. Interfaces* **2016**, *8*, 3333–3339.

[79] Paul, U. C.; Fragouli, D.; Bayer, I. S.; Athanassiou, A. Functionalized Cellulose Networks for Efficient Oil Removal from Oil–Water Emulsions. *Polymers* **2016**, *8*, 52.

[80] Alexander, S.; Smith, G. N.; James, C.; Rogers, S. E.; Guittard, F.; Sagisaka, M.; Eastoe, J. Low-Surface Energy Surfactants with Branched Hydrocarbon Architectures. *Langmuir* **2014**, *30*, 3413–3421.

[81] Alexander, S.; Eastoe, J.; Lord, A. M.; Guittard, F.; Barron, A. R. Branched Hydrocarbon Low Surface Energy Materials for Superhydrophobic Nanoparticle Derived Surfaces. *ACS Appl. Mater. Interfaces* **2016**, *8*, 660–666.

[82] Gürsoy, M.; Harris, M. T.; Downing, J. O.; Barrientos-Palomo, S. N.; Carletto, A.; Yaprak, A. E.; Karaman, M.; Badyal, J. P. S. Bioinspired Fog Capture and Channel Mechanism Based on the Arid Climate Plant *Salsola crassa*. *Colloids Surf., A* **2017**, *529*, 195–202.

[83] Dorrer, C.; Rühe, J. Superaerophobicity: Repellence of Air Bubbles from Submerged, Surface-Engineered Silicon Substrates. *Langmuir* **2012**, *28*, 14968–14973.

[84] Montes Ruiz-Cabello, F. J.; Rodríguez-Valverde, M. A.; Marmur, A.; Cabrerizo-Vílchez, M. A. Comparison of Sessile Drop and Captive Bubble Methods on Rough Homogeneous Surfaces: A Numerical Study. *Langmuir* **2011**, *27*, 9638–9643.

[85] Morra, M.; Occhiello, E.; Garbassi, F. The Wetting Behavior of Grafted Hydrophilic Acrylic Monomers. *Colloid Polym. Sci.* **1993**, *271*, 696–704.

[86] Edberg, S. C.; Rice, E. W.; Karlin, R. J.; Allen, M. J. *Escherichia coli*: The Best Biological Drinking Water Indicator for Public Health Protection. *J. Appl. Microbiol.* **2000**, *88*, 106S–116S.

[87] Plano, L. R. W.; Garza, A. C; Shibata, T.; Elmir, S. M.; Kish, J.; Sinigalliano, C. D.; Gidley, M. L.; Miller, G.; Withum, K.; Fleming, L. E.; Solo-Gabriele, H. M. Shedding of *Staphylococcus aureus* and Methicillin-Resistant *Staphylococcus aureus* from Adult and Pediatric Bathers in Marine Waters. *BMC Microbiol.* **2011**, *11*, 5.

[88] Wenzel, R. N. Resistance of Solid Surfaces to Wetting by Water. *Ind. Eng. Chem.* **1936**, 28, 988–994.

[89] Cassie, A. B. D.; Baxter, S. Wettability of Porous Surfaces. *Trans. Faraday Soc.* **1944**, 40, 546–551.

[90] Bohn, H. F.; Federle, W. Insect Aquaplaning: *Nepenthes* Pitcher Plants Capture Prey with the Peristome, a Fully Wettable Water-Lubricated Anisotropic Surface. *Proc. Natl Acad. Sci. USA* **2004**, 101, 14138–14143.

[91] Barthlott, W.; Neinhuis, C. Purity of the Sacred Lotus, or Escape from Contamination in Biological Surfaces. *Planta* **1997**, 202, 1–8.

[92] Sagisaka, M.; Narumi, T.; Niwase, M.; Narita, S.; Ohata, A.; James, C.; Yoshizawa, A.; Taffin de Givenchy, E.; Guittard, F.; Alexander, S.; Eastoe, J. Hyperbranched Hydrocarbon Surfactants Give Fluorocarbon-Like Low Surface Energies. *Langmuir* **2014**, *30*, 6057–6063.

[93] Yara-Varón, E.; Li, Y.; Balcells, M.; Canela-Garayoa, R.; Fabiano-Tixier, A.-S.; Chemat, F. Vegetable Oils as Alternative Solvents for Green Oleo-Extraction, Purification and Formulation of Food and Natural Products. *Molecules* **2017**, *22*, 1474.

[94] Schofield, W. C. E.; Badyal, J. P. S. A Substrate-Independent Approach for Bactericidal Surfaces. *ACS Appl. Mater. Interfaces* **2009**, *1*, 2763–2767.

[95] Salton, M. R. J. Lytic Agents, Cell Permeability, and Monolayer Penetrability. *J. Gen. Physiol.* **1968**, *52*, 227–252.

[96] Gottenbos, B.; Grijpma, D. W.; van der Mei, H. C.; Feijen, J.; Busscher, H. J. Antimicrobial Effects of Positively Charged Surfaces on Adhering Gram-Positive and Gram-Negative Bacteria. *J. Antimicrob. Chemother.* **2001**, *48*, 7–13.

[97] Buffet-Bataillon, S.; Tattevin, P.; Bonnaure-Mallet, M.; Jolivet-Gougeon, A. Emergence of Resistance to Antibacterial Agents: The Role of Quaternary Ammonium Compounds—A Critical Review. *Int. J. Antimicrob. Agents* **2012**, *39*, 381–389.

[98] Bagherifard, S.; Hickey, D. J.; de Luca, A. C.; Malheiro, V. N.; Markaki, A. E.; Guagliano, M.; Webster, T. J. The Influence of Nanostructured Features on Bacterial Adhesion and Bone Cell Functions on Severely Shot Peened 316L Stainless Steel. *Biomaterials* **2015**, *73*, 185–197.

[99] Sonohara, R.; Muramatsu, N.; Ohshima, H.; Kondo, T. Difference in Surface Properties Between *Escherichia coli* and *Staphylococcus aureus* as Revealed by Electrophoretic Mobility Measurements. *Biophys. Chem.* **1995**, 55, 273–277.

Chapter 4

Atomised Spray Plasma Deposition of Highly Antibacterial Polymer–Metallosurfactant Nanocomposite Coatings

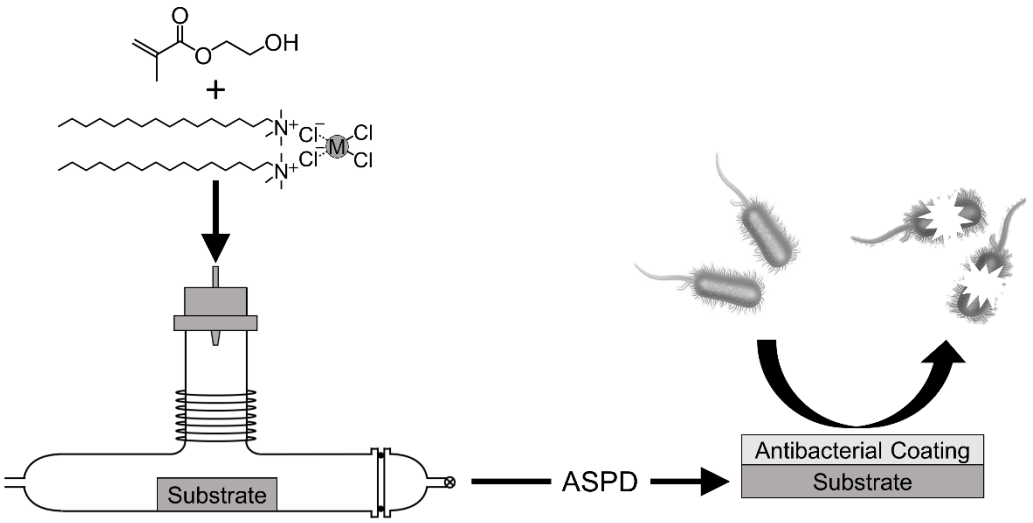

4.1 Introduction

Bacterial colonisation of surfaces (biofilm formation) such as medical devices,[1] implants,[2] and those in a healthcare setting[3] contribute to the spreading of bacterial infections posing a huge threat to human health.[4] Biofilms are significantly more resistant to antibiotics than planktonic bacteria and so antibacterial surfaces which can prevent biofilm formation are necessary for limiting the spread of infections.[5] There are three main types of antibacterial surface coating: bacteria-repelling, contact-killing, and biocide-releasing coatings. Bacteria-repelling coatings resist the adsorption of bacteria preventing biofilm formation and are commonly prepared using for example poly(ethylene glycol) films.[6] Contact-killing coatings consist of antimicrobial compounds, such as those containing cationic quaternary ammonium groups, tethered to a polymer coating and can kill bacteria upon adsorption onto the surface.[7] For both of these types of antibacterial surface, the antimicrobial action requires close proximity between the surface and the bacteria. As a consequence, these surfaces are readily contaminated due to the formation of a layer of dead bacteria which both blocks the

active antibacterial groups and provides a surface for adsorption of live bacteria, resulting in the deactivation of such coatings.[8] The antibacterial action of biocide-releasing coatings on the other hand is due to the leaching of antibacterial compounds allowing killing of bacteria both within close proximity and further from the surface.[9] These surfaces offer the ability to deliver a high concentration of antibacterial agent locally however the duration of antibacterial action is ultimately shorter due to the finite reservoir of antibacterial agent.[9] The ability to control the release rate of the antibacterial agent is therefore highly desirable.

Biocide-releasing coatings have been prepared in the past by fabrication methods including dip coating,[10,11,12] spin coating,[13] solvent casting,[14] sol–gel,[15,16] electrodeposition,[17,18] graft polymerisation,[19] photo-polymerisation,[20] thermal spraying,[21] chemical vapour deposition,[22] and self-assembled monolayer formation[23] to incorporate biocides such as metal ions and antibiotics into thin films. However, these techniques have many drawbacks such as requiring the use of solvents,[15,16,19,20] high temperatures,[15,16,21,22] or specific substrates,[23] as well as being multi-step,[10,11,12,13,17,18,20] or lengthy[14,16,19] processes. The use of plasma deposition is therefore attractive as this provides a solventless, low temperature, and substrate-independent route for depositing thin antibacterial films.[24,25]

Biocide-releasing antibacterial coatings have been prepared by impregnating plasma polymers with silver ions through immersion however these again suffer from being multi-step processes.[26,27,28,29,30,31,32] Other multi-step processes have been reported where a plasma polymer layer is used as a barrier layer to control the release rate of biocide agents including Zn ions[33] and antibiotics such as ciprofloxacin,[34] vancomycin,[35] and ampicillin[36]. A single-step technique which simultaneously uses plasma polymerisation and metal-sputtering has been used to incorporate Ag[37,38,39] or Cu[40] into an organosilicon matrix has been reported however the deposition rate for this technique is very low[37,38,39] and the metal content must be high (>38%) to impart antibacterial properties[40]. The same technique has been used to prepare Ag/hydrocarbon nanocomposites.[41,42] A similar technique which deposits Ag-containing nanocomposites by simultaneous sputtering of polymer and metal from independent magnetron sources also suffers from slow deposition rates.[43,44] A single-step atmospheric pressure plasma chemical vapour deposition (APCVD) technique using a plasma jet results in much greater deposition rates, however requires much

greater plasma power,[45,46,47,48] the use of solvent to inject the metal containing solution into the plasma,[45,46,47,48,49] or results in poor antibacterial properties for coatings with high silver content[50]. Antibacterial silver-containing hydroxyapatite coatings have also been prepared using a single-step plasma spray process however the preparation of the precursor powder is a lengthy process involving the use of solvents and a high temperature heat treatment step.[51] Another disadvantage of the previously mentioned biocide-releasing coatings is the cytotoxicity of the released antibacterial agent, especially when metals such as silver are used.[52,53] Furthermore, there is the increasing risk of silver-resistant[54] and antibiotic-resistant bacteria.[55] Therefore, there is a need to develop a deposition technique which overcomes the above-mentioned disadvantages and which can prepare biocompatible biocide-releasing coatings.

A new class of metal-based surfactant materials known as metallosurfactants have an amphiphilic structure similar to surfactant molecules but however show interesting additional properties due to having a d or f block metal complexed to the surfactant.[56] In addition to changing the metal used, the ratio of metal to surfactant,[57] the length of surfactant alkyl chain,[58] and whether the metal is concentrated in the head group,[59] tail group,[60] or as the counter ion[61] of the surfactant can all be tailored to change the physical and chemical properties of the metallosurfactant. Therefore, these have a wide range of possible applications including for solubilisation of dyes,[62,63] protein binding,[64] drug delivery,[65] anti-cancer,[66] CO-releasing for biomedical applications,[58] magnetic resonance imaging,[67] bio-imaging,[68] templating for mesostructures,[69] nanoparticle synthesis,[70,71] catalysis,[72] and light-driven hydrogen generation[73]. Furthermore, the amphiphilic nature of metallosurfactants allows for different or enhanced interactions with biomolecules compared to non-amphiphilic metal complexes and therefore they have great potential for biological and medicinal applications.[74] One of these biological properties of metallosurfactants is their antimicrobial activity towards both bacterial and fungal species.[75,76,77,78,79,80,81,82,83,84,85,86,87,88,89,90] Whilst many surfactant molecules on their own are antibacterial[91,92,93], there is a great enhancement in these properties upon formation of a metallosurfactant.[94,95,96,97,98,99,100] This increase in antibacterial activity is due to the greater hydrophobic character of the metallosurfactant which allows for easier permeation through, and therefore greater damage of, the lipid layers of bacterial/fungal cell membranes.[101,102] Increasing the hydrophobicity by extending the

length of the surfactant alkyl chain[103] or by employing double chain systems over single chain ones[104] are effective ways to improve antibacterial activity. Furthermore, metallosurfactants have been shown to have low cytotoxicity towards healthy human cells.[105] All previous reports of antibacterial metallosurfactants have tested these properties in solution. Whilst metallosurfactants have been incorporated into coatings for optoelectronic devices,[106] ultrathin redox-active surfaces,[107] and corrosion mitigation surfaces,[108] their antibacterial properties have not yet been exploited for antibacterial surface coatings.

Atomised spray plasma deposition (ASPD) is a single-step, room temperature, solventless method for the preparation of functional coatings.[109,110] This encompasses the nebulisation of liquid or slurry droplets into a non-equilibrium electrical discharge. At low energy inputs, high levels of structural retention (functionality) can be attained. In this chapter, highly antibacterial biocide-releasing polymer–metallosurfactant coatings are prepared by ASPD using 2-hydroxyethyl methacrylate and two different metallosurfactants[111]: bishexadecyltrimethyl ammonium iron(II) tetrachloride (Fe:CTAC) and bishexadecyltrimethyl ammonium copper(II) tetrachloride (Cu:CTAC), Scheme 4.1. ASPD coated non-woven polypropylene cloth sheets displayed high antibacterial activity against both the *E. coli* (Gram-negative) and *S. aureus* (Gram-positive) bacterial species tested.

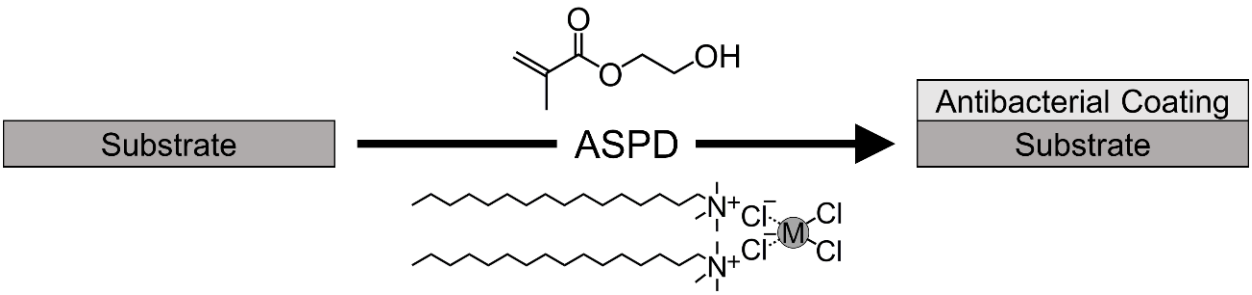

Scheme 4.1: Atomised spray plasma deposition of antibacterial 2-hydroxyethyl methacrylate–2% w/v M:CTAC (M denotes Cu or Fe) nanocomposite layers.

4.2 Experimental

4.2.1 Atomised Spray Plasma Deposition

Precursor materials used were 2-hydroxyethyl methacrylate (HEMA, 97%, Sigma-Aldrich Ltd.), and metallosurfactants bishexadecyltrimethyl ammonium iron (II) tetrachloride (Fe:CTAC (1:2)) and bishexadecyltrimethyl ammonium copper (II) tetrachloride (Cu:CTAC (1:2)), Structure 4.1. The metallosurfactant powders were prepared and supplied by P. Garg (Department of Chemistry and Centre of Advanced Studies in Chemistry, Panjab University, India).[111] Metallosurfactant powders were dissolved at a 2% w/v loading in liquid monomer and after shaking to dissolve, the mixtures were loaded into a sealable glass delivery tube. This precursor mixture was then degassed using several freeze–pump–thaw cycles. Substrates used for antibacterial testing were pieces of non-woven polypropylene sheet (0.11 mm thickness, 22.7 ± 1.1 μm fibre diameter, Spunbound, 70 g m^{-2}, Avoca Technical Ltd, UK). These pieces were washed prior to coating by soaking in absolute ethanol (+99.8 wt %, Fisher Scientific UK Ltd.) for 15 min and then dried under vacuum in order to make sure they were sterile and clean. Uncoated control samples were washed in the same way. At least 4 different batches of each type of coated sample, as well as the control uncoated non-woven polypropylene sheet, were tested for antimicrobial activity. Silicon (100) wafers (0.014–0.024 Ω cm resistivity, Silicon Valley Microelectronics Inc.) were also placed at the edges of the polypropylene sheet pieces to allow for thickness measurements, sessile drop contact angle analysis, and infrared spectroscopy analysis. These were cleaned prior to coating by sonication in a 1:1 v/v propan-2-ol (+99.5 wt%, Fisher Scientific Ltd.) / cyclohexane (+99.5%, Fisher Scientific Ltd.) mixture, followed by UV/ozone treatment (model UV.TC.EU.003, BioForce Nanosciences Inc.), and a final sonication step in the propan-2-ol / cyclohexane mixture. After air drying, substrates were placed downstream in line-of-sight from the ASPD atomiser, Figure 4.1.

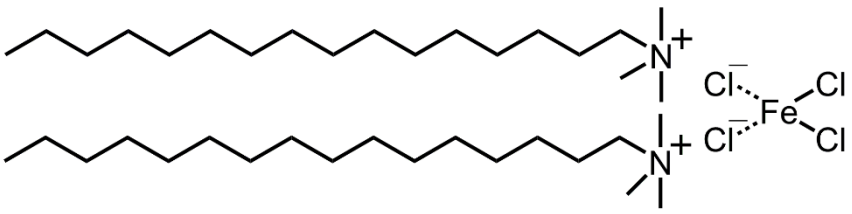

Bishexadecyltrimethyl ammonium iron (II) tetrachloride (Fe:CTAC)

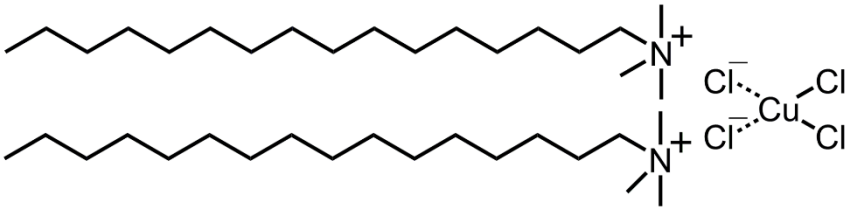

Bishexadecyltrimethyl ammonium copper (II) tetrachloride (Cu:CTAC)

Structure 4.1: Metallosurfactant structures

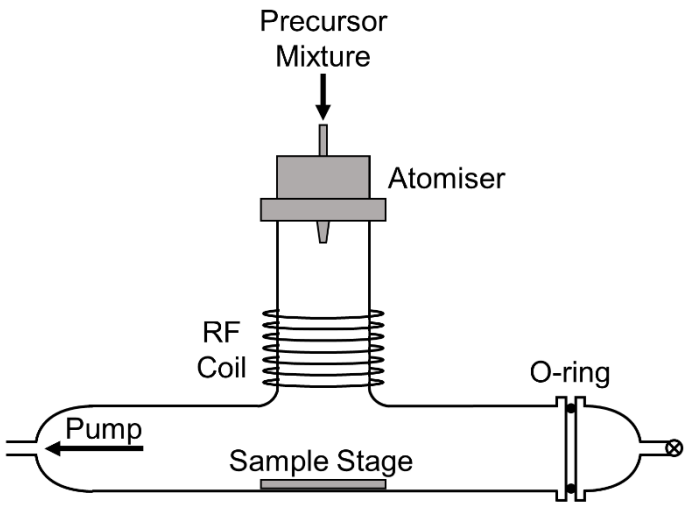

Figure 4.1: Atomised spray plasma deposition (ASPD) chamber.[112]

Atomised spray plasma deposition (ASPD) was carried out in an electrodeless, cylindrical, T-shape glass reactor (volume 1195 cm^3, base pressure less than $3x10^{-3}$ mbar, and a leak rate better than $2x10^{-9}$ mol s^{-1}) enclosed in a Faraday cage.[113] The chamber was pumped by a 30 L min^{-1} two-stage rotary pump (model E2M2, Edwards Vacuum Ltd.) attached to a liquid nitrogen cold trap, and the system pressure monitored by a thermocouple gauge. An L–C impedance matching network was used

to minimise the standing wave ratio for power transmitted from a 13.56 MHz radio frequency (RF) power supply to a copper coil (4 mm diameter, 7 turns, spanning 5.5 cm). The copper coil was located 12.5 cm downstream from the atomiser nozzle (20 µm diameter median droplet size, model No. 8700-120, Sono-Tek Corp.[114,115]), which was driven by a broadband ultrasonic generator (120 kHz, model No. 06-05108, Sono-Tek Corp.). Prior to each coating deposition, the chamber was scrubbed with detergent, rinsed with propan-2-ol and acetone (+99%, Fisher Scientific Ltd.), and oven dried. Next, a continuous wave air plasma was ignited for 30 min at 0.2 mbar pressure and 50 W power in order to remove any remaining trace contaminants from the chamber walls. Ambient temperature deposition was carried out using a 50 W continuous wave plasma in conjunction with atomisation of the precursor into the reaction chamber employing an optimised flow rate of $8 \pm 1 \times 10^{-4}$ mL s^{-1}. Upon plasma extinction, the atomiser was switched off and the system was evacuated to base pressure, followed by venting to atmosphere.

4.2.2 Scanning Electron Microscopy

Electron micrographs of ASPD coated non-woven polypropylene sheet pieces were acquired as described in Section 3.2.4 (page 72). A working distance of 14–21 mm was used. SEM cross-section analysis was also performed on ASPD coated silicon wafer substrates to determine film thickness. For SEM cross-section analysis, coated silicon wafer substrates were fractured following freezing in liquid nitrogen, and then mounted onto carbon disks supported on 45° tilt aluminium stubs.

4.2.3 Infrared Spectroscopy

Fourier transform infrared (FTIR) analysis was carried out using an FTIR spectrometer (model Spectrum One, Perkin Elmer Inc.) equipped with a liquid nitrogen cooled mercury cadmium telluride (MCT) detector. The spectra were averaged over 285 scans at a resolution of 4 cm^{-1} across the 450–4000 cm^{-1} range. Reflection–absorption infrared spectroscopy (RAIRS) of ASPD nanocomposite layer coated silicon wafers was performed using a variable angle reflection–absorption accessory (Specac Ltd.) fitted with mirrors aligned at an angle of 66° to the substrate normal (sampling depth of 0.5–20 µm for RAIRS[116]). Attenuated–total–reflection (ATR) spectra of 2-hydroxyethyl methacrylate, Cu:CTAC, Fe:CTAC, and ASPD nanocomposite layer coated non-woven polypropylene sheet were obtained using a

single reflection type II-a diamond brazed into tungsten carbide accessory (model Golden Gate, Specac Ltd.).

4.2.4 Sessile Drop Contact Angle

Sessile drop contact angle analysis was carried out on coated silicon wafer substrates with a video capture system in combination with a motorised syringe (VCA2500XE, AST Products Inc.). 1 µL droplets of ultrahigh-purity water (BS 3978 grade 1) were dispensed for water contact angle measurements. Following dispensation of the probe liquid onto the coated substrate, a snapshot of the image was taken using the Hauppange WinTV software and analysed using the ImageJ software (using the Low Bond Axisymmetric Drop Shape Analysis plugin). The water contact angle (WCA) was observed not to vary with time.

4.2.5 Antibacterial Activity

For antibacterial testing, the non-woven polypropylene sheet samples were cut into pieces of 0.5 cm x 0.5 cm size. Gram-negative *Escherichia coli* BW25113 (CGSC 7636; *rrnB3* Δ*lacZ4787 hsdR514* Δ(*araBAD*)*567* Δ(*rhaBAD)568 rph-1*) and Gram-positive *Staphylococcus aureus* (FDA209P, an MSSA strain; ATCC 6538P) bacterial cultures were prepared as described in Section 3.2.7 (page 73).

Sterile 96 well plates (Sarstedt AG) were loaded with the uncoated, ASPD 2-hydroxyethyl methacrylate or ASPD 2-hydroxyethyl methacrylate–metallosurfactant coated non-woven polypropylene sheet. Next, 10 µL of the prepared bacteria solution was placed onto each sheet (so that the microorganisms could interact with the surface), and left to incubate (Bacterial Incubator 250, LMS Ltd) at 30 °C for 16 h. Next, autoclaved Luria-Bertani broth media (90 µL) was pipetted into each well and mixed with the bacteria on the sample surface to recover the bacteria as a 10-fold dilution (10^{-1}). Further ten-fold serial dilutions were performed to give 10^{-2}, 10^{-3}, 10^{-4}, 10^{-5} and 10^{-6} samples. Colony-forming unit (CFU) plate counting was performed as described in Section 3.2.7 (page 73).

4.3 Results

4.3.1 Deposition Rate

The optimal atomised spray plasma deposition (ASPD) rate for the 2-hydroxyethyl methacrylate precursor was measured to be 749 ± 293 nm min^{-1} at a liquid flow rate of 8 ± 1 x10^{-4} mL s^{-1}, Table 4.1. This film growth rate is an order of magnitude greater than that reported for conventional vapour phase plasma deposition of 2-hydroxyethyl methacrylate (13.4 nm min^{-1} for pulsed plasma deposition, 30 nm min^{-1} for continuous wave plasma deposition)[117] and can be attributed to the higher precursor flow rate which results from the atomisation of liquid droplets.[109] The optimal atomised spray plasma deposition rate for the 2-hydroxyethyl methacrylate–metallosurfactant nanocomposites was measured to be 2507 ± 604 nm min^{-1} and 3019 ± 888 nm min^{-1} for Fe:CTAC and Cu:CTAC, respectively.

Table 4.1: Thickness measurements made by SEM cross-section analysis of ASPD coated silicon wafer substrates. Error bars denote the sample standard deviation.

Coating	**Thickness / µm**	**Deposition Rate / nm min^{-1}**
ASPD 2-hydroxyethyl methacrylate	5.6 ± 3.2	749 ± 293
ASPD 2-hydroxyethyl methacrylate–2% Fe:CTAC	22.3 ± 5.0	2507 ± 604
ASPD 2-hydroxyethyl methacrylate–2% Cu:CTAC	29.4 ± 8.1	3019 ± 888

4.3.2 Scanning Electron Microscopy

Scanning electron microscopy (SEM) showed that in the absence of metallosurfactant, the ASPD poly(2-hydroxyethyl methacrylate) coatings exhibited a smooth appearance, Figure 4.2. The untreated non-woven polypropylene cloth was shown to have a very similar appearance. The incorporation of metallosurfactants into the poly(2-hydroxyethyl methacrylate) coating enhances the surface roughness for both Fe:CTAC and Cu:CTAC systems. There is no obvious difference in surface roughness between the Fe:CTAC and Cu:CTAC coatings. The overall structure of the cloth is not altered due to the coating, only the fibres are coated, Figure 4.3.

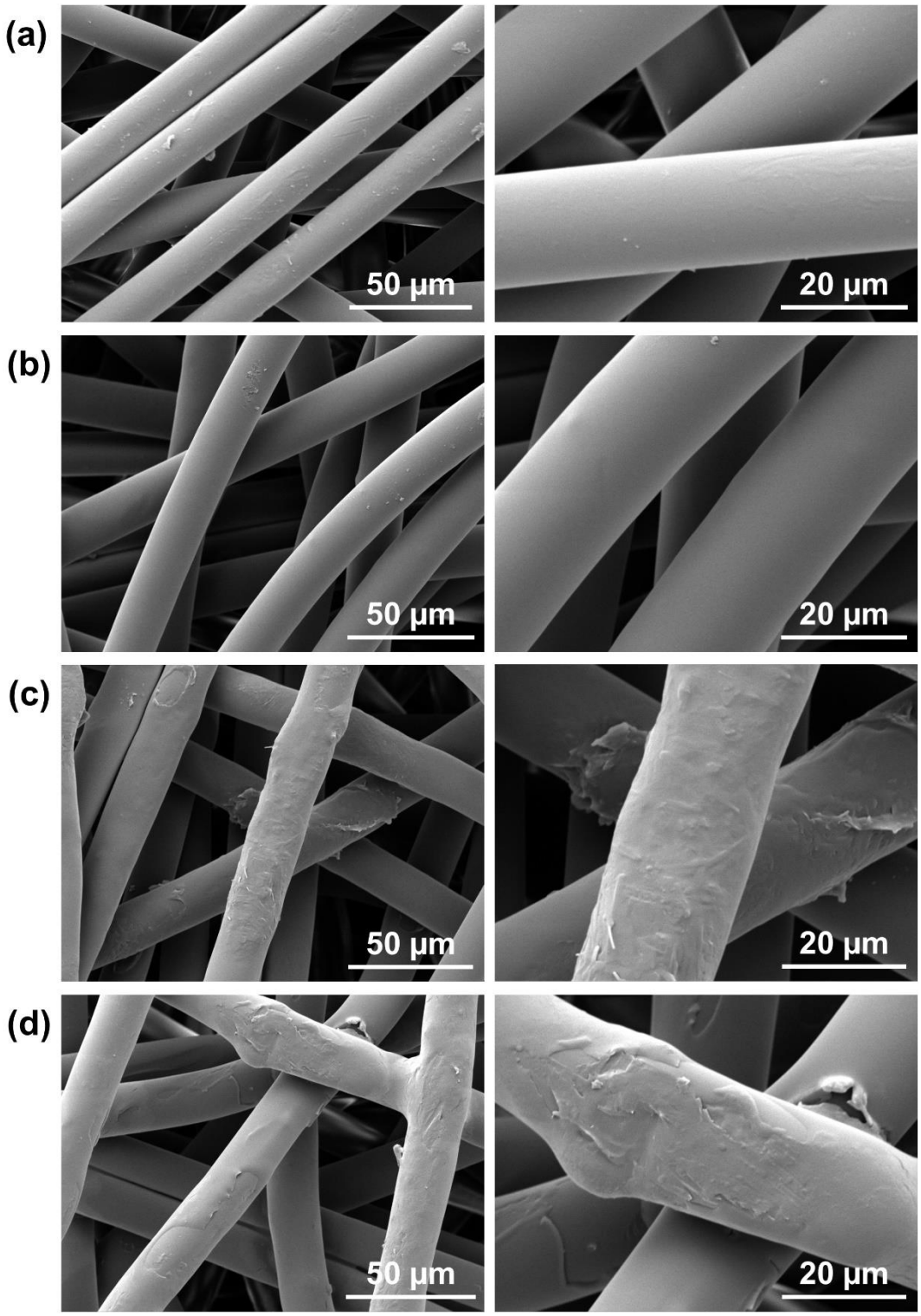

Figure 4.2: SEM micrographs of non-woven polypropylene cloth: (a) untreated; (b) ASPD poly(2-hydroxyethyl methacrylate); (c) ASPD 2-hydroxyethyl methacrylate–2% w/v Fe:CTAC; (d) ASPD 2-hydroxyethyl methacrylate–2% w/v Cu:CTAC.

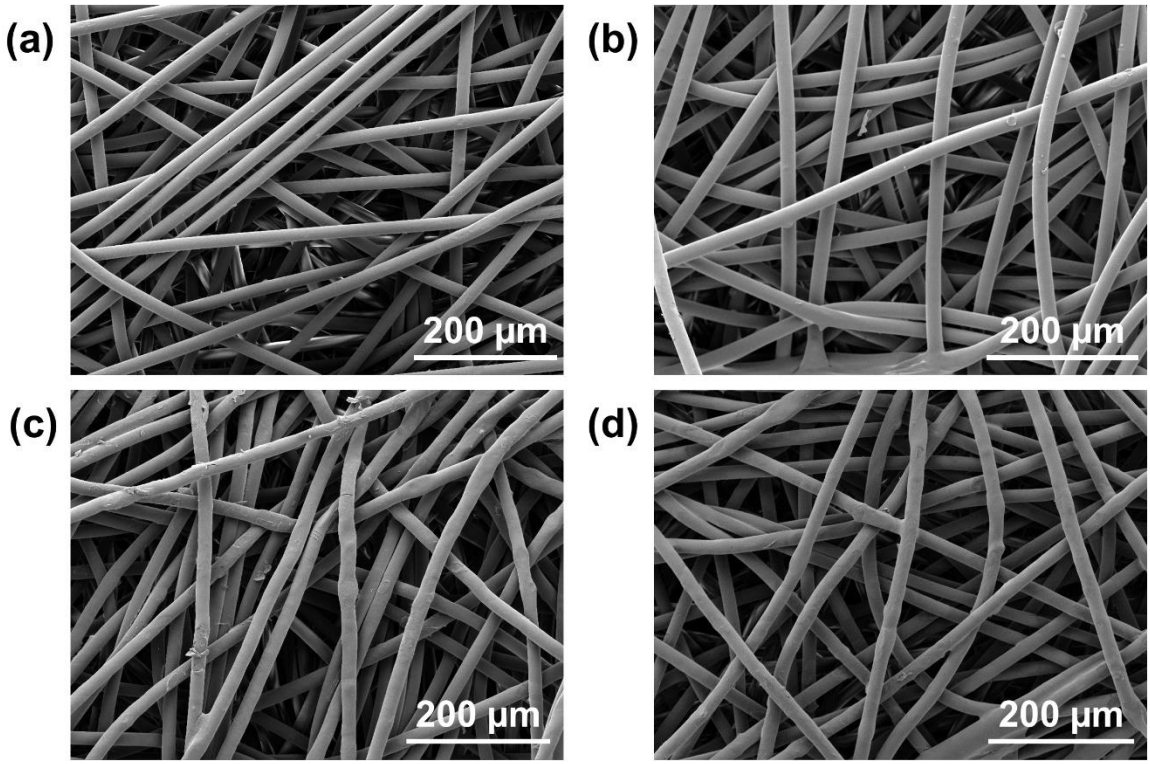

Figure 4.3: SEM micrographs of non-woven polypropylene cloth: (a) untreated; (b) ASPD poly(2-hydroxyethyl methacrylate); (c) ASPD 2-hydroxyethyl methacrylate–2% w/v Fe:CTAC; (d) ASPD 2-hydroxyethyl methacrylate–2% w/v Cu:CTAC.

4.3.3 Infrared Spectroscopy

Infrared spectroscopy showed high levels of structural retention for the ASPD poly(2-hydroxyethyl methacrylate) layers on silicon wafer pieces, Figure 4.4 and Table 4.2. Characteristic poly(2-hydroxyethyl methacrylate) absorbances include: O–H stretching (3400 cm^{-1}), antisymmetric CH_3 stretching (2949 cm^{-1}), symmetric CH_3 stretching (2883 cm^{-1}), C=O stretching (1727 cm^{-1}), and C–H stretching (1455 cm^{-1}).[109,117,118] Disappearance of the peaks due to the C=C bond associated with the precursor molecule confirmed polymerisation via the 2-hydroxyethyl methacrylate C=C group during ASPD: $=CH_2$ twisting (815 cm^{-1}), $=CH_2$ wagging (942 cm^{-1}), and C=C stretching (1637 cm^{-1}).[118,119] These peaks are replaced by a peak at 750 cm^{-1} attributed to $–CH_2–$ twisting.[109] Similar results were obtained when coated on non-woven polypropylene cloth substrate, Figure 4.5.

The infrared spectra of the ASPD 2-hydroxyethyl methacrylate–2% w/v Fe:CTAC and ASPD 2-hydroxyethyl methacrylate–2% w/v Cu:CTAC layers showed similar characteristic poly(2-hydroxyethyl methacrylate) absorbances, Figure 4.4 and

Table 4.2. Metallosurfactant incorporation into the layers is evident due to the appearance of an absorption band at 2851 cm^{-1} (Fe:CTAC containing layer) and 2852 cm^{-1} (Cu:CTAC containing layer) associated with symmetric CH_2 stretching of metallosurfactant alkyl chains, Figure 4.6. In addition, absorbance bands are also now observed at 2921 cm^{-1} (Fe:CTAC containing layer) and 2924 cm^{-1} (Cu:CTAC containing layer) attributed to antisymmetric CH_2 stretching of metallosurfactant alkyl chains, Figure 4.6. The weaker $–CH_2–$ rocking and twisting absorbances associated with the metallosurfactant precursors are not observed in the ASPD layers—this is probably due to the low (2% w/v) metallosurfactant concentration in the 2-hydroxyethyl methacrylate precursor mixture.

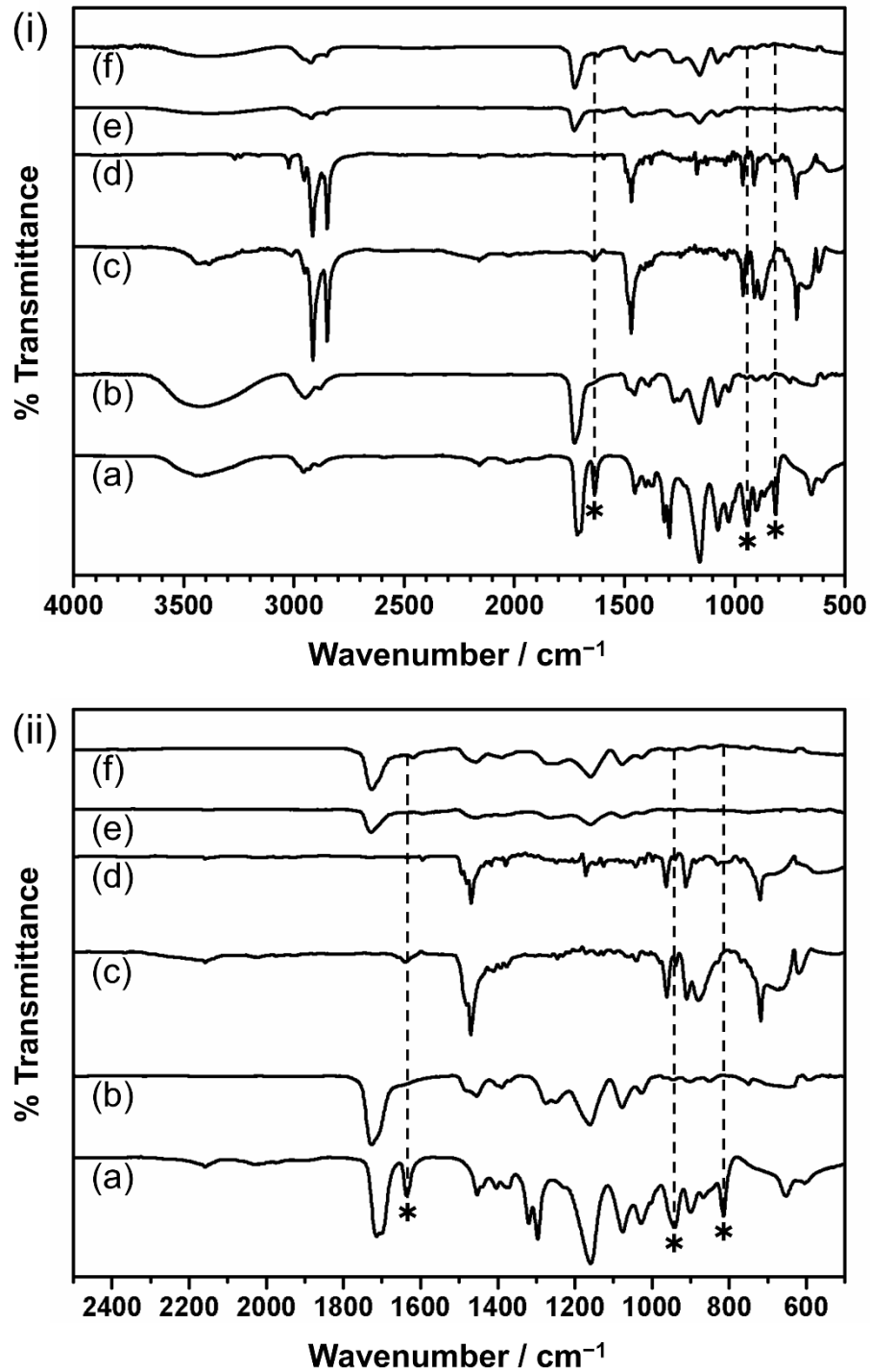

Figure 4.4: Infrared spectra: (a) ATR 2-hydroxyethyl methacrylate liquid precursor; (b) RAIRS ASPD 2-hydroxyethyl methacrylate polymer layer on silicon substrate; (c) ATR Fe:CTAC solid precursor; (d) ATR Cu:CTAC solid precursor; (e) RAIRS ASPD 2-hydroxyethyl methacrylate–2% w/v Fe:CTAC layer on silicon substrate; and (f) RAIRS ASPD 2-hydroxyethyl methacrylate–2% w/v Cu:CTAC layer on silicon substrate across (i) 500–4000 cm^{-1} and (ii) 500–2500 cm^{-1} range. ✱ denotes absorbances associated with the polymerisable C=C double bond contained in the 2-hydroxyethyl methacrylate precursor. [Infrared spectroscopy data acquired by I. Castañeda-Montes].

Table 4.2: Infrared assignments for ASPD 2-hydroxyethyl methacrylate–metallosurfactant nanocomposite layers on silicon wafer substrates.

Assignment	Absorption Frequency / cm^{-1}					
	2-Hydroxyethyl methacrylate monomer	**Fe:CTAC solid**	**Cu:CTAC solid**	**ASPD 2-hydroxyethyl methacrylate**	**ASPD HEMA–2% Fe:CTAC**	**ASPD HEMA–2% Cu:CTAC**
O–H stretching	3400	–	–	3400	3400	3400
Antisymmetric CH_3 stretching	2957	2952	2953	2949	2956	2955
Antisymmetric CH_2 stretching	2931	2914	2915	–	2921	2924
Symmetric CH_3 stretching	2887	2872	2868	2883	2875	2877
Symmetric CH_2 stretching	–	2849	2849	–	2851	2852
C=O stretching	1714	–	–	1727	1729	1726
C=C stretching	1637	–	–	–	–	–
C–H stretching	1454	1470	1469	1455	1456	1456
$–CH_2–$ rocking	–	962	963	–	–	–
$=CH_2$ wagging	942	–	–	–	–	–
$=CH_2$ twisting	815	–	–	–	–	–
$–CH_2–$ twisting	–	718	720	750	749	750

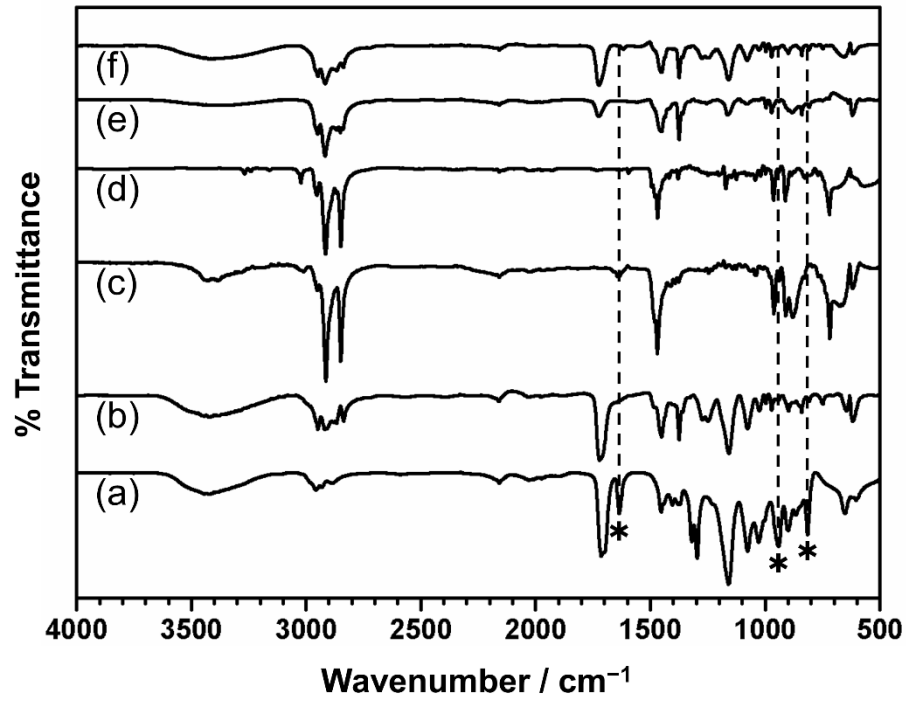

Figure 4.5: Infrared spectra: (a) ATR 2-hydroxyethyl methacrylate liquid precursor; (b) ATR ASPD 2-hydroxyethyl methacrylate polymer layer on cloth substrate; (c) ATR Fe:CTAC solid precursor; (d) ATR Cu:CTAC solid precursor; (e) ATR ASPD 2-hydroxyethyl methacrylate–2% w/v Fe:CTAC layer on cloth substrate; and (f) ATR ASPD 2-hydroxyethyl methacrylate–2% w/v Cu:CTAC layer on cloth substrate. ∗ denotes absorbances associated with the polymerisable C=C double bond contained in the 2-hydroxyethyl methacrylate precursor. [Infrared spectroscopy data acquired by I. Castañeda-Montes].

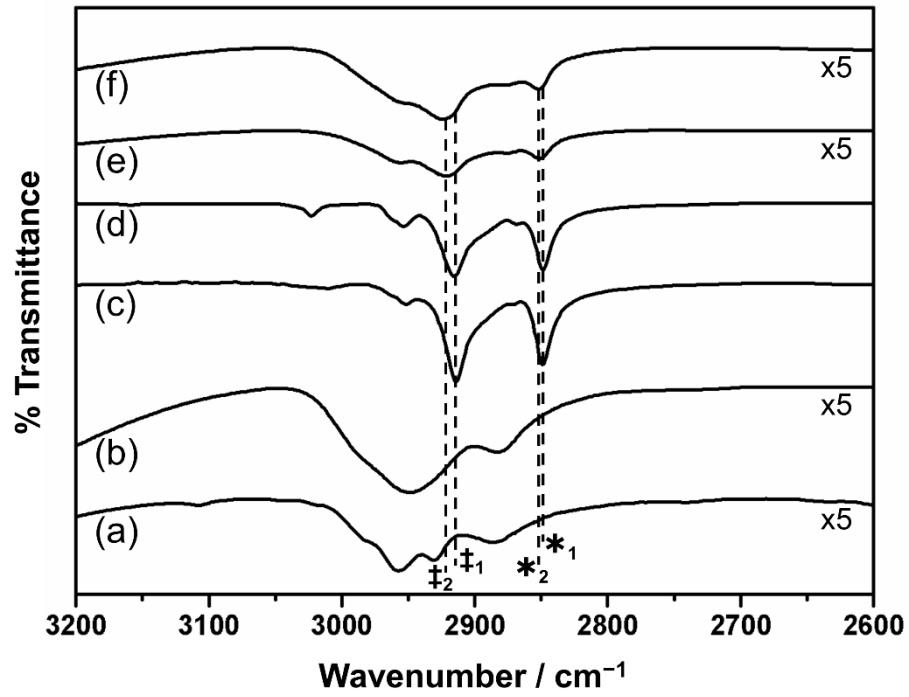

Figure 4.6: Infrared spectra: (a) ATR 2-hydroxyethyl methacrylate liquid precursor (x5 magnification); (b) RAIRS ASPD 2-hydroxyethyl methacrylate polymer layer on silicon substrate (x5 magnification); (c) ATR Fe:CTAC solid precursor; (d) ATR Cu:CTAC solid precursor; (e) RAIRS ASPD 2-hydroxyethyl methacrylate–2% w/v Fe:CTAC layer on silicon substrate (x5 magnification); and (f) RAIRS ASPD 2-hydroxyethyl methacrylate–2% w/v Cu:CTAC layer on silicon substrate (x5 magnification). $*_1$ and $*_2$ denote symmetric CH_2 stretching absorbances associated with the metallosurfactant precursors and ASPD 2-hydroxyethyl methacrylate–2% w/v metallosurfactant layers, respectively. $‡_1$ and $‡_2$ denote antisymmetric CH_2 stretching absorbances associated with the metallosurfactant precursors and ASPD 2-hydroxyethyl methacrylate–2% w/v metallosurfactant layers, respectively. [Infrared spectroscopy data acquired by I. Castañeda-Montes].

4.3.4 Sessile Drop Contact Angle

Static water contact angle measurements of ASPD 2-hydroxyethyl methacrylate on silicon wafer showed hydrophilic behaviour with a water contact angle (WCA) of 51 ± 3°, Figure 4.7. This is in line with previous reports for the WCA of poly(2-hydroxyethyl methacrylate) films[120,121,122] or for a poly(2-hydroxyethyl methacrylate) membrane[123]. Incorporation of metallosurfactant into the coating resulted in even more hydrophilic surfaces with WCA = 32 ± 5° and 30 ± 4° for ASPD 2-hydroxyethyl methacrylate–2% w/v Fe:CTAC and ASPD 2-hydroxyethyl methacrylate–2% w/v Cu:CTAC surfaces, respectively. This increase in hydrophilicity (decrease in WCA) upon incorporation of metallosurfactant is partly due to the added surface roughness as observed in the scanning electron microscopy images. The roughness however does not completely

explain the drop in contact angle from 51 ± 3° to 32 ± 5° and 30 ± 4° upon incorporation of Fe:CTAC and Cu:CTAC respectively because this would result in a Wenzel roughness factor (Equation 2.2) of 1.35–1.38 suggesting an approximately 35–38% increase in surface area. The scanning electron microscopy images do not show such a large increase in surface area and so the increase in hydrophilicity must also be due to a change in surface chemistry upon incorporation of metallosurfactant.

The difference in WCA between the metallosurfactant-containing coatings and the ASPD 2-hydroxyethyl methacrylate coating provides further evidence for the incorporation of the metallosurfactants into the coatings in addition to the evidence provided by scanning electron microscopy (added surface roughness) and infrared spectroscopy (appearance of metallosurfactant symmetric and antisymmetric CH_2 stretching absorbances). Furthermore, the samples are visually different in colour. The ASPD 2-hydroxyethyl methacrylate coatings appear colourless in colour whereas the ASPD 2-hydroxyethyl methacrylate–2% w/v Fe:CTAC and ASPD 2-hydroxyethyl methacrylate–2% w/v Cu:CTAC layers are orange and yellow in colour, respectively. These colours match the colour of the parent metallosurfactant powder.[111]

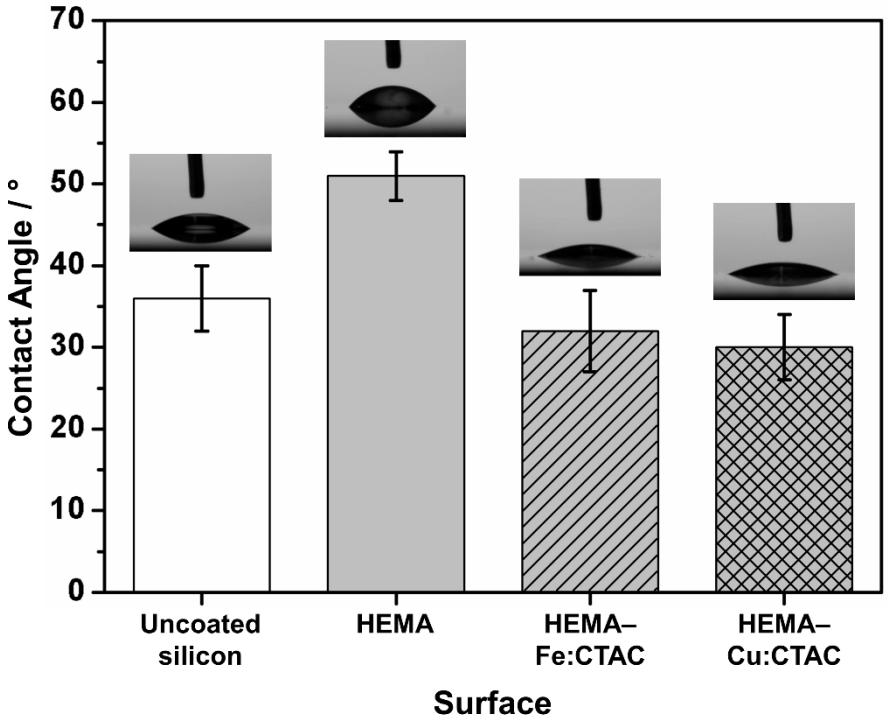

Figure 4.7: Water contact angle (WCA) for ASPD 2-hydroxyethyl methacrylate and ASPD 2-hydroxyethyl methacrylate–metallosurfactant (2% w/v metallosurfactant loading) nanocomposite layers on silicon wafer substrates. 2-hydroxyethyl methacrylate is abbreviated as HEMA. Error bars denote the sample standard deviation.

4.3.5 Antibacterial Activity

ASPD 2-hydroxyethyl methacrylate–2% w/v Fe:CTAC and ASPD 2-hydroxyethyl methacrylate–2% w/v Cu:CTAC coated non-woven polypropylene sheets displayed high antibacterial activity against both the *E. coli* (Gram-negative) and *S. aureus* (Gram-positive) bacterial species tested. Both metallosurfactant-containing coatings reduced the number of both *E. coli* and *S. aureus* bacteria to zero at 10^{-1} dilution (n = 4), Figure 4.8. Control untreated non-woven polypropylene sheet displayed *E. coli* and *S. aureus* bacterial counts of 4.20 ± 1.47 x 10^9 CFU mL^{-1} at 10^{-6} dilution (n = 7, standard deviation error) and 2.93 ± 0.81 x 10^9 CFU mL^{-1} at 10^{-6} dilution (n = 3, standard deviation error) respectively, confirming a lack of antibacterial activity for the polypropylene substrate used. Testing of ASPD 2-hydroxyethyl methacrylate coated non-woven polypropylene sheet also confirmed an absence of antibacterial activity for the poly(2-hydroxyethyl methacrylate) polymer with this control showing *E. coli* and *S. aureus* bacterial counts of 3.88 ± 0.62 x 10^9 CFU mL^{-1} at 10^{-6} dilution (n = 4, standard deviation error) and 9.63 ± 3.30 x 10^8 CFU mL^{-1} at 10^{-5} dilution (n = 3, standard deviation error) respectively. A Student's T-test analysis of the results indicates that there is no statistically significant difference between the untreated non-woven polypropylene sheet and ASPD 2-hydroxyethyl methacrylate coated non-woven polypropylene sheet with respect to *E. coli* ($t(9) = 0.5$, $p = 0.69$) but that there is a significant statistical difference between the results when tested against *S. aureus* ($t(4) = 3.9$, $p = 0.017$).

ASPD 2-hydroxyethyl methacrylate–Fe:CTAC and ASPD 2-hydroxyethyl methacrylate–Cu:CTAC coated non-woven polypropylene sheets containing a lower concentration of metallosurfactant (1% w/v concentration) were not found to be as effective against *E. coli*, Figure 4.9. They did however still show signs of some antibacterial activity when compared with the controls, with *E. coli* displaying a greater sensitivity towards the Cu:CTAC coating at this lower metallosurfactant concentration. A Student's T-test analysis of the results indicates that there is a significant statistical difference between the untreated non-woven polypropylene sheet and ASPD 2-hydroxyethyl methacrylate coated non-woven polypropylene sheet ($t(5) = 3.5$, $p = 0.028$). The same analysis also confirms that there is a significant statistical difference between the results of the ASPD 2-hydroxyethyl methacrylate coated non-woven

polypropylene sheet and the ASPD 2-hydroxyethyl methacrylate–1% w/v Fe:CTAC coated non-woven polypropylene sheet ($t(5) = 2.7$, $p = 0.027$).

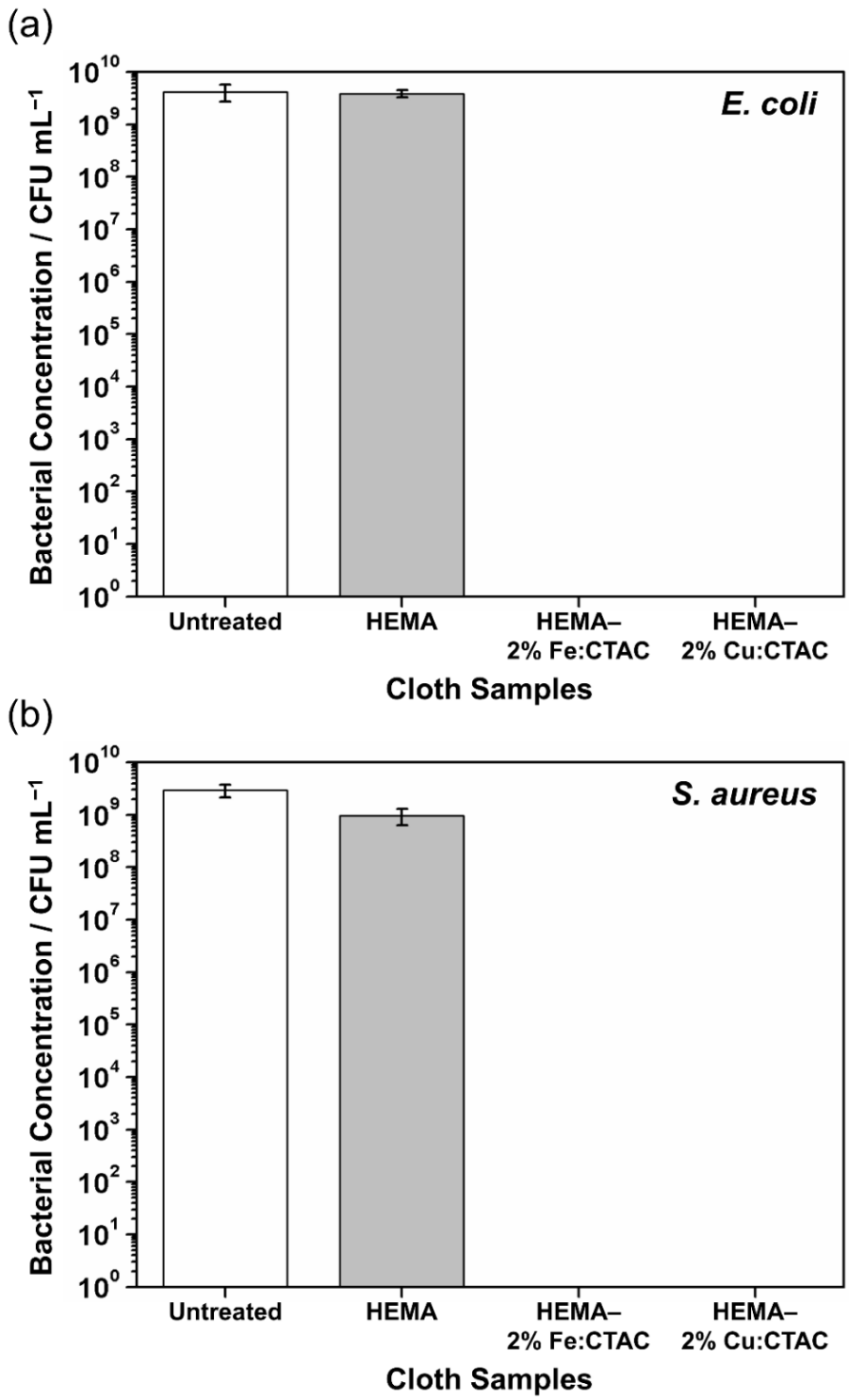

Figure 4.8: Antibacterial activity against (a) *E. coli* (Gram-negative) and (b) *S. aureus* (Gram-positive) bacteria of untreated non-woven polypropylene sheet control; ASPD 2-hydroxyethyl methacrylate coated non-woven polypropylene sheet; ASPD 2-hydroxyethyl methacrylate–2% w/v Fe:CTAC coated non-woven polypropylene sheet; and ASPD 2-hydroxyethyl methacrylate–2% w/v Cu:CTAC coated non-woven polypropylene sheet. ASPD coatings containing metallosurfactant killed all bacteria (bacterial concentration = 0 CFU mL^{-1}). Reported values are averaged over at least 4 different values with standard deviation error. [Antibacterial testing performed by S. N. Barrientos-Palomo and Dr G. J. Sharples].

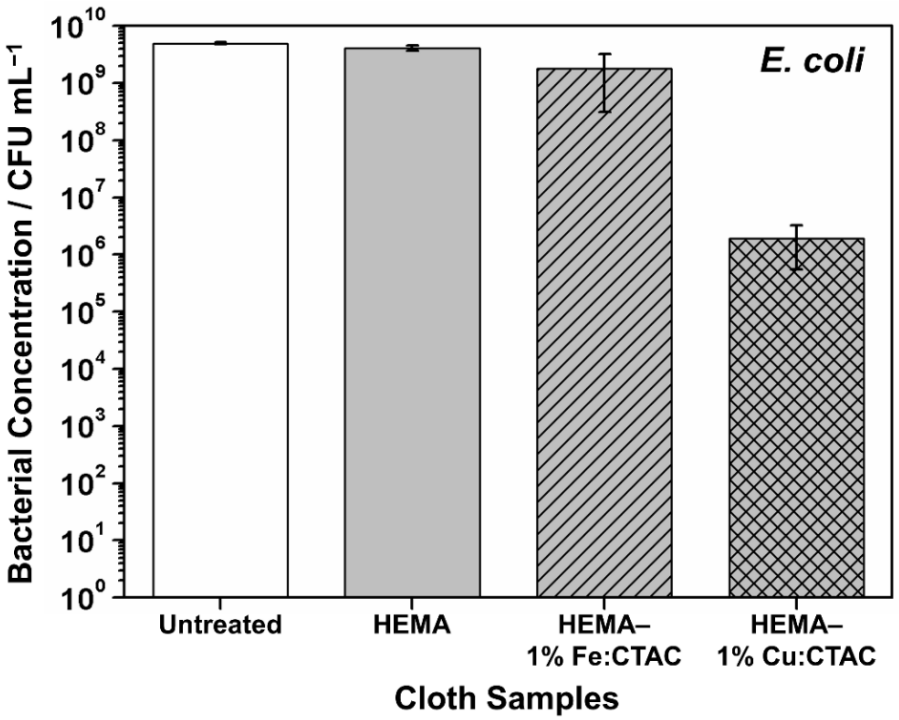

Figure 4.9: Antibacterial activity against *E. coli* (Gram-negative) bacteria of untreated non-woven polypropylene sheet control; ASPD 2-hydroxyethyl methacrylate coated non-woven polypropylene sheet; ASPD 2-hydroxyethyl methacrylate–1% w/v Fe:CTAC coated non-woven polypropylene sheet; and ASPD 2-hydroxyethyl methacrylate–1% w/v Cu:CTAC coated non-woven polypropylene sheet. Reported values are averaged over at least 3 different values with standard deviation error. [Antibacterial testing performed by P. Garg, S. N. Barrientos-Palomo, and Dr G. J. Sharples].

Reducing the number of both *E. coli* and *S. aureus* bacteria to zero at 10^{-1} dilution results in both ASPD 2-hydroxyethyl methacrylate–2% w/v Fe:CTAC and ASPD 2-hydroxyethyl methacrylate–2% w/v Cu:CTAC coatings having a Log Kill^{124} = 9.6 ± 0.1 (>>99.99%), Figure 4.10. Even at the lower metallosurfactant concentration of 1% w/v, the ASPD coating containing Cu:CTAC shows good antibacterial activity with Log Kill = 3.4 ± 0.2 (99.96%) against *E. coli*, Figure 4.10. At this lower 1% w/v concentration, the Fe:CTAC coating only has a Log Kill = 0.5 ± 0.5 (64.52%) against *E. coli*. Control ASPD 2-hydroxyethyl methacrylate coated non-woven polypropylene sheet has a Log Kill = 0.03 ± 0.10 (6.67%) against *E. coli*.

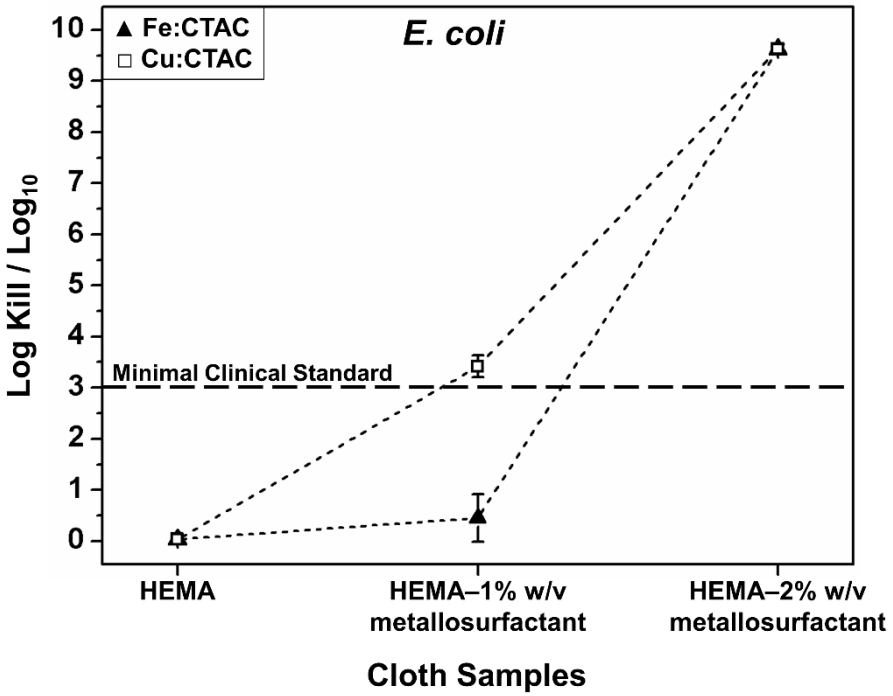

Figure 4.10: Log kill (reduction) against *E. coli* (Gram-negative) bacteria of ASPD 2-hydroxyethyl methacrylate coated non-woven polypropylene sheet; ASPD 2-hydroxyethyl methacrylate–Fe:CTAC coated non-woven polypropylene sheet; and ASPD 2-hydroxyethyl methacrylate–Cu:CTAC coated non-woven polypropylene sheet. Reported values are averaged over at least 3 different values with standard deviation error. Dashed line (long dashes) indicates the minimal clinical standard of Log Kill rate (Log Kill > 3) set by the Clinical and Laboratory Standards Institute (CLSI).[125] [Antibacterial testing performed by P. Garg, S. N. Barrientos-Palomo, and Dr G. J. Sharples].

4.4 Discussion

Atomised spray plasma deposition (ASPD) provides a single-step, low temperature, solventless approach for the preparation of functional coatings.[109,110] Metallosurfactants bishexadecyltrimethyl ammonium iron(II) tetrachloride (Fe:CTAC) and bishexadecyltrimethyl ammonium copper(II) tetrachloride (Cu:CTAC) have been dissolved into 2-hydroxyethyl methacrylate precursor and through ASPD, polymer–metallosurfactant nanocomposite coatings have been prepared for the first time. Scanning electron microscopy (SEM) confirmed incorporation of metallosurfactants into coatings by revealing an added surface roughness upon addition of metallosurfactant compared to smooth metallosurfactant-free coatings, Figure 4.2. Infrared spectroscopy provided further evidence of metallosurfactant incorporation into the ASPD layers due to the appearance of metallosurfactant symmetric and antisymmetric CH_2 stretching absorbances, Figure 4.6 and Table 4.2. Furthermore, a

lower water contact angle for the metallosurfactant containing coatings also confirmed their incorporation, with this increase in hydrophilicity being attributed to the impact of surface roughening upon the Wenzel[126] state of wetting, Figure 4.7. The hydrophilicity of the ASPD 2-hydroxyethyl methacrylate layers is also thought to add anti-fouling properties to the coating as poly(2-hydroxyethyl methacrylate) surfaces have previously been shown to resist bacterial adhesion.[127] As a result, the coatings reported here could be described as being dual-function antibacterial surfaces: bacteria-repelling and biocide-releasing.[128]

The antibacterial activity of metallosurfactants has been shown in solution for many different combinations of metal and surfactant.[75,80,81,83,84,85,88,89,94,95] The polymer–metallosurfactant nanocomposite coated cloths in the present study display high levels of antibacterial activity against both Gram-negative *E. coli* and Gram-positive *S. aureus*, Figure 4.8. For both Fe:CTAC and Cu:CTAC metallosurfactants, a 2% w/v metallosurfactant loading in 2-hydroxyethyl methacrylate precursor yielded a Log Kill = 9.6 ± 0.1 (>>99.99%) against both *E. coli* and *S. aureus*, which greatly exceeds the level of bacterial killing required to meet the minimal clinical standard (Log Kill > 3 [99.9%]) according to the guidelines of the Clinical Laboratory Standards Institute (CLSI)[125], Figure 4.10. Although less active at the lower metallosurfactant concentration of 1% w/v, the ASPD 2-hydroxyethyl methacrylate–Cu:CTAC coating also exceeds the Log Kill > 3 criterion with Log Kill = 3.4 ± 0.2 (99.96%), Figure 4.10. It is surprising that the coatings containing 1% w/v metallosurfactant are do not show higher antibacterial activity given that the minimum inhibitory concentration (MIC) of a similar metallosurfactant (Ag:CTAB) is 0.5 mg mL^{-1}.[82] This MIC is however tested against different strains of *E. coli* and *S. aureus* than the strains used in this work and so it is possible that the bacterial strains used in this work are less susceptible towards metallosurfactants, or that the Cu:CTAC and Fe:CTAC metallosurfactants used in this work are less potent than Ag:CTAB.

Another possible reason for the lack of potency of the 1% w/v coatings, as well as an explanation for the large difference in effectiveness between the 1% w/v and the 2% w/v coatings, could be the release kinetics of the metallosurfactant from the coating. It has previously been shown that antibiotic species initially release from poly(2-hydroxyethyl methacrylate) as a burst followed by slower release.[129] It has also been shown that higher loading concentrations result in higher concentrations of

antibiotic being released from poly(2-hydroxyethyl methacrylate) coatings after a fixed period of time.[130] This suggests that species release from poly(2-hydroxyethyl methacrylate) coatings under first order release kinetics. Therefore, during the 16 h of incubation as part of the antibacterial testing, a greater concentration of metallosurfactant will have been released from the coatings containing 2% w/v compared to the 1% w/v coatings. If the amount of metallosurfactant released after 16 h by the 1% w/v coatings is less than the MIC, but for the 2% w/v coatings this is greater than the MIC, this would explain the large difference in antibacterial activity and the reduced antibacterial activity of the 1% w/v coatings.

Non-ionic metallosurfactants where the metal forms part of the head group are known have antibacterial activity due to bacterial cell wall penetration as a result of their high hydrophobicity[86,90,101] which arises due to the long surfactant alkyl chains and which is further increased upon chelation.[100] An increase in hydrophobicity results in an increased lipophilicity of the overall complex which increases its ability to permeate through the lipid layers of bacteria.[102] Ionic metallosurfactants where a metal ion forms part of the counter ion to the surfactant also kill bacterial due to alkyl chain penetration of the bacterial cell wall[87] with lipophilicity, and hence permeation ability, again being increased upon complexation.[97,103] The adsorption tendency of the surfactants towards the bacterial cellular membrane is also increased as a result of metal complexation.[96] These ionic complexes do however also have additional ways of interacting with and destroying the bacteria. One is through the electrostatic interaction between the positively charged metal ions and the head group of the surfactant molecules with the negatively charged bacterial cells[77,78,87] which disrupts the integrity of the cell membrane leading to leakage of cellular content.[131] Further to that, due to the ionic nature of these metallosurfactants, there is the potential for release of highly potent metal ions[77,78,97] which adds another mechanism of attack due to the generation of reactive oxygen species which can result in oxidative damage of the bacterial membrane.[132] These additional interactions with the bacteria help to explain why, for the same surfactant alkyl chain length, ionic metallosurfactants have been shown to have a much greater antibacterial activity compared to non-ionic metallosurfactants.[77,78] Furthermore, this accounts for the high antibacterial activity observed in the present study which utilises ionic metallosurfactants consisting of highly potent Cu(II)[133] and Fe(II)[134] ions and long hydrophobic surfactant alkyl chains

(CTAC) as part of a double-chain metallosurfactant system (double-chain systems are more hydrophobic than single-chain[104]).

TEM analysis of a double chain Ag:CTAB metallosurfactant to determine the mechanism of action against *E. coli* and *S. aureus* bacteria proved that the metallosurfactants initially come into contact with the bacterial cell wall before penetrating inside resulting in cell death.[82] In the case of Gram-negative *E. coli*, cell penetration occurs after perturbation of the membrane which removes the flagella present on the surface of *E. coli* damaging the outer wall.[82] For Gram-positive *S. aureus*, contact between bacteria and metallosurfactant results in separation of plasma membrane from the cell wall allowing penetration of the metallosurfactant.[82] The mechanism of bacterial killing of the Cu:CTAC and Fe:CTAC metallosurfactants used in this work is thought to be the same due to the similar nature of the metallosurfactants used. Therefore, the antibacterial activity of the ASPD 2-hydroxyethyl methacrylate–metallosurfactant cloths reported here is thought to be due to the leaching of metallosurfactant from the polymer nanocomposite allowing the metallosurfactants to then penetrate and kill the bacteria using the three modes of attack discussed above: electrostatic disruption of outer cell membrane, physical disruption of cell membrane due to surfactant alkyl chains, and metal ion release into bacteria.

In this present study, it has been observed that at 1% w/v loading of metallosurfactant in 2-hydroxyethyl methacrylate precursor, Gram-negative *E. coli* is more susceptible to killing by coatings containing Cu:CTAC compared to those containing Fe:CTAC, Figure 4.9. Such higher antibacterial activity for a copper-containing[105] metallosurfactant compared to one containing iron[76] has been shown in the past using hexadecylpyridinium chloride as the surfactant. This increased activity for copper over iron is thought to be due to several reasons. Firstly, the higher electronegativity[135] of copper (1.90) compared to iron (1.83) results in a lower electron density on the CTAC surfactant in Cu:CTAC compared to Fe:CTAC.[99] Therefore the Cu:CTAC complex is more hydrophobic than Fe:CTAC and hence can permeate the bacterial cell wall membrane more easily.[99] Moreover, the larger ionic size of copper results in a greater effective area of the metallosurfactant on the cell membrane resulting in greater antibacterial activity.[98] Finally, copper ions are more potent than iron ions and so if discharge of metal ions plays a role in the bacterial killing

mechanism then this greater activity of copper ions results in a greater overall activity of the copper containing metallosurfactant.[136]

4.5 Conclusions

Highly antibacterial polymer–metallosurfactant nanocomposite coatings have been prepared in a single-step using atomised spray plasma deposition (ASPD). The fabricated nanocomposite coatings on non-woven polypropylene cloth show high antibacterial activity against both Gram-negative *Escherichia coli* (Log Kill > 9) and Gram-positive *Staphylococcus aureus* (Log Kill > 9) bacteria. This single-step approach offers a solventless, low-temperature method for conformally coating any substrate with highly antibacterial coatings. The simplicity of this approach makes it a promising route for biomedical applications.

4.6 References

[1] Percival, S. L.; Suleman, L.; Vuotto, C.; Donelli, G. Healthcare-Associated Infections, Medical Devices and Biofilms: Risk, Tolerance and Control. *J. Med. Microbiol.* **2015**, *64*, 323–334.

[2] Arciola, C. R.; Campoccia, D.; Speziale, P.; Montanaro, L.; Costerton, J. W. Biofilm Formation in *Staphylococcus* Implant Infections. A Review of Molecular Mechanisms and Implications for Biofilm-Resistant Materials. *Biomaterials* **2012**, *33*, 5967–5982.

[3] Page, K.; Wilson, M.; Parkin, I. P. Antimicrobial Surfaces and Their Potential in Reducing the Role of the Inanimate Environment in the Incidence of Hospital-Acquired Infections. *J. Mater. Chem.* **2009**, *19*, 3819–3831.

[4] Römling, U.; Balsalobre, C. Biofilm Infections, Their Resilience to Therapy and Innovative Treatment Strategies. *J. Intern. Med.* **2012**, *272*, 541–561.

[5] Glinel, K.; Thebault, P.; Humblot, V.; Pradier, C. M.; Jouenne, T. Antibacterial Surfaces Developed from Bio-Inspired Approaches. *Acta Biomater.* **2012**, *8*, 1670–1684.

[6] Banerjee, I.; Pangule, R. C.; Kane, R. S. Antifouling Coatings: Recent Developments in the Design of Surfaces That Prevent Fouling by Proteins, Bacteria, and Marine Organisms. *Adv. Mater.* **2011**, *23*, 690–718.

[7] Siedenbiedel, F.; Tiller, J. C. Antimicrobial Polymers in Solution and on Surfaces: Overview and Functional Principles. *Polymers* **2012**, *4*, 46–71.

[8] Wei, T.; Tang, Z.; Yu, Q.; Chen, H. Smart Antibacterial Surfaces with Switchable Bacteria-Killing and Bacteria-Releasing Capabilities. *ACS Appl. Mater. Interfaces* **2017**, *9*, 37511–37523.

[9] Cloutier, M.; Mantovani, D.; Rosei, F. Antibacterial Coatings: Challenges, Perspectives, and Opportunities. *Trends Biotechnol.* **2015**, *33*, 637–652.

[10] Agarwal, A.; Weis, T. L.; Schurr, M. J.; Faith, N. G.; Czuprynski, C. J.; McAnulty, J. F.; Murphy, C. J.; Abbott, N. L. Surfaces Modified with Nanometer-Thick Silver-Impregnated Polymeric Films that Kill Bacteria but Support Growth of Mammalian Cells. *Biomaterials* **2010**, *31*, 680–690.

[11] Grunlan, J. C.; Choi, J. K.; Lin, A. Antimicrobial Behavior of Polyelectrolyte Multilayer Films Containing Cetrimide and Silver. *Biomacromolecules* **2005**, *6*, 1149–1153.

[12] Chuang, H. F.; Smith, R. C.; Hammond, P. T. Polyelectrolyte Multilayers for Tunable Release of Antibiotics. *Biomacromolecules* **2008**, *9*, 1660–1668.

[13] Zhuk, I.; Jariwala, F.; Attygalle, A. B.; Wu, Y.; Libera, M. R.; Sukhishvili, S. A. Self-Defensive Layer-by-Layer Films with Bacteria-Triggered Antibiotic Release. *ACS Nano* **2014**, *8*, 7733–7745.

[14] Kanmani, P.; Rhim, J.-W. Physicochemical Properties of Gelatin/Silver Nanoparticle Antimicrobial Composite Films. *Food Chem.* **2014**, *148*, 162–169.

[15] Chung, R.-J.; Hsieh, M.-F.; Huang, C.-W.; Perng, L.-H.; Wen, H.-W.; Chin, T.-S. Antimicrobial Effects and Human Gingival Biocompatibility of Hydroxyapatite Sol–Gel Coatings. *J. Biomed. Mater. Res. B Appl. Biomater.* **2006**, *76*, 169–178.

[16] Ye, J.; He, J.; Wang, C.; Yao, K.; Gou, Z. Copper-Containing Mesoporous Bioactive Glass Coatings on Orbital Implants for Improving Drug Delivery Capacity and Antibacterial Activity. *Biotechnol. Lett.* **2014**, *36*, 961–968.

[17] Cometa, S.; Iatta, R.; Ricci, M. A.; Ferretti, C.; De Giglio, E. Analytical Characterization and Antimicrobial Properties of Novel Copper Nanoparticle–Loaded Electrosynthesized Hydrogel Coatings. *J. Bioact. Compat. Polym.* **2013**, *28*, 508–522.

[18] De Giglio, E.; Cafagna, D.; Cometa, S.; Allegretta, A.; Pedico, A.; Giannossa, L. C.; Sabbatini, L.; Mattioli-Belmonte, M.; Iatta, R. An Innovative, Easily Fabricated, Silver Nanoparticle-Based Titanium Implant Coating: Development and Analytical Characterization. *Anal. Bioanal. Chem.* **2013**, *405*, 805–816.

[19] Zan, X.; Kozlov, M.; McCarthy, T. J.; Su, Z. Covalently Attached, Silver-Doped Poly(vinyl alcohol) Hydrogel Films on Poly(L-lactic acid). *Biomacromolecules* **2010**, *11*, 1082–1088.

[20] Ho, C. H.; Tobis, J.; Sprich, C.; Thomann, R.; Tiller, J. C. Nanoseparated Polymeric Networks with Multiple Antimicrobial Properties. *Adv. Mater.* **2004**, *16*, 957–961.

[21] Noda, I.; Miyaji, F.; Ando, Y.; Miyamoto, H.; Shimazaki, T.; Yonekura, Y.; Miyazaki, M.; Mawatari, M.; Hotokebuchi, T. Development of Novel Thermal Sprayed Antibacterial Coating and Evaluation of Release Properties of Silver Ions. *J. Biomed. Mater. Res., Part B* **2008**, *89B*, 456–465.

[22] Ozkan, E.; Crick, C. C.; Taylor, A.; Allan, E.; Parkin, I. P. Copper-Based Water Repellent and Antibacterial Coatings by Aerosol Assisted Chemical Vapour Deposition. *Chem. Sci.* **2016**, *7*, 5126–5131.

[23] Dacarro, G.; Cucca, L.; Grisoli, P.; Pallavicini, P.; Patrini, M.; Taglietti, A. Monolayers of Polyethilenimine on Flat Glass: A Versatile Platform for Cations Coordination and Nanoparticles Grafting in the Preparation of Antibacterial Surfaces. *Dalton Trans.* **2012**, *41*, 2456–2463.

[24] Vasilev, K.; Griesser, S. S.; Griesser, H. J. Antibacterial Surfaces and Coatings Produced by Plasma Techniques. *Plasma Process. Polym.* **2011**, *8*, 1010–1023.

[25] Kratochvíl, J.; Kuzminova, A.; Kylián, O. State-of-the-Art, and Perspectives of, Silver/Plasma Polymer Antibacterial Nanocomposites. *Antibiotics* **2018**, *7*, 78.

[26] Vasilev, K.; Sah, V.; Anselme, K.; Ndi, C.; Mateescu, M.; Dollmann, B.; Martinek, P.; Ys, H.; Ploux, L.; Griesser, H. J. Tunable Antibacterial Coatings That Support Mammalian Cell Growth. *Nano Lett.* **2010**, *10*, 202–207.

[27] Kumar, V.; Jolivalt, C.; Pulpytel, J.; Jafari, R.; Arefi-Khonsari, F. Development of Silver Nanoparticle Loaded Antibacterial Polymer Mesh using Plasma Polymerization Process. *J. Biomed. Mater. Res.* **2013**, *101A*, 1121–1132.

[28] Deng, X.; Nikiforov, A. Y.; Coenye, T.; Cools, P.; Aziz, G.; Morent, R.; De Geyter, N.; Leys, C. Antimicrobial Nano-Silver Non-Woven Polyethylene Terephthalate Fabric via an Atmospheric Pressure Plasma Deposition Process. *Sci. Rep.* **2015**, *5*, 10138.

[29] Deng, X.; Nikiforov, A.; Vujosevic, D.; Vuksanovic, V.; Mugoša, B.; Cvelbar, U.; De Geyter, N.; Morent, R.; Leys, C. Antibacterial Activity of Nano-Silver Non-Woven Fabric Prepared by Atmospheric Pressure Plasma Deposition. *Mater. Lett.* **2015**, *149*, 95–99.

[30] Kulaga, E.; Ploux, L.; Roucoules, V. Effect of Ageing and Sterilization on Plasma Multilayer System. *Polym. Degrad. Stab.* **2015**, *116*, 1–13.

[31] Jiang, H.; Manolache, S.; Wong, A. C. L.; Denes, F. S. Plasma-Enhanced Deposition of Silver Nanoparticles onto Polymer and Metal Surfaces for the Generation of Antimicrobial Characteristics. *J. Appl. Polym. Sci.* **2004**, *93*, 1411–1422.

[32] Fahmy, A.; Friedrich, J.; Poncin-Epaillard, F.; Debarnot, D. Plasma Polymerized Allyl Alcohol/O_2 Thin Films Embedded with Silver Nanoparticles. *Thin Solid Films* **2016**, *616*, 339–347.

[33] Lotz, A.; Heller, M.; Dohm, N.; Cierniak, P.; Bender, K.; Jansen, B.; Förch, R. Antimicrobial Efficacy and Optimized Cell Adhesion from Defined Plasma Polymerised Multilayer Structures Involving Zn Acetylacetonate and Allylamine. *J. Mater. Chem.* **2012**, *22*, 19455–19461.

[34] Kwok, C. S.; Horbett, T. A.; Ratner, B. D. Design of Infection-Resistant Antibiotic-Releasing Polymers II. Controlled Release of Antibiotics Through a Plasma-Deposited Thin Film Barrier. *J. Controlled Release* **1999**, *62*, 301–311.

[35] Simovic, S.; Losic, D.; Vasilev, K. Controlled Drug Release from Porous Materials by Plasma Polymer Deposition. *Chem. Commun.* **2010**, *46*, 1317–1319.

[36] Kratochvíl, J.; Kahoun, D.; Štěrba, J.; Langhansová, H.; Lieskovská, J.; Fojtíková, P.; Hanuš, J.; Kousal, J.; Kylián, O.; Straňák, V. Plasma Polymerized C:H:N:O Thin Films for Controlled Release of Antibiotic Substances. *Plasma Process. Polym.* **2018**, *15*, 1700160.

[37] Guillemot, G.; Despax, B.; Raynaud, P.; Zanna, S.; Marcus, P.; Schmitz, P.; Mercier-Bonin, M. Plasma Deposition of Silver Nanoparticles onto Stainless Steel for the Prevention of Fungal Biofilms: A Case Study on *Saccharomyces cerevisiae*. *Plasma Process. Polym.* **2008**, *5*, 228–238.

[38] Saulou, C.; Despax, B.; Raynaud, P.; Zanna, S.; Seyeux, A.; Marcus, P.; Audinot, J.-N.; Mercier-Bonin, M. Plasma-Mediated Nanosilver-Organosilicon Composite Films Deposited on Stainless Steel: Synthesis, Surface Characterization, and Evaluation of Anti-Adhesive and Anti-Microbial Properties on the Model Yeast *Saacharomyces cerevisiae*. *Plasma Process. Polym.* **2012**, *9*, 324–338.

[39] Allion-Maurer, A.; Saulou-Bérion, C.; Briandet, R.; Zanna, S.; Lebleu, N.; Marcus, P.; Raynaud, P.; Despax, B.; Mercier-Bonin, M. Plasma-Deposited Nanocomposite Polymer-Silver Coating Against *Escherichia coli* and *Staphylococcus aureus*: Antibacterial Properties and Ageing. *Surf. Coat. Technol.* **2015**, *281*, 1–10.

[40] Daniel, A.; Le Pen, C.; Archambeau, C.; Reniers, F. Use of a PECVD–PVD Process for the Deposition of Copper Containing Organosilicon Thin Films on Steel. *Appl. Surf. Sci.* **2009**, *256S*, S82–S85.

[41] Lischer, S.; Körner, E.; Balazs, D. J.; Shen, D.; Wick, P.; Grieder, K.; Haas, D.; Heuberger, M.; Hegemann, D. Antibacterial Burst-Release From Minimal Ag-Containing Plasma Polymer Coatings. *J. R. Soc. Interface* **2011**, *8*, 1019–1030.

[42] Körner, E.; Hanselmann, B.; Cierniak, P.; Hegemann, D. Tailor-Made Silver Release Properties of Silver-Containing Functional Plasma Polymer Coatings Adjusted Through a Macroscopic Kinetics Approach. *Plasma Chem. Plasma Process.* **2012**, *32*, 619–627.

[43] Zaporojtchenko, V.; Podschun, R.; Schürmann, U.; Kulkarni, A.; Faupel, F. Physio-Chemical and Antimicrobial Properties of Co-Sputtered Ag–Au/PTFE Nanocomposite Coatings. *Nanotechnology* **2006**, *17*, 4904–4908.

[44] Chen, W.; Liu, Y.; Courtney, H. S.; Bettenga, M.; Agrawal, C. M.; Bumgardner, J. D.; Ong, J. L. In vitro Anti-Bacterial and Biological Properties of Magnetron Co-Sputtered Silver-Containing Hydroxyapatite Coating. *Biomaterials* **2006**, *27*, 5512–5517.

[45] Spange, S.; Pfuch, A.; Wiegand, C.; Beier, O.; Hipler, U. C.; Grünler, B. Atmospheric Pressure Plasma CVD as a Tool to Functionalise Wound Dressings. *J. Mater. Sci.: Mater. Med.* **2015**, *26*, 76.

[46] Zimmermann, R.; Pfuch, A.; Horn, K.; Weisser, J.; Heft, A.; Röder, M.; Linke, R.; Schnabelrauch, M.; Schimanski, A. An Approach to Create Silver Containing Antibacterial Coatings by Use of Atmospheric Pressure Plasma Chemical Vapour Deposition (APCVD) and Combustion Chemical Vapour Deposition (CCVD) in an Economic Way. *Plasma Process. Polym.* **2011**, *8*, 295–304.

[47] Beier, O.; Pfuch, A.; Horn, K.; Weisser, J.; Schnabelrauch, M.; Schimanski, A. Low Temperature Deposition of Antibacterially Active Silicon Oxide Layers Containing Silver Nanoparticles, Prepared by Atmospheric Pressure Plasma Chemical Vapor Deposition. *Plasma Process. Polym.* **2013**, *10*, 77–87.

[48] Gerullis, S.; Pfuch, A.; Spange, S.; Kettner, F.; Plaschkies, K.; Küzün, B.; Kosmachev, P. V.; Volokitin, G. G.; Grünler, B. Thin Antimicrobial Silver, Copper, or Zinc Containing SiO_x Films on Wood Polymer Composites (WPC) Applied by Atmospheric Pressure Plasma Chemical Vapour Deposition (APCVD) and Sol–Gel Technology. *Eur. J. Wood Prod.* **2018**, *76*, 229–241.

[49] Liguori, A.; Traldi, E.; Toccaceli, E.; Laurita, R.; Pollicino, A.; Focarete, M. L.; Colombo, V.; Gherardi, M. Co-Deposition of Plasma-Polymerized Polyacrylic Acid and Silver Nanoparticles for the Production of Nanocomposite Coatings Using a Non-Equilibrium Atmospheric Plasma Jet. *Plasma Process. Polym.* **2016**, *13*, 623–632.

[50] Deng, X.; Leys, C.; Vujosevic, D.; Vuksanovic, V.; Cvelbar, U.; De Geyter, N.; Morent, R.; Nikiforov, A. Engineering of Composite Organosilicon Thin Films with Embedded Silver Nanoparticles via Atmospheric Pressure Plasma Process for Antibacterial Activity. *Plasma Process. Polym.* **2014**, *11*, 921–930.

[51] Roy, M.; Fielding, G. A.; Beyenal, H.; Bandyopadhyay, A.; Bose, S. Mechanical, In vitro Antimicrobial, and Biological Properties of Plasma-Sprayed Silver-Doped Hydroxyapatite Coating. *ACS Appl. Mater. Interfaces* **2012**, *4*, 1341–1349.

[52] AshaRani, P. V.; Mun, G. L. K.; Hande, M. P.; Valiyaveettil, S. Cytotoxicity and Genotoxicity of Silver Nanoparticles in Human Cells. *ACS Nano* **2009**, *3*, 279–290.

[53] Sun, J.; Wang, S.; Zhao, D.; Hun, F. H.; Weng, L.; Liu, H. Cytotoxicity, Permeability, and Inflammation of Metal Oxide Nanoparticles in Human Cardiac Microvascular Endothelial Cells. *Cell Biol. Toxicol.* **2011**, *27*, 333–342.

[54] Mijnendonckx, K.; Leys, N.; Mahillon, J.; Silver, S.; Van Houdt, R. Antimicrobial Silver: Uses, Toxicity and Potential for Resistance. *Biometals* **2013**, *26*, 609–621.

[55] Høiby, N.; Bjarnsholt, T.; Givskov, M.; Molin, S.; Ciofu, O. Antibiotic Resistance of Bacterial Biofilms. *Int. J. Antimicrob. Agents* **2010**, *35*, 322–332.

[56] Griffiths, P. C.; Fallis, I. A.; Chuenpratoom, T.; Watanesk, R. Metallosurfactants: Interfaces and Micelles. *Adv. Colloid Interface Sci.* **2006**, *122*, 107–117.

[57] Veeralakshmi, S.; Nehru, S.; Sabapathi, G.; Arunachalam, S.; Venuvanalingam, P.; Kumar, P.; Anusha, C.; Ravikumar, V. Single and Double Chain Surfactant–Cobalt(III) Complexes: The Impact of Hydrophobicity on the Interaction with Calf Thymus DNA, and their Biological Activities. *RSC Adv.* **2015**, *5*, 31746–31758.

[58] Marin-Garcia, M.; Benseny-Cases, N.; Camacho, M.; Perrie, Y.; Suades, J.; Barnadas-Rodriguez, R. Metallosomes for Biomedical Applications by Mixing Molybdenum Carbonyl Metallosurfactants and Phospholipids. *Dalton Trans.* **2018**, *47*, 14293–14303.

[59] Dong, R.; Hao, J. Reverse Vesicles of Ferrum Laurate Metallosurfactant in Non-Aqueous Solution Dried to Produce Solid Shells. *ChemPhysChem* **2012**, *13*, 3794–3797.

[60] Parera, E.; Marin-Garcia, M.; Pons, R.; Comelles, F.; Suades, J.; Barnadas-Rodriguez, R. Supramolecular Arrangement of Molybdenum Carbonyl Metallosurfactants with CO-Releasing Properties. *Organometallics* **2016**, *35*, 484–493.

[61] Garg, P.; Kaur, G.; Chaudhary, G. R. Transition Metal Based Single Chained Surfactants: Synthesis, Aggregation Behavior and Enhanced Photoluminescence Properties of Fluorescein. *RSC Adv.* **2016**, *6*, 108573–108582.

[62] Garg, P.; Kaur, G.; Chaudhary, G. R. Chromium-Based Metallosurfactants: Synthesis, Physicochemical Characterization and Probing of Their Interactions with Xanthene Dyes. *New J. Chem.* **2018**, *42*, 1141–1150.

[63] Kaur, G.; Garg, P.; Chaudhary, G. R. Role of Manganese-Based Surfactant Towards Solubilization and Photophysical Properties of Fluorescein. *RSC Adv.* **2016**, *6*, 7066–7077.

[64] Garg, P.; Kaur, G.; Chaudhary, G. R.; Gawali, S. L.; Hassan, P. A. Structural and SAXS Analysis of Protein Folding/Unfolding with Cationic Single Chain Metallosurfactants. *J. Mol. Liq.* **2018**, *271*, 157–165.

[65] Kaur, B.; Chaudhary, G. R.; Kaur, G. Cholesterol-Induced Physicochemical Changes in Dodecylamine-Based Metallosomes: Drug Entrapping Ability and Interactions with Biological Molecules. *J. Mater. Chem. B* **2019**, *7*, 3679–3691.

[66] Riyasdeen, A.; Senthilkumar, R.; Periasamy, V. S.; Preethy, P.; Srinag, S.; Zeeshan, M.; Krishnamurthy, H.; Arunachalam, S.; Akbarsha, M. A. Antiproliferative and Apoptosis-Induction Studies of a Metallosurfactant in Human Breast Cancer Cell MCF-7. *RSC Adv.* **2014**, *4*, 49953–49959.

[67] Gong, P.; Chen, Z.; Chen, Y.; Wang, W.; Wang, X.; Hu, A. High-Relaxivity MRI Contrast Agents Prepared From Miniemulsion Polymerization Using Gadolinium(III)-Based Metallosurfactants. *Chem. Commun.* **2011**, *47*, 4240–4242.

[68] Mauro, M.; De Paoli, G.; Otter, M.; Donghi, D.; D'Alfonso, G.; De Cola, L. Aggregation Induced Colour Change for Phosphorescent Iridium(III) Complex-Based Anionic Surfactants. *Dalton Trans.* **2011**, *40*, 12106–12116.

[69] Amos, K. E.; Brooks, N. J.; King, N. C.; Xie, S.; Canales-Vázquez, J.; Danks, M. J.; Jervis, H. B.; Zhou, W.; Seddon, J. M.; Bruce, D. W. A Systematic Study of the Formation of Mesostructured Silica using Surfactant Ruthenium Complexes in High- and Low-Concentration Regimes. *J. Mater. Chem.* **2008**, *18*, 5282–5292.

[70] Kaur, G.; Dogra, V.; Kumar, R.; Kumar, S.; Bhanjana, G.; Dilbaghi, N.; Singhal, N. K. DNA Interaction, Anti-Proliferative Effect of Copper Oxide Nanocolloids Prepared from Metallosurfactant Based Microemulsions Acting as Precursor, Template and Reducing Agent. *Int. J. Pharm.* **2018**, *535*, 95–105.

[71] Kaur, N.; Kaur, G.; Bhalla, A.; Dhau, J. S.; Chaudhary, G. R. Metallosurfactant Based Pd–Ni Alloy Nanoparticles as a Proficient Catalyst in the Mizoroki Heck Coupling Reaction. *Green Chem.* **2018**, *20*, 1506–1514.

[72] Yagyu, T.; Tonami, M.; Tsuchimoto, K.; Takahashi, C.; Jitsukawa, K. Preparation of Palladium(II) Complexes with Long Alkyl Chain Ligand Incorporated in Micelle. *Inorg. Chim. Acta.* **2012**, *392*, 428–432.

[73] Kagalwala, H. N.; Chirdon, D. N.; Mills, I. N.; Budwal, N.; Bernhard, S. Light-Driven Hydrogen Generation from Microemulsions Using Metallosurfactant Catalysts and Oxalic Acid. *Inorg. Chem.* **2017**, *56*, 10162–10171.

[74] Schattschneider, C.; Kettenmann, S. D.; Hinojosa, S.; Heinrich, J.; Kulak, N. Biological Activity of Amphiphilic Metal Complexes. *Coord. Chem. Rev.* **2019**, *385*, 191–207.

[75] Kaur, G.; Garg, P.; Kaur, B.; Chaudhary, G. R.; Kumar, S.; Dilbaghi, N.; Hassan, P. A.; Aswal, V. K. Synthesis, Thermal and Surface Activity of Cationic Single Chain Metal Hybrid Surfactants and Their Interaction with Microbes and Proteins. *Soft Matter* **2019**, *15*, 2348–2358.

[76] Kaur, G.; Garg, P.; Kaur, B.; Chaudhary, G. R.; Kumar, S.; Dilbaghi, N.; Hassan, P. A.; Gawali, S. L. Cationic Double Chained Metallosurfactants: Synthesis, Aggregation, Cytotoxicity, Antimicrobial Activity and Their Impact on the Structure of Bovine Serum Albumin. *Soft Matter* **2018**, *14*, 5306–5318.

[77] Dogra, V.; Kaur, G.; Jindal, S.; Kumar, R.; Kumar, S.; Singhal, N. K. Bactericidal Effects of Metallosurfactants Based Cobalt Oxide/Hydroxide Nanoparticles Against Staphylococcus Aureus. *Sci. Total Environ.* **2019**, *681*, 350–364.

[78] Dogra, V.; Kaur, G.; Kaur, A.; Kumar, R.; Kumar, S. In Vitro Assessment of Antimicrobial and Genotoxic Effect of Metallosurfactant Based Nickel Hydroxide Nanoparticles Against Escherichia Coli and Its Genomic DNA. *Colloid Surface. B* **2018**, *170*, 99–108.

[79] Sharma, N. K.; Singh, M. New Class of Platinum Based Metallosurfactant: Synthesis, Micellization, Surface, Thermal Modelling and in vitro Biological Properties. *J. Mol. Liq.* **2018**, *268*, 55–65.

[80] Srinivasan, S.; Annaraj, J.; Athappan, P. R. Spectral and Redox Studies on Mixed Ligand Complexes of Cobalt(III) Phenanthroline/bipyridyl and Benzoylhydrazones, their DNA Binding and Antimicrobial Activity. *J. Inorg. Biochem.* **2005**, *99*, 876–882.

[81] Kaur, G.; Singh, P.; Mehta, S. K.; Kumar, S.; Dilbaghi, N.; Chaudhary, G. R. A Facile Route for the Synthesis of Co, Ni and Cu Metallic Nanoparticles with Potential Antimicrobial Activity Using Novel Metallosurfactants. *Appl. Surf. Sci.* **2017**, *404*, 254–262.

[82] Kaur, G.; Kumar, S.; Kant, R.; Bhanjana, G.; Dilbaghi, N.; Guru, S. K.; Bhushan, S.; Jaglan, S. One-Step Synthesis of Silver Metallosurfactant as an Efficient Antibacterial and Anticancer Material. *RSC Adv.* **2016**, *6*, 57084–57097.

[83] Chandar, S. C. N.; Sangeetha, D.; Arumugham, M. N. Synthesis, Structure, CMC values, Thermodynamics of Micellization, Steady-State Photolysis and Biological Activities of Hexadecylamine Cobalt(III) Dimethyl Glyoximato Complexes. *Transition Met. Chem.* **2011**, *36*, 211–216.

[84] Chandar, S. C. N.; Santhakumar, K.; Arumugham, M. N. Metallosurfactant Schiff Base Cobalt(III) Coordination Complexes. Synthesis, Characterization, Determination of CMC Values and Biological Activities. *Transition Met. Chem.* **2009**, *34*, 841–848.

[85] Hafiz, A. A. Crystal Structure of Benzyl Triphenyl Phosphonium Chlorometallate: Some Surface and Biological Properties of Their Metallosurfactant Derivatives. *J. Iran. Chem. Soc.* **2008**, *5*, 106–114.

[86] Kumar, R. S.; Arunachalam, S.; Periasamy, V. S.; Preethy, C. P.; Riyasdeen, A.; Akbarsha, M. A. Surfactant–Cobalt(III) Complexes: Synthesis, Critical Micelle Concentration (CMC) Determination, DNA Binding, Antimicrobial and Cytotoxicity Studies. *J. Inorg. Biochem.* **2009**, *103*, 117–127.

[87] Adawy, A. I.; Knowdiary, M. M. Structure and Biological Behaviors of Some Metallo Cationic Surfactants. *J. Surfact. Deterg.* **2013**, *16*, 709–715.

[88] Chandar, S. C. N.; Sangeetha, D.; Arumugham, M. N. Octadecylamine Cobalt(III) Dimethyl Glyoximato Complexes: Synthesis, Thermodynamics of Micellization, Steady-State Photolysis and Biological Activities. *Transition Met. Chem.* **2014**, *39*, 159–165.

[89] Vignesh, G.; Sugumar, K.; Arunachalam, S.; Vignesh, S.; James, R. A.; Arun, R.; Premkumar, K. Studies on the Synthesis, Characterization, Human Serum Albumin Binding and Biological Activity of Single Chain Surfactant–Cobalt(III) Complexes. *Luminescence* **2016**, *31*, 523–532.

[90] Sasikala, K.; Arunachalam, S. Antimicrobial Activity, Spectral Studies and Micellar Properties of Some Surfactant-Cobalt(III) Complexes. *Chem. Sci. Trans.* **2013**, *2*, S157–S166.

[91] Rodrigues, L.; Banat, I. M.; Teixeira, J.; Oliveira, R. Biosurfactants: Potential Applications in Medicine. *J. Antimicrob. Chemother.* **2006**, *57*, 609–618.

[92] Jennings, M. C.; Minbiole, K. P. C.; Wuest, W. M. Quaternary Ammonium Compounds: An Antimicrobial Mainstay and Platform for Innovation to Address Bacterial Resistance. *ACS Infect. Dis.* **2015**, *1*, 288–303.

[93] Pinazo, A.; Manresa, M. A.; Marques, A. M.; Bustelo, M.; Espuny, M. J.; Pérez, L. Amino Acid–Based Surfactants: New Antimicrobial Agents. *Adv. Colloid Interface Sci.* **2016**, *228*, 17–39.

[94] Kaur, G.; Kumar, S.; Dilbaghi, N.; Kaur, B.; Kant, R.; Guru, S. K.; Bhushan, S.; Jaglan, S. Evaluation of Bishexadecyltrimethyl Ammonium Palladium Tetrachloride Based Dual Functional Colloidal Carrier as an Antimicrobial and Anticancer agent. *Dalton Trans.* **2016**, *45*, 6582–6591.

[95] Chaudhary, G. R.; Singh, P.; Kaur, G.; Mehta, S. K.; Kumar, S.; Dilbaghi, N. Multifaceted Approach for the Fabrication of Metallomicelles and Metallic Nanoparticles Using Solvophobic Bisdodecylaminepalladium (II) Chloride as Precursor. *Inorg. Chem.* **2015**, *54*, 9002–9012.

[96] Negm, N. A.; Zaki, M. F.; Salem, M. A. I. Cationic Schiff Base Amphiphiles and Their Metal Complexes: Surface and Biocidal Activities Against Bacteria and Fungi. *Colloids Surf. B* **2010**, *77*, 96–103.

[97] Tawfik, S. M.; Hefni, H. H. Synthesis and Antimicrobial Activity of Polysaccharide Alginate Derived Cationic Surfactant–Metal(II) Complexes. *Int. J. Biol. Macromol.* **2016**, *82*, 562–572.

[98] Badawi, A. M.; Azzam, E. M. S.; Morsy, S. M. I. Surface and Biocidal Activity of Some Synthesized Metallo Azobenzene Isothiouronium Salts. *Bioorg. Med. Chem.* **2006**, *14*, 8661–8665.

[99] Negm, N. A.; Said, M. M.; Morsy, S. M. I. Pyrazole Derived Cationic Surfactants and Their Tin and Copper Complexes: Synthesis, Surface Activity, Antibacterial and Antifungal Efficacy. *J. Surfact. Deterg.* **2010**, *13*, 521–528.

[100] Abdel-Salam, F. H. Synthesis, Biological Study and Complexation Behavior of Some Anionic Schiff Base Amphiphiles. *J. Surfact. Deterg.* **2010**, *13*, 423–431.

[101] Kumar, R. S.; Arunachalam, S. Synthesis, Micellar Properties, DNA Binding and Antimicrobial Studies of Some Surfactant–Cobalt(III) Complexes. *Biophys. Chem.* **2008**, *136*, 136–144.

[102] Negm, N. A.; Zaki, M. F. Structural and Biological Behaviors of Some Nonionic Schiff-Base Amphiphiles and Their Cu(II) and Fe(III) Metal Complexes. *Colloids Surf. B* **2008**, *64*, 179–183.

[103] Sharma, N. K.; Singh, M. Multifunctional Supramolecular Ionic Metallosurfactants (SMIMSs) for Antimicrobial, Anticancer and Serum Albumins Binding. *J. Mol. Liq.* **2018**, *263*, 463–471.

[104] Veeralakshmi, S.; Nehru, S.; Arunachalam, S.; Kumar, P.; Govindaraju, M. Study of Single and Double Chain Surfactant–Cobalt(III) Complexes and their Hydrophobicity, Micelle Formation, Interaction with Serum Albumins and Antibacterial Activities. *Inorg. Chem. Front.* **2014**, *1*, 393–404.

[105] Kaur, G.; Kumar, S.; Dilbaghi, N.; Bhanjana, G.; Guru, S. K.; Bhushan, S.; Jaglan, S.; Hassan, P. A.; Aswal, V. K. Hybrid Surfactants Decorated with Copper Ions: Aggregation Behavior, Antimicrobial Activity and Anti-Proliferative Effect. *Phys. Chem. Chem. Phys.* **2016**, *18*, 23961–23970.

[106] Fernández-Hernández, J. M.; De Cola, L.; Bolink, H. J.; Clemente-León, M.; Coronado, E.; Forment-Aliaga, A.; López-Muñoz, A.; Repetto, D. White Light-Emitting Electrochemical Cells Based on the Langmuir−Blodgett Technique. *Langmuir* **2014**, *30*, 14021–14029.

[107] Joy, S.; Pal, P.; Mondal, T. K.; Talapatra, G. B.; Goswami, S. Synthesis of Amphiphilic Azo-Anion-Radical Complexes of Chromium(III) and the Development of Ultrathin Redox-Active Surfaces by the Langmuir–Schaefer Technique. *Chem. Eur. J.* **2012**, *18*, 1761–1771.

[108] Gonawala, S.; Leopoldino, V. R.; Kpogo, K.; Verani, C. N. Langmuir–Blodgett Films of Salophen-Based Metallosurfactants as Surface Pretreatment Coatings for Corrosion Mitigation. *Chem. Commun.* **2016**, *52*, 11155–11158.

[109] Wood, T. J.; Ward, L. J.; Badyal, J. P. S. Super-Adhesive Polymer–Silica Nanocomposite Layers. *ACS Appl. Mater. Interfaces* **2013**, *5*, 9678–9683.

[110] Ward, L. J.; Schofield, W. C. E.; Badyal, J. P. S.; Goodwin, A. J.; Merlin, P. J. Atmospheric Pressure Plasma Deposition of Structurally Well-Defined Polyacrylic Acid Films. *Chem. Mater.* **2003**, *15*, 1466–1469.

[111] Garg, P.; Kaur, G.; Chaudhary, G. R.; Kaur, S.; Gawali, S. L.; Hassan, P. A. Investigating the Structural Integrity of Bovine Serum Albumin in Presence of Newly Synthesized Metallosurfactants. *Colloid. Surface. B* **2018**, *164*, 116–124.

[112] Castaneda-Montes, I.; Ritchie, A. W.; Badyal, J. P. S. Atomised Spray Plasma Deposition of Hierarchical Superhydrophobic Nanocomposite Surfaces. *Colloids Surf., A* **2018**, *558*, 192–199.

[113] Ehrlich, C. D.; Basford, J. A. Recommended Practices for the Calibration and Use of Leaks. *J. Vac. Sci. Technol. A*, **1992**, *10*, 1–17.

[114] Berger, H. L.; Mowbray, D. F.; Copeman, R. A.; Russell, R. J. Ultrasonic Atomizing Nozzle and Method. U.S. Patent US 7,712,680 B2, May 11, 2010.

[115] Sono-Tek, http://www.sono-tek.com/drop-size-and-distribution/ (Accessed 15 January 2019).

[116] Chakrabarti, C. L.; Akh, G.; Hutton, J. C. ATR and Reflectance IR Spectroscopy, Applications. *Spectrochim. Acta B* **1999**, *33*, 153–193.

[117] Tarducci, C.; Schofield, W. C. E.; Badyal, J. P. S. Monomolecular Functionalization of Pulsed Plasma Deposited Poly(2-hydroxyethyl methacrylate) Surfaces. *Chem. Mater.* **2002**, *14*, 2541–2545.

[118] Lin-Vien, D.; Colthup, N. B.; Fateley, W. G.; Grasselli, J. G. The Handbook of Infrared and Raman Characteristic Frequencies of Organic Molecules; Academic Press, Inc.: San Diego, 1991.

[119] Wood, T. J.; Brown, P. S.; Badyal, J. P. S. Atomized Spray Plasma Deposition of Structurally Well-Defined Bioactive Coatings. *Plasma Chem. Plasma Process.* **2014**, *34*, 1019–1031.

[120] Xu, C.; Wu, T.; Mei, Y.; Drain, C. M.; Batteas, J. D.; Beers, K. L. Synthesis and Characterisation of Tapered Copolymer Brushes via Surface-Initiated Atom Transfer Radical Copolymerization. *Langmuir* **2005**, *21*, 11136–11140.

[121] Yang, W. J.; Cai, T.; Neoh, K.-G.; Kang, E.-T. Biomimetic Anchors for Antifouling and Antibacterial Polymer Brushes on Stainless Steel. *Langmuir* **2011**, *27*, 7065–7076.

[122] Yano, T.; Yah, W. O.; Yamaguchi, H.; Terayama, Y.; Nishihara, M. Kobayashi, M.; Takahara, A. Precise Control of Surface Physicochemical Properties for Electrospun Fiber Mats by Surface-Initiated Radical Polymerization. *Polym. J.* **2011**, *43*, 838–848.

[123] Bayramoglu, G.; Oktem, H. A.; Arica, M. Y. A Dye–Ligand Immobilized Poly(2-hydroxyethylmethacrylate) Membrane Used for Adsorption and Isolation of Immunoglobulin G. *Biochem. Eng. J.* **2007**, *34*, 147–155.

[124] Hugo, W. B.; Denyer, S. P.; Hodges, N. A.; Gorman, S. P. *Hugo and Russell's Pharmaceutical Microbiology*, 7th ed.; Wiley-Blackwell: Oxford, U.K., 2004.

[125] Harrison, J. J.; Turner, R. J.; Ceri, H. Persister Cells, The Biofilm Matrix and Tolerance to Metal Cations in Biofilm and Planktonic *Pseudomonas aeruginosa*. *Environ. Microbiol.* **2005**, *7*, 981–994.

[126] Wenzel, R. N. Resistance of Solid Surfaces to Wetting by Water. *Ind. Eng. Chem.* **1936**, *28*, 988–994.

[127] Mrabet, B.; Nguyen, M. N.; Majbri, A.; Mahouche, S.; Turmine, M.; Bakhrouf, A.; Chehimi, M. M. Anti-Fouling Poly(2-hydroxyethyl methacrylate) Surface Coatings with Specific Bacteria Recognition Capabilities. *Surf. Sci.* **2009**, *603*, 2422–2429.

[128] Yu, Q.; Wu, Z.; Chen, H. Dual-Function Antibacterial Surfaces for Biomedical Applications. *Acta Biomater.* **2015**, *16*, 1–13.

[129] Anderson, E. M.; Noble, M. L.; Garty, S.; Ma, H.; Bryers, J. D.; Shen, T. T.; Ratner, B. D. Sustained Release of Antibiotic from Poly(2-hydroxyethyl methacrylate) to Prevent Blinding Infections After Cataract Surgery. *Biomaterials* **2009**, *30*, 5675.

[130] De Giglio, E.; Cometa, S.; Ricci, M. A.; Cafagna, D.; Savino, A. M.; Sabbatini, L.; Orciani, M.; Ceci, E.; Novello, L. Tantillo, G. M.; Mattioli-Belmonte, M. Ciprofloxacin-Modified Electrosynthesized Hydrogel Coatings to Prevent Titanium-Implant-Associated Infections. *Acta Biomater.* **2011**, *7*, 882–891.

[131] Gilbert, P.; Moore, L. E. Cationic Antiseptics: Diversity of Action Under a Common Epithet. *J. Appl. Microbiol.* **2005**, *99*, 703–715.

[132] Dutta, R. K.; Nenavathu, B. P.; Gangishetty, M. K.; Reddy, A. V. R. Studies on Antibacterial Activity of ZnO Nanoparticles by ROS Induced Lipid Peroxidation. *Colloids Surf., B* **2012**, *94*, 143–150.

[133] Chatterjee, A. K.; Chakraborty, R.; Basu, T. Mechanism of Antibacterial Activity of Copper Nanoparticles. *Nanotechnology* **2014**, *25*, 135101.

[134] Auffan, M.; Achouak, W.; Rose, J.; Roncato, M.-A.; Chanéac, C.; Waite, D. T.; Masion, A.; Woicik, J. C.; Wiesner, M. R.; Bottero, J.-Y. Relation Between the Redox State of Iron-Based Nanoparticles and Their Cytotoxicity Toward *Escherichia coli*. *Environ. Sci. Technol.* **2008**, *42*, 6730–6735.

[135] Allred, A. L. Electronegativity Values from Thermochemical Data. *J. Inorg. Nucl. Chem.* **1961**, *17*, 215–221.

[136] Agarwala, M.; Choudhury, B.; Yadav, R. N. S. Comparative Study of Antibiofilm Activity of Copper Oxide and Iron Oxide Nanoparticles Against Multidrug Resistant Biofilm Forming Uropathogens. *Indian J. Microbiol.* **2014**, *54*, 365–368.

Chapter 5

Atomised Spray Plasma Deposition of Tunable High Refractive Index Hybrid and Nanocomposite Coatings

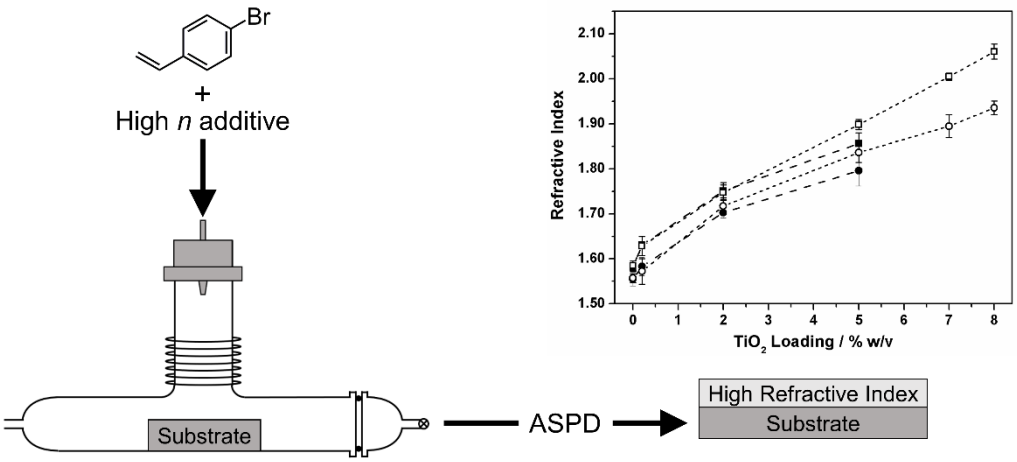

5.1 Introduction

When light passes through the boundary between two different materials it changes direction, or refracts, due to a change in speed. The extent to which the light will refract can be determined by the law of refraction, also known as Snell's Law:

$$n_1 \sin\theta_1 = n_2 \sin\theta_2 \qquad (5.1)$$

where θ_1 and θ_2 are the angles of incidence and refraction respectively, measured with respect to the normal line at the interface, and n_1 and n_2 are the refractive indices of the respective materials, Figure 5.1. The refracted light can either bend towards or away from the normal depending on the relative refractive indices of the two materials. If the light passes through a boundary into a medium of higher refractive index it will refract towards the normal whereas it will refract away from the normal when passing into a lower refractive index material, Figure 5.1. Furthermore, the larger the difference in refractive index between the two media, the greater the difference in angles of incidence and refraction, and hence the greater the extent of refraction.

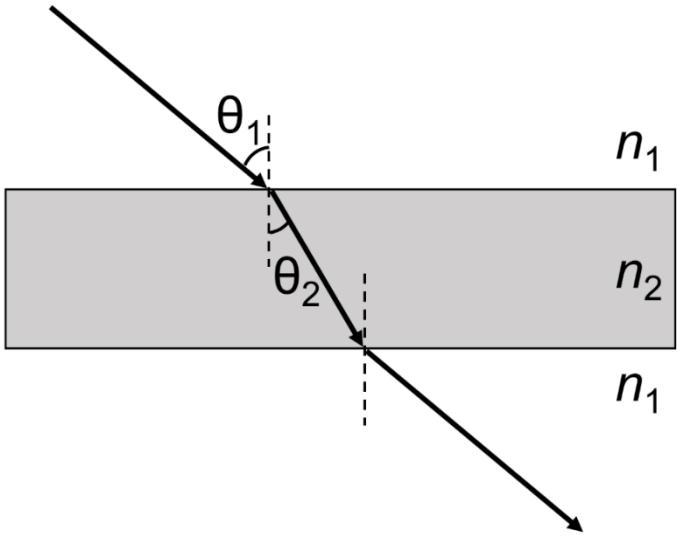

Figure 5.1: Schematic showing a beam of light refracting as it passes from a material of refractive index n_1 into a material of refractive index n_2 where $n_2 > n_1$.

High refractive index materials attract a great deal of interest because of their wide ranging applications, including optical lenses,[1] optical waveguides,[2,3] anti-reflective coatings,[4] and as encapsulants for both light-emitting diodes (LEDs)[5,6] and photovoltaic cells.[7] Most common polymer materials have a refractive index (*n*) of between 1.3–1.7.[8] However, more recently, high refractive index polymers (HRIPs) with refractive indices as high as 1.85 have been reported.[9,10,11] These HRIPs are prepared by introducing atoms or substituents of high molar refraction into the polymer chain. Such substituents include aromatic rings,[12] halogens (except for fluorine),[13] sulfur,[14] phosphorus,[15] and silicon.[16] Although these materials offer the advantages of being light-weight and easy to process, their preparation requires lengthy and costly synthetic procedures.[17,18] Given that inorganic materials have an inherently high refractive index, one way to achieve higher refractive index coatings is through the use of pure inorganic thin films. Coatings of ZnO, ZrO_2 and TiO_2 are reported to have refractive indices of 1.87,[19] 1.96,[20] and 2.28,[21] respectively. These coatings also require multiple-step preparation procedures as well as elevated temperatures (incompatible with plastic substrates).

Hybrid organic–inorganic composite materials potentially offer high refractive indices, and can be prepared using a variety of different methods. The most common is the sol–gel method in which a metal alkoxide precursor is mixed with an organic material followed by heating during which hydrolysis and condensation of the metal alkoxide results in the formation of metal oxide domains within the organic matrix to

yield coatings with refractive index values in the n = 1.7–1.9 range.[22,23,24,25,26,27,28,29,30,31,32,33] Sol–gel coatings containing TiO_2 have been reported with refractive index n = 1.92–2.05 values and the inorganic loading is high (49–90 wt%).[34,35,36,37,38] Other composite coatings contain inorganic materials such as PbS,[39,40] Si,[41] and V_2O_5[42] to give high refractive index coatings, however these require the use of H_2S gas,[39,40] a complex milling process,[41] and the coatings absorb strongly in the visible range.[42] In all of these cases, the inorganic content tends to be high (40–90 wt%) and the synthesis is lengthy requiring solvents in addition to elevated temperatures.

Another method that has been used to prepare organic–inorganic composite coatings is the dispersion of inorganic nanoparticles into an organic polymer prior to coating of substrates. A key requirement of this method is to use nanoparticles of <25 nm in size (well below one tenth of the wavelength of visible light) in order to avoid Rayleigh scattering leading to poor optical transparency.[43] As with sol–gel coatings, high refractive indices in the range 1.7–1.972 have been reported, but again rely upon high levels of inorganic material loadings (45–97 wt%).[44,45,46,47,48,49] Carbon black particles have been used at lower loadings (n = 1.833; 10 wt% content), however agglomeration can easily occur attenuating the coating transparency.[50]

It is also possible to disperse inorganic nanoparticles into monomers prior to polymerisation.[51,52,53] The highest refractive index reported for this approach is 1.972 at 50 wt% loading of graphene oxide.[54] As with the sol–gel coatings, these nanoparticle/monomer dispersions, as well as for the nanoparticle/polymer dispersions, all require high temperature (120–300 °C) or additional UV curing steps following substrate coating. Therefore, there exists a demand for ambient temperature single-step methods for fabricating high refractive index coatings with low levels of inorganic content.

Atomised spray plasma deposition (ASPD) is a single-step, room temperature, solventless method for the preparation of functional coatings.[55,56] This encompasses the nebulisation of liquid or slurry droplets into a non-equilibrium electrical discharge. At low energy inputs, high levels of structural retention (functionality) can be attained. In this article, high refractive index polymer coatings are prepared by ASPD using 4-bromostyrene precursor (n = 1.595[57]). The refractive index is further increased by mixing the 4-bromostyrene precursor with a higher refractive index solid (9-vinylcarbazole, n = 1.683[58]) or functionalised titania nanoparticles ($n_{anatase}$ = 2.45; n_{rutile}

= 2.70[26]) for ASPD, leading to high refractive index hybrid polymer or polymer–titania nanocomposite coatings respectively, Scheme 5.1.

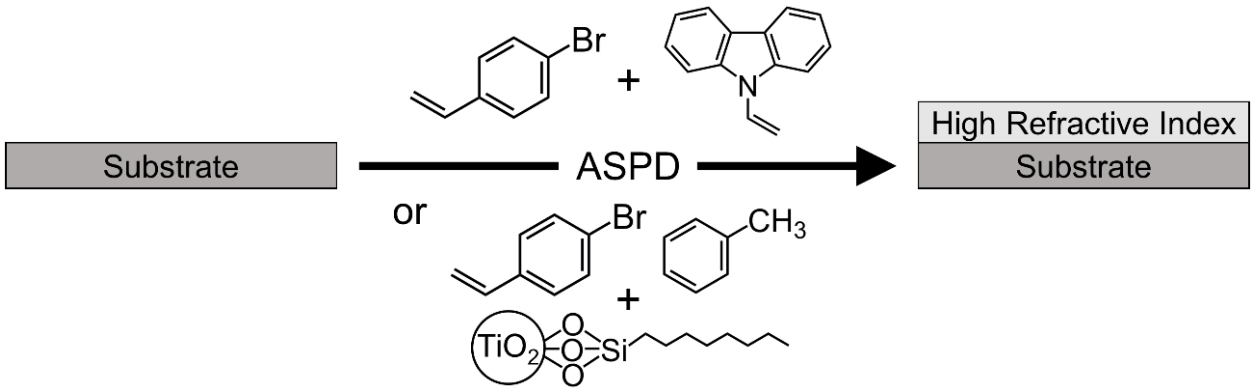

Scheme 5.1: Atomised spray plasma deposition of 4-bromostyrene–9-vinylcarbazole hybrid layers and 4-bromostyrene / toluene + TiO_2 nanocomposite layers.

5.2 Experimental

5.2.1 Atomised Spray Plasma Deposition

Precursor materials used were 4-bromostyrene (+95%, Apollo Scientific Ltd.), 9-vinylcarbazole (98%, Sigma-Aldrich Ltd.), and trimethoxyoctylsilane functionalised titania nanoparticles (21 nm average particle size, Aeroxide T805®, Evonik Industries AG). For the case of 4-bromostyrene precursor mixed with trimethoxyoctylsilane functionalised titania nanoparticles, 20% or 40% v/v of toluene (99.99 wt%, Fisher Scientific Ltd.) was added to improve dispersion.[59] Liquid–solid slurry monomer–nanoparticle mixtures were sonicated for 60 min to fully disperse the nanoparticles (Clifton ultrasonic bath, Nickel-Electro Ltd.), and then loaded into a sealable glass delivery tube. This precursor slurry mixture was then degassed using several freeze–pump–thaw cycles. Substrates used for coating were silicon (100) wafers (0.014–0.024 Ω cm resistivity, Silicon Valley Microelectronics Inc.) and quartz slides (20 mm x 10 mm x 1 mm, UQG Ltd.). These were cleaned, dried, and placed downstream in line-of-sight from the ASPD atomiser as described in Section 4.2.1 (page 115).

Atomised spray plasma deposition (ASPD) was performed using the equipment and procedure as described in Section 4.2.1 (page 115). Ambient temperature deposition was carried out using a 30 W continuous wave plasma in conjunction with atomisation of the precursor into the reaction chamber employing an optimised flow

rate of 15 ± 1 x 10^{-4} mL s^{-1}. Upon plasma extinction, the atomiser was switched off and the system was evacuated to base pressure, followed by venting to atmosphere.

5.2.2 Refractive Index

The refractive indices and thicknesses of coated silicon wafer substrates were determined using a spectrophotometer (model nkd-6000, Aquila Instruments Ltd.). The obtained transmittance-reflectance curves (350–1000 nm wavelength range and parallel (*p*) polarized light source at a 30° incident angle) were fitted to the Cauchy model for dielectric materials,[60] using a modified Levenberg–Marquardt method (version 2.2 software, Pro-Optix, Aquila Instruments Ltd.).[61]

5.2.3 UV-Vis Transmittance Spectroscopy

UV-vis transmittance spectra of coated quartz slides were acquired in the wavelength range 200–1000 nm using a UV-Vis-NIR spectrophotometer (model Cary 5000 UV-Vis-NIR, Agilent Technologies Inc.).

5.2.4 Infrared Spectroscopy

Fourier transform infrared (FTIR) analysis was carried out as described in Section 4.2.3 (page 117). Reflection–absorption infrared spectroscopy (RAIRS) was performed on ASPD hybrid and nanocomposite layer coated silicon wafers. Attenuated–total–reflection (ATR) spectroscopy was carried out for 4-bromostyrene, 9-vinylcarbazole, toluene, and trimethoxyoctylsilane-TiO_2 nanoparticles.

5.2.5 Scanning Electron Microscopy

Electron micrographs of ASPD coated silicon wafer substrates were acquired as described in Section 3.2.4 (page 72). A working distance of 12–15 mm was used. SEM cross-section analysis was performed as described in Section 4.2.2 (page 117) to cross-check the film thicknesses measured using the spectrophotometer, Table 5.1, Table 5.2, and Table 5.3.

5.3 Results

5.3.1 Deposition Rate

The optimal atomised spray plasma deposition (ASPD) rate (in terms of quality of coverage) for the 4-bromostyrene precursor was measured to be 325 ± 63 nm min^{-1}.

This film growth rate is an order of magnitude greater than that reported for conventional vapour phase plasma deposition of styrene (10–20 nm min^{-1}),[62] and can be attributed to the higher precursor flow rate associated with the atomisation of liquid droplets.[55] Scanning electron microscopy images of the ASPD layers showed that the surfaces were relatively smooth, Figure 5.2.

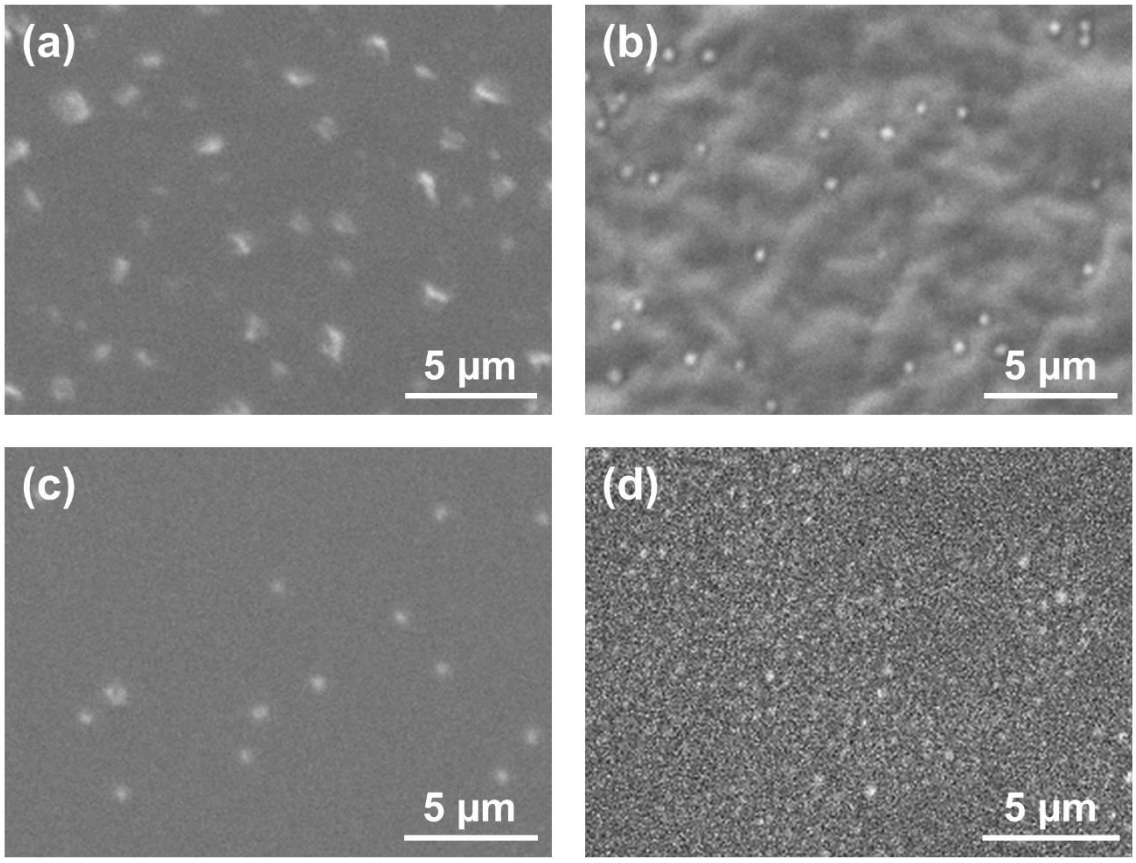

Figure 5.2: SEM micrographs of ASPD coatings on flat silicon wafer substrates: (a) 4-bromostyrene; (b) 4-bromostyrene–9-vinylcarbazole (50% w/v 9-vinylcarbazole); (c) 4-bromostyrene / toluene (3:2 v/v); and (d) 3:2 v/v 4-bromostyrene / toluene + TiO_2 (8% w/v).

5.3.2 Refractive Index

The refractive index of the ASPD 4-bromostyrene layer ($n_{635\ nm}$ = 1.569 ± 0.005) was found to be comparable to the literature value for the 4-bromostyrene precursor ($n_{589.3\ nm}$ = 1.595[57]), Figure 5.3 and Table 5.1. Incorporation of the high refractive index solid compound 9-vinylcarbazole ($n_{poly(vinyl\ carbazole)}$ = 1.683[58]) into the ASPD 4-bromostyrene layer led to an enhancement in the optical properties yielding refractive indices as high as $n_{635\ nm}$ = 1.648 ± 0.008 for a loading of 50% w/v 9-vinylcarbazole, Figure 5.3 and Table 5.1. The improvement in refractive index was across the entire measured

wavelength range. For 9-vinylcarbazole concentrations exceeding 50% w/v, the precursor mixture became too viscous to sustain homogeneous atomisation. The observed rise in refractive index value with increasing 9-vinylcarbazole content demonstrates how the optical properties of the ASPD 4-bromostyrene coatings can be easily tuned in order to achieve a desired refractive index by simply varying the 9-vinylcarbazole loading in the precursor mixture.

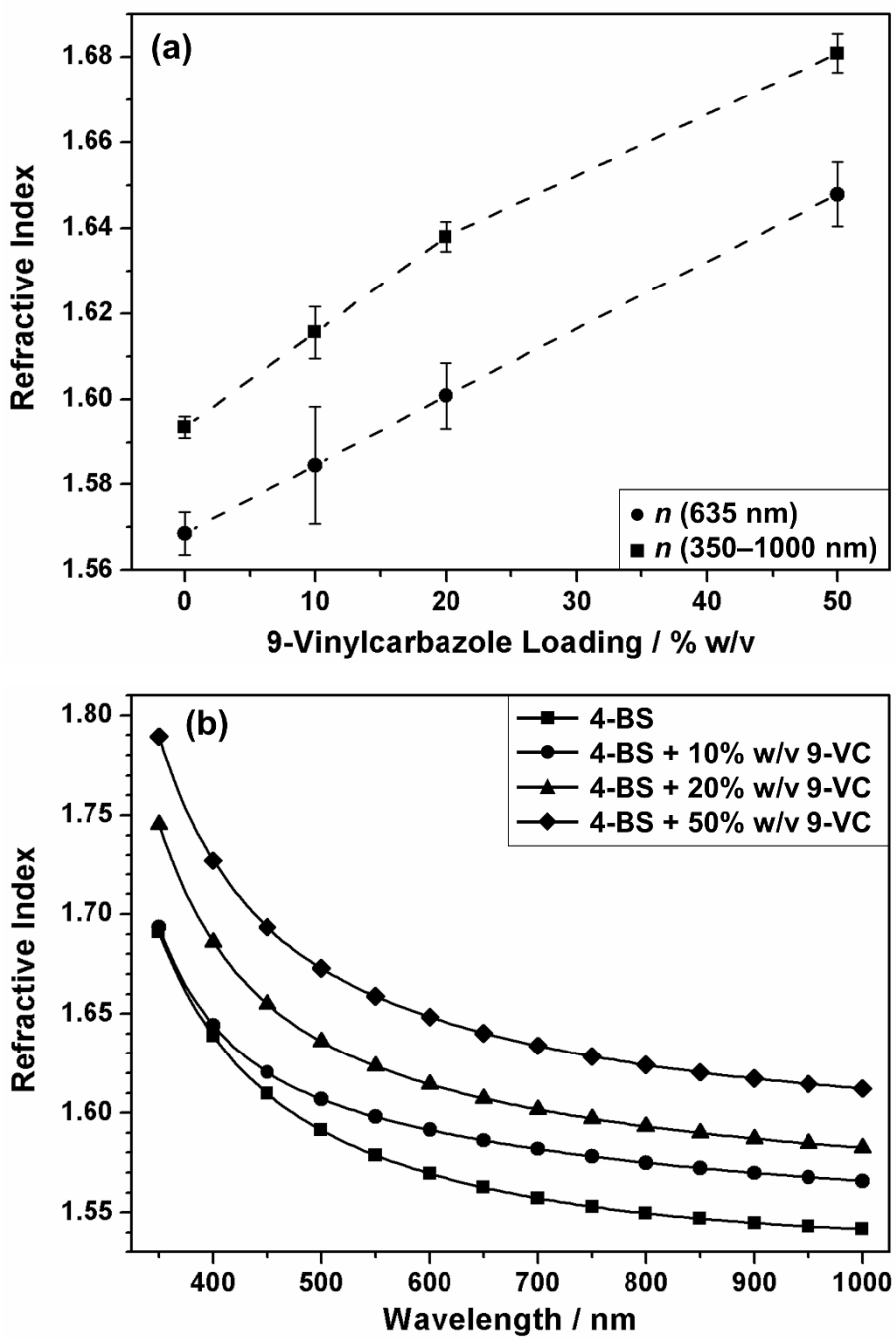

Figure 5.3: (a) Refractive index at 635 nm and averaged over 350–1000 nm wavelength range for ASPD 4-bromostyrene–9-vinylcarbazole hybrid layers on flat silicon wafer substrates as a function of 9-vinylcarbazole concentration in the precursor mixture; and (b) refractive index variation of ASPD 4-bromostyrene layer and ASPD 4-bromostyrene–9-vinylcarbazole hybrid layers across the 350–1000 nm wavelength range (lines represent different precursor compositions, actual measurements were made every 5 nm between 350 nm and 1000 nm—a symbol every 50 nm makes it easier to distinguish between the lines). 4-bromostyrene and 9-vinylcarbazole have been abbreviated to 4-BS and 9-VC respectively. Error bars denote the sample standard deviation.

Table 5.1: Spectrophotometer refractive index (*n*) (averaged over 350–1000 nm, and at 635 nm), and thickness (d) of ASPD 4-bromostyrene–9-vinylcarbazole hybrid layers on flat silicon wafer substrates. Spectrophotometer thickness values of selected samples was cross-checked using SEM cross-section analysis, Table 5.3. Error bars denote the sample standard deviation.

Coating	**Refractive Index**		**Thickness**
	***n* (350–1000 nm)**	***n* (635 nm)**	**d / nm**
4-bromostyrene	1.593 ± 0.002	1.569 ± 0.005	1910 ± 319
4-bromostyrene–10% w/v 9-vinylcarbazole	1.616 ± 0.006	1.585 ± 0.014	2090 ± 186
4-bromostyrene–20% w/v 9-vinylcarbazole	1.638 ± 0.004	1.601 ± 0.008	1809 ± 330
4-bromostyrene–50% w/v 9-vinylcarbazole	1.681 ± 0.005	1.648 ± 0.008	2413 ± 717

An even greater enhancement in refractive index values was achieved for the case of ASPD 4-bromostyrene–titania nanocomposite layers, Figure 5.4 and Table 5.2. This required the addition of some toluene to the 4-bromostyrene carrier in order to help disperse the hydrophobic trimethoxyoctylsilane-TiO_2 nanoparticles within the precursor mixture. In the absence of nanoparticles, the ASPD 4-bromostyrene / toluene (4:1 v/v) layer displayed a slightly lower refractive index ($n_{635\ nm}$ = 1.555 ± 0.015) compared to the pure 4-bromostyrene coating ($n_{635\ nm}$ = 1.569 ± 0.005)—which is expected due to the addition of a lower refractive index liquid into the precursor mixture ($n_{632.8\ nm\ (toluene)}$ = 1.4939).[63] Incorporation of trimethoxyoctylsilane-TiO_2 nanoparticles into this host 4-bromostyrene / toluene layer led to a significant increase in refractive index yielding values as high as $n_{635\ nm}$ = 1.796 ± 0.034 for a precursor slurry loading of 5% w/v titania nanoparticles dispersed in a 4:1 v/v 4-bromostyrene / toluene mixture, Figure 5.4 and Table 5.2. The refractive index of these ASPD 4-bromostyrene / toluene + titania nanocomposite layers is greatly enhanced across the entire measured wavelength range (350–1000 nm). For the same nanoparticle loading, the refractive index could be increased further by raising the toluene content ($n_{635\ nm}$ = 1.836 ± 0.022 for 5% w/v titania nanoparticles dispersed in a 3:2 v/v 4-bromostyrene / toluene mixture)—this can be attributed to a better dispersion of nanoparticles in the precursor mixture by using larger amounts of toluene. At this reduced 3:2 v/v ratio of 4-bromostyrene / toluene, the TiO_2 nanoparticle loading could be extended to beyond 5% w/v. A precursor slurry loading of 8% w/v titania gave refractive indices as high as $n_{635\ nm}$ = 1.936 ± 0.015, Figure 5.4 and Table 5.2. Control experiments with the titania loading kept constant at 5% w/v whilst lowering the 4-bromostyrene / toluene ratio further did not lead to any additional improvement in the refractive index beyond this optimal value (5% w/v TiO_2 nanoparticles in a 2:3 v/v 4-bromostyrene / toluene mixture gave $n_{635\ nm}$ = 1.819 ± 0.015). For TiO_2 nanoparticle concentrations exceeding 8% w/v nanoparticle loading, the precursor mixture became too viscous to sustain homogeneous atomisation. The significant enhancement in refractive index values attained with increasing trimethoxyoctylsilane-TiO_2 nanoparticle loading at relatively low concentrations further demonstrates the capability to fine tune the nanocomposite layer optical properties.

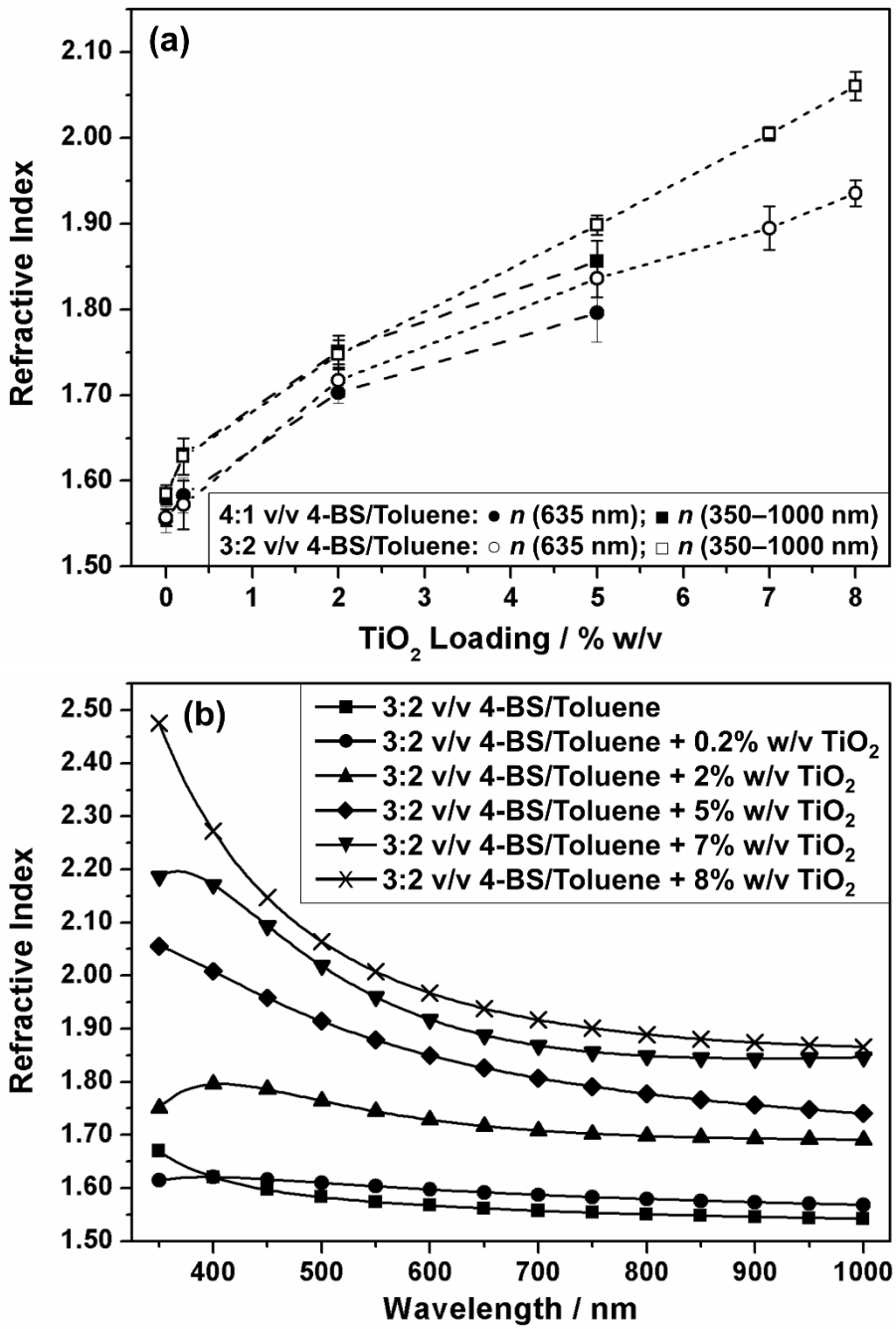

Figure 5.4: (a) Refractive index at 635 nm and averaged over 350–1000 nm wavelength range for ASPD 4-bromostyrene / toluene + titania nanocomposite layers on flat silicon wafer substrates as a function of trimethoxyoctylsilane functionalised-titania loading concentration; and (b) refractive index variation of ASPD 4-bromostyrene / toluene (3:2 v/v) layer and ASPD 4-bromostyrene / toluene (3:2 v/v) + x% w/v trimethoxyoctylsilane-TiO_2 nanocomposite layers across the 350–1000 nm wavelength range (lines represent different precursor compositions, actual measurements were made every 5 nm between 350 nm and 1000 nm—a symbol every 50 nm makes it easier to distinguish between the lines). 4-bromostyrene has been abbreviated to 4-BS. Error bars denote the sample standard deviation.

Table 5.2: Spectrophotometer refractive index (*n*) (averaged over 350–1000 nm, and at 635 nm), and thickness (d) of ASPD 4-bromostyrene / toluene + titania nanocomposite layers on flat silicon wafer substrates. Spectrophotometer thickness values of selected samples was cross-checked using SEM cross-section analysis, Table 5.3. Error bars denote the sample standard deviation.

Coating	**Refractive Index**		**Thickness**
	***n* (350–1000 nm)**	***n* (635 nm)**	**d / nm**
4:1 v/v 4-bromostyrene / toluene	1.581 ± 0.009	1.555 ± 0.015	2439 ± 278
4:1 v/v 4-bromostyrene / toluene + 0.2% w/v TiO_2	1.631 ± 0.006	1.583 ± 0.020	1968 ± 148
4:1 v/v 4-bromostyrene / toluene + 2% w/v TiO_2	1.751 ± 0.019	1.703 ± 0.012	2338 ± 199
4:1 v/v 4-bromostyrene / toluene + 5% w/v TiO_2	1.856 ± 0.024	1.796 ± 0.034	1897 ± 178
3:2 v/v 4-bromostyrene / toluene	1.584 ± 0.010	1.557 ± 0.010	1782 ± 202
3:2 v/v 4-bromostyrene / toluene + 0.2% w/v TiO_2	1.628 ± 0.021	1.572 ± 0.028	2048 ± 215
3:2 v/v 4-bromostyrene / toluene + 2% w/v TiO_2	1.747 ± 0.017	1.717 ± 0.019	2179 ± 399
3:2 v/v 4-bromostyrene / toluene + 5% w/v TiO_2	1.898 ± 0.011	1.836 ± 0.022	2085 ± 98
3:2 v/v 4-bromostyrene / toluene + 7% w/v TiO_2	2.005 ± 0.008	1.895 ± 0.026	2002 ± 62
3:2 v/v 4-bromostyrene / toluene + 8% w/v TiO_2	2.060 ± 0.017	1.936 ± 0.015	2019 ± 163
2:3 v/v 4-bromostyrene / toluene + 5% w/v TiO_2	1.908 ± 0.032	1.819 ± 0.015	2099 ± 112

Table 5.3: Comparison of thickness measurements using spectrophotometer and scanning electron microscopy (SEM) of selected ASPD 4-bromostyrene–9-vinylcarbazole hybrid and 4-bromostyrene / toluene + titania nanocomposite coated flat silicon wafer samples. Error bars denote the sample standard deviation.

Coating	Thickness / nm	
	Spectrophotometer	SEM
4-bromostyrene	2000	1958 ± 22
4-bromostyrene–50% w/v 9-vinylcarbazole	3147	3177 ± 184
3:2 v/v 4-bromostyrene / toluene	1998	1887 ± 100
3:2 v/v 4-bromostyrene / toluene + 8% w/v TiO_2	1940	1900 ± 46

5.3.3 UV-Vis Transmittance Spectroscopy

UV-vis transmittance spectra of the ASPD 4-bromostyrene / toluene (3:2 v/v) layers show that the coatings exhibit good transparency in the wavelength range between 450–1000 nm, Figure 5.5. Upon incorporation of 8% w/v trimethoxyoctylsilane-TiO_2 nanoparticles, the UV-vis transmittance dropped, but still remained greater than 50% between 450–1000 nm, Figure 5.5.

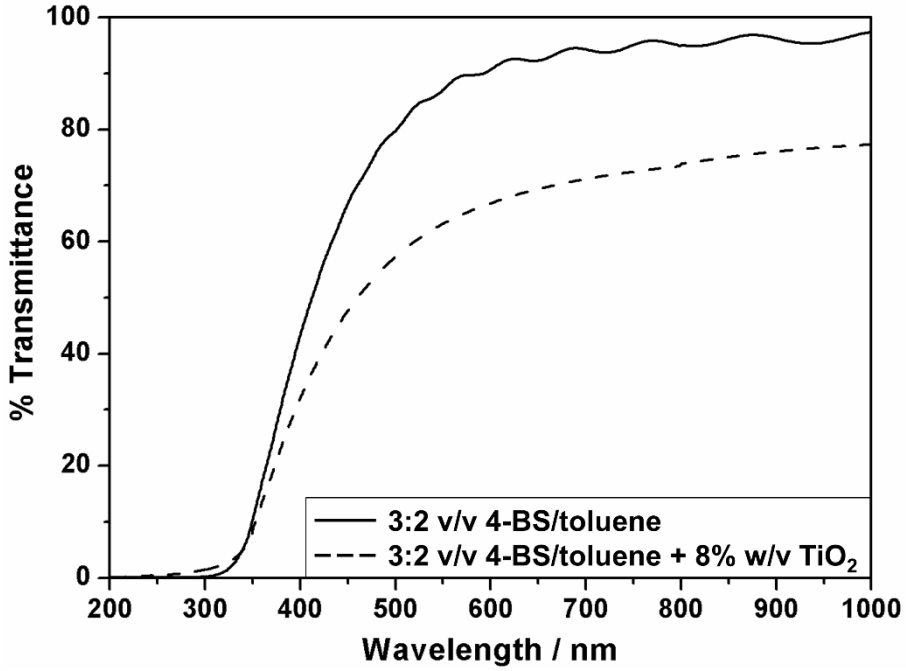

Figure 5.5: UV-vis transmittance spectra for ASPD 4-bromostyrene / toluene (3:2 v/v) layer (solid line) and 4-bromostyrene / toluene + 8% w/v TiO_2 (3:2 v/v) nanocomposite layer (dashed line) on flat quartz slides. 4-bromostyrene has been abbreviated to 4-BS.

5.3.4 Infrared Spectroscopy

Infrared spectroscopy showed high levels of structural retention for the ASPD poly(4-bromostyrene) layers, Figure 5.6 and Table 5.4. Characteristic poly(4-bromostyrene) ring absorbances include: aromatic C–H stretching (3028 cm^{-1}, 3059 cm^{-1}, 3084 cm^{-1}), para substituted benzene ring C=C stretching (1488 cm^{-1}, 1590 cm^{-1}), and aromatic C–Br (para) stretching (1073 cm^{-1}).[64,65] Disappearance of the peaks due to the vinyl C=C bond associated with the precursor molecule confirmed polymerisation via the 4-bromostyrene vinyl group during ASPD: $=CH_2$ wagging (909 cm^{-1}), $=CH_2$ twisting (986 cm^{-1}), and C=C stretching (1629 cm^{-1}).[64,66]

The infrared spectrum of the ASPD 4-bromostyrene–50% w/v 9-vinylcarbazole layer clearly shows incorporation of 9-vinylcarbazole into the hybrid polymer layer due to the appearance of an absorption band at 1336 cm^{-1} associated with C–N stretching.[67] A characteristic ortho substituted benzene ring absorbance is also now observed at 1453 cm^{-1} attributed to the extended 9-vinylcarbazole aromatic structure.[68] As with the ASPD 4-bromostyrene layer, disappearance of the absorbances associated with the vinyl C=C bond present in the 9-vinylcarbazole precursor is consistent with conventional polymerisation taking place at the vinyl C=C double bond: $=CH_2$ wagging (851 cm^{-1}), $=CH_2$ twisting (960 cm^{-1}), and C=C stretching (1637 cm^{-1}).[64,66]

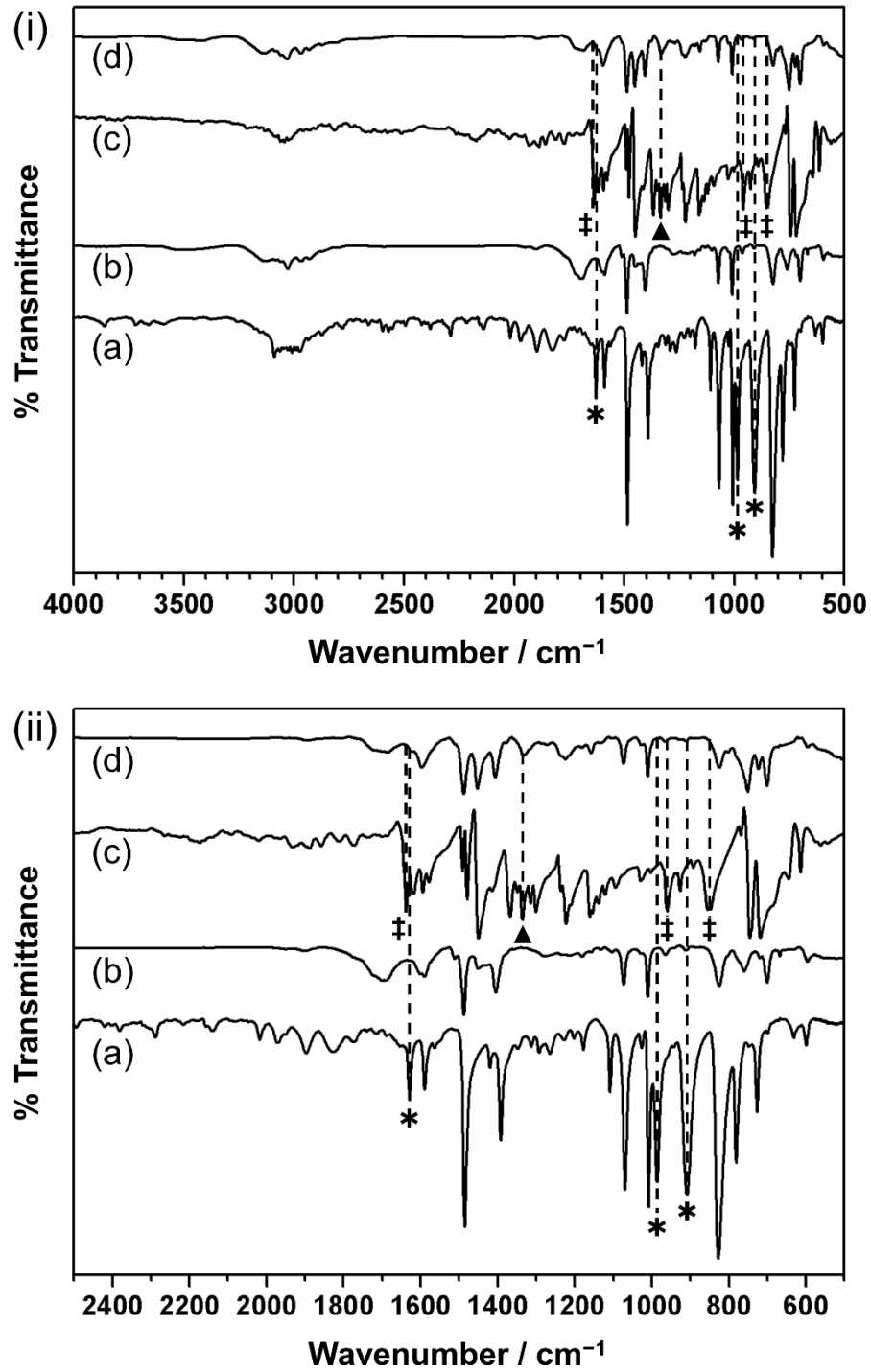

Figure 5.6: Infrared spectra: (a) ATR 4-bromostyrene liquid precursor; (b) RAIRS ASPD 4-bromostyrene layer on silicon substrate; (c) ATR 9-vinylcarbazole solid precursor; and (d) RAIRS ASPD 4-bromostyrene–9-vinylcarbazole hybrid polymer layer (50% w/v 9-vinylcarbazole) on silicon substrate across (i) 500–4000 cm^{-1} and (ii) 500–2500 cm^{-1} range. ∗ and ‡ denote absorbances associated with the polymerisable vinyl C=C double bond contained in the 4-bromostyrene and 9-vinylcarbazole precursors respectively. ▲ denotes C–N stretching absorbance at 1336 cm^{-1}. Assignments are given in Table 5.4. [Infrared spectroscopy data acquired by I. Castañeda-Montes].

Table 5.4: Infrared assignments for ASPD 4-bromostyrene–9-vinylcarbazole hybrid layers on flat silicon wafer substrates.

Assignment	**Absorption Frequency / cm^{-1}**			
	4-bromostyrene monomer	**ASPD 4-bromostyrene**	**9-vinylcarbazole solid**	**ASPD 4-bromostyrene–50% 9-vinylcarbazole**
Aromatic C–H stretching	3027, 3064, 3089	3028, 3059, 3084	3026, 3061, 3079, 3087	3031, 3059, 3081
Vinyl C–H stretching	2991, 3009, 3047	–	3016, 3043	–
Vinyl C=C stretching	1629	–	1637	–
Ring C=C stretching	1486, 1590	1488, 1590	1450, 1594	1453, 1489, 1598
C–N stretching	–	–	1336	1334
C–Br stretching (Aryl–Br)	1070	1073	–	1074
C–C stretching (ring breathing)	1008	1010	1003	1010
Vinyl $=CH_2$ twisting	986	–	960	–
Vinyl $=CH_2$ wagging	909	–	851	–
Aromatic CH deformation out-of-plane	781, 828	825	719, 746	751, 825

For the ASPD 4-bromostyrene / toluene + titania nanocomposite layer, TiO_2 nanoparticle incorporation throughout the bulk of the layers is evident from the broad absorption band at around 660 cm^{-1} associated with Ti–O–Ti stretching[69], Figure 5.7 and Table 5.5. Aliphatic C–H stretching absorbances at 2871 cm^{-1} and 2920 cm^{-1} are indicative of some toluene molecule reactions.[64] This incorporation of toluene into the nanocomposite structure also shifts the characteristic para substituted benzene ring C=C stretching absorbances of 4-bromostyrene towards higher wavenumbers (1489 cm^{-1}, 1601 cm^{-1})—which is consistent with having a mixture of para (para C=C stretching of 4-bromostyrene precursor: 1486 cm^{-1}, 1590 cm^{-1}) and mono (mono C=C stretching of toluene precursor: 1495 cm^{-1}, 1605 cm^{-1}) substituted benzene rings.[64]

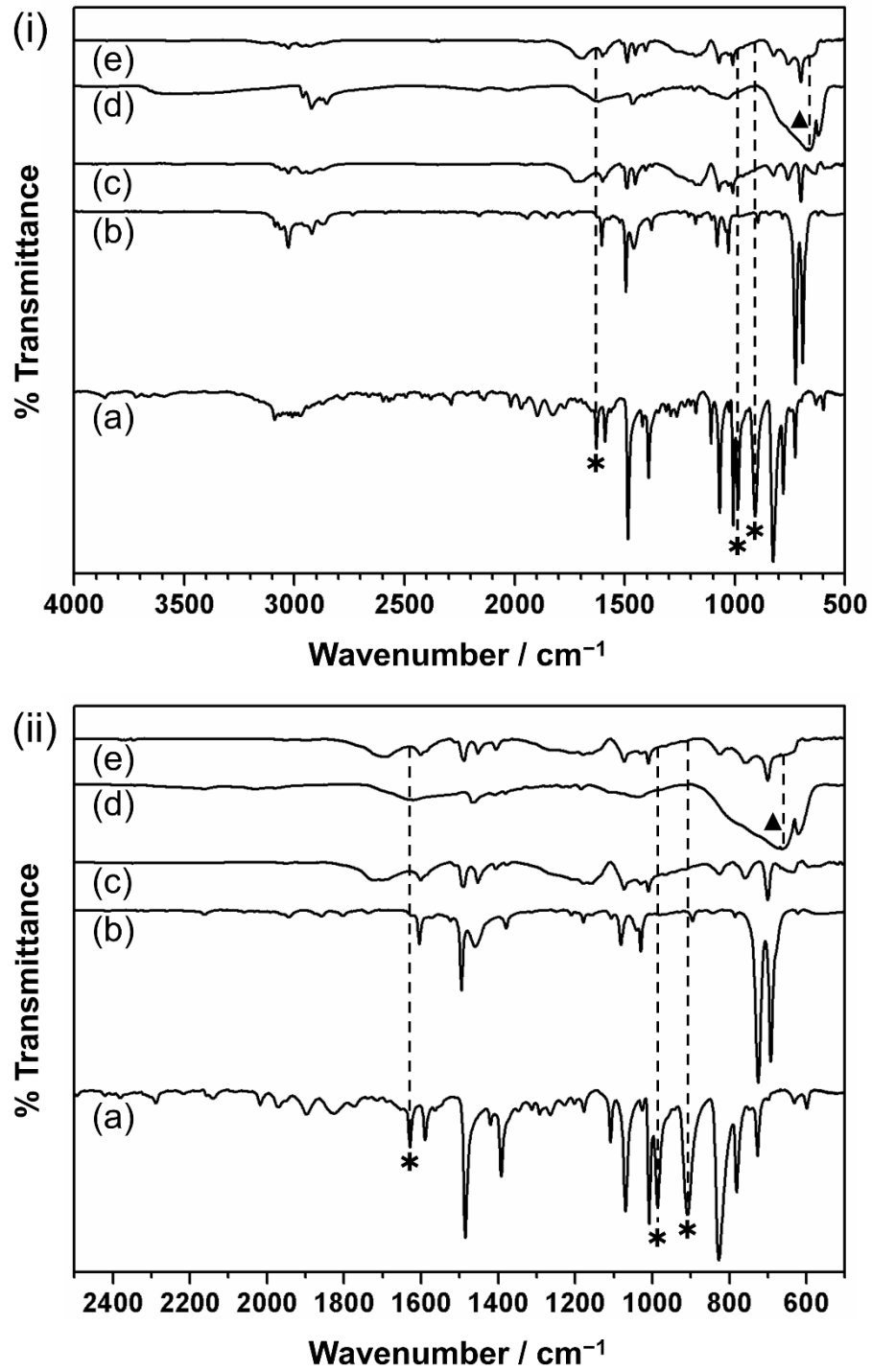

Figure 5.7: Infrared spectra: (a) ATR 4-bromostyrene liquid precursor; (b) ATR toluene liquid precursor; (c) RAIRS ASPD 4-bromostyrene / toluene (3:2 v/v) layer on silicon substrate; (d) ATR trimethoxyoctylsilane-TiO_2 nanoparticles; and (e) RAIRS ASPD 4-bromostyrene / toluene + trimethoxyoctylsilane-TiO_2 nanocomposite layer (8% w/v nanoparticle concentration, 3:2 v/v 4-bromostyrene / toluene) on silicon substrate across (i) 500–4000 cm^{-1} and (ii) 500–2500 cm^{-1} range. ✱ denotes absorbances associated with the polymerisable vinyl C=C double bond contained in the 4-bromostyrene precursor. ▲ denotes Ti–O–Ti stretching absorbance at 660 cm^{-1}. Assignments are given in Table 5.5. [Infrared spectroscopy data acquired by I. Castañeda-Montes].

Table 5.5: Infrared assignments for ASPD 4-bromostyrene / toluene + titania nanocomposite layers on flat silicon wafer substrates.

Assignment	**Absorption Frequency / cm^{-1}**				
	4-bromostyrene monomer	**Toluene**	**ASPD 4-bromostyrene / toluene (3:2 v/v)**	**Trimethoxyoctylsilane -TiO_2 solid**	**ASPD 4-bromostyrene / toluene (3:2 v/v) + 8% TiO_2**
Aromatic C–H stretching	3027, 3064, 3089	3027, 3062, 3087	3026, 3060, 3083	–	3027, 3060, 3083
Vinyl C–H stretching	2991, 3009, 3047	–	–	–	–
Aliphatic C–H stretching	–	2871, 2920	2871, 2928	2854, 2878, 2922, 2960	2870, 2929
Vinyl C=C stretching	1629	–	–	–	–
Ring C=C stretching	1486, 1590	1495, 1605	1490, 1601	–	1489, 1601
C–Br stretching (Aryl–Br)	1070	–	1073	–	1073
C–C stretching (ring breathing)	1008	–	1010	–	1010
Vinyl =CH_2 twisting	986	–	–	–	–
Vinyl =CH_2 wagging	909	–	–	–	–
Aromatic CH deformation out-of-plane	781, 828	693	701, 826	–	701, 825
Ti–O–Ti stretching	–	–	–	660	660

5.4 Discussion

The refractive index of a polymer is dependent upon the molar refractions and molar volumes of both the polymer backbone and the functional groups present.[70] It can be predicted by summing the molar refractions of all the polymer substituents, and therefore high refractive index polymers contain substituents with a high molar refraction.[71] Aromatic rings and halogen atoms (except for fluorine) have a high molar refraction due to their large polarizability and high electron density.[9] Hence, incorporation of these groups into a polymeric coating is an effective way for enhancing its index of refraction. This accounts for why the refractive index measured for the ASPD 4-bromostyrene layer is high, Figure 5.3 and Table 5.1. Infrared spectroscopy of the ASPD 4-bromostyrene layer supports this by confirming the presence of aromatic groups (aromatic C–H and C=C stretches) and bromine atoms (aromatic C–Br stretch), Figure 5.6 and Table 5.4.

Further enhancement in refractive index has been achieved through the mixing of the highly aromatic molecule 9-vinylcarbazole with the 4-bromostyrene precursor, Figure 5.3 and Table 5.1. This increases the refractive index across the entire wavelength range measured. The observed enhancement in refractive index (Δn = +0.079) at maximum 9-vinylcarbazole loading (50% w/v) is in line with previous reports which utilise 9-vinylcarbazole to increase n using a blade coating[72] or moulding process[73] followed by UV polymerisation. In contrast, greater refractive indices are achieved in the present study through the use of a host polymer with greater refractive index. Furthermore, the syntheses of these previously reported polymer systems require several additives (crosslinking agent, UV starter to initiate polymerisation, stabiliser) as well as UV irradiation and high temperature baking steps—none of which are required for the single-step ASPD process.

Higher refractive indices have been reported in the past by incorporating titania into high refractive index coatings using the sol–gel method[22,24,25,26,27,28,29,30,31,32,33,34,35,36,37,38,74], or by nanoparticle dispersion into polymers[45,46,47,49,75,76,77] and monomer mixtures[53]. These rely upon the inherently high refractive index of titania (n = 2.45 for anatase; n = 2.70 for rutile).[26] This has been extended to the present study by dispersing low loadings of trimethoxyoctylsilane functionalised titania nanoparticles (consisting of a mixture of anatase and rutile[78]) into the 4-bromostyrene precursor for ASPD, Figure 5.4 and Table 5.2. Alkyl group surface

functionalisation of the TiO_2 nanoparticles assists dispersion in the 4-bromostyrene precursor. Toluene addition to the precursor mixture further assists dispersion of the nanoparticles in 4-bromostyrene.[59] The refractive index obtained for the 3:2 v/v 4-bromostryene / toluene + 8% w/v titania ASPD nanocomposite coating ($n_{635\,nm}$ = 1.936) exceeds a previous report where titania is added prior to UV-induced monomer polymerisation (n = 1.861[53]). Furthermore, the refractive index reported here exceeds earlier values for low loading polymer–inorganic nanocomposite coatings (≤10 wt% inorganic material): n = 1.81 (8 wt% HfO_2)[79] and n = 1.833 (10 wt% carbon black)[50]. Coatings containing titania where the refractive index is slightly greater than the 1.936 value reported in the present study include preparation by nanoparticle dispersion into polymers[49,75], and the sol–gel method[35,36,37,38]. In all of these cases however, the titania loading is far greater (30–93.4 wt%) than that employed here, as well as the requirement for complex synthetic procedures, long times, the use of solvents, high temperatures, and post deposition curing steps. In contrast, the ASPD technique is a straightforward single-step, solventless, low temperature technique, and therefore offers a much simpler approach to depositing high refractive index polymer–titania nanocomposite coatings. Furthermore, in contrast to conventional spin-coating processes which require multiple deposition cycles to build up the thickness, the ASPD method offers both continuous thickness control as well as fast deposition rates.

5.5 Conclusions

High refractive index hybrid polymer and polymer–titania nanocomposite coatings have been prepared in a single-step using atomised spray plasma deposition (ASPD). The fabricated polymer–inorganic nanocomposite coatings have very high refractive indices at low levels of titania loading (8 wt%) compared to previously reported polymer–titania coatings (which typically have loadings >30 wt%). This single-step approach offers a solventless, low-temperature method for conformally coating any substrate with a high refractive index coating or a coating with a desired refractive index. The simplicity of this approach makes it a promising route for depositing thin films for optical applications.

5.6 References

[1] Matsuda, T.; Funae, Y.; Yoshida, M.; Yamamoto, T.; Takaya, T. Optical Material of High Refractive Index Resin Composed of Sulfur-Containing Aromatic Methacrylates. *J. Appl. Polym. Sci.* **2000**, *76*, 50–54.

[2] Zevin, M.; Reisfeld, R. Preparation and Properties of Active Waveguides Based on Zirconia Glasses. *Opt. Mater.* **1997**, *8*, 37–41.

[3] Bernini, R.; Cennamo, N.; Minardo, A.; Zeni, L. Planar Waveguides for Fluorescence-Based Biosensing: Optimization and Analysis. *IEEE Sens. J.* **2006**, *6*, 1218–1226.

[4] Krogman, K. C.; Druffel, T.; Sunkara, M. K. Anti-Reflective Optical Coatings Incorporating Nanoparticles. *Nanotechnology* **2005**, *16*, S338–S343.

[5] Mont, F. W.; Kim, J. K.; Schubert, M. F.; Schubert, E. F.; Siegel, R. W. High-Refractive-Index TiO_2-Nanoparticle-Loaded Encapsulants for Light-Emitting Diodes. *J. Appl. Phys.* **2008**, *103*, 083120.

[6] Kim, J.-S.; Yang, S.-C.; Bae, B.-S. Thermally Stable Transparent Sol–Gel Based Siloxane Hybrid Material with High Refractive Index for Light Emitting Diode (LED) Encapsulation. *Chem. Mater.* **2010**, *22*, 3549–3555.

[7] Ma, M.; Mont, F. W.; Poxson, D. J.; Cho, J.; Schubert, E. F.; Welser, R. E.; Sood, A. K. Enhancement of Photovoltaic Cell Response due to High-Refractive-Index Encapsulants. *J. Appl. Phys.* **2010**, *108*, 043102.

[8] Liu, J.-G.; Ueda, M. High Refractive Index Polymers: Fundamental Research and Practical Applications. *J. Mater. Chem.* **2009**, *19*, 8907–8919.

[9] Macdonald, E. K.; Shaver, M. P. Intrinsic High Refractive Index Polymers. *Polym. Int.* **2015**, *64*, 6–14.

[10] Higashihara, T.; Ueda, M. Recent Progress in High Refractive Index Polymers. *Macromolecules* **2015**, *48*, 1915–1929.

[11] Griebel, J. J.; Namnabat, S.; Kim, E. T.; Himmelhuber, R.; Moronta, D. H.; Chung, W. J.; Simmonds, A. G.; Kim, K.-J.; van der Laan, J.; Nguyen, N. A.; Dereniak, E. L.; Mackay, M. E.; Char, K.; Glass, R. S.; Norwood, R. A.; Pyun, J. New Infrared Transmitting Material via Inverse Vulcanization of Elemental Sulfur to Prepare High Refractive Index Polymers. *Adv. Mater.* **2014**, *26*, 3014–3018.

[12] Wen, P.; He, R.; Li, X.-D.; Lee, M.-H. Syntheses and Characterizations of High Refractive Index and Low Birefringence Polyimides Containing Spirobifluorene in the Side Chain. *Polymer* **2017**, *117*, 76–83.

[13] Minns, R. A.; Gaudiana, R. A. Design and Synthesis of High Refractive Index Polymers. II *J. Macromol. Sci. A* **1992**, *29*, 19–30.

[14] You, N.-H.; Suzuki, Y.; Yorifuji, D.; Ando, S.; Ueda, M. Synthesis of High Refractive Index Polyimides Derived from 1,6-Bis(*p*-aminophenylsulfanyl)-3,4,8,9-tetrahydro-2,5,7,10-tetrathiaanthracene and Aromatic Dianhydrides. *Macromolecules* **2008**, *41*, 6361–6366.

[15] Olshavsky, M.; Allcock, H. R. Polyphosphazenes with High Refractive Indices: Optical Dispersion and Molar Refractivity. *Macromolecules*, **1997**, *30*, 4179–4183.

[16] Bhagat, S. D.; Chatterjee, J.; Chen, B.; Stiegman, A. E. High Refractive Index Polymers Based on Thiol–Ene Cross-Linking Using Polarizable Inorganic/Organic Monomers. *Macromolecules* **2012**, *45*, 1174–1181.

[17] Olshavsky, M. A.; Allcock, H. R. Polyphosphazenes with High Refractive Indices: Synthesis, Characterization, and Optical Properties. *Macromolecules* **1995**, *28*, 6188–6197.

[18] Li, C.; Li, Z.; Liu, J.-G.; Zhao, X.-J.; Yang, H.-X.; Yang, S.-Y. Synthesis and Characterization of Organo-Soluble Thioether-Bridged Polyphenylquinoxalines with Ultra-High Refractive Indices and Low Birefringences. *Polymer* **2010**, *51*, 3851–3858.

[19] Zhao, D.; Mourey, D. A.; Jackson, T. N. Low-Temperature Pulsed-PECVD ZnO Thin-Film Transistors. *J. Electron. Mater.* **2010**, *39*, 554–558.

[20] Ehrhart, G.; Capoen, B.; Robbe, O.; Boy, P.; Turrell, S.; Bouazaoui, M. Structural and Optical Properties of *n*-Propoxide Sol–Gel Derived ZrO_2 Thin Films. *Thin Solid Films* **2006**, *496*, 227–233.

[21] Antonello, A.; Guglielmi, M.; Bello, V.; Mattei, G.; Chiasera, A.; Ferrari, M.; Martucci, A. Titanate Nanosheets as High Refractive Layer in Vertical Microcavity Incorporating Semiconductor Quantum Dots. *J. Phys. Chem. C* **2010**, *114*, 18423–18428.

[22] Yuwono, A. H.; Xue, J.; Wang, J.; Elim, H. I.; Ji, W.; Li, Y.; White, T. J. Transparent Nanohybrids of Nanocrystalline TiO_2 in PMMA with Unique Nonlinear Optical Behavior. *J. Mater. Chem.* **2003**, *13*, 1475–1479.

[23] Gorin, A.; Copperwhite, R.; Elmaghrum, S.; McDonagh, C.; Oubaha, M. Hybrid Zirconium Sol-Gel Thin Films with High Refractive Index. *Proc. SPIE* **2011**, *8191*, 81911Q-1–81911Q-7.

[24] Ho, W. F.; Uddin, M. A.; Chan, H. P. The Stability of High Refractive Index Polymer Materials for High-Density Planar Optical Circuits. *Polym. Degrad. Stab.* **2009**, *94*, 158–161.

[25] Chang, C.-C.; Chen, W.-C. High-Refractive-Index Thin Films Prepared from Aminoalkoxysilane-Capped Pyromellitic Dianhydride-Titania Hybrid Materials. *J. Polym. Sci., Part A-1: Polym. Chem.* **2001**, *39*, 3419–3427.

[26] Yuwono, A. H.; Liu, B.; Xue, J.; Wang, J.; Elim, H. I.; Ji, W.; Li, Y.; White, T. J. Controlling the Crystallinity and Nonlinear Optical Properties of Transparent TiO_2–PMMA Nanohybrids. *J. Mater. Chem.* **2004**, *14*, 2978–2987.

[27] Guan, C.; Lü, C.-L.; Liu, Y.-F.; Yang, B. Preparation and Characterization of High Refractive Index Thin Films of TiO_2/Epoxy Resin Nanocomposites. *J. Appl. Polym. Sci.* **2006**, *102*, 1631–1636.

[28] Kusabe, M.; Kozuka, H.; Abe, S.; Suzuki, H. Sol–Gel Preparation and Properties of Hydroxypropylcellulose–Titania Hybrid Thin Films. *J. Sol-Gel Sci. Technol.* **2007**, 44, 111–118.

[29] Chang, C.-M.; Chang, C.-L.; Chang, C.-C. Synthesis and Optical Properties of Soluble Polyimide/Titania Hybrid Thin Films. *Macromol. Mater. Eng.* **2006**, *291*, 1521–1528.

[30] Oda, S.; Uchiyama, H.; Kozuka, H. Sol–Gel-Derived Titania-Hydroxypropylcellulose Hybrid Thin Films of High Refractive Indices: Solution Components Affecting the Refractive Index and Uncracking Critical Thickness. *J. Sol-Gel Sci. Technol.* **2012**, *61*, 484–493.

[31] Lee, L.-H.; Chen, W.-C. High-Refractive-Index Thin Films Prepared from Trialkoxysilane-Capped Poly(methyl methacrylate)–Titania Materials. *Chem. Mater.* **2001**, *13*, 1137–1142.

[32] Lü, C.; Cui, Z.; Guan, C.; Guan, J.; Yang, B.; Shen, J. Research on Preparation, Structure and Properties of TiO_2/Polythiourethane Hybrid Optical Films with High Refractive Index. *Macromol. Mater. Eng.* **2003**, *288*, 717–723.

[33] Flaim, T. D.; Wang, Y.; Mercado, R. High-Refractive-Index Polymer Coatings for Optoelectronics Applications. *Proc. SPIE* **2004**, *5250*, 423–434.

[34] Liou, G.-S.; Lin, P.-H.; Yen, H.-J.; Yu, Y.-Y.; Chen, W.-C. Flexible Nanocrystalline-Titania/Polyimide Hybrids with High Refractive Index and Excellent Thermal Dimensional Stability. *J. Polym. Sci., Part A-1: Polym. Chem.* **2010**, *48*, 1433–1440.

[35] Su, H.-W.; Chen, W.-C. High Refractive Index Polyimide–Nanocrystalline-Titania Hybrid Optical Materials. *J. Mater. Chem.* **2008**, *18*, 1139–1145.

[36] Rao, Y.; Chen, S. Molecular Composites Comprising TiO_2 and Their Optical Properties. *Macromolecules* **2008**, *41*, 4838–4844.

[37] Liou, G.-S.; Lin, P.-H.; Yen, H.-J.; Yu, Y.-Y.; Tsai, T.-W.; Chen, W.-C. Highly Flexible and Optical Transparent 6F-PI/TiO_2 Optical Hybrid Films with Tunable Refractive Index and Excellent Thermal Stability. *J. Mater. Chem.* **2010**, *20*, 531–536.

[38] Himmelhuber, R.; Gangopadhyay, P.; Norwood, R. A.; Loy, D. A.; Peyghambarian, N. Titanium Oxide Sol-Gel Films with Tunable Refractive Index. *Opt. Mater. Express* **2011**, *1*, 252–258.

[39] Lü, C.; Guan, C.; Liu, Y.; Cheng, Y.; Yang, B. PbS/Polymer Nanocomposite Optical Materials with High Refractive Index. *Chem. Mater.* **2005**, *17*, 2448–2454.

[40] Zimmermann, L.; Weibel, M.; Caseri, W.; Suter, U. W. High Refractive Index Films of Polymer Nanocomposites. *J. Mater. Res.* **1993**, *8*, 1742–1748.

[41] Papadimitrakopoulos, F.; Wisniecki, P.; Bhagwagar, D. E. Mechanically Attrited Silicon for High Refractive Index Nanocomposites. *Chem. Mater.* **1997**, *9*, 2928–2933.

[42] Oubaha, M.; Elmaghrum, S.; Copperwhite, R.; Corcoran, B.; McDonagh, C.; Gorin, A. Optical Properties of High Refractive Index Thin Films Processed at Low Temperature. *Opt. Mater.* **2012**, *34*, 1366–1370.

[43] Althues, H.; Henle, J.; Kaskel, S. Functional Inorganic Nanofillers for Transparent Polymers. *Chem. Soc. Rev.* **2007**, *36*, 1454–1465.

[44] Liu, L.; Zheng, Z.; Wang, X. Preparation and Properties of Polythiourethane/ZnS Nanocomposites with High Refractive Index. *J. Appl. Polym. Sci.* **2010**, *117*, 1978–1983.

[45] Liu, J.-G.; Nakamura, Y.; Ogura, T.; Shibasaki, Y.; Ando, S.; Ueda, M. Optically Transparent Sulfur-Containing Polyimide–TiO_2 Nanocomposite Films with High Refractive Index and Negative Pattern Formation from Poly(amic acid)–TiO_2 Nanocomposite Film. *Chem. Mater.* **2008**, *20*, 273–281.

[46] Elim, H. I.; Cai, B.; Kurata, Y.; Sugihara, O.; Kaino, T.; Adschiri, T.; Chu, A.-L.; Kambe, N. Refractive Index Control and Rayleigh Scattering Properties of Transparent TiO_2 Nanohybrid Polymer. *J. Phys. Chem. B* **2009**, *113*, 10143–10148.

[47] Kurata, Y.; Sugihara, O.; Kaino, T.; Komatsu, K.; Kambe, N. Thermo-Optic Controllable Hybrid Photonic Polymers Containing Inorganic Nanoparticles. *J. Opt. Soc. Am. B* **2009**, *26*, 2377–2381.

[48] Lü, C.; Cui, Z.; Li, Z.; Yang, B.; Shen, J. High Refractive Index Thin Films of ZnS/Polythiourethane Nanocomposites. *J. Mater. Chem.* **2003**, *13*, 526–530.

[49] Liu, B.-T.; Tang, S.-J.; Yu, Y.-Y.; Lin, S.-H. High-Refractive-Index Polymer/Inorganic Hybrid Films Containing High TiO_2 Contents. *Colloids Surf., A* **2011**, *377*, 138–143.

[50] Xue, P.; Wang, J.; Bao, Y.; Li, Q.; Wu, C. Synergistic Effect Between Carbon Black Nanoparticles and Polyimide on Refractive Indices of Polyimide/Carbon Black Nanocomposites. *New J. Chem.* **2012**, *36*, 903–910.

[51] Luo, K.; Zhou, S.; Wu, L. High Refractive Index and Good Mechanical Property UV-Cured Hybrid Films Containing Zirconia Nanoparticles. *Thin Solid Films* **2009**, *517*, 5974–5980.

[52] Lü, C.; Cui, Z.; Wang, Y.; Li, Z.; Guan, C.; Yang, B.; Shen, J. Preparation and Characterization of ZnS–Polymer Nanocomposite Films with High Refractive Index. *J. Mater. Chem.* **2003**, *13*, 2189–2195.

[53] Rao, Y.; Antalek, B.; Minter, J.; Mourey, T.; Blanton, T.; Slater, G.; Slater, L.; Fornalik, J. Organic Solvent-Dispersed TiO_2 Nanoparticle Characterization. *Langmuir* **2009**, *25*, 12713–12720.

[54] Zhang, G.; Zhang, H.; Zhang, X.; Zhu, S.; Zhang, L.; Meng, Q.; Wang, M.; Li, Y.; Yang, B. Embedding Graphene Nanoparticles into Poly(N,N'-dimethylacrylamine) to Prepare Transparent Nanocomposite Films with High Refractive Index. *J. Mater. Chem.* **2012**, *22*, 21218–21224.

[55] Wood, T. J.; Ward, L. J.; Badyal, J. P. S. Super-Adhesive Polymer–Silica Nanocomposite Layers. *ACS Appl. Mater. Interfaces* **2013**, *5*, 9678–9683.

[56] Ward, L. J.; Schofield, W. C. E.; Badyal, J. P. S.; Goodwin, A. J.; Merlin, P. J. Atmospheric Pressure Plasma Deposition of Structurally Well-Defined Polyacrylic Acid Films. *Chem. Mater.* **2003**, *15*, 1466–1469.

[57] Walling, C.; Briggs, E. R.; Wolfstirn, K. B.; Mayo, F. R. Copolymerization. X. The Effect of Meta- and Para-Substitution on the Reactivity of the Styrene Double Bond. *J. Am. Chem. Soc.* **1948**, *70*, 1537–1542.

[58] van Krevelen, D. W.; te Nijenhuis, K. *Properties of Polymers*, 4th ed.; Elsevier B. V.: Amsterdam, The Netherlands, 2009; p 923.

[59] Iijima, M.; Kobayakawa, M.; Kamiya, H. Tuning the Stability of TiO_2 Nanoparticles in Various Solvents by Mixed Silane Alkoxides. *J. Colloid Interf. Sci.* **2009**, *337*, 61–65.

[60] Diebold, A. C.; Chism, W. W. Characterisation and Metrology of Medium Dielectric Constant Gate Dielectric Films. In *High Dielectric Constant Materials: VSLI MOSFET Applications*; Huff, H. R., Gilmer, D. C., Eds. Springer-Verlag: Berlin, 2005; p 486.

[61] Lovering, D. *NKD-6000 Technical Manual*; Aquila Instruments: Cambridge, U.K., 1999.

[62] Fahmy, A.; Mix, R.; Schönhals, A.; Friedrich, J. Structure of Plasma-Deposited Copolymer Films Prepared from Acrylic Acid and Styrene: Part 1 Dependence on the Duty Cycle. *Plasma Process. Polym.* **2012**, *9*, 273–284.

[63] Beysens, D.; Calmettes, P. Temperature Dependence of the Refractive Indices of Liquids: Deviation from the Lorentz–Lorentz Formula. *J. Chem. Phys.* **1977**, *66*, 766–771.

[64] Lin-Vien, D.; Colthup, N. B.; Fateley, W. G.; Grasselli, J. G. The Handbook of Infrared and Raman Characteristic Frequencies of Organic Molecules; Academic Press, Inc.: San Diego, 1991.

[65] Katritzky, A. R.; Lagowski, J. M. Infrared Absorption of Substituents in Aromatic Systems. Part V. Halogeno-compounds. *J. Chem. Soc.* **1960**, 2421–2422.

[66] Wood, T. J.; Brown, P. S.; Badyal, J. P. S. Atomized Spray Plasma Deposition of Structurally Well-Defined Bioactive Coatings. *Plasma Chem. Plasma Process.* **2014**, *34*, 1019–1031.

[67] Li, Y.; Yang, J.; Xu, J. In Situ IR Spectroscopic Study of Poly(N-vinylcarbazole) Film During Electrochemical Doping. *J. Appl. Polym. Sci.* **1996**, *61*, 2085–2089.

[68] Reyna-González, J. M.; Aguilar-Martínez, M.; Bautista-Martínez, J. A.; Rivera, E.; González, I.; Roquero, P. Influence of the Acidity Level on the Electropolymerization of *N*-vinylcarbazole: Electrochemical Study and Characterization of Poly(3,6-*N*-vinylcarbazole). *Polymer* **2006**, *47*, 6664–6672.

[69] Pirson, A.; Mohsine, A.; Marchot, P.; Michaux, B.; Van Cantfort, O.; Pirard, J. P.; Lecloux, A. J. Synthesis of SiO_2-TiO_2 Xerogels by Sol-Gel Process. *J. Sol-Gel Sci. Technol.* **1995**, *4*, 179–185.

[70] Lü, C.; Yang, B. High Refractive Index Organic–Inorganic Nanocomposites: Design, Synthesis and Application. *J. Mater. Chem.*, **2009**, *19*, 2884–2901.

[71] Yang, C.-J.; Jenekhe, S. A. Group Contribution to Molar Refraction and Refractive Index of Conjugated Polymers. *Chem. Mater.* **1995**, *7*, 1276–1285.

[72] Eiselt, T.; Preinfalk, J.; Gleißner, U.; Lemmer, U.; Hanemann, T. Development and Characterization of Adjustable Refractive Index Scattering Epoxy Acrylate Polymer Layers. *Proc. SPIE* **2016**, *9939*, 99390Q-1–99390Q-7.

[73] Gleißner, U.; Bonaus, S.; Megnin, C.; Hanemann, T. Refractive Index Increase of Acrylate-Based Polymers by Adding Soluble Aromatic Guest-Molecules. *Polym. Adv. Technol.* **2017**, *28*, 506–510.

[74] Chang, C.-C.; Cheng, L.-P.; Huang, F.-H.; Lin, C.-Y.; Hsieh, C.-F.; Wang, W.-H. Preparation and Characterization of TiO_2 Hybrid Sol for UV-Curable High-Refractive-Index Organic–Inorganic Hybrid Thin Films. *J. Sol-Gel Sci. Technol.* **2010**, *55*, 199–206.

[75] Chau, J. L. H.; Lin, Y.-M.; Li, A.-K.; Su, W.-F.; Chang, K.-S.; Hsu, S. L.-C.; Li, T.-L. Transparent High Refractive Index Nanocomposite Thin Films. *Mater. Lett.* **2007**, *61*, 2908–2910.

[76] Tao, P.; Li, Y.; Rungta, A.; Viswanath, A.; Gao, J.; Benicewicz, B. C.; Siegel, R. W.; Schadler, L. S. TiO_2 Nanocomposites with High Refractive Index and Transparency. *J. Mater. Chem.* **2011**, *21*, 18623–18629.

[77] Nakayama, N.; Hayashi, T. Preparation and Characterization of TiO_2 and Polymer Nanocomposite Films with High Refractive Index. *J. Appl. Polym. Sci.* **2007**, *105*, 3662–3672.

[78] Suh, Y. J.; Cho, K. Immobilization of Nanoscale Sunscreening Agents onto Natural Halloysite Micropowder. *Mater. Trans.* **2015**, *56*, 899–904.

[79] Bae, W. J.; Trikeriotis, M.; Sha, J.; Schwartz, E. L.; Rodriguez, R.; Zimmerman, P; Giannelis, E. P.; Ober, C. K. High Refractive Index and High Transparency HfO_2 Nanocomposites for Next Generation Lithography. *J. Mater. Chem.* **2010**, *20*, 5186–5189.

Chapter 6

Conclusions and Further Work

Nanocomposite coatings provide a useful way of tailoring surface properties of solid materials for various applications. In this thesis, three nanocomposite coatings have been prepared with the nanofiller material being chosen to either enhance the properties of, or to add functionality to, the resulting thin films, Figure 6.1.

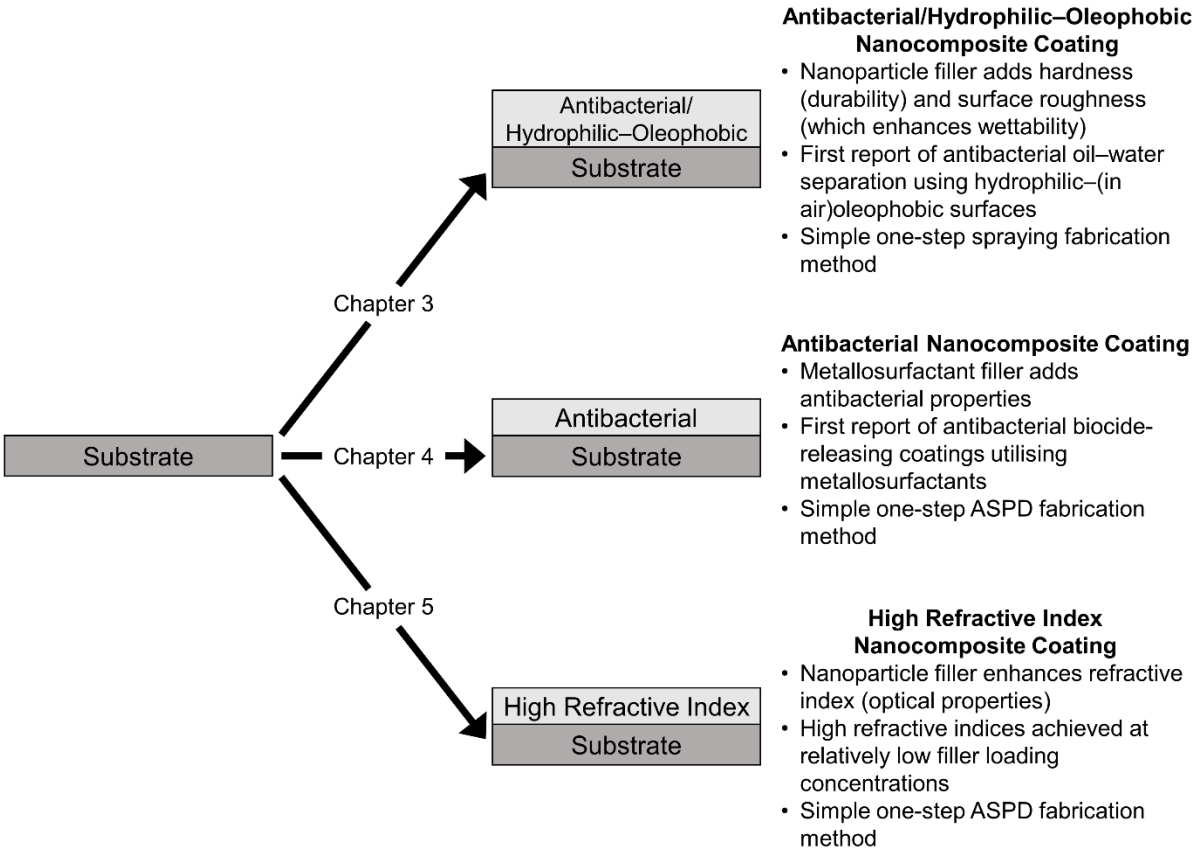

Figure 6.1: Summary of the three nanocomposite coatings prepared and characterised in this thesis.

Chapter 3 demonstrates how nanocomposite coatings can be used to modify the wetting properties of a substrate. Incorporating low loading concentrations of nanoparticles into fast-switching oleophobic–hydrophilic polymer–fluorosurfactant complexes results in nanocomposites of enhanced wettability (greater hydrophilicity and oleophobicity) due to the added surface roughness. These surfaces provide high-efficiency continuous oil–water separation for various different oil–water mixtures.

Nanoparticle incorporation also improves the coating hardness (durability). The use of a cationic polymer containing quaternary ammonium centres to prepare these polymer–nanoparticle–fluorosurfactant complexes imparts antibacterial surface properties against both Gram-negative (*Escherichia coli*) and Gram-positive (*Staphylococcus aureus*) bacteria. As a result, multifunctional fast-switching oleophobic–hydrophilic nanocomposite coatings are prepared, the first report of antibacterial oil–water separation using oleophobic–hydrophilic surfaces which are oleophobic in air (previous reports are only oil repellent underwater). This overcomes the drawbacks associated with underwater oleophobic surfaces which include the need for the filter to be constantly in a wetted state otherwise oil will pass through. In addition to being the first report of antibacterial oleophobic(in air)–hydrophilic surfaces, the main advantage of these polymer–nanoparticle–fluorosurfactant complexes is that they can be deposited in a single step by spraying or solvent-casting.

Further to the above polymer–nanoparticle–fluorosurfactant complexes, an attempt was made in Chapter 3 to prepare oleophobic–hydrophilic polymer–nanoparticle–surfactant complexes using a non-fluorinated highly branched hydrocarbon chain as an alternative to the fluorosurfactant. The initial studies demonstrate that positive switching parameters (oil contact angle greater than water contact angle) can still be obtained however the oil repellency is too low to consider these surfaces oleophobic. Therefore, the non-fluorinated polymer–nanoparticle–surfactant complexes could be developed further with the aim of increasing the oil repellency. This could possibly be achieved through the use of a more highly branched surfactant than the one tested in this work. This would be highly desirable due to the harm fluorinated materials cause to the environment.

The use of nanomaterials to add additional properties to polymers is demonstrated in Chapter 4 where antibacterial metallosurfactants are incorporated at low loading concentrations into plasma polymer films rendering the coating highly antimicrobial (Log Kill > 9) against both *Escherichia coli* (Gram-negative) and *Staphylococcus aureus* (Gram-positive) bacteria. The antibacterial properties of these metallosurfactants has not previously been utilised in surface coatings. These polymer–metallosurfactant nanocomposites are prepared in a single-step using an atomised spray plasma deposition (ASPD) process. This single-step approach offers a solventless, low-temperature method for conformally coating any substrate with highly antibacterial coatings and its simplicity makes it a promising route to prepare

these coatings for biomedical applications. The antibacterial activity of the polymer–metallosurfactant nanocomposites is thought to be due to leaching of the metallosurfactant from the film. Although out of the scope of this work, this could be confirmed by further work. Previous work in the literature has shown that thin plasma polymer layers deposited on top of antibacterial release-based coatings can control the rate of release by acting as a barrier layer. Therefore, in addition to investigating the leaching rate, the ability to control the rate of metallosurfactant release could be investigated by depositing thin plasma polymer layers of varying thickness on top of the polymer–metallosurfactant nanocomposite. The ability to control the release rate of the antibacterial agent would enhance the long-term stability of the coating. Poly(2-hydroxyethyl methacrylate) coatings have previously been shown to have anti-fouling properties due to their hydrophilicity. Bacterial adhesion studies could be performed to test this and to confirm if these nanocomposite coatings can be described as being dual-function antibacterial surfaces: bacteria-repelling and biocide-releasing.

The atomised spray plasma deposition technique used in Chapter 4 was further used in Chapter 5 for the deposition of high refractive index nanocomposite coatings. Titania nanoparticles are incorporated into a polymer at low loading concentrations to increase the refractive index of the film. The resulting polymer–titania nanocomposite coatings have refractive indices greater than previously reported polymer–titania coatings where the titania loading is much greater than that used in this work. The ASPD technique used overcomes disadvantages associated with alternative methods for depositing high refractive index coatings where elevated temperatures, solvents, UV curing steps, and much greater inorganic loadings are necessary. The simplicity of this approach makes it a promising route for depositing thin films for optical applications. With the 4-bromostyrene / toluene + titania nanocomposite used here, thin films with any desired refractive index up to 1.936 can be easily deposited by varying the precursor mixture composition. Other host polymers could be tested and may give rise to greater refractive indices if either the host polymer itself is more refractive or, if as a result of changing the polymer, greater loading concentrations of titania can be used without compromising the atomisation of the precursor mixture. Further studies could also test different nanoparticle additives.

Overall, it has been demonstrated throughout this thesis that incorporation of nanomaterials into polymers allows the properties of surface coatings to be tailored for various applications. The nanocomposites prepared in this work will be applicable to

a range of applications including provision of safe drinking water, environmental pollution clean-up, antibacterial surfaces for biomedical applications, and high refractive films for optical applications.

Appendix 1

Oleophobic–Hydrophilic Coatings by Plasma Polymerisation and Fluorosurfactant Complexation

A1.1 Introduction

In Chapter 3, fast-switching oleophobic–hydrophilic surfaces were prepared in one step using polymer–fluorosurfactant complexes. Another way of preparing such surfaces is by using a two-step method where the polymer is first deposited onto the surface followed by fluorosurfactant complexation.[1,2,3] Although this adds an extra step to the process, the use of plasma polymerisation to deposit the polymer allows for pin-hole free coverage of the substrate as well as the ability to coat a wide range of materials. It does however remove the possibility of incorporating nanoparticles (roughness) into the coatings unless further additional steps are performed.[4] In this short study, fast-switching oleophobic–hydrophilic plasma polymer–fluorosurfactant surfaces have been prepared in two steps by complexing both cationic and amphoteric fluorosurfactants to maleic anhydride and 2-(trifluoromethyl)maleic anhydride plasma polymer layers.

A1.2 Experimental

A1.2.1 Pulsed Plasma Polymer—Fluorosurfactant Coatings

Precursor materials used were maleic anhydride briquettes (+99%, Sigma-Aldrich Ltd., ground into a fine powder) and 2-(trifluoromethyl)maleic anhydride (97%, Apollo Scientific Ltd.). Precursors were loaded into a sealable glass tube and degassed via several freeze-pump-thaw cycles prior to deposition. Plasmachemical surface functionalisation was carried out in a cylindrical glass chamber (5 cm diameter, 530 cm^3 volume) enclosed within a Faraday cage. This was connected to a two-stage rotary pump via a liquid nitrogen cold trap (base pressure less than 2×10^{-3} mbar and air leak rate better than 6×10^{-9} mol s^{-1}).[5] An inductor-capacitor (L-C) impedance matching network was used to minimise the standing wave ratio (SWR), for the power transmitted from a 13.56 MHz radio frequency (RF) generator to a copper coil (4 mm diameter, 9 turns, spanning 8 cm) externally wound around the glass chamber. A

signal generator (model TG503, Thurlby Thandar Instruments Ltd.) was used to trigger the RF power supply, and the pulse shape monitored with an oscilloscope (model V252, Hitachi Ltd.). Prior to each plasma deposition, the reactor was scrubbed with detergent, rinsed in propan-2-ol (99.5%, Fischer Scientific Ltd.), and further cleaned using a 50 W air plasma at 0.2 mbar pressure for 30 min. Substrates used for coating were glass microscope slides (Academy Science Ltd.) These were cleaned by sonication in a 1:1 v/v propan-2-ol / cyclohexane (+99.5%, Fisher Scientific Ltd.) mixture, followed by UV/ozone treatment (model UV.TC.EU.003, BioForce Nanosciences Inc.), and a final sonication step in the propan-2-ol / cyclohexane mixture. After air drying, substrates were inserted into the centre of the chamber followed by evacuation to system base pressure. Next, precursor vapour was admitted into the chamber via a needle control valve at 0.15 mbar pressure, and the electrical discharge ignited using a pulse duty cycle on-period (t_{on}) of 20 µs and an off-period (t_{off}) of 1200 µs, in conjunction with 10 W peak power (P_{on}). Deposition times were 90 min and 30 min for maleic anhydride and 2-(trifluoromethyl)maleic anhydride, respectively. Upon extinction of the plasma, the precursor vapour was allowed to continue purging through the chamber for 15 min. Finally, the system was evacuated to base pressure, and vented to atmosphere.

Plasma polymer coated glass substrates were immediately immersed into a 5% v/v fluorosurfactant solution in high-purity water (ISO 3696 grade 2) for 60 min followed by rinsing with high-purity water and drying in air. Fluorosurfactants employed for complexation with the plasma polymer maleic anhydride and 2-(trifluoromethyl)maleic anhydride surfaces were a cationic ammonium chloride fluorosurfactant (S-106A, Chemguard, Inc.) and an amphoteric betaine fluorosurfactant (Capstone FS-50, DuPont Ltd.).

A1.2.2 Sessile Drop Contact Angle

Sessile drop contact angle analysis was carried out on coated glass slide substrates with a video capture system in combination with a motorised syringe (VCA2500XE, AST Products Inc.). 1 µL droplets of ultrahigh-purity water (BS 3978 grade 1) and hexadecane (99%, Sigma-Aldrich Ltd.) were dispensed for water and oil contact angle measurements respectively. Following dispensation of the probe liquid onto the coated substrate, a snapshot of the image was taken and analysed using the VCA-2500

Dynamic/Windows software. The water contact angle (WCA) was measured as soon as the droplet was placed onto the surface and again after a period of 10 s—this was done in order to observe any change in the WCA over a short time period due to the "switching" behaviour of these surfaces (a short time of 10 s was chosen because coatings required for oil–water separation applications need to switch quickly in order to attain high efficiencies). The hexadecane contact angle (HCA) was measured as soon as the droplet was placed onto the surface and it was observed not to vary with time. The reported contact angle measurements were made after rinsing samples with water and drying in air. Switching parameters were determined by calculating the difference between the equilibrium hexadecane and water static contact angles.

A1.3 Results

A1.3.1 Sessile Drop Contact Angle

Fluorosurfactant complexed to the pulsed plasma maleic anhydride film displayed oleophobicity and hydrophilicity in a fashion similar to that observed previously[2], Table A1.1 and Figure A1.1. The maleic anhydride surfaces complexed to the amphoteric fluorosurfactant showed higher oil repellency (and hence a greater switching parameter) compared to those complexed with the cationic fluorosurfactant—this is due to the lower surface tension of the amphoteric fluorosurfactant ($\gamma_{\text{amphoteric fluorosurfactant}} = 15.5$[6] mN m^{-1}; $\gamma_{\text{cationic fluorosurfactant}} = 28.6$[7] mN m^{-1}). Prior to fluorosurfactant complexation, the maleic anhydride plasma layer displayed the opposite wetting behaviour (water contact angle is greater than hexadecane contact angle).

Pulsed plasma 2-(trifluoromethyl)maleic anhydride polymer films complexed with either cationic or amphoteric fluorosurfactant showed similar wetting properties to the maleic anhydride polymer–fluorosurfactant films however both the water and hexadecane contact angles were higher for the coatings containing 2-(trifluoromethyl)maleic anhydride, Table A1.1 and Figure A1.1. This is due to one of the CH_3 groups in maleic anhydride being exchanged for a CF_3 group in 2-(trifluoromethyl)maleic anhydride) and as a result the coating is slightly more repellent towards both test liquids. This is also observed in the 2-(trifluoromethyl)maleic anhydride polymer films prior to fluorosurfactant complexation. In all cases, the switching parameters for the 2-(trifluoromethyl)maleic anhydride containing coatings are similar to the corresponding maleic anhydride surfaces.

Table A1.1: Water contact angle after 0 s and 10 s (reached equilibrium) and hexadecane contact angle (does not change with time) for pulsed plasma polymer coated flat glass substrates and pulsed plasma polymer surfaces complexed with fluorosurfactant.

Coating	**Contact Angle / °**			
	Water ***t*** **= 0 s**	**Water** ***t*** **= 10 s**	**Hexadecane**	**Switching**
Uncoated glass	25 ± 2	25 ± 2	<10	−15 ± 2
Pulsed plasma maleic anhydride	92 ± 1	77 ± 2	<10	−67 ± 2
Pulsed plasma maleic anhydride–cationic fluorosurfactant	36 ± 11	<10	66 ± 8	56 ± 8
Pulsed plasma maleic anhydride–amphoteric fluorosurfactant	18 ± 6	<10	80 ± 1	70 ± 1
Pulsed plasma 2-(trifluoromethyl)maleic anhydride	95 ± 1	90 ± 2	27 ± 6	−63 ± 6
Pulsed plasma 2-(trifluoromethyl)maleic anhydride–cationic fluorosurfactant	34 ± 12	31 ± 12	83 ± 1	52 ± 12
Pulsed plasma 2-(trifluoromethyl)maleic anhydride–amphoteric fluorosurfactant	18 ± 1	13 ± 3	87 ± 1	74 ± 3

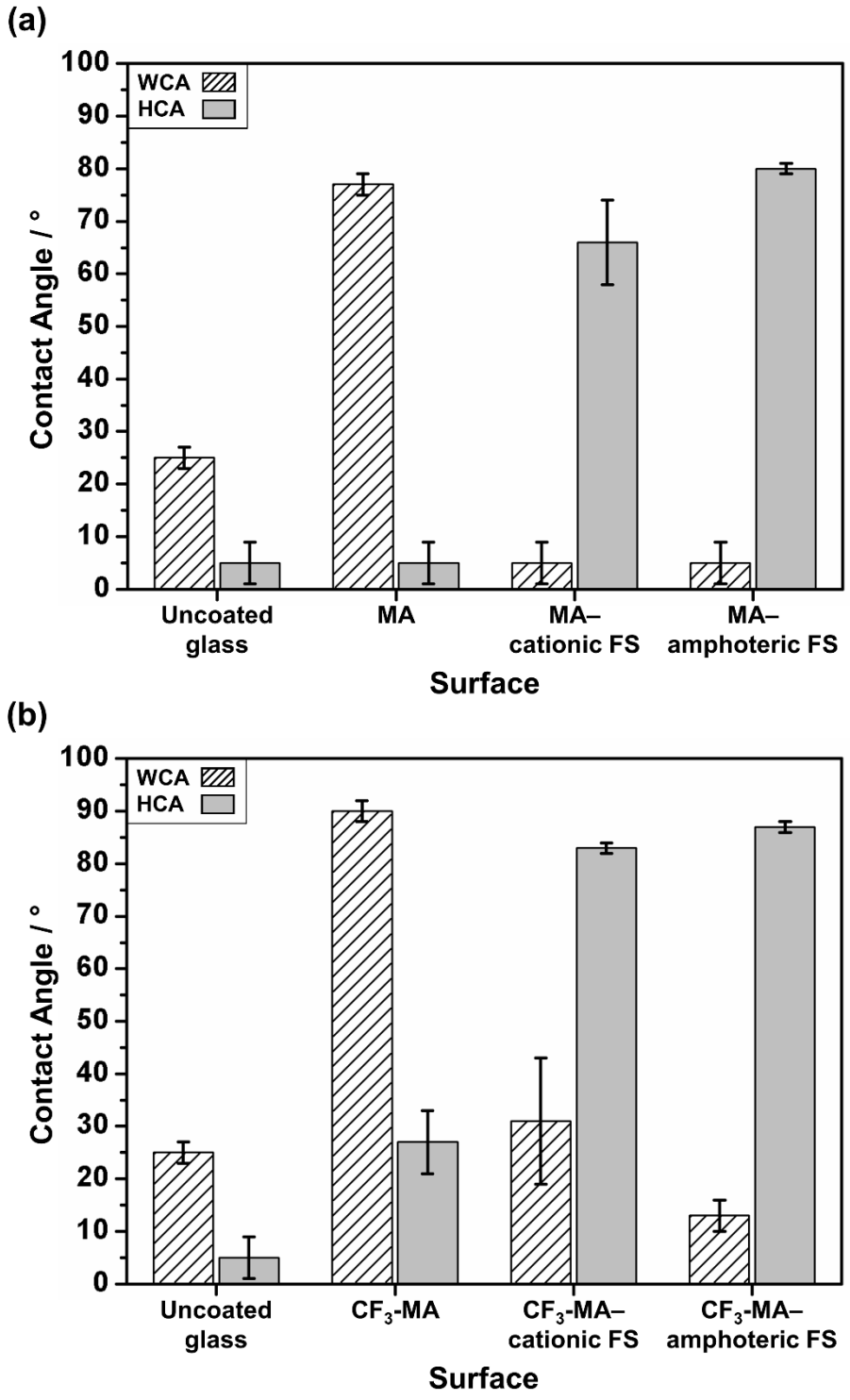

Figure A1.1: Water contact angle (WCA) after 10 s (reached equilibrium) and hexadecane contact angle (HCA; does not change with time) for pulsed plasma polymer coated flat glass substrates and pulsed plasma polymer surfaces complexed with fluorosurfactant. Pulsed plasma polymers are: (a) maleic anhydride (abbreviated as MA); and (b) 2-(trifluoromethyl)maleic anhydride (abbreviated as CF_3-MA). Fluorosurfactant is abbreviated as FS. [Plasma polymerisation performed by A. Carletto]. Error bars denote the sample standard deviation.

A1.4 Discussion

Fast-switching oleophobic–hydrophilic surfaces have been prepared by complexation of fluorosurfactant with plasma polymer coatings, Table A1.1 and Figure A1.1. The fluorosurfactant is able to complex to the polymer backbone through electrostatic interaction.[8,9] Compared to maleic anhydride plasma polymer, polymer–fluorosurfactant films prepared using 2-(trifluoromethyl)maleic anhydride showed an increase in both water and hexadecane contact angles—this can be attributed to the presence of the oleophobic CF_3 groups in the 2-(trifluoromethyl)maleic anhydride plasma polymer. The switching parameters of the polymer–fluorosurfactant coatings are however similar for both the maleic anhydride and 2-(trifluoromethyl)maleic anhydride polymers used.

The oil repellency of plasma polymer–fluorosurfactant complex surfaces can be attributed to the low surface energy terminal CF_3 groups of the fluorosurfactant being orientated towards the air–solid interface.[10] As a result, the hydrophilic ionic surfactant head groups are localised in the sub-surface region where they are complexed to the hydrophilic polymer counterionic groups. Upon contact with the surface, water molecules are able to diffuse towards these underlying hydrophilic groups either via a water-induced surface rearrangement of the fluorosurfactant chains allowing penetration of the water molecules[11], or due to the presence of defects in the fluorinated layer allowing permeation of the water.[12] Oil droplets on the other hand are unable to penetrate any film defects due to their much larger size[13] and so are repelled by the top-most low-surface-energy fluorinated chains.[11] Hence, the plasma polymer–fluorosurfactant complex surfaces display the observed switching oleophobic–hydrophilic properties (the difference between the static water and oil contact angles).

Previously reported plasma polymer–fluorosurfactant complex surfaces have shown a similar oil repellency to that observed in this work however the switching parameters reported here are slightly larger due to the greater hydrophilicity (lower water contact angle).[1,2] Furthermore, the fast-switching time for the reported maleic anhydride and 2-(trifluoromethyl)maleic anhydride plasma polymer–fluorosurfactant coatings (<10 s) is much quicker than that reported for films utilising acrylic acid plasma polymers (70 s).[3] The oil repellency could be enhanced by incorporation of nanoparticles to add surface roughness however this would add additional steps to the fabrication process.[4]

A1.5 Conclusions

Fast-switching oleophobic–hydrophilic coatings have been prepared using plasma polymer–fluorosurfactant complexes. These can be deposited using a two-step process consisting of plasma polymerisation followed by fluorosurfactant complexation. Although not tested, it is envisioned that when coated onto porous substrates (e.g. stainless steel mesh) these surfaces could provide oil–water separation. Other applications could include antifogging surfaces.

A1.6 References

[1] Hutton, S. J.; Crowther, J. M.; Badyal, J. P. S. Complexation of Fluorosurfactants to Functionalized Solid Surfaces: Smart Behavior. *Chem. Mater.* **2000**, *12*, 2282–2286.

[2] Lampitt, R. A.; Crowther, J. M.; Badyal, J. P. S. Switching Liquid Repellent Surfaces. *J. Phys. Chem. B* **2000**, *104*, 10329–10331.

[3] Molina, R.; Gomez, M.; Kan, C.-W.; Bertran, E. Hydrophilic-oleophobic coatings on cellulosic materials by plasma assisted polymerization in liquid phase and fluorosurfactant complexation. *Cellulose* **2014**, *21*, 729–739.

[4] Brown, P. S.; Bhushan, B. Mechanically Durable, Superoleophobic Coatings Prepared by Layer-by-Layer Technique for Anti-Smudge and Oil–Water Separation. *Sci. Rep.* **2015**, *5*, 8701.

[5] Ehrlich, C. D.; Basford, J. A. Recommended Practices for the Calibration and Use of Leaks. *J. Vac. Sci. Technol. A* **1992**, *10*, 1–17.

[6] ChemPoint, DuPont™ Capstone® Fluorosurfactant FS-50 Technical Information. https://www.chempoint.com/products/chemours/capstone-fluorosurfactants/capstone-surfactants-and-coating-additives/capstone-fs-50 (accessed Aug 15, 2019).

[7] Chemguard, Chemguard S-106A Fluorosurfactant Technical Information. https://www.chemguard.com/pdf/specialty-chemicals/datasheets/S-106A%20TDS%2011-09-06.pdf (accessed Sep 27, 2019).

[8] Antonietti, M.; Henke, S.; Thünemann, A. Highly Ordered Materials with Ultra-Low Surface Energies: Polyelectrolyte–Surfactant Complexes with Fluorinated Surfactants. *Adv. Mater.* **1996**, *8*, 41–45.

[9] Goddard, E. D. Polymer–Surfactant Interaction Part II. Polymer and Surfactant of Opposite Charge. *Colloids Surf.* **1986**, *19*, 301–329.

[10] Thünemann, A. F.; Lieske, A.; Paulke, B.–R. Low Surface Energy Coatings from Waterborne Nano-Dispersions of Polymer Complexes. *Adv. Mater.* **1999**, *11*, 321–324.

[11] Yoon, H.; Na, S. H.; Choi, J. Y.; Latthe, S. S.; Swihart, M. T.; Al-Deyab, S. S.; Yoon, S. S. Gravity-Driven Hybrid Membrane for Oleophobic–Superhydrophilic Oil–Water Separation and Water Purification by Graphene. *Langmuir* **2014**, *30*, 11761–11769.

[12] Li, L.; Wang, Y.; Gallaschun, C.; Risch, T.; Sun, J. Why Can a Nanometer-Thick Polymer Coated Surface Be More Wettable to Water than to Oil? *J. Mater. Chem.* **2012**, *22*, 16719–16722.

[13] Wang, Y.; Knapp, J.; Legere, A.; Raney, J.; Li, L. Effect of End-Groups on Simultaneous Oleophobicity/Hydrophilicity and Anti-Fogging Performance of Nanometer-Thick Perfluoropolyethers (PFPEs). *RSC Adv.* **2015**, *5*, 30570–30576.

Appendix 2

Literature Review Tables

A2.1 Simultaneously Oleophobic–Hydrophilic Coatings

Table A2.1: Summary of approaches for the preparation of simultaneously oleophobic-hydrophilic surfaces.

Approach	Materials	Coating Method	Substrates	Water CA / °	Oil CA (hexadecane unless stated otherwise) / °	Switching Parameter / °	Applications Shown	Advantages	Disadvantages	Date Published	Ref
Polymer–fluorosurfactant	Poly(methacrylic acid) / Hoe L 3658-1	Spin	Glass	Glycerol = 41.8	63.0	21.2	–	One-step coating process	Poor hydrophilicity towards glycerol. Poor oleophobicity	14/08/95	1
	Poly[(acrylamidopropyl)trimethylammonium chloride] / Fluowet SB	Solvent casting	Glass and aluminium sheet	75 ± 1	80 ± 1	5	–	One-step coating process	Very poor hydrophilicity. Poor oleophobicity	07/04/99	2
	Poly[(acrylamidophenyldiazosulfonate)-co-(1-hydroxy-2-methylethyl methacrylate)-co-(methacrylate)] / Hoe L 3658-1	Solvent casting	Glass	52	55	3	–	One-step coating process	Poor hydrophilicity. Poor oleophobicity	25/08/99	3
	Poly(ethyleneimine) / Fluowet SB	Solvent casting	Glass	69	80	11	–	One-step coating process	Very poor hydrophilicity. Poor oleophobicity	1999	4
	Polystyrene / Fluoromodified montmorillonite (FOMMT)	Spin	Glass	32 ± 4	58 ± 5	26	–	One-step coating process	Poor hydrophilicity. Very poor oleophobicity	18/04/09	5
	Poly(styrene-co-maleic anhydride) / DuPont Zonyl FSD	Spin	Silicon, glass	<10	112 ± 5	102	Anti-fogging, self-cleaning,	One-step coating process. Fast	Poor oleophobicity	30/04/18 28/05/15	6, 7

	Poly(styrene-alt-maleic anhydride) / DuPont Zonyl FSD	Spin	Silicon, glass	<10	80 ± 2	70	oil–water separation	switching. Good hydrophilicity			
	Poly(diallyldimethyl ammonium chloride) / DuPont Capstone FS-50	Spray (layer-by-layer)	Glass	10 ± 2	79 ± 1	69	Self-cleaning, anti-smudge, anti-fogging, oil–water separation	Good hydrophilicity	Multi-step (4) coating process. After third step samples must be dried at high temperature. Poor oleophobicity	03/03/15 10/09/15	8, 9, 10
Polymer–fluorosurfactant/ nanoparticles	Poly(diallyldimethyl ammonium chloride) / Sodium perfluorooctanoate / SiO_2 (10-25 nm)	Dip	SS mesh	0	95 ± 2	95	Oil–water separation, water soluble dye removal	One-step coating process	Poor oleophobicity	05/09/14	11
	Poly(diallyldimethyl ammonium chloride) / DuPont Capstone FS-50 / SiO_2 (7 nm)	Spray (layer-by-layer)	Glass	<5	157 ± 1	152	Self-cleaning, anti-smudge, anti-fogging, oil–water separation	Excellent hydrophilicity. Excellent oleophobicity	Multi-step (4) coating process. After third step samples must be dried at high temperature	03/03/15 10/09/15	8, 9
Plasma polymer–fluorosurfactant	Acrylic acid plasma polymer / Hoechst AG, Hoe L 3658-1	Plasma polymerisation followed by dip	Glass	<20	82 ± 4	62	–	Plasma deposition allows for a wide range of substrate materials to be used	Two-step coating process. Poor oleophobicity	24/05/00	12
	Maleic anhydride plasma polymer / DuPont Zonyl FSD	Plasma polymerisation followed by dip	Glass	22 ± 2	79 ± 1	57	–	Plasma deposition allows for a wide range of substrate materials to be used	Two-step coating process. Poor oleophobicity	17/08/00	13
Plasma treatment	Poly(ethylene glycol) diacrylate / CF_4 gas	Spin followed by CF_4 plasma treatment	Glass	30.7	60.7	30	–	–	Two-step coating process. Poor hydrophilicity. Poor oleophobicity	06/11/17	14
Fluorosurfactant/ (nano)particle composite	Polyethylene glycol / Zonyl FSN-100 / Ti(OBu)4 / SiO_2	Dip	Glass	15	108	93	Self-cleaning, oil–water separation	Excellent hydrophilicity on polyester fabric. Good oleophobicity on polyester fabric	Complex procedure for preparation of coating solution. Poor oleophobicity on glass	01/12/16	15
			Polyester fabric	0	146	146					
	Capstone FS-50 / TiO_2 (5–10 nm) / TiO_2 (21 nm)	Spray or painting	Various substrates	0	160	160	Oil–water separation, controllable oil transportation	One-step coating process. Excellent hydrophilicity. Excellent oleophobicity.	One-step coating process becomes multi-step if durability is required. Coating	08/03/18	16

	OR Pentadecafluorooctanoic acid (PFOA) / TiO_2 (21 nm) / Tetraethyl orthosilicate (TEOS)							Good durability when adhesive particles added to coating	not transparent (not anti-fogging)		
	Capstone FS-50 / Al_2O_3 NPs	Dip	Cotton	0	154 ± 0.8	154	Removal of water from oil–water mixture by absorption, oil–water separation	One-step coating process. Excellent hydrophilicity. Excellent oleophobicity	Synthesis requires high temp drying of cotton both before and after coating	11/04/19	17
	ZnO tetrapods / Tetraethylorthosilicate (TEOS) / Potassium perfluorooctanesulfonate (PFOS)	Spray (x2) followed by dip	SS mesh	0	Viscous oil = 160 ± 5	160	Oil–water separation	Excellent hydrophilicity. Excellent oleophobicity	Multi-step (3) coating process. ZnO tetrapod synthesis requires extremely high temps (950 °C)	28/05/19	18
	Capstone FS-50 / SiO_2 / Aluminium phosphate	Spray	Glass	0	154.3 ± 1.5	154.3	Oil–water separation	Excellent hydrophilicity. Excellent oleophobicity	Aluminium phosphate synthesis requires high temp. High temp curing steps required after spray coating	26/08/19	19
Fluorinated polymers/polymer blends	3-isocyanatopropyldimethylchlorosilane (ICPDMS) / Zonyl FSN-100	Two step grafting method (2x dip)	Silicon	30 (Adv)	79 (Adv)	49	Self-cleaning, anti-fogging	–	Two-step coating process. Poor hydrophilicity. Poor oleophobicity	31/10/07 06/12/07 19/06/08	20, 21, 22
			Glass fiber membrane discs	30	105	75	Oil–water separation	–	Two-step coating process. Poor hydrophilicity. Poor oleophobicity	01/10/08	23
	3-isocyanatopropyldimethylchlorosilane (ICPDMS) / Zonyl FSO-100	Two step grafting method (2x dip)	Silicon	15 (Adv)	57 (Adv)	42	Anti-fogging	–	Two-step coating process. Poor oleophobicity	06/12/07	21
	f-PEG macromer (from methacryloylchloride and Zonyl FSN) / Hydroxyethyl methacrylate	Spin	Silicon	40 (Adv)	73 (Adv)	33	Anti-fogging	One-step coating process	Poor hydrophilicity. Poor oleophobicity	28/04/11	24

	f-PEG macromer (from methacryloylchloride and Zonyl FSN) / Acrylic acid			41 (Adv)	70 (Adv)	29					
	Zdol (perfluoropolyether (PFPE) polymer)	Dip	Silicon	41.9 ± 1.8	70.7 ± 1.7	28.8	–	One-step coating process	Poor hydrophilicity. Poor oleophobicity	05/07/12	25
		Dip	Silicon	46.5 ± 0.9	70.1 ± 0.9	23.6	Anti-fogging	One-step coating process	Poor hydrophilicity. Poor oleophobicity	25/03/15	26
	Fluorinated 3,4-ethylenedioxythiophene (EDOT) monomer	Electrode position	Gold plate (working electrode)	86	93.3	7.3	–	–	Very poor hydrophilicity. Poor oleophobicity	12/05/15	27
	Z-03 (perfluoropolyether (PFPE) polymer)	Dip followed by UV irradiation (10 min)	Silicon	0	60.6 ± 0.6	60.6	Anti-fogging, self-cleaning	Excellent hydrophilicity	Two-step coating process. Poor oleophobicity	01/06/16	28
	Ztetraol (perfluoropolyether (PFPE) polymer)	Dip	Glass	34.5 ± 0.9	70.6 ± 0.3	36.1	Oil–water separation	One-step coating process. Excellent hydrophilicity on glass membrane	Poor hydrophilicity on glass. Poor oleophobicity. Oil does still pass through coated membrane but at a slower rate than water	29/10/18	29
			Glass membrane	0	93.2 ± 12.4	93.2					
Fluoroalkyl end-capped oligomers	Fluoroalkylated acrylic acid oligomer / dipentaerythritol hexa-acrylate / methyl methacrylate / photo-initiator	Spin followed by light-curing (3 min)	Composite blocks	21	75	54	Self-cleaning	–	Complex synthesis procedure. Two-step coating process. Poor oleophobicity	10/02/08	30
Fluoroalkyl end-capped oligomers/inorganic nanocomposites	Perfluoropolyether dicarboxylic acid / TEOS / SiO_2	Dip	Filter paper	0	Dodecane = 109	109	Oil–water separation	One-step coating process. Excellent hydrophilicity	Poor oleophobicity	05/02/15	31
	Perfluoro-3-di-n-butylaminopropionyl fluoride / $CaCO_3$ / CaF_2 nanocomposite	Dip	PET fabric	0	Dodecane = 105	105	Oil–water separation	One-step coating process. Excellent hydrophilicity	Poor oleophobicity	2016	32

Fluorosilanization	(tridecafluoro-1,1,2,2-tetrahydrooctyl) triethoxysilane	Chemical vapour deposition	Cotton fabric	0	158 ± 3	158	Self-cleaning, oil–water separation	One-step coating process. Excellent hydrophilicity. Excellent oleophobicity	Chemical vapour deposition takes 24 h	18/06/14	33
	(heptadecafluoro-1,1,2,2-tetrahydrodecyl) trichlorosilane	Chemical vapour deposition followed by O_2 plasma treatment	Cellulose filter paper	0	154	154	Paper-based microfluidic devices for oil–water separation	Excellent hydrophilicity. Excellent oleophobicity	Multi-step (3) coating process (one of which is a plasma step)	22/06/16 01/09/16	34, 35
Membranes	1H,1H,2H,2H-Heptadecafluorodecyl polyhedral oligomeric silsequioxane (Fluorodecyl POSS) / Polydimethylsiloxane (PDMS)	Spin followed by applied electric field	PDMS sheet	56	72	16	Oil–water separation	–	Two-step coating process. Poor hydrophilicity. Poor oleophobicity	12/06/12	36
	Poly(vinylidene fluoride) (PVDF) / Additive polymer AP1 (PVDF backbone with side chains containing hydrophilic internal segments and oleophobic terminal segments)	Dry wet spinning	Membrane	26 ± 2.60	74 ± 5.92	48	Anti-fouling	–	Complex synthesis procedure. Poor oleophobicity	19/02/13	37
				26 ± 2	75 ± 3	49		–	Complex synthesis procedure. Poor oleophobicity	24/04/14	38
	Graphene oxide grafted poly(acrylonitrile-co-maleimide)-polyethersulfone membrane	Dry wet spinning	Membrane	22.6 ± 2.5	Dichloroethane: 112.5 ± 3.2	89.9	Oil–water separation	–	Complex synthesis procedure. Poor oleophobicity.	19/07/16	39
	Triblock copolymer additive containing both hydrophilic and oleophobic segments [P(VDF-co-CTFE)-g-PMAA-g-fPEG]	Dry wet spinning	Polyvinylidene fluoride (PVDF) membrane	36	72	36	Oil–water separation	–	Triblock copolymer additive requires multi-step synthesis. Poor hydrophilicity. Poor oleophobicity	03/04/18	40

Polycrystalline anatase TiO_2 thin films	Titanium isopropoxide	Dip followed by UV illumination (48 h)	Glass	2	25	23	–	Excellent hydrophilicity	Two-step coating process. Samples must be calcined at very high temperature after first step. Very poor oleophobicity	01/06/00	41
Non-fluorinated materials	Methyltrimethoxysilane (MTMS) / Hydrochloric acid	Dip	Porous paper handsheets	0	Motor oil = 64.7 ± 1.4	64.7	–	One-step coating process using environmentally friendly materials. Excellent hydrophilicity	Poor oleophobicity	12/06/15	42
	Methyltrimethoxysilane (MTMS) / Hydrochloric acid	Dip	SS mesh	<10	Motor oil = 57	47	Oil–water separation	One-step coating process using environmentally friendly materials. Good hydrophilicity	Very poor oleophobicity	09/05/17	43

A2.2 Oleophobic–Hydrophobic to Hydrophilic Switching Coatings

Table A2.2: Summary of approaches for the fabrication of oleophobic-hydrophobic to hydrophilic switching surfaces.

Approach	Materials	Coating Method	Substrates	Water CA / ° (t = 0 s)	Water CA / ° (after switching)	Switching time	Oil CA (hexadecane unless stated otherwise) / °	Switching Parameter / °	Applications Shown	Advantages	Disadvantages	Date Published	Ref
Polymer–fluorosurfactant	Poly(diallyldimethylammonium chloride) / Sodium perfluorooctanoate	Spin	Glass	97 ± 1	52 ± 2	10 min	72	20	Anti-fouling, oil–water separation	One-step coating process	Very slow switching. Poor hydrophilicity. Poor oleophobicity. Plasma treatment decreases switching time but this limits possible applications	21/12/11	44
	Chitosan / Sodium perfluorooctanoate	Spray	Glass	–	67 ± 2	10 min	134 ± 1	67	Anti-fouling, oil–water separation	One-step coating process	Very slow switching. Very poor hydrophilicity. Chitosan must be dissolved in acid before use adding materials and costs to the process	27/03/14	45
	Poly(ethylene-alt-maleic anhydride) / DuPont Zonyl FSD	Spin	Silicon, glass	88 ± 2	<10	10 s	74 ± 1	64	Anti-fogging, self-cleaning, oil–water separation	One-step coating process. Fast switching. Good hydrophilicity	Poor oleophobicity	30/04/14 28/05/15	6, 7
	Poly(diallyldimethylammonium chloride) / Sodium perfluorooctanoate	Spray	SS mesh	123 ± 2	42 ± 2	7 min	83 ± 2	41	Oil–water separation	One-step coating process	Very slow switching. Poor hydrophilicity. Poor oleophobicity. Plasma treatment decreases switching time	28/01/15	46

											but this limits possible applications		
	Poly(diallyldimethylammonium chloride) / Poly(sodium 4-styrene sulfonate) / Sodium perfluorooctanoate	Dip (layer-by-layer)	Glass	110 ± 1	28 ± 1	5 h of UV irradiation	75 ± 2 (before and after UV irradiation)	47	Anti-fouling, oil–water separation	Excellent hydrophilicity on cotton fabric. Excellent oleophobicity on cotton fabric	Multi-step (6 layers) coating process. Very slow switching (5 h UV illumination). Poor oleophobicity on glass	17/09/16	47
			Cotton fabric	156 ± 1	0	5 h of UV irradiation	150 ± 1 (before and after UV irradiation)	150					
Polymer–fluorosurfactant/nanoparticles	Poly(diallyldimethylammonium chloride) / Sodium perfluorooctanoate / SiO_2	Spray	Glass	165 ± 2	0	9 min	155 ± 1	155	Anti-fouling, oil–water separation	One-step coating process. Excellent hydrophilicity. Excellent oleophobicity	Very slow switching. Plasma treatment decreases switching time but this limits possible applications	21/12/11	44
	Chitosan / Sodium perfluorooctanoate / SiO_2 (20 nm)	Spray	Glass	–	0	20 s	157 ± 1	157	Anti-fouling, oil–water separation	One-step coating process. Excellent hydrophilicity. Excellent oleophobicity	Chitosan must be dissolved in acid before use adding materials and costs to the process	27/03/14	45
	Poly(diallyldimethylammonium chloride) / Sodium perfluorooctanoate / SiO_2 (20 nm)	Spray	SS mesh	167 ± 1	0	7 min	158 ± 1	158	Oil–water separation	One-step coating process. Excellent hydrophilicity. Excellent oleophobicity	Very slow switching. Plasma treatment decreases switching time but this limits possible applications	28/01/15	46
	Chitosan / Sodium perfluorononanoate / Fe_3O_4 (30 nm)	Dip	Melamine sponge	–	0	4.8 s	142 ± 2	142	Removal of water from oil–water mixture by absorption, oil–water separation	One-step coating process. Ultrafast switching. Excellent hydrophilicity. Good oleophobicity	Chitosan must be dissolved in acid before use adding materials and costs to the process. Coated sponges must be dried at high temperature	19/10/16	48

	Poly(diallyldimethylammonium chloride) / Sodium perfluorooctanoate / Tetraethyl orthosilicate / Carbon soot	Candle soot coating / Chemical vapour deposition / Solvent casting	SS mesh	43	0	60 s	137	137	Oil–water separation	Excellent hydrophilicity. Good oleophobicity	Multi-step (3) coating process. Slow switching	07/02/17	49
	Poly(diallyldimethylammonium chloride) / Capstone FS-63 / SiO_2 (7 nm)	Spray	Glass	54 ± 17	<10	<10 s	138 ± 5	128	**Oil–water separation and antibacterial**	One-step coating process. Fast switching. Excellent hydrophilicity. Good oleophobicity. **First reported paper showing an antibacterial oleophobic(in air)–hydrophilic coating**	–	11/10/18	This work 50
			SS mesh	–	0	<10 s	143 ± 4	143					
Plasma polymer–fluorosurfactant	Acrylic acid plasma polymer (from liquid) / Chemguard S-106A	Plasma polymerisation followed by dip	Filter paper	119	0	70 s	76	76	–	Excellent hydrophilicity. Plasma deposition allows for a wide range of substrate materials to be used	Two-step coating process. Slow switching. Poor oleophobicity	04/12/13	51
Fluorosurfactant/(nano)particle composite	Heptadecafluorononanoic acid / $Ti(OBu)_4$ / SiO_2 (100-170 nm)	Dip	Polyester fabric	152 (absence of ammonia vapour)	0 (in presence of ammonia vapour)	3 s	151 (both in presence and absence of ammonia vapour)	151	Removal of water from oil–water mixture by absorption, oil–water separation	One-step coating process. Ultrafast switching. Excellent hydrophilicity. Excellent oleophobicity	Switching requires exposure to ammonia vapour	18/02/15	52
	Perfluorooctanoic acid / Kaolin / Diethoxydimethylsilane (DEDMS) / Triethoxymethylsilane (MTES)	Solvent casting	Glass	–	0	2 s	151 ± 1	151	Self-cleaning	One-step coating process. Ultrafast switching. Excellent hydrophilicity. Excellent oleophobicity	Kaolin particles must be dried at high temperature for 5 h to remove water before use. Coated substrates must	13/12/16	53

											be dried at high temperature		
	SiO_2 nanoparticles / fluorinated alkyl-polyethylene glycol phosphate (FA-PEG-phosphate) / 1H,1H,2H,2H-perfluorodecyltriethoxysilane (FAS)	Dip	Cotton fabric	>90	0	1.58 s	153	153	Anti-fouling	Ultrafast switching. Excellent hydrophilicity. Excellent oleophobicity	Two-step coating process	23/07/18	54
	Perfluorooctanoic acid / Kaolin / bis(3-trimethoxysilylpropyl)amine	Solvent casting	Glass	–	0	2 s	151 ± 1	151	Removal of water from oil–water mixture by absorption, oil–water separation, water-soluble dye removal, self-cleaning	One-step coating process. Ultrafast switching. Excellent hydrophilicity. Excellent oleophobicity	Kaolin particles must be dried at high temperature for 5 h to remove water before use. Coated substrates must be dried at high temperature. Separation efficiency a little low (92%)	11/09/18	55
	Perfluorooctanoic acid / Kaolin / bis[3-(trimethoxysilyl)propyl]ethylene diamine	Solvent casting	Glass	125	0	A few mins (treatment at pH >12)	150	150	Oil–water separation	One-step coating process. Excellent hydrophilicity (after treatment at pH >12). Excellent oleophobicity	Slow switching (requiring treatment at pH>12). Coated substrates must be dried at high temperature	18/06/19	56
Fluorinated polymers/polymer blends	Hydroxy(polyethyleneoxy)-propylether-terminated PDMS block copolymer / 4,4'-methylene-bis(phenylene isocyanate) / 1,2-diol functional PFPE / 2,2,3,3-tetrafluoro-1,4-butanediol	Solvent casting	–	115	34	60 min	60	26	Oil and dirt repellent surfaces	–	Complex synthesis procedure. Very slow switching. Poor hydrophilicity. Very poor oleophobicity	26/03/02	57

	1-(1H,1H,2H,2H-perfluorodecyloxy)-3-(3,6,9-trioxadecyloxy)-propan-2-yl acrylate / 2-(N,N-dimethylamino)ethyl methacrylate	Spin	Glass	48	28	30 s	70	42	Anti-fogging, oil-repellent surfaces	–	Complex synthesis procedure. Poor oleophobicity	21/07/10	58
	Poly(ethylene glycol) diacrylate (PEGDA) / 2-hydroxy-2-methyl propiophenone (Darocurl 173) / 1H,1H,2H,2H-heptadecafluorodecyl polyhedral oligomeric silsequioxane (fluorodecyl POSS)	Dip followed by UV illumination (5 min)	SS mesh	–	0	100 s	Rapeseed oil = 125 (Adv)	125	Oil–water separation	Excellent hydrophilicity. Excellent oleophobicity on polyester fabric	Two-step coating process. Slow switching on SS mesh. Very slow switching on polyester fabric	28/08/12 22/12/11	59, 60
			Polyester fabric	–	0	1400 s	Rapeseed oil = 152 (Adv)	152					
	Fluorinated 3,4-ethylenedioxypyrrole (EDOP) monomer / Bis(trifluoromethane)sulfonimide salts	Electrodeposition	Gold plate (working electrode)	Unstable (CA decreases until it reaches a stable state)	–	–	79.3–115.7	–	–	–	Monomer synthesis is complex (9 steps). Unknown switching time and final WCA. Poor oleophobicity	18/07/13	61
	3,4-ethylenedioxythiophene (EDOT)-Py^+ / 3,4-ethylenedioxythiophene (EDOT)-F_8 monomers	Electro-codeposition	Gold plate (working electrode)	155	78	30 min reduction at -1 V vs SCE	Diiodomethane = 128	50	–	–	Monomer syntheses are complex. Very slow switching requiring reduction at -1 V. Very poor hydrophilicity	18/04/14	62
	F-PEG (Zonyl FS-3100) / 1,6-diisocyanatohexane	Two-step grafting method (2x dip)	Cellulose sponge	–	0	5 s	120	120	Oil–water separation, anti-fouling	Fast switching. Excellent hydrophilicity.	Lengthy (2 day), complex method to prepare cellulose sponge. Two-step coating process	26/06/17	63

	Poly (ethylene glycol)diacrylate / 2-carboxyethyl acrylate / 1H,1H-perfluoro-n-decyl-functionalized pentaerythritol tetra(3-mercaptopropionate) (F-PETMP) / SiO_2 / 2,2-dimethoxy-2-phenylacetophenone (DMPA) (photoinitiator)	Spray followed by UV photopolymerisation (5 min)	Glass	57.2	0	9 s	155.6	155.6	Oil–water separation	Fast switching. Excellent hydrophilicity. Excellent oleophobicity	Two-step coating process	31/08/18	64
Fluoroalkyl end-capped oligomers	Fluoroalkylated trimethoxyvinylsilane-acryloylmorpholine co-oligomers	–	Glass	72	0	30 min	Dodecane = 60	60	–	Excellent hydrophilicity	Very slow switching. Very poor oleophobicity	18/05/96 16/09/97	65, 66
	Fluoroalkylated co-oligomer of *N,N*-dimethylacrylamide and methacrylate monomer-bearing silsequioxane unit	Dip	PMMA film	60	30	30 min	Dodecane = 34	4	–	One-step coating process	Very slow switching. Very poor oleophobicity	16/11/01	67
	Fluoroalkylated *N,N*-dimethylacrylamide oligomer / phthalocyanine complex	Solvent casting	Polystyrene film	11	0	30 min	Dodecane = 53	53	–	One-step coating process. Excellent hydrophilicity	Very slow switching. Very poor oleophobicity	26/12/03	68
Fluoroalkyl end-capped oligomers/inorganic polymer hybrids	Fluoroalkylated *N,N*-dimethylacrylamide oligomer / SiO_2 polymer hybrid	Dip	Glass	44	0	30 min	Dodecane = 42	42	–	One-step coating process. Excellent hydrophilicity	Very slow switching. Very poor oleophobicity	04/01/05	69
	Fluoroalkylated acrylic acid oligomer / SiO_2 polymer hybrid-	Dip	Glass	25	0	30 min	Dodecane = 57	57	Anti-bacterial surfaces	One-step process. Excellent hydrophilicity	Very slow switching. Very poor oleophobicity	04/05/05	70

	hibitane composite												
	Fluoroalkylated 2-methacryloxyethannesulfonic acid-N,N-dimethylacrylamide co-oligomer / SiO_2 polymer hybrid	Dip	Glass	9	0	5 min	Dodecane = 51	51	–	One-step coating process. Excellent hydrophilicity	Very slow switching. Very poor oleophobicity	13/04/06	71
	Fluoroalkylated vinyltrimethoxysilane-SiO_2 oligomeric nanoparticles / tributyl[3-(trimethoxysilyl)propyl]phosphonium chloride ionogel	Solvent casting	PMMA film	52	0	30 min	Dodecane = 33	33	–	One-step coating process. Excellent hydrophilicity	Very slow switching. Very poor oleophobicity	29/03/16	72
Fluoroalkyl end-capped oligomers/inorganic nanocomposites	Fluoroalkylated acrylic acid oligomer / hydroxyapatite nanocomposite	Dip	Glass	27	0	15 min	Dodecane = 58	58	–	One-step coating process. Excellent hydrophilicity	Very slow switching. Very poor oleophobicity	08/02/08	73
	Fluoroalkylated acrylic acid oligomer / SiO_2 nanocomposite	Spray	Aluminium plate	–	12	A few seconds	Oleic triglyceride = 62	50	–	One-step coating process. Ultrafast switching	Very poor oleophobicity	18/09/08	74
	Fluoroalkylated vinyltrimethoxysilane oligomer / tri-n-butyl-[(3-trimethoxysilyl)propyl] phosphonium chloride / SiO_2 nanocomposite	Dip	Glass	10	0	5 min	Dodecane = 62	62	–	One-step coating process. Excellent hydrophilicity	Very slow switching. Very poor oleophobicity	04/08/10	75
	Fluoroalkylated vinyltrimethoxysilane oligomer / $CaSi_2$ nanocomposite	Dip	Glass	129	0	5 min	Dodecane = 118	118	–	One-step coating process. Excellent hydrophilicity	Very slow switching. Poor oleophobicity	13/09/14	76
	Perfluoropolyether dicarboxylic acid / TEOS /	Dip	Glass	63	0	10 min	Dodecane = 129	129	Oil–water separation	One-step coating process. Excellent hydrophilicity	Very slow switching. Poor oleophobicity	05/02/15	31

	SiO_2 nanocomposite												
	Perfluoro-3-di-n-propylaminopropionyl fluoride / $CaCO_3$ / CaF_2 nanocomposite	Dip	Glass	150	0	5 min	Dodecane = 117	117	Oil–water separation	One-step coating process. Excellent hydrophilicity	Very slow switching. Poor oleophobicity	2016	32
	Fluoroalkyl end-capped vinyltrimethoxysilane oligomeric silica nanocomposite	Dip	Glass	137	0	25 min	Dodecane = 97	97	Fluorocarbon oil–hydrocarbon oil separation	One-step coating process. Excellent hydrophilicity	Very slow switching. Poor oleophobicity	20/07/17	77
	Fluoroalkyl end-capped vinyltrimethoxysilane oligomeric silica / phosphonic acid nanocomposite	Solvent casting	Glass	–	0	10 s	Dodecane = 107	107	–	One-step coating process. Fast switching. Excellent hydrophilicity	Poor oleophobicity. Wetting is surprisingly opposite on filter paper	2017	78
Membrane	Poly(methacrylic acid) (PMAA) / sodium 1-dodecanesulfonate (SDS) / 3-aminopropyltriethoxysilane (APTS)	Plasma induced graft polymerisation followed by dip	Polyvinylidene fluoride (PVDF) membrane	17	3	6 s	Diiodomethane = 68	65	Anti-fouling	Fast switching. Excellent hydrophilicity.	Complex synthesis procedure. Two-step coating process. Very poor oleophobicity	04/02/19	79

A2.3 Antibacterial Oil–Water Separation

Table A2.3: Summary of approaches for the preparation of surfaces which are antibacterial and can also separate oil and water.

Coating Type	Materials	Coating Method	Substrates	Water CA / °	Hexadecane CA / °	Switching Parameter / °	Antibacterial Properties	Applications	Advantages	Disadvantages	Date published	Ref
Hydrophilic–Underwater Oleophobic	pH-responsive copolymer / Poly(ureaformaldehyde) nanoparticles / Hexamethylene diisocyanate	Spray coating	Cotton fabric	150 (pH> 7). 120 -> 0 (pH = 1, after 15 s)	Dichloromethane = 155.2 (underwater)	155.2 (pH = 1, after 15 s)	*E. coli* (88.67% [pH = 1])	Oil–water separation. Antibacterial	Ability to switch wettability	Is only oleophobic underwater. Poor antibacterial properties. Have to change pH to switch surface (immerse in pH solution for 30 min and dry at 80 °C).	14/08/17	80
	Polydopamine / Silver particles / 1-dodecanethiol / 11-mercaptoundecanoic acid	Dip coating	Cotton fabric	153 (droplet of pH = 1-7). 0 (droplet of pH = 13, t = 25 s)	–	–	*E. coli* (85% [4.5h]) and *S. aureus* (80% [4.5h])	Oil–water separation. Antibacterial	Ability to switch wettability	Is only oleophobic underwater. Poor antibacterial properties. Have to change pH to switch surface. Multiple step method	01/11/18	81
	Chitosan / Glutaraldehyde	Dip coating	Polyphenylene sulfide membrane	0	Trichloromethane = 152.16 (underwater)	152.16	*S. aureus* (inhibition zone measurements)	Oil–water separation. Antibacterial	Use of chitosan, a green and inexhaustible resource in nature	Is only oleophobic underwater. Antibacterial properties only tested against S. aureus – no data though	22/01/19	82
	Chitosan / Glutaraldehyde	Dip coating	Polypropylene membrane	0	Trichloromethane = 154.1 (underwater)	154.1	*E. coli* (plate counting – only images are shown, no data) and *S. aureus* (inhibition zone measurements)	Oil–water separation. Antibacterial	Use of chitosan, a green and inexhaustible resource in nature	Is only oleophobic underwater. Antibacterial properties don't look to be too excellent – no data though	21/05/19	83

Janus membrane	Silver nanoparticles / Stearic acid (one side)	Dip coating	Cellulose membrane	Hydrophilic side = 0. Hydrophobic side = 150.3	Hydrophilic side = 0. Hydrophobic side = 0	–	*E. coli* and *S. aureus* (inhibition zone measurements)	Oil–water separation. Antibacterial	Can separate both water-in-oil and oil-in-water emulsions	Janus membrane: hydrophilic side is underwater oleophobic. Long, multiple step synthesis. Antibacterial properties arise due to leaching of Ag NPs	07/08/19	84
Oleophilic–Hydrophobic	Reduced graphene oxide	Dip coating	Cloth (sparse and dense)	130 (sparse), 141 (dense)	Not reported but oleophilic	–	*E. coli* Sparse cloth kills: 40% (8h), 60% (16h), 75% (24h), Dense cloth kills: 80% (8h), 95% (16h), 98% (24h)	Oil–water separation (sparse). Oil absorption (dense). Antibacterial	Thermal reduction of GO avoids use of toxic reducing agents and allows in situ reduction	Undesirable wetting (WCA>HCA). Poor antibacterial properties. Multiple heating/drying steps.	16/06/16	85
	Polydopamine / Silver nanoparticles / 1H,1H,2H,2H-perfluorodecanethiol	Electrospinning of membrane	Poly(lactic acid) membrane	158.6 ± 1.2	0	−158.6	*E. coli* (98.2% [6h]) and *S. aureus* (99.0% [6h])	Oil–water separation. Antibacterial	Membrane is biodegradable	Undesirable wetting (WCA>HCA). Multiple step synthesis.	20/09/18	86
	Cyanuric chloride / Chloropropyltriethoxysilane	Hydrogel -> Aerogel (by freeze-drying)	Nanocrystalline cellulose (NCC) aerogel	–	–	–	*E. coli* (log reduction = 5.89 (5 min) and *S. aureus* (log reduction = 6.19 (5 min). All bacteria killed after 5 min	Oil absorption from oil–water mixture. Antibacterial	Excellent antibacterial properties	Undesirable wetting (WCA>HCA). Long, multiple step synthesis.	11/04/19	87
Oleophobic–Hydrophilic	Poly(diallyldimethylammonium chloride) / Capstone FS-63 / SiO_2 (7 nm)	Spray	Cloth	<10	142 ± 6	142	*E. coli* (+99.99% killing) and *S. aureus* (+99.97% killing)	Oil–water separation. Antibacterial	One-step coating process. Fast switching. Excellent hydrophilicity. Good oleophobicity. **First reported paper showing an**	–	11/10/18	This work 50

									antibacterial oleophobic(in air)– hydrophilic coating			

A2.4 References

[1] Antonietti, M.; Henke, S.; Thünemann, A. Highly Ordered Materials with Ultra-Low Surface Energies: Polyelectrolyte-Surfactant Complexes with Fluorinated Surfactants. *Adv. Mater.* **1996**, *8*, 41–45.

[2] Thünemann, A. F.; Lochhaas, K. H. Surface and Solid-State Properties of a Fluorinated Polyelectrolyte-Surfactant Complex. *Langmuir* **1999**, *15*, 4867–4874.

[3] Thünemann, A. F.; Schnoller, U.; Nuyken, O.; Voit, B. Self-Assembled Complexes of Diazosulfonate Polymers with Low Surface Energies. *Macromolecules* **1999**, *32*, 7414–7421.

[4] Thünemann, A. F.; Lieske, A.; Paulke, B.-R. Low Surface Energy Coatings from Waterborne Nano-Dispersions of Polymer Complexes. *Adv. Mater.* **1999**, *11*, 321–324.

[5] Turri, S.; Valsecchi, R.; Vigano, M.; Levi, M. Hydrophilic-oleophobic behaviour in thin films from fluoromodified nanoclays and polystyrene. *Polym. Bull.* **2009**, *63*, 235–243.

[6] Brown, P. S.; Atkinson, O. D. L. A.; Badyal, J. P. S. Ultrafast Oleophobic-Hydrophilic Switching Surfaces for Antifogging, Self-Cleaning, and Oil-Water Separation. *ACS Appl. Mater. Interfaces* **2014**, *6*, 7504–7511.

[7] Badyal, J. P. S; Atkinson, O. D. L. A.; Brown, P. S. Ultra Fast Oleophobic-Hydrophilic Switching Surfaces. World Patent WO 2015075446 A2, May 28, 2015.

[8] Brown, P. S.; Bhushan, B. Mechanically durable, superoleophobic coatings prepared by layer-by-layer technique for anti-smudge and oil-water separation. *Sci. Rep.* **2015**, *5*, 8701.

[9] Brown, P. S.; Bhushan, B. Bioinspired, roughness-induced, water and oil super-philic and super-phobic coatings prepared by adaptable layer-by-layer technique. *Sci. Rep.* **2015**, *5*, 14030.

[10] Bhushan, B.; Brown, P. S. Multilayer Coatings and Methods of Making and Using Thereof. World Patent WO 2017034616 A1, Mar. 2, 2017.

[11] Yoon, H.; Na, S.-H.; Choi, J.-Y.; Latthe, S. S.; Swihart, M. T.; Al-Deyab, S. S.; Yoon, S. S. Gravity-Driven Hybrid Membrane for Oleophobic-Superhydrophilic Oil-Water Separation and Water Purification by Graphene. *Langmuir* **2014**, *30*, 11761–11769.

[12] Hutton, S. J.; Crowther, J. M.; Badyal, J. P. S. Complexation of Fluorosurfactants to Functionalized Solid Surfaces: Smart Behavior. *Chem. Mater.* **2000**, *12*, 2282–2286.

[13] Lampitt, R. A.; Crowther, J. M.; Badyal, J. P. S. Switching Liquid Repellent Surfaces. *J. Phys. Chem. B* **2000**, *104*, 10329–10331.

[14] Peng, S.; Ma, Y. Fabrication of Hydrophilic and Oil-Repellent Surface via CF_4 Plasma Treatment. *Mater. Des.* **2018**, *139*, 293–297.

[15] Shen, T.; Li, S.; Wang, Z.; Wang, L. Rare bi-wetting TiO2-F/SiO2/F-PEG fabric coating for self-cleaning and oil/water separation. *RSC Adv.* **2016**, *6*, 115196–115203.

[16] Li, F.; Wang, Z.; Huang, S.; Pan, Y.; Zhao, X. Flexible, Durable, and Unconditioned Superoleophobic/Superhydrophilic Surfaces for Controllable Transport and Oil–Water Separation. *Adv. Funct. Mater.* **2018**, *28*, 1706867.

[17] Li, F.; Bhushan, B.; Pan, Y.; Zhao, X. Bioinspired Superoleophobic/Superhydrophilic Functionalized Cotton for Efficient Separation of Immiscible Oil-Water Mixtures and Oil-Water Emulsions. *J. Colloid Interface Sci.* **2019**, *548*, 123–130.

[18] Bajpayee, A.; Alivio, T. E. G.; McKay, P.; Banerjee, S. Functionalized Tetrapodal ZnO Membranes Exhibiting Superoleophobic and Superhydrophilic Character for Water/Oil Separation Based on Differential Wettability. *Energy Fuels* **2019**, *33*, 5024–5034.

[19] Sun, Y.; Guo, Z. Novel and Cutting-Edge Applications for a Solvent-Responsive Superoleophobic–Superhydrophilic Surface: Water-Infused Omniphobic Surface and Separating Organic Liquid Mixtures. *Chem. Eng. J.* **2020**, *381*, 122629.

[20] Howarter, J. A.; Youngblood, J. P. Self-Cleaning and Anti-Fog Surfaces via Stimuli-Responsive Polymer Brushes. *Adv. Mater.* **2007**, *19*, 3838–3843.

[21] Howarter, J. A.; Youngblood, J. P. Self-Cleaning and Next Generation Anti-Fog Surfaces and Coatings. *Macromol. Rapid Commun.* **2008**, *29*, 455–466.

[22] Youngblood, J. P.; Howarter, J. A. Stimuli-Responsive Polymeric Surface Materials. U.S. Patent US 20080146734 A1, Nov. 30, 2007.

[23] Howarter, J. A.; Youngblood, J. P. Amphiphile grafted membranes for the separation of oil-in-water dispersions. *J. Colloid Interface Sci.* **2009**, *329*, 127–132.

[24] Howarter, J. A.; Genson, K. L.; Youngblood, J. P. Wetting Behavior of Oleophobic Polymer Coatings Synthesized from Fluorosurfactant-Macromers. *ACS Appl. Mater. Interfaces* **2011**, *3*, 2022–2030.

[25] Li, L.; Wang, Y.; Gallaschun, C.; Risch, T.; Sun, J. Why can a nanometer-thick polmyer coated surface be more wettable to water than to oil? *J. Mater. Chem.* **2012**, *22*, 16719–16722.

[26] Wang, Y.; Knapp, J.; Legere, A.; Raney, J.; Li, L. Effect of end-groups on simultaneous oleophobicity/hydrophilicity and anti-fogging performance of nanometer-thick perfluoropolyethers (PFPEs). *RSC Adv.* **2015**, *5*, 30570–30576.

[27] Darmanin, T.; Guittard, F. Highly Polar Linkers (Urea, Carbamate, Thiocarbamate) for Superoleophobic/Superhydrophobic or Oleophobic/Hydrophilic Properties. *Adv. Mater. Interfaces* **2015**, *2*, 1500081.

[28] Wang, Y.; Dugan, M.; Urbaniak, B.; Li, L. Fabricating Nanometer-Thick Simultaneously Oleophobic/Hydrophilic Polymer Coatings via a Photochemical Approach. *Langmuir* **2016**, *32*, 6723–6729.

[29] Wang, Y.; You, C.; Kowall, C.; Li, L. A Nanometer-Thick, Mechanically Robust, and Easy-to-Fabricate Simultaneously Oleophobic/Hydrophilic Polymer Coating for Oil–Water Separation. *Ind. Eng. Chem. Res.* **2018**, *57*, 15395–15399.

[30] Okada, A.; Nikaido, T.; Ikeda, M.; Okada, K.; Yamauchi, J.; Foxton, R. M.; Sawada, H.; Tagami, J.; Matin, K. Inhibition of Biofilm Formation using Newly Developed Coating Materials with Self-cleaning Properties. *Dent. Mater. J.* **2008**, *27*, 565–572.

[31] Sumino, E.; Saito, T.; Noguchi, T.; Sawada, H. Facile creation of superoleophobic and superhydrophilic surface by using perfluoropolyether dicarboxylic acid/silica nanocomposites. *Polym. Adv. Technol.* **2015**, *26*, 345–352.

[32] Saito, T.; Tsushima, Y.; Honda, T.; Kamiya, T.; Fujita, M.; Sawada, H. Facile Creation of Modified Surface Possessing the Controlled Wettability between Superamphiphobic and Superoleophobic-Superhydrophilic Characteristics by using Perfluorocarboxamides/Calcium Carbonate/Calcium Fluoride Nanocomposites: Application to the Separation of Oil and Water. *J. Compos. Mater.* **2016**, *50*, 3831–3842.

[33] Pan, S.; Guo, R.; Xu, W. Durable Superoleophobic Fabric Surfaces with Counterintuitive Superwettability for Polar Solvents. *AIChE J.* **2014**, *60*, 2752–2756.

[34] Li, C.; Boban, M.; Snyder, S. A.; Kobaku, S. P. R.; Kwon, G.; Mehta, G.; Tuteja, A. Paper-Based Surfaces with Extreme Wettabilities for Novel, Open-Channel Microfluidic Devices. *Adv. Funct. Mater.* **2016**, *26*, 6121–6131.

[35] Tuteja, A.; Li, C. Silane Based Surfaces with Extreme Wettabilities. U.S. Patent US 2016251803 A1, Jan. 9, 2016.

[36] Kwon, G.; Kota, A. K.; Li, Y.; Sohani, A.; Mabry, J. M.; Tuteja, A. On-Demand Separation of Oil-Water Mixtures. *Adv. Mater.* **2012**, *24*, 3666–3671.

[37] Zhu, X.; Loo, H.-E.; Bai, R. A novel membrane showing both hydrophilic and oleophilic surface properties and its non-fouling performances for potential water treatment applications. *J. Membrane Sci.* **2013**, *436*, 47–56.

[38] Zhu, X.; Tu, W.; Wee, K.-H.; Bai, R. Effective and low fouling oil/water separation by a novel hollow fiber membrane with both hydrophilic and oleophobic surface properties. *J. Membrane Sci.* **2014**, *466*, 36–44.

[39] Prince, J. A.; Bhuvana, S.; Anbharasi, V.; Ayyanar, N.; Boodhoo, K. V. K.; Singh, G. Ultra-wetting graphene-based PES ultrafiltration membrane - A novel approach for successful oil-water separation. *Water Res.* **2016**, *103*, 311–318.

[40] Shen, S. S.; Liu, K. P.; Yang, J. J.; Li, Y.; Bai, R. B.; Zhou, X. J. Application of a Triblock Copolymer Additive Modified Polyvinylidene Fluoride Membrane for Effective Oil/Water Separation. *R. Soc. Open Sci.* **2018**, *5*, 171979.

[41] Nakajima, A.; Koizumi, S.-I.; Watanabe, T.; Hashimoto, K. Photoinduced Amphiphilic Surface on Polycrystalline Anatase TiO2 Thin Films. *Langmuir* **2000**, *16*, 7048–7050.

[42] Tang, Z.; Hess, D. W.; Breedveld, V. Fabrication of Oleophobic Paper with Tunable Hydrophilicity by Treatment with Non-Fluorinated Chemicals. *J. Mater. Chem. A* **2015**, *3*, 14651–14660.

[43] Jiang, L.; Tang, Z.; Park-Lee, K. J.; Hess, D. W.; Breedveld, V. Fabrication of Non-Fluorinated Hydrophilic-Oleophobic Stainless Steel Mesh for Oil-Water Separation. *Sep. Purif. Technol.* **2017**, *184*, 394–403.

[44] Yang, J.; Zhang, Z.; Xu, X.; Zhu, X.; Men, X.; Zhou, X. Superhydrophilic-superoleophobic coatings. *J. Mater. Chem.* **2012**, *22*, 2834–2837.

[45] Yang, J.; Song, H.; Yan, X.; Tang, H.; Li, C. Superhydrophilic and superoleophobic chitosan-based nanocomposite coatings for oil/water separation. *Cellulose* **2014**, *21*, 1851–1857.

[46] Yang, J.; Yin, L.; Tang, H.; Song, H.; Gao, X.; Liang, K.; Li, C. Polyelelctrolyte-fluorosurfactant complex based meshes with superhydrophilicity and superoleophobicity for oil/water separation. *Chem. Eng. J.* **2015**, *268*, 245–250.

[47] Tang, H.; Fu, Y.; Yang, C.; Zhu, D.; Yang, J. A UV-driven superhydrophilic/superoleophobic polyelectrolyte multilayer film on fabric and its application in oil/water separation. *RSC Adv.* **2016**, *6*, 91301–91307.

[48] Su, C.; Yang, H.; Song, S.; Lu, B.; Chen, R. A magnetic superhydrophilic/oleophobic sponge for continuous oil-water separation. *Chem. Eng. J.* **2017**, *309*, 366–373.

[49] Liu, D.; Yu, Y.; Chen, X.; Zheng, Y. Selective Separation of Oil and Water with Special Wettability Mesh Membranes. *RSC Adv.* **2017**, *7*, 12908–12915.

[50] Ritchie, A. W.; Cox, H. J.; Barrientos-Palomo, S. N.; Sharples, G. J.; Badyal, J. P. S. Bioinspired Multifunctional Polymer–Nanoparticle–Surfactant Complex Nanocomposite Surfaces for Antibacterial Oil–Water Separation. *Colloids Surf., A* **2019**, *560*, 352–359.

[51] Molina, R.; Gomez, M.; Kan, C.-W.; Bertran, E. Hydrophilic-oleophobic coatings on cellulosic materials by plasma assisted polymerization in liquid phase and fluorosurfactant complexation. *Cellulose* **2014**, *21*, 729–739.

[52] Xu, Z.; Zhao, Y.; Wang, H.; Wang, X.; Lin, T. A Superamphiphobic Coating with an Ammonia-Triggered Transition to Superhydrophilic and Superoleophobic for Oil-Water Separation. *Angew. Chem. Int. Ed.* **2015**, *54*, 4527–4530.

[53] Qu, M.; Ma, X.; He, J.; Feng, J.; Liu, S.; Yao, Y.; Hou, L.; Liu, X. Facile Selective and Diverse Fabrication of Superhydrophobic, Superoleophobic-Superhydrophilic and Superamphiphobic Materials from Kaolin. *ACS Appl. Mater. Interfaces* **2017**, *9*, 1011–1020.

[54] Zhou, H.; Wang, H.; Yang, W.; Niu, H.; Wei, X.; Fu, S.; Liu, S.; Shao, H.; Lin, T. Durable Superoleophobic–Superhydrophilic Fabrics with High Anti-Oil-Fouling Property. *RSC Adv.* **2018**, *8*, 26939–26947.

[55] Qu, M.; Ma, L.; Zhou, Y.; Zhao, Y.; Wang, J.; Zhang, Y.; Zhu, X.; Liu, X.; He, J. Durable and Recyclable Superhydrophilic–Superoleophobic Materials for Efficient Oil/Water Separation and Water-Soluble Dyes Removal. *ACS Appl. Nano Mater.* **2018**, *1*, 5197–5209.

[56] Qu, M.; Ma, L.; Wang, J.; Zhang, Y.; Zhao, Y.; Zhou, Y.; Liu, X.; He, J. Multifunctional Superwettable Material with Smart pH Responsiveness for Efficient and Controllable Oil/Water Separation and Emulsified Wastewater Purification. *ACS Appl. Mater. Interfaces* **2019**, *11*, 24668–24682.

[57] Vaidya, A.; Chaudhury, M. K. Synthesis and Surface Properties of Environmentally Responsive Segmented Polyurethanes. *J. Colloid Interface Sci.* **2002**, *249*, 235–245.

[58] Wang, Y.; Dong, Q.; Wang, Y.; Wang, H.; Li, G.; Bai, R. Investigation on RAFT Polymerization of a Y-Shaped Amphiphilic Fluorinated Monomer and Anti-Fog and Oil-Repellent Properties of the Polymers. *Rapid Commun.* **2010**, *31*, 1816–1821.

[59] Kota, A. K.; Kwon, G.; Choi, W.; Mabry, J. M.; Tuteja, A. Hygro-responsive membranes for effective oil-water separation. *Nat. Commun.* **2012**, *3*, 1025.

[60] Tuteja, A; Kota, A. K.; Kwon, G.; Mabry, J. M. Superhydrophilic and Oleophobic Porous Materials for Making and Using the same. World Patent WO 2011159699 A2, Dec. 22, 2011.

[61] Darmanin, T.; Guittard, F. Superoleophobic polymers with metal ion affinity towards materials with both oleophobic and hydrophilic properties. *J. Colloid Interface Sci.* **2013**, *408*, 101–106.

[62] Taleb, S.; Darmanin, T.; Guittard, F. Elaboration of Voltage and Ion Exchange Stimuli-Responsive Conducting Polymers with Selective Switchable Liquid-Repellency. *ACS Appl. Mater. Interfaces* **2014**, *6*, 7953–7960.

[63] Chen, J.; Zhang, Y.; Chen, C.; Xu, M.; Wang, G.; Zeng, Z.; Wang, L.; Xue, Q. Cellulose Sponge with Superhydrophilicity and High Oleophobicity Both in Air and Under Water for Efficient Oil–Water Emulsion Separation. *Macromol. Mater. Eng.* **2017**, *302*, 1700086.

[64] Xiong, L.; Guo, W.; Alameda, B. M.; Sloan, R. K.; Walker, W. D.; Patton, D. L. Rational Design of Superhydrophilic/Superoleophobic Surfaces for Oil–Water Separation via Thiol–Acrylate Photopolymerization. *ACS Omega* **2018**, *3*, 10278–10285.

[65] Sawada, H.; Ikematsu, Y.; Kawase, T.; Hayakawa, Y. Synthesis and Surface Properties of Novel Fluoroalkylated Flip-Flop-Type Silane Coupling Agents. *Langmuir* **1996**, *12*, 3529–3530.

[66] Sawada, H.; Yasue, T. Fluoro silicone oligomers having oil repellency and hydrophilic property and their manufacture. Japanese Patent JP 09241331 A, Sept. 16, 1997.

[67] Sawada, H.; Yoshioka, H.; Ohashi, R.; Kawase, T. Synthesis and Properties of Novel Fluoroalkyl End-Capped Oligomers Containing Silsesquioxane Segments. *J. Appl. Polym. Sci.* **2002**, *86*, 3486–3493.

[68] Sasazawa, K.; Okitsu, I.; Aburatani, A.; Kawase, T.; Sawada, H. Solubilization of Phthalocyanines into Methanol with Fluoroalkyl End-Capped N-(1,1-Dimethyl-3-oxobutyl)- and N,N-Dimethyl-Acrylamide Oligomers. *J. Appl. Polym. Sci.* **2004**, *93*, 521–525.

[69] Sawada, H.; Yoshioka, H.; Kawase, T.; Takahashi, H.; Abe, A.; Ohashi, R. Synthesis and Applications of a Variety of Fluoroalkyl End-Capped Oligomers/Silica Gel Polymer Hybrids. *J. Appl. Polym. Sci.* **2005**, *98*, 169–177.

[70] Sawada, H.; Koizumi, M.; Tojo, T.; Ohnishi, T.; Tomita, T. Synthesis of novel fluoroalkyl end-capped oligomers/silica gel polymer hybrids possessing antibacterial activity. *Polym. Adv. Technol.* **2005**, *16*, 459–465.

[71] Sasazawa, K.; Kurachi, J.; Narumi, T.; Nishi, H.; Yamamoto, Y.; Sawada, H. Preparation and Applications of Novel Fluoroalkyl End-Capped Sulfonic Acid Oligomers-Silica Gel Polymer Hybrids. *J. Appl. Polym. Sci.* **2007**, *103*, 110–117.

[72] Sutoh, Y.; Tsuzuki-ishi, T.; Sugiya, M.; Sawada, H. Preparation and Applications of Fluoroalkyl End-Capped Vinyltrimethoxysilane Oligomeric Nanoparticle Ionogels. *J. Sol-Gel Sci. Technol.* **2016**, *79*, 210–219.

[73] Takashima, H.; Iwaki, K.-I.; Furukuwa, R.; Takishita, K.; Sawada, H. Preparation and applications of a variety of fluoroalkyl end-capped oligomer/hydroxyapatite composites. *J. Colloid Interface Sci.* **2008**, *320*, 436–444.

[74] Kakehi, H.; Muira, M.; Isu, N.; Sawada, H. Surface Modification of Aluminum Plate with Fluoroalkyl End-capped Acrylic Acid Oligomer/silica Nanocomposites-Oleophobic to Hydrophilic Switching Behavior Adapted to the Environmental Change on the Modified Plate Surface. *Polym. J.* **2008**, *40*, 1081–1086.

[75] Sawada, H.; Okada, Y.; Goto, Y.; Fukui, T.; Shibukawa, T.; Kodama, S.; Sugiya, M. Application of Ionic Liquid as Surface Modifier: Switching Behaviour of Novel Fluoroalkyl End-capped Vinytrimethoxysilane Oligomer – Tri-n-butyl-[(3-trimethoxysilyl)propyl] phosphonium Chloride Silica Nanocomposites between Superhydrophilicity and Oleophobicity. *J. Jpn. Soc. Colour Mater.* **2010**, *83*, 368–373.

[76] Saito, T.; Tsushima, Y.; Sawada, H. Facile creation of superoleophobic and superhydrophilic surface by using fluoroalkyl end-capped vinyltrimethoxysilane oligomer/calcium silicide nanocomposites-development of these nanocomposites to environmental cyclical type-fluorine recyle through formation of calcium fluoride. *Colloid Polym. Sci.* **2015**, *293*, 65–73.

[77] Katayama, S.; Fujii, S.; Saito, T.; Yamazaki, S.; Sawada, H. Preparation of Fluoroalkyl End-Capped Vinyltrimethoxysilane Oligomeric Silica Nanocomposites Containing Gluconamide Units Possessing Highly Oleophobic/Superhydrophilic, and Superoleophilic/Superhydrophobic Characteristics on the Modified Surfaces. *Polymers* **2017**, *9*, 292.

[78] Yamashita, K.; Sasahara, S.; Sawada, H. Preparation of Fluoroalkyl End-Capped Vinyltrimethoxysilane Oligomeric Silica/Phosphonic Acids Nanocomposites Possessing Superoleophobic/Superhydrophilic and Superoleophilic/Superhydrophobic Characteristics: Application of These Nanocomposites to the Separation of Oil and Water. *J. Coat. Technol. Res.* **2017**, *14*, 1183–1193.

[79] Ma, Z.; Zhang, S.; Chen, G.; Xiao, K.; Li, M.; Gao, Y.; Liang, S.; Huang, X. Superhydrophilic and Oleophobic Membrane Functionalized with Heterogeneously Tailored Two-Dimensional Layered Double Hydroxide Nanosheets for Antifouling. *J. Membr. Sci.* **2019**, *577*, 165–175.

[80] Fu, Y.; Jin, B.; Zhang, Q.; Zhan, X.; Chen, F. pH-Induced Switchable Superwettability of Efficient Antibacterial Fabrics for Durable Selective Oil/Water Separation. *ACS Appl. Mater. Interfaces* **2017**, *9*, 30161–30170.

[81] Liao, X.; Li, H.; Su, X.; Zhan, H.; Lai, X.; Zeng, X. Mussel-Inspired Cotton Fabric with pH-Responsive Superwettability for Bidirectional Oil–Water Separation. *J. Mater. Sci.* **2019**, *54*, 3648–3660.

[82] Huang, H.; Li, Y.; Zhao, L.; Yu, Y.; Xu, J.; Yin, X.; Chen, S.; Wu, J.; Yue, H.; Wang, H.; Wang, L. A Facile Fabrication of Chitosan Modified PPS-Based Microfiber Membrane for Effective Antibacterial Activity and Oil-In-Water Emulsion Separation. *Cellulose* **2019**, *26*, 2599–2611.

[83] Yu, Y.; Liu, M.; Huang, H.; Zhao, L.; Lin, P.; Huang, S.; Xu, J.; Wang, H.; Wang, L. Low Cost Fabrication of Polypropylene Fiber Composite Membrane with Excellent Mechanical, Superhydrophilic Antifouling and Antibacterial Properties for Effective Oil-In-Water Emulsion Separation. *React. Funct. Polym.* **2019**, *142*, 15–24.

[84] Lv, Y.; Li, Q.; Hou, Y.; Wang, B.; Zhang, T. Facile Preparation of an Asymmetric Wettability Janus Cellulose Membrane for Switchable Emulsions' Separation and Antibacterial Property. *ACS Sustainable Chem. Eng.* **2019**, *7*, 15002–15011.

[85] Upadhyay, R. K.; Dubey, A.; Waghmare, P. R.; Priyadarshini, R.; Roy, S. S. Multifunctional Reduced Graphene Oxide Coated Cloths for Oil/Water Separation and Antibacterial Application. *RSC Adv.* **2016**, *6*, 62760–62767.

[86] Liu, L.; Yuan, W. A Hierarchical Functionalized Biodegradable PLA Electrospun Nanofibrous Membrane with Superhydrophobicity and Antibacterial Properties for Oil/Water Separation. *New J. Chem.* **2018**, *42*, 17615–17624.

[87] Zhang, Y.; Yin, M.; Lin, X.; Ren, X.; Huang, T.-S.; Kim, I. S. Functional Nanocomposite Aerogels Based on Nanocrystalline Cellulose for Selective Oil/Water Separation and Antibacterial Applications. *Chem. Eng. J.* **2019**, *371*, 306–313.